Computational Modeling of Multiphysics Multidomain Multiphase Flow in Fracturing Porous Media

Leakage Hazards in CO_2 Geosequestration

Mehdi Musivand Arzanfudi

Computational Modeling of Multiphysics Multidomain Multiphase Flow in Fracturing Porous Media

Leakage Hazards in CO_2 Geosequestration

Mehdi Musivand Arzanfudi

Computational Modeling of Multiphysics Multidomain Multiphase Flow in Fracturing Porous Media

Leakage Hazards in CO_2 Geosequestration

Proefschrift

ter verkrijging van de graad van doctor
aan de Technische Universiteit Delft,
op gezag van de Rector Magnificus prof.ir. K.C.A.M. Luyben;
voorzitter van het College voor Promoties,
in het openbaar te verdedigen op
vrijdag 4 november 2016 om 10:00 uur

door

Mehdi MUSIVAND ARZANFUDI

PhD degree in Aerospace Engineering,
Master of Science in Aerospace Engineering,
Amirkabir University of Technology
geboren te Hamedan, Iran

Dit proefschrift is goedgekeurd door de

promotor: Prof. dr. ir. L.J. Sluys
copromotor: Dr. R. Al-Khoury

Samenstelling promotiecommissie

Rector Magnificus,	voorzitter
Prof. dr. ir. L.J. Sluys,	Technische Universiteit Delft, promotor
Dr. R. Al-Khoury,	Technische Universiteit Delft, copromotor

Onafhankelijke leden:

Prof. dr. M. Celia,	Princeton University, USA
Prof. dr. ing. R. Helmig,	Universität Stuttgart, Germany
Prof. dr. C. Jommi,	Technische Universiteit Delft
Prof. dr. B.A. Schrefler,	University of Padova, Italy
Prof. dr. R. Zimmerman,	Imperial College London, UK
Prof. dr. M.A. Hicks,	Technische Universiteit Delft, reserve lid

ISBN 978-94-6186-727-8

Summary

Geological CO_2 sequestration, also known as CO_2 geo-sequestration, is a process to mitigate CO_2 emission into the earth atmosphere in an attempt to reduce the likely greenhouse effect. It involves injection of carbon dioxide, normally in a supercritical state, into a carefully selected underground formation. Selection of an appropriate geological formation for CO_2 geo-sequestration requires a good knowledge of the involved processes and phenomena that occur at the subsurface, and in particular, an estimate of the amount of leakage that might take place in time. Modeling leakage of CO_2 in a deformable porous medium constitutes the focal point of this thesis.

To this aim, a computationally efficient multiphysics multidomain multiphase numerical modeling framework has been developed which accounts for all important physical processes, interacting domains, and different material phases. The computational efficiency is achieved via tailoring several state of the art numerical techniques in order to attain an accurate, geometry-independent, and mesh-independent model. Deriving such a model for thermo-hydrodynamic-mechanical behavior of a multiphase domain, exhibiting deformation and crack propagation requires a well-designed conceptual model, a descriptive mathematical formulation and an innovative numerical method. The conceptual model distinguishes different domains representing a porous matrix domain, an abandoned wellbore domain, a fracture domain and a fracture-matrix domain. The mathematical formulation adopts the representative elementary volume (REV) averaging based conservation equations for porous media, the drift-flux model averaging of Navier-Stokes equations for the wellbore and fracture domains, and equations of state and constitutive relationships for the involved brine, CO_2, air, and solid phases. The numerical solution method adopts a mixed discretization scheme, in which, the standard Galerkin finite element method (SG), the partition of unity finite element method (PUM) within the framework of the extended finite element method (XFEM), and the level-set method (LS) are tailored together to obtain an accurate, geometry-independent, and mesh-independent solution.

The thesis introduces four computational models. The first model deals with CO_2 leakage via formation layer boundaries, which is capable of simulating multiphase flow in rigid heterogeneous layered porous media, with particular emphasis on the inter-layer leakage of CO_2. This model is presented in Chapter 2. The second model deals with CO_2 leakage via abandoned wellbores, which is capable of simulating all important physical phenomena and processes occurring along the wellbore path, including fluid dynamics, buoyancy, phase change, compressibility, thermal interaction, wall friction and slip between phases, together with a jump in density and enthalpy between the air and the CO_2. This model is presented in Chapter 3. The third model introduces the integration of the first and second models to create an integrated wellbore-reservoir

numerical tool for the simulation of sequestrated CO_2 multi-path leakage through formation layers and abandoned wellbores. This model is presented in Chapter 4. Finally, the fourth model deals with fracturing and CO_2 leakage through cracks. It presents a fully coupled thermo-hydrodynamic-mechanical computational model for multiphase flow in a deformable and fracturing porous media. This model is presented in Chapter 5. These four models cover all important CO_2 sequestration processes and leakage mechanisms which might occur in a CO_2 geo-sequestration site.

The numerical examples show that the proposed computational model, despite the relatively large number of degrees of freedom of different physical nature per node, is computationally efficient. Physically, the numerical examples show that for the normal initial and boundary conditions encountered in CO_2 geo-sequestration, leakage via abandoned wellbores and leakage via formation layers can be equally important. Deformation and fracturing, together with leakage via the fractures seem, following the studied cases, a secondary concern. Although the leakage via abandoned wellbores and the leakage via formation layers appear to be equally important in terms of the quantity of leaked CO_2, the leakage through the wellbore comes with a greater risk because it can rapidly reach the ground surface. The results of leakage via the fractures show that, in case of having a relatively less permeable cap-rock, the risk of leakage via the fractures increases.

The proposed computational models presented in this thesis can be utilized as a framework for the development of efficient and comprehensive numerical software, in such a way that engineers can carry out realistic simulations on relatively limited hardware resources and CPU time. This is due to the computational efficiency of the proposed mixed discretization scheme. Further extensions of this work include: tailoring to other applications, improvement of the constitutive relationships of the solid phase, adding crack initiation and velocity, and adding dynamic forces effects to the solid medium in order to account for the seismic forces.

Samenvatting

Ondergrondse opslag van CO_2, ook wel bekend als CO_2 geo-sequestratie, is een proces om de CO_2-uitstoot in de atmosfeer van de aarde te verminderen, in een poging om waarschijnlijke broeikaseffecten te verminderen. Het gaat om de injectie van kooldioxide, gewoonlijk in een superkritische toestand, in zorgvuldig geselecteerde ondergrondse formaties. Keuze van een geschikte geologische formatie voor CO_2 geo-sequestratie vereist een goede kennis van de relevante processen en fenomenen die in de ondergrond gebeuren, en in het bijzonder, een schatting van de hoeveelheid gelekte CO_2 in de tijd. Modelleren van lekkage van CO_2 in een vervormbaar poreus medium is het hoofdthema van dit proefschrift.

Met dit doel, is een numeriek efficiënt multifysisch multidomein multifase rekenraamwerk ontwikkeld, dat rekening houdt met alle belangrijke fysische processen, interactiedomeinen en verschillende fasen van het materiaal. De numerieke efficiëntie wordt bereikt door het afstemmen van verschillende geavanceerde numerieke technieken om een nauwkeurig geometrie-onafhankelijk en mesh-onafhankelijk model te realiseren. Afleiden van een dergelijk model voor thermo-hydrodynamisch-mechanisch gedrag in een multifase domein, rekening houdend met vervorming en scheurgroei, vereist een goed ontworpen conceptueel model, een beschrijvende wiskundige formulering en een innovatieve numerieke methode. Het conceptueel model bestaat uit verschillende domeinen, namelijk een poreus matrix domein, een verlaten boorput domein, en een breuk domein. De wiskundige formulering is opgebouwd uit een representatief elementair volume (REV) op basis van middeling van behoudswetten voor poreuze media, een drift-flux model middeling van Navier-Stokes vergelijkingen voor de boorput en de breuk domeinen, en toestandsvergelijkingen en constitutieve relaties voor de pekel, CO_2, lucht en vaste fasen. De numerieke methode gebruikt een gemengde discretisatie, waarin de standaard Galerkin eindige elementenmethode (SG), de “partition of unity” eindige elementenmethode (PUM) in het kader van de uitgebreide eindige elementenmethode (XFEM), en de “level-set” methode (LS) gekoppeld zijn om een nauwkeurige, geometrie-onafhankelijke, en mesh-onafhankelijke oplossing te verkrijgen.

Het proefschrift introduceert vier numerieke modellen. Het eerste model heeft betrekking op CO_2-lekkage via laaggrenzen van de ondergrondse formaties, dat in staat is multifase stroming in stijve heterogene gelaagde poreuze media te simuleren, met bijzondere nadruk op de tussen-laagse lekkage van CO_2. Dit model wordt beschreven in Hoofdstuk 2. Het tweede model behandelt CO_2 lekkage via verlaten putboringen, die belangrijke fysische verschijnselen en processen kan nabootsen die zich voor doen langs

het boorput pad, zoals vloeistofdynamica, drijfvermogen, faseverandering, samendrukbaarheid, thermische interactie, wandwrijving en slip tussen fasen. Dit gaat gepaard met een sprong in de dichtheid en enthalpie tussen de lucht en het CO_2. Dit model wordt beschreven in Hoofdstuk 3. Het derde model introduceert de integratie van de eerste twee modellen om een geïntegreerd boorput-reservoir numeriek model voor het simuleren van multi-pad lekkage van CO_2 door de lagen en verlaten boorputten te realiseren. Dit model wordt gepresenteerd in Hoofdstuk 4. Tot slot gaat het vierde model over scheuren en CO_2-lekkage via deze scheuren. Het representeert een volledig gekoppeld thermo-hydrodynamisch-mechanisch numeriek model voor multifase stroming in een gedeformeerd en scheurend poreus medium. Dit model wordt gepresenteerd in Hoofdstuk 5. Deze vier modellen hebben betrekking op alle belangrijke CO_2-sequestratie processen en lekkage mechanismen die ter plaatse kunnen optreden tijdens CO_2 geo-sequestratie.

De numerieke voorbeelden tonen aan dat het voorgestelde numeriek model, ondanks het relatief grote aantal vrijheidsgraden van verschillend fysische aard per knoop, numeriek efficiënt is. Fysisch, laten de numerieke voorbeelden zien dat voor de normale begin- en grenscondities aangetroffen in CO_2 geo-sequestratie lekkage via verlaten boorputten en lekkage via de lagen van de formaties net zo belangrijk kan zijn. Naar aanleiding van de bestudeerde gevallen, blijken vervorming en scheuren, samen met lekkage via de scheuren, van secundaire zorg te zijn. Hoewel de lekkage via verlaten boorputten en de lekkage via formaties even belangrijk lijkt te zijn voor de hoeveelheid gelekte CO_2, brengt de lekkage door de boorput een groter risico met zich mee, omdat het snel het maaiveld kan bereiken. Uit de resultaten van lekkage via de scheuren blijkt dat bij een relatief minder doorlatende afsluitende laag het risico van lekkage via de scheuren toeneemt.

De voorgestelde numerieke modellen in dit proefschrift kunnen worden gebruikt als een kader voor de ontwikkeling van efficiënte en uitgebreide numerieke software, op een zodanige wijze dat ingenieurs realistische simulaties op relatief beperkte hardware middelen en in beperkte CPU-tijd kunnen uitvoeren. Dit komt door de numerieke efficiëntie van de voorgestelde gemengde discretisatie. Toekomstige uitbreidingen van het huidige werk: gebruik voor andere toepassingen, verbetering van de constitutieve relaties van de vaste fase, toevoegen van scheur-initiatie en snelheid, en het toevoegen van dynamische kracht effecten op het vaste medium ter verrekening van de seismische krachten.

Contents

1

Introduction

The main objective of this thesis is the development of a computational tool for the simulation of CO_2 sequestration in geological formations. Focus is placed on modeling the thermo-hydrodynamic-mechanical behavior of the sequestered CO_2, the hosting porous medium reservoir, and the surrounding layer formations.

Development of an accurate and computationally efficient computational tool for such a physical domain requires a well-designed conceptual model, a descriptive mathematical formulation and an innovative numerical solution. This chapter gives a short introduction to these three modeling aspects. The conceptual model is designed to describe the involved physical geometry and processes, which comprise almost all important phenomena occurring in short and long terms. The mathematical formulation comprises basic balance equations, which are necessary to describe CO_2 geosequestration, and detailed constitutive relationships, necessary for describing the formation brine, the CO_2 and the air. Details of the balance equations are given in the subsequent chapters. The numerical solution method comprises the novelty of the discretization technique and the multi-domain coupling procedure. A brief description of the objectives of this work and the thesis outline is also given.

1.1 Conceptual model

1.1.1 Physical processes

Geological CO_2 sequestration, commonly known as CO_2 geo-sequestration, involves injection of carbon dioxide, normally in a supercritical state, into a carefully selected underground formation. Oil and gas fields, saline formations, coal seams, and saline-filled basalt formations have been suggested as feasible storage sites. CO_2 injected into saline formations basically undergoes four storage (trapping) mechanisms (Fig. 1.1).

During the injection stage, and in the first couple of years after injection, the dominant process is advective two-phase flow, when the CO_2 systematically displaces the formation brine under its buoyancy forces and rises to the top of the reservoir, to be trapped underneath an impermeable cap rock layer. This period is identified as the structural or stratigraphic trapping mechanism. Residual trapping simultaneously occurs in this period where an important amount of CO_2 molecules resides in the formation pores. At a later stage, the CO_2 starts to dissolve in the brine and the brine dissolves in CO_2. In the long term, chemical reactions between the CO_2-water mix and the formation solid phase will take place.

The focus of this work is placed on the structural stratigraphic trapping. This means that dissolution, diffusion, and chemical reactions are not considered. All other important physical processes and phenomena, including buoyancy, phase change, compressibility of fluids and solid skeleton, thermal effects, including convective and conductive heat transfer as well as dependency on temperature of the fluid properties, wall friction, slip between phases are, wherever applied, considered.

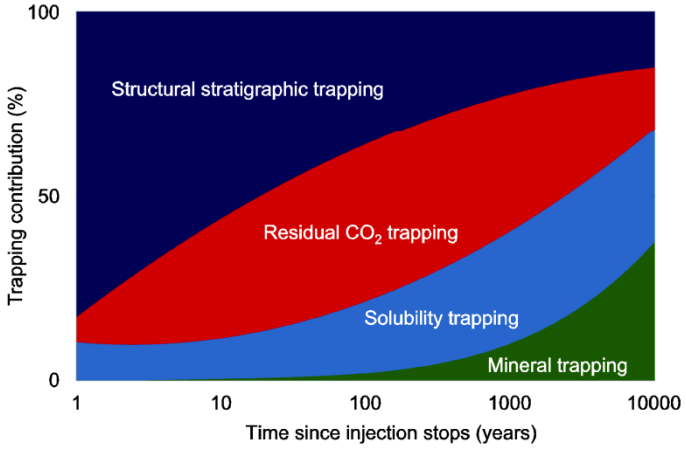

Fig. 1.1 CO_2 trapping mechanisms over time (see Metz et al. 2005)

1.1.2 Modeling approach

The geometry is assumed to comprise a permeable reservoir surrounded by geological formations of different physical properties. The CO_2 is injected at a point or a surface at the side or bottom of the reservoir. The reservoir is bounded by a cap rock which can be impermeable or weakly permeable. The cap rock can be fractured and a crack might propagate through it. The geometry may contain abandoned wellbores which can go through the whole domain and reaching to the ground surface. In this thesis, the geometry of the formation layers is assumed two-dimensional, though the mathematical formulation is three-dimensional. Thus, in terms of computational mechanics, the numerical solution can readily be extended to three-dimensions, but in terms of software

development, it is demanding. The abandoned wellbores and the cracks are considered one-dimensional. Fig. 1.2. shows schematically the conceptual geometry.

Three interacting phases exist in the domain: a solid phase, referred to as the porous matrix; a brine phase, referred to as the wetting phase; and a CO_2 phase, referred to as the non-wetting phase. The solid phase exhibits deformation and crack propagation due to combined mechanical, hydraulic, thermomechanical, and fluid dynamic forces. The brine phase exists initially in the reservoir and exhibits flow due to Darcy and buoyancy forces. It is compressible and can change mass density and viscosity with temperature and pressure. The CO_2 phase is compressible and can change phase due to changing pressure and temperature.

Two interacting fluid flow mechanisms exist: a Darcy flow mechanism, and a Navier-Stokes flow mechanism. The first occurs in the porous formation layers, and the second occurs in the abandoned wellbores and the fractures.

Three interacting leakage mechanisms exist: (i) leakage through layers boundaries; (ii) leakage through crack aperture or wellbore sealing cap; and/or (iii) leakage through the fracture-matrix boundaries.

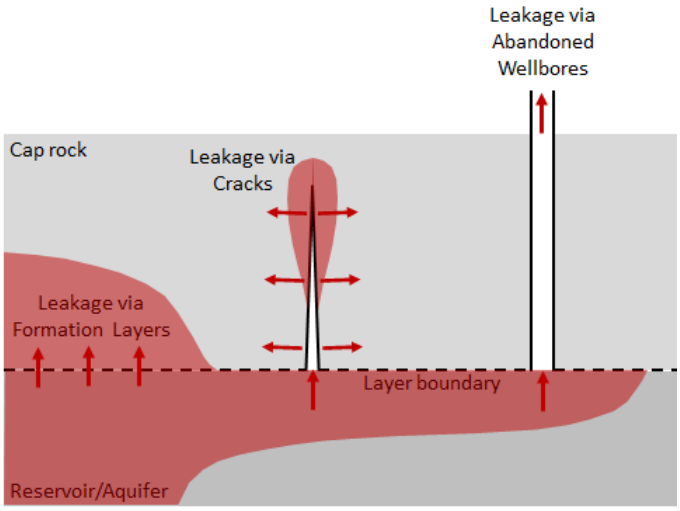

Fig. 1.2 Modeling approach

1.2 Mathematical formulation

Describing the conceptual model mathematically requires basically two theories: poromechanics and fluid dynamics. The poromechanics theory is utilized to describe the thermo-hydro-mechanical behavior of the porous domain, and the fluid dynamics theory is utilized to describe the behavior of the fluid flow in the wellbores and the fractures. For the first, the fluid flow is governed by Darcy's law, and for the second, the fluid flow is governed by the Navier-Stokes equations. The solid phase behavior is governed

by the equilibrium equations for static condition. The averaging theory is utilized for both, the porous domain and the fluid dynamics domains.

In this section, the basic balance equations for multiphase fluid and heat flow in a deformable porous domain and for fluid dynamics are given. Details of balance equations for specific applications are given in their corresponding chapters.

1.2.1 Porous medium balance equations

The use of averaging procedure to describe physical and/or chemical processes and phenomena at the macroscopic level of a porous medium domain is inevitable due to the fact that such a domain is highly heterogeneous and its geometry is complicated, and, for geological formations, out of reach. The REV averaging theory is utilized in this work (Fig. 1.3).

In the REV averaging theory, the macroscopic quantities are obtained from local volume/mass averaging of the corresponding microscopic quantities. The interfacial effects are explicitly accounted for, including the possibility of exchange of mass, momentum and energy between the constituents. The averaging process is conducted by integrating the involved microscopic quantities over a REV of volume dv and area da. REV is chosen considerably larger than the constituent individual size scales, and at the same time a lot smaller than the size scale of the physical system. The multiphase domain is postulated as a superposition of all involved phases, and each spatial point is simultaneously occupied by the material points of all phases. However, the state of motion of each phase is described independently. The averaging theory has been described elegantly by Lewis and Schrefler (1998), from whom this outline is derived.

The averaged macroscopic conservation equation can be written as (Lewis and Schrefler 1998)

$$\underbrace{\frac{\partial}{\partial t}\left(\langle\rho\rangle_\pi \bar{\psi}_\pi\right)}_{\text{storage}} + \underbrace{\operatorname{div}\left(\langle\rho\rangle_\pi \bar{\psi}_\pi \bar{\mathbf{v}}_\pi\right)}_{\text{advection}} - \underbrace{\operatorname{div}\mathbf{i}_\pi}_{\text{diffussion}} - \underbrace{\langle\rho\rangle_\pi \bar{b}_\pi}_{\text{external supply}} - \underbrace{\langle\rho\rangle_\pi e_\pi(\rho\psi)}_{\substack{\text{inter-phase interaction} \\ \text{due to mass exchange}}} - \underbrace{\langle\rho\rangle_\pi I_\pi}_{\substack{\text{inter-phase mechanical} \\ \text{interaction}}} = \underbrace{\langle\rho\rangle_\pi \bar{G}_\pi}_{\text{net production}} \tag{1.1}$$

subjected to

$$\sum_\pi \langle\rho\rangle_\pi \left[e_\pi(\rho\psi) + I_\pi\right] = 0 \tag{1.2}$$

where π is a phase, the superscript bar denotes a mass averaged value, $\langle\ \rangle_\pi$ is the volume average operator, ρ is the mass density, ψ is a generic conserved variable, G is the net production of ψ; $\mathbf{i}_\pi$ is the flux vector associated with $\bar{\psi}_\pi$; $\bar{b}_\pi$ is an external

supply associated with $\overline{\psi}_\pi$; and $\overline{\mathbf{v}}_\pi$ is the mass averaged velocity of π phase. The last two terms on the left-hand side of Eq. (1.1) describe possible chemical and physical exchanges between phases: $e_\pi(\rho\psi)$ describes an exchange term associated with ψ due to phase changes or mass exchanges between phases, and I_π describes the mechanical interaction between phases.

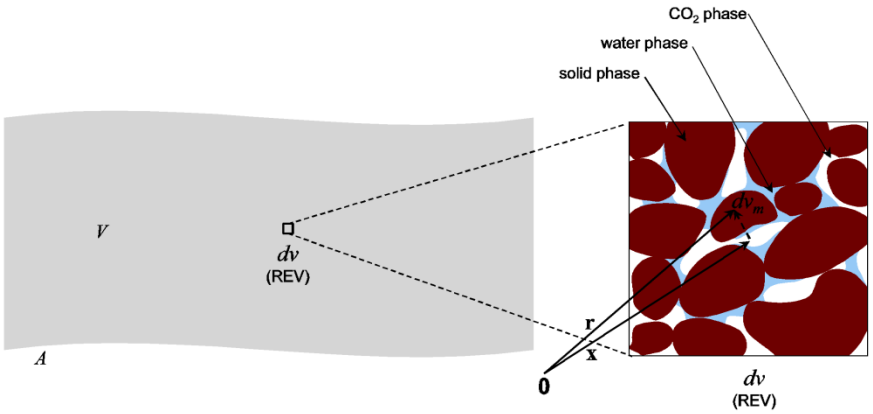

Fig. 1.3 REV of a multiphase medium.

1.2.1.1 Linear momentum balance equation

The averaged macroscopic linear momentum balance equation of phase $\pi = s, w, \mathrm{CO}_2$ can be derived from Eq. (1.1), by specifying (Lewis and Schrefler 1998)

$$\overline{\boldsymbol{\psi}}_\pi = \overline{\mathbf{v}}_\pi$$

$$\mathbf{i}_\pi = \breve{\mathbf{t}}_\pi \qquad \text{such that} \qquad \breve{\mathbf{t}}_\pi \cdot \mathbf{n} = \frac{1}{da}\int_{da} (\mathbf{t} - \rho\tilde{\dot{\mathbf{r}}}_\pi \otimes \tilde{\dot{\mathbf{r}}}_\pi)\cdot\mathbf{n}\gamma_\pi da_m$$

$$\overline{\mathbf{b}}_\pi = \overline{\mathbf{g}}_\pi = \frac{1}{\langle\rho\rangle_\pi\, dv}\int_{dv} \rho\mathbf{g}\gamma_\pi dv_m$$

$$\overline{\mathbf{G}}_\pi = 0 \tag{1.3}$$

$$e_\pi(\rho\dot{\mathbf{r}}) = \frac{1}{\langle\rho\rangle_\pi\, dv}\sum_{\alpha\neq\pi}^{k}\int_{da_{\pi\alpha}} \rho\left[\mathbf{v}_\pi \otimes (\mathbf{w} - \dot{\mathbf{r}})\right]\mathbf{t}\cdot\mathbf{n}_{\pi\alpha} da_m$$

$$\mathbf{I}_\pi = \mathbf{T}_\pi = \frac{1}{\langle\rho\rangle_\pi\, dv}\sum_{\alpha\neq\pi}^{k}\int_{da_{\pi\alpha}} \mathbf{t}\cdot\mathbf{n}_{\pi\alpha} da_m$$

where $\breve{\mathbf{t}}_\pi$ is the intra-phase stress tensor, $\bar{\mathbf{g}}_\pi$ describes the external momentum supply related to the gravitational forces, $e_\pi(\rho\dot{\mathbf{r}})$ is the momentum exchange between phases due to mass exchange, and $\mathbf{T}_\pi$ is the momentum exchange due to mechanical interaction between phases in-contact. In what follows, we assume $\bar{\mathbf{g}}_\pi = \mathbf{g}$, a constant gravitational acceleration.

For a linear isotropic solid, using the entropy inequality of Hassanizadeh and Gray (1990), and taking the solid grain compressibility into consideration via what is known as Biot's constant, α, the momentum balance equation for the multiphase domain can be derived from Eqs. (1.1) and (1.3), with $\pi = s$, as (Lewis and Schrefler 1998)

$$\mathrm{div}\left[\mathbf{D}(\mathbf{Lu} - \frac{1}{3}\mathbf{m}\beta_s T) - \mathbf{I}\alpha(S_w p_w + S_{\mathrm{CO}_2} p_{\mathrm{CO}_2})\right] + \rho_{eff}\,\mathbf{g} = 0 \qquad (1.4)$$

in which $\mathbf{D}$ is the stiffness matrix of the solid, $\mathbf{L}$ is the displacement-strain operator, $\mathbf{u}$ is the displacement vector of the solid phase, β_s is the thermal expansion coefficient of solid phase, $\mathbf{m} = \begin{bmatrix}1 & 1 & 1 & 0 & 0 & 0\end{bmatrix}^T$, and $\mathbf{I}$ is the identity tensor.

The linear momentum equation of the fluid phases can be derived from Eqs. (1.1) and (1.3), with $\pi = w, \mathrm{CO}_2$, and described in terms of Darcy's law, as (Lewis and Schrefler 1998):

Water phase

$$\phi S_w \bar{\mathbf{v}}_{w/s} = \frac{\mathbf{k}k_{rw}}{\mu_w}\left(-\nabla p_w + \left\langle\left\langle \rho \right\rangle\right\rangle_w \mathbf{g}\right) \qquad (1.5)$$

CO_2 phase

$$\phi S_{\mathrm{CO}_2} \bar{\mathbf{v}}_{\mathrm{CO}_2/s} = \frac{\mathbf{k}k_{r\mathrm{CO}_2}}{\mu_{\mathrm{CO}_2}}\left(-\nabla p_{\mathrm{CO}_2} + \left\langle\left\langle \rho \right\rangle\right\rangle_{\mathrm{CO}_2} \mathbf{g}\right) \qquad (1.6)$$

where $\left\langle\left\langle\ \right\rangle\right\rangle_\pi$ is the intrinsic volume average operator, $\mathbf{k}$ is the intrinsic permeability tensor, k_{rw} and $k_{r\mathrm{CO}_2}$ are the water and CO_2 phases relative permeability (functions of saturation), respectively; μ_w and μ_{CO_2} are the water and CO_2 phases viscosity, respectively; and $\bar{\mathbf{v}}_{w/s}$ and $\bar{\mathbf{v}}_{\mathrm{CO}_2/s}$ are the mass averaged values of the water and CO_2 phases relative to the solid phase, respectively.

1.2.1.2 Mass balance equations

The averaged macroscopic balance equation of phase $\pi = s, w, \mathrm{CO}_2$ can be derived from Eq. (1.1) by specifying:

Solid phase

$$\bar{\psi}_\pi = 1 \quad ; \quad \mathbf{i}_\pi = 0 \quad ; \quad \bar{b}_\pi = 0 \quad ; \quad I_\pi = 0 \quad ; \quad \bar{G}_\pi = 0 \quad ; \quad \langle \rho \rangle_\pi \, e_\pi(\rho) = 0 \tag{1.7}$$

Water phase

$$\bar{\psi}_w = 1 \quad ; \quad \mathbf{i}_w = 0 \quad ; \quad \bar{b}_w = 0 \quad ; \quad I_w = 0 \quad ; \quad \bar{G}_w = 0 \quad ; \quad \langle \rho \rangle_w \, e_w(\rho) = -\dot{m} \tag{1.8}$$

CO_2 phase

$$\begin{aligned} &\bar{\psi}_{CO_2} = 1 \quad ; \quad \mathbf{i}_{CO_2} = 0 \quad ; \quad \bar{b}_{CO_2} = 0 \quad ; \quad I_{CO_2} = 0 \quad ; \quad \bar{G}_{CO_2} = 0 \\ &\langle \rho \rangle_{CO_2} \, e_{CO_2}(\rho) = +\dot{m} \end{aligned} \tag{1.9}$$

where $\dot{m}$ is the mass exchange between two phases.

In this thesis, the fluid is assumed homogeneous, compressible and non-isothermal, and exhibits no diffusion and no mass exchange. In this case, the mass balance equations for the fluid phases can be derived as (Arzanfudi and Al-Khoury 2014):

CO_2 component mass balance equation

$$\begin{aligned} &\left(\frac{\alpha - \phi}{K_s} \rho_{CO_2} S_{CO_2} + \phi S_{CO_2} \frac{\partial \rho_{CO_2}}{\partial p_w} \right) \frac{\partial p_w}{\partial t} + \alpha \rho_{CO_2} S_{CO_2} \mathbf{m}^T \mathbf{L} \frac{\partial \mathbf{u}}{\partial t} \\ &- \left(\rho_{CO_2} S_{CO_2} \beta_s (\alpha - \phi) - \phi S_{CO_2} \frac{\partial \rho_{CO_2}}{\partial T} \right) \frac{\partial T}{\partial t} \\ &- \left(\frac{\alpha - \phi}{K_s} \rho_{CO_2} S_{CO_2} \left(p_w - p_{CO_2} - S_{CO_2} \frac{\partial p_c}{\partial S_{CO_2}} \right) \right. \\ &\qquad \left. - \phi \left(\rho_{CO_2} - S_{CO_2} \frac{\partial \rho_{CO_2}}{\partial p_c} \frac{\partial p_c}{\partial S_{CO_2}} \right) \right) \frac{\partial S_{CO_2}}{\partial t} \\ &- \operatorname{div} \left(\rho_{CO_2} \frac{\mathbf{k} k_{rCO_2}}{\mu_{CO_2}} \nabla p_w \right) - \operatorname{div} \left(\rho_{CO_2} \frac{\mathbf{k} k_{rCO_2}}{\mu_{CO_2}} \frac{\partial p_c}{\partial S_{CO_2}} \nabla S_{CO_2} \right) \\ &+ \operatorname{div} \left(\rho_{CO_2} \frac{\mathbf{k} k_{rCO_2}}{\mu_{CO_2}} \rho_{CO_2} \mathbf{g} \right) = 0 \end{aligned} \tag{1.10}$$

Water component mass balance equation

$$\begin{aligned}
&\left(\frac{\alpha-\phi}{K_s}\rho_w S_w+\phi S_w\frac{\partial\rho_w}{\partial p_w}\right)\frac{\partial p_w}{\partial t}+\alpha\rho_w S_w\mathbf{m}^T\mathbf{L}\frac{\partial\mathbf{u}}{\partial t}\\
&\quad-\left(\rho_w S_w\beta_s(\alpha-\phi)-\phi S_w\frac{\partial\rho_w}{\partial T}\right)\frac{\partial T}{\partial t}\\
&\quad-\left(\frac{\alpha-\phi}{K_s}\rho_w S_w\left(p_w-p_{\mathrm{CO}_2}-S_{\mathrm{CO}_2}\frac{\partial p_c}{\partial S_{\mathrm{CO}_2}}\right)+\phi\rho_w\right)\frac{\partial S_{\mathrm{CO}_2}}{\partial t}\\
&\quad-\mathrm{div}\left(\rho_w\frac{\mathbf{k}k_{rw}}{\mu_w}\nabla p_w\right)+\mathrm{div}\left(\rho_w\frac{\mathbf{k}k_{rw}}{\mu_w}\rho_w\mathbf{g}\right)=0
\end{aligned}\tag{1.11}$$

1.2.1.3 Energy balance equation

The average macroscopic energy balance equation of phase $\pi=s,w,\mathrm{CO}_2$ can be obtained from Eq. (1.1) by specifying (Lewis and Schrefler 1998)

$$\begin{aligned}
&\bar{\psi}_\pi=\bar{E}_\pi+\frac{1}{2}\bar{\mathbf{v}}_\pi\cdot\bar{\mathbf{v}}_\pi\\
&i_\pi=\breve{\mathbf{t}}_\pi\cdot\bar{\mathbf{v}}_\pi-\breve{q}_\pi\\
&\quad\text{where}\quad\breve{q}_\pi=\mathrm{div}\breve{\mathbf{q}}_\pi=\frac{1}{da}\int_{da}\left(\mathbf{t}\cdot\tilde{\dot{\mathbf{r}}}-\mathbf{q}-\rho\left(E+\frac{1}{2}\tilde{\dot{\mathbf{r}}}_\pi\cdot\tilde{\dot{\mathbf{r}}}_\pi\right)\tilde{\dot{\mathbf{r}}}_\pi\right)\cdot\mathbf{n}\gamma_\pi da_m\\
&\bar{b}_\pi=\mathbf{g}\cdot\bar{\mathbf{v}}_\pi+h_\pi\\
&I_\pi=\mathbf{T}_\pi\cdot\bar{\mathbf{v}}_\pi+Q_\pi\quad\text{where}\qquad Q_\pi=\frac{1}{\langle\rho\rangle_\pi dv}\sum_{\alpha\neq\pi}^{k}\int_{da^{\pi\alpha}}(\mathbf{t}\cdot\tilde{\dot{\mathbf{r}}}-\mathbf{q})\cdot\mathbf{n}^{\pi\alpha}da_m\\
&e_\pi(\rho\psi)=\mathbf{e}_\pi(\rho\tilde{\dot{\mathbf{r}}}^\pi)\cdot\bar{\mathbf{v}}^\pi+\frac{1}{2}e_\pi(\rho)\bar{\mathbf{v}}^\pi\cdot\bar{\mathbf{v}}^\pi+e_\pi(\rho E')\quad\text{with}\qquad E'=E+\frac{1}{2}\tilde{\dot{\mathbf{r}}}_\pi\cdot\tilde{\dot{\mathbf{r}}}_\pi\\
&\bar{G}_\pi=0
\end{aligned}\tag{1.12}$$

where $\bar{E}_\pi$ is the averaged specific energy, $\breve{\mathbf{t}}_\pi$ and $\mathbf{T}_\pi$ are the macroscopic stress tensors, defined in Eq. (1.3), $\breve{\mathbf{q}}_\pi$ is the macroscopic heat flux vector, h_π is the intrinsic heat source, Q_π is the energy exchange due to mechanical interaction, and $e_\pi(\rho\psi)$ represents the exchange of internal energy due to phase change and mass exchange.

In case of no diffusion and no mass exchange, the energy balance equation for the multiphase domain can be derived from Eqs. (1.1) and (1.12) as (Lewis and Schrefler 1998)

$$\left((1-\phi)\rho_s C_s^p + \phi S_w \rho_w C_w^p + \phi S_{\mathrm{CO}_2} \rho_{\mathrm{CO}_2} C_{\mathrm{CO}_2}^p\right)\frac{\partial T}{\partial t} + \left(\rho_w C_w^p \left(\frac{\mathbf{k}k_{rw}}{\mu_w}\left(-\nabla p_w + \rho_w \mathbf{g}\right)\right) + \rho_{\mathrm{CO}_2} C_{\mathrm{CO}_2}^p \left(\frac{\mathbf{k}k_{r\mathrm{CO}_2}}{\mu_{\mathrm{CO}_2}}\left(-\nabla p_{\mathrm{CO}_2} + \rho_{\mathrm{CO}_2}\mathbf{g}\right)\right)\right)\cdot\nabla T - \nabla^T\cdot\left(\boldsymbol{\lambda}_{eff}\nabla T\right) = 0 \tag{1.13}$$

in which $\boldsymbol{\lambda}_{eff} = \boldsymbol{\lambda}_s + \boldsymbol{\lambda}_w + \boldsymbol{\lambda}_{\mathrm{CO}_2}$, is the effective thermal conductivity of the multiphase medium; $\boldsymbol{\lambda}_w$, $\boldsymbol{\lambda}_{\mathrm{CO}_2}$, and $\boldsymbol{\lambda}_s$ are the thermal conductivity of the wetting, non-wetting and solid phases, respectively; and C_w^p, $C_{\mathrm{CO}_2}^p$, and C_s^p are the isobaric specific heat capacity of the wetting, non-wetting and solid phases, respectively.

1.2.2 Fluid dynamics balance equations

The dynamics of fluid flow in a wellbore or a fracture is governed by Navier-Stokes equations. A general description of the Navier-Stokes equations is given in this section (Reddy and Gartling 2010; Lewis et al. 2004). Specific details of these equations will be given in the subsequent chapters.

The fluid is represented as a continuum, and the equations encompass the conservation of mass, momentum and energy.

Mass balance

$$\frac{\partial \rho}{\partial t} + \nabla\cdot\left(\rho\mathbf{v}\right) = 0 \tag{1.14}$$

where ρ is the mass density of the fluid, and $\mathbf{v}$ is the velocity vector.

Momentum balance

$$\frac{\partial\left(\rho\mathbf{v}\right)}{\partial t} + \mathrm{div}\left(\rho\mathbf{v}\otimes\mathbf{v}\right) = -\nabla p + \mathrm{div}\boldsymbol{\tau} + \rho\mathbf{g} \tag{1.15}$$

where p is the pressure, $\mathbf{g}$ is the gravitational vector, and $\boldsymbol{\tau}$ is the deviatoric stress tensor, expressed as

$$\boldsymbol{\tau} = \mu\left(\nabla\mathbf{v} + \nabla^T\mathbf{v}\right) + \lambda\mathrm{div}\left(\mathbf{v}\right)\mathbf{I} \tag{1.16}$$

in which μ and λ are the Lamé parameters, and **I** is the identity tensor.

Energy balance

$$\frac{\partial(\rho E)}{\partial t} + \mathrm{div}(\rho E\mathbf{v} + p\mathbf{v}) = \mathrm{div}(k\nabla T) + \mathrm{div}(\boldsymbol{\tau}\mathbf{v}) + \rho\mathbf{g}\cdot\mathbf{v} \qquad (1.17)$$

where $E = e + |\mathbf{v}|^2/2$ is the total energy, and e is the internal energy.

1.2.3 Constitutive models

In this section, details of the constitutive relationships for the CO_2, brine and air are given. The CO_2 is assumed compressible and exhibits phase change. The water is assumed compressible and its mass density and viscosity can change with temperature and pressure. The air is assumed an ideal gas.

1.2.3.1 CO_2 constitutive relationships

Sequestered CO_2 in a geological formation most likely exists in a supercritical state. When the CO_2 plume reaches a crack or an abandoned wellbore, and leaks into them, the CO_2 phase can change from its initial supercritical state to liquid, liquid/gas mixture or gas, depending on the pressure and temperature conditions at any certain level in the crack or the wellbore. The CO_2 phase state can be described by its phase diagrams, namely the pressure-temperature diagram and the pressure-density diagram.

Fig. 1.4 shows the CO_2 pressure-temperature and pressure-density phase diagrams. They show that at different combinations of pressure and temperatures the CO_2 exhibits different states: gas, liquid, solid and supercritical. The pressure-temperature diagram depicts a triple point where the CO_2 is in a triple gas, liquid and solid state. It shows also a critical point at $T_C^{CO2} = 304.1\,\mathrm{K}$ and $p_C^{CO2} = 7.38\,\mathrm{MPa}\ (73.8\ \mathrm{bar})$. Beyond this point, the CO_2 is in a supercritical state. Below this point the CO_2 phase changes to liquid, gas or a liquid/gas mixture. The liquid/gas mixture is formed when the pressure equals to the "saturated vapor pressure"; i.e. the pressure at which the gas (vapor) phase and the liquid phase are in thermodynamic equilibrium (along the solid line between the liquid and gas phases in the pressure-temperature phase diagram). This behavior is mathematically formulated in literature and several constitutive relationships have been introduced. The density-pressure diagram in Fig. 1.4 depicts an example of the CO_2 equation of state, which has been utilized in this thesis.

As the problem dealt with in this work covers a wide range of pressures and temperatures, the CO_2 constitutive properties must cover all phases that might be formed in the system, including supercritical, liquid, gas and liquid/gas mixture (saturated vapor region). In the followings, constitutive relationships describing the CO_2 density, enthalpy and viscosity are given.

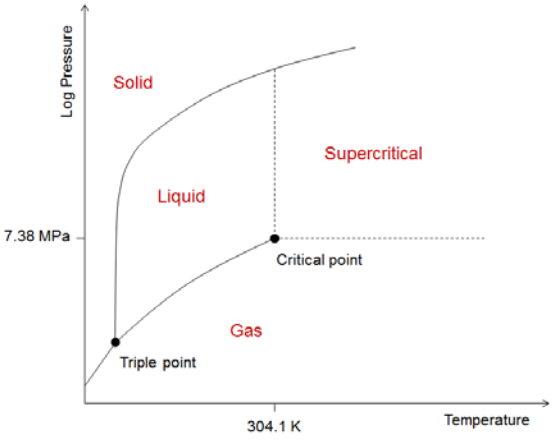

(a)

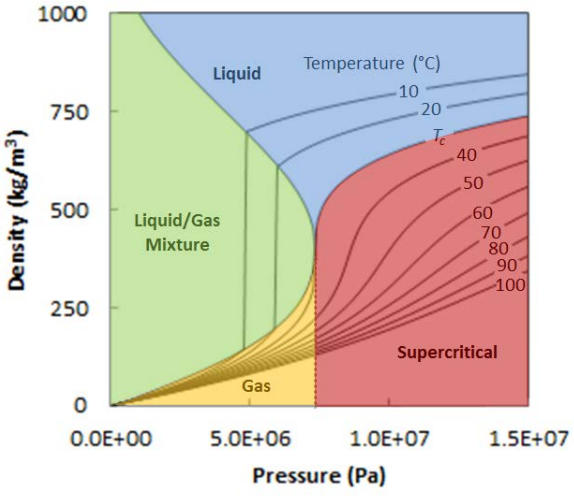

(b)

Fig. 1.4 CO_2 phase diagram: (a) pressure-temperature plane, and a) pressure-density plane.

1.2.3.1.1 CO_2 density

There are several constitutive relationships for CO_2 density, but mainly for pure CO_2. For CO_2 with water, Spycher et al. (2003) introduced an equation of state based on Redlich-Kwong model, expressed as

$$p_{CO_2} = \frac{R\theta}{V_{CO_2} - b_{CO_2}} - \frac{a_{CO_2}}{\theta^{0.5} V_{CO_2}\left(V_{CO_2} + b_{CO_2}\right)} \tag{1.18}$$

where V_{CO_2} is the molar volume of CO_2 phase, R is the universal gas constant, and a_{CO_2} and b_{CO_2} are the intermolecular attraction and repulsion, respectively. Spycher et al. (2003) utilized experimental data to evaluate these parameters, giving

$$\begin{aligned} a_{CO_2} &= 7.54 - 4.13\times10^{-3}T \quad \text{Pa m}^6\ \text{K}^{0.5}\ \text{mol}^{-2} \\ b_{CO_2} &= 27.8\times10^{-6} \quad \text{m}^3/\text{mol} \end{aligned} \tag{1.19}$$

The molar volume - density relationship is defined as

$$\rho = \frac{M_{CO_2}}{V} \tag{1.20}$$

where M_{CO_2} is the molar mass of CO_2 ($= 44\times10^{-3}$ kg/mol).

Substituting Eq. (1.20) into Eq. (1.18), after rearrangement, yields

$$\left(\frac{a_{CO_2} b_{CO_2}}{pT^{0.5}}\right)\rho^3 + M_{CO_2}\left(\frac{RTb_{CO_2}}{p} - \frac{a_{CO_2}}{pT^{0.5}} + {b_{CO_2}}^2\right)\rho^2 + {M_{CO_2}}^2\left(\frac{RT}{p}\right)\rho - {M_{CO_2}}^3 = 0 \tag{1.21}$$

Fig. 1.5 shows three isothermal curves for CO_2. The figure clearly shows the supercritical behavior of CO_2 for temperatures: T = 50°C and T = 70°C, where the gas and the fluid are combined to form a single fluid. For T = 30°C, there is a sharp transition between the vapor phase and the saturated liquid phase.

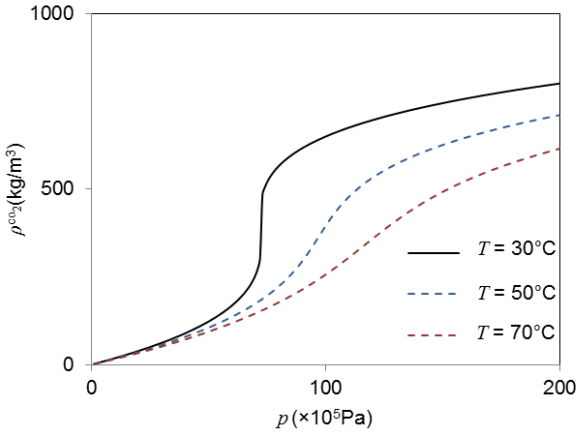

Fig. 1.5 Isothermal curves of CO_2 in density-pressure phase diagram.

1.2.3.1.2 CO_2 enthalpy

The CO_2 specific enthalpy presented by Span and Wagner (1996) is utilized. It reads

$$h = RT\left(1+\tau\left(\frac{\partial f^0}{\partial \tau}+\frac{\partial f^r}{\partial \tau}\right)+\delta\frac{\partial f^r}{\partial \delta}\right) \tag{1.22}$$

with f^0 representing the Helmholtz energy of an ideal gas, and f^r representing the residual part of the Helmholtz energy. They are functions of temperature and density, as

$$f^0(\delta,\tau) = \ln(\delta) + a_1^\circ + a_2^\circ\tau + a_3^\circ \ln(\tau) + \sum_{i=4}^{8} a_i^\circ \ln\left[1-\exp\left(-\tau\theta_i^\circ\right)\right] \tag{1.23}$$

and

$$f^r(\delta,\tau) = \sum_{i=1}^{7} n_i \delta^{d_i}\tau^{t_i} + \sum_{i=8}^{34} n_i \delta^{d_i}\tau^{t_i} e^{-\delta^{c_i}} + \sum_{i=35}^{39} n_i \delta^{d_i}\tau^{t_i} e^{-\alpha_i(\delta-\varepsilon_i)^2-\beta_i(\tau-\gamma_i)^2} + \sum_{i=40}^{42} n_i \Delta^{b_i}\delta e^{-C_i(\delta-1)^2-D_i(\tau-1)^2} \tag{1.24}$$

with

$$\Delta = \left\{(1-\tau)+A_i\left[(\delta-1)^2\right]^{1/(2\beta_i)}\right\}^2 + B_i\left[(\delta-1)^2\right]^{a_i} \tag{1.25}$$

where $\tau = T_C^{CO2}/T$ and $\delta = \rho/\rho_C^{CO2}$ are the inverse reduced temperature and reduced density, respectively; and ρ_C^{CO2} and T_C^{CO2} are the CO_2 density and temperature at the critical condition. The reader is referred to Span and Wagner (1996) to obtain the values of the coefficients a_i°, θ_i°, n_i, d_i, t_i, c_i, α_i, ε_i, β_i, γ_i, C_i, D_i, A_i, B_i and a_i.

Fig. 1.6 shows the CO_2 specific enthalpy versus pressure for different temperatures. As for the density-pressure phase diagram, it shows the supercritical behavior of pure CO_2 at T = 45°C and T = 60°C, while for T = 30°C, there is a clear distinction between the gas phase and the saturated liquid phase.

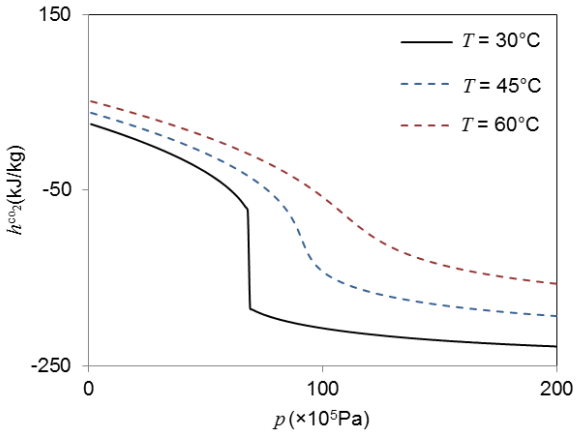

Fig. 1.6 CO_2 specific enthalpy versus pressure for different temperatures

1.2.3.1.3 CO_2 viscosity

The CO_2 viscosity can be determined following Fenghour et al. (1998), as

$$\mu = 1.00697\sqrt{T} \Big/ \left[0.235156 - 0.491266 \ln \tau^* + 5.211155\times10^{-2} \left(\ln \tau^* \right)^2 + 5.347906\times10^{-2} \left(\ln \tau^* \right)^3 - 1.537102\times10^{-2} \left(\ln \tau^* \right)^4 \right] + 0.4071119\times10^{-2}\rho + 0.7198037\times10^{-4}\rho^2 + \frac{0.2411697\times10^{-16}\rho^6}{\left(\tau^*\right)^3} + 0.2971072\times10^{-22}\rho^8 - 0.1627888\times10^{-22}\frac{\rho^8}{\tau^*} \tag{1.26}$$

in which $\tau^* = T / 251.196$ is a reduced temperature, where T is in Kelvin; ρ is the density of CO_2 in kg/m^3; and μ is in $\mu Pa.s$.

Fig. 1.7 depicts CO_2 viscosity versus pressure for three different temperatures. A similar trend in phase change as that for the CO_2 density, Fig. 1.5, can be observed.

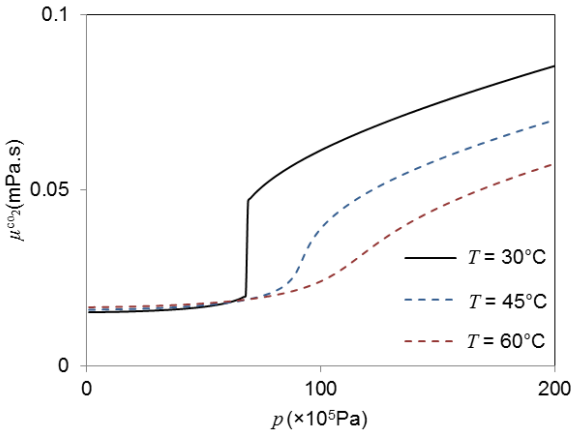

Fig. 1.7 CO_2 viscosity versus pressure for three different temperatures.

1.2.3.2 Constitutive laws for brine

Similar to the CO_2, the pressure-temperature-density of the brine has been mathematically formulated and introduced in literature. Here, the brine constitutive relationships, which have been utilized in this thesis, are given.

1.2.3.2.1 Brine density

The brine density is a function of pressure, temperature and salinity given by (Adams and Bachu 2002)

$$\begin{aligned}\rho=&\rho^w+s\{0.668+0.44s\\&+1\times10^{-6}\left[300p-2400ps+T\left(80+3\left(T-3300s-13p+47ps\right)\right)\right]\}\end{aligned} \tag{1.27}$$

where ρ^w is the pure water density in g cm^{-3}, s is the salinity in ppm/10^6 (or μmol/mol/10^6), T is in °C, and p is in MPa. The density of pure water is obtained from IAPWS (2007), as

$$\rho^w=\frac{p}{R^wTp_{rw}^*\dfrac{\partial\Gamma^w}{\partial p_{rw}^*}} \tag{1.28}$$

with

$$\Gamma^w=\sum_{i=1}^{34}n_i\left(7.1-p_{rw}^*\right)^{I_i}\left(\tau_*^w-1.222\right)^{J_i} \tag{1.29}$$

in which $p_{rw}^{*} = p / p_{*}^{w}$, $\tau_{*}^{w} = \theta_{*}^{w} / \theta$, and p_{*}^{w}, τ_{*}^{w}, n_i, I_i and J_i are constants, values of which can be found in IAPWS (2007).

Fig. 1.8 depicts pure water and brine densities versus temperature for different salinities. The figure shows that the water density increases significantly with increasing salinity.

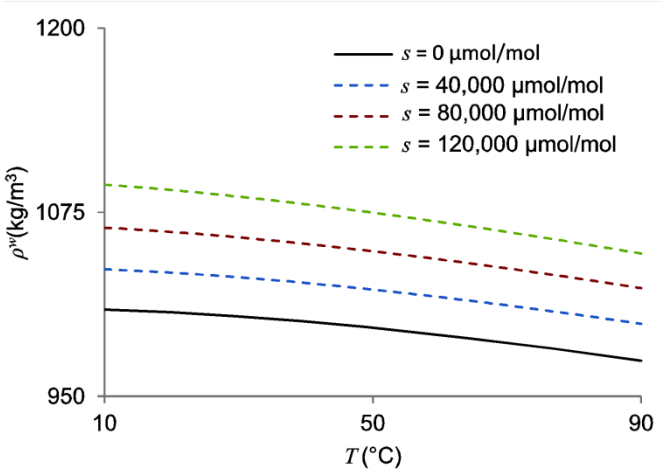

Fig. 1.8 Density of pure water and brine versus temperature.

1.2.3.2.2 Brine enthalpy

The specific enthalpy of brine can be calculated as

$$h = \left(1 - X_w^{\mathrm{NaCl}}\right) h^w + X_w^{\mathrm{NaCl}} \left(h^{\mathrm{NaCl}} + \Delta h_{s \to w}^{\mathrm{NaCl}}\right) \tag{1.30}$$

where h^w is the pure water enthalpy, h^{NaCl} is the salt (sodium chloride) enthalpy in solid state and $\Delta h_{s \to w}^{\mathrm{NaCl}}$ is the enthalpy of dissolution of salt in water. Pure water enthalpy is calculated as

$$h^w = RT\tau_{*}^{w} \frac{\partial \Gamma^w}{\partial \tau_{*}^{w}} \tag{1.31}$$

where Γ^w can be obtained from Eq. (1.29).

The sodium chloride enthalpy is calculated by assuming negligible volume work effect; and based on the work of Daubert and Danner (1989), after converting the units to kJ/kg, it gives

$$h^{\mathrm{NaCl}} = 6.2817 \times 10^{-1} \theta + 5.3705 \times 10^{-4} \theta^2 - 3.8028 \times 10^{-7} \theta^3 + 1.1978 \times 10^{-10} \theta^4 \tag{1.32}$$

where θ is in Kelvin. The enthalpy of dissolution of salt into water is calculated as (Michaelides 1981)

$$\Delta h_{s\to w}^{\mathrm{NaCl}} = \frac{C^{pw}}{1.0\times10^{3}\left(1+M^{\mathrm{NaCl}}\chi_w^{\mathrm{NaCl}}\right)}\sum_{i=0}^{3}\sum_{j=0}^{2}a_{ij}T^{i}\left(\chi_w^{\mathrm{NaCl}}\right)^{j} \tag{1.33}$$

where $C^{pw}=4.184$ kJ/kg°C is water specific heat, M^{NaCl} is the molar mass of sodium chloride, χ_w^{NaCl} is the molality of sodium chloride in water, T is the temperature in degree Celsius, $\Delta h_{s\to w}^{\mathrm{NaCl}}$ is in kJ/kg and the values of a_{ij} can be found in Michaelides (1981).

Fig. 1.9 shows pure water and brine enthalpy versus pressure for different salinities. The figure shows that the enthalpy decreases with increasing salinity.

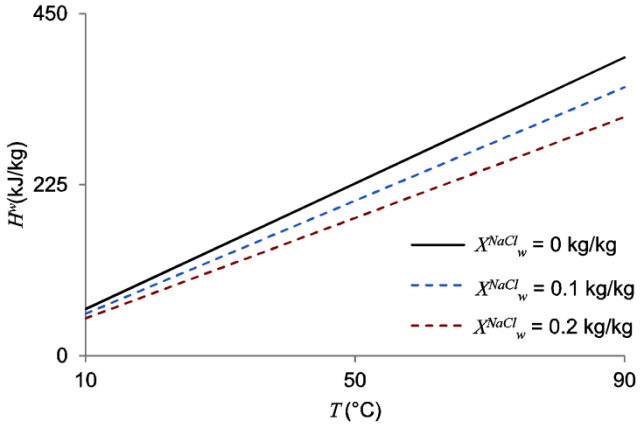

Fig. 1.9 Enthalpy of pure water and brine versus temperature for different values of salinity.

1.2.3.2.3 Brine viscosity

The brine viscosity can be obtained according to Kumagai and Yokoyama (1999) as

$$\mu=(a_1+a_2\theta)\chi_w^{\mathrm{NaCl}}+(a_3+a_4\theta)\sqrt{\chi_w^{\mathrm{NaCl}}} +a_9(p_w-0.1)+\mu^{w}\Big|_{p_{ref}=0.1\ \mathrm{MPa}} \tag{1.34}$$

where μ is in mPa.s, θ is in K, p_w is in MPa, and χ_w^{NaCl} and χ_w^{CO2} are the molalities of NaCl and CO_2 in mol/kg, respectively. The last term on the right-hand side of Eq. (1.34) is the viscosity of pure water at a reference pressure p_{ref} = 0.1 MPa. The

values of the constant parameters a_1 to a_9 can be obtained from Kumagai and Yokoyama (1999).

The viscosity of pure water at 0.1 MPa, can be calculated using the relationship suggested by Sengers and Watson (1986), which reads

$$\mu^w\Big|_{p_w = 0.1\ \text{MPa}} = \mu_0^w \times \mu_1^w$$

$$\mu_0^w = \frac{\sqrt{\left(\tau^w\right)^{-1}}}{\sum_{i=0}^{3} \frac{a_i}{\left(\tau^w\right)^{-i}}} \tag{1.35}$$

$$\mu_1^w = \exp\left\{\delta^w \sum_{i=0}^{5}\sum_{j=0}^{6} b_{ij}\left(\tau^w - 1\right)^i \left(\delta^w - 1\right)^j\right\}$$

in which $\tau^w = \theta_C^w / \theta$ is the inverse reduced temperature; $\delta^w = \rho^w / \rho_C^w$ is the reduced density of water; ρ_C^w and θ_C^w are the water density and temperature at the critical condition; and a_i and b_{ij} are constant parameters which can be obtained from Sengers and Watson (1986).

Fig. 1.10 depicts pure water and brine viscosity versus pressure for different salinities. The figure shows that the viscosity increases with increasing salinity.

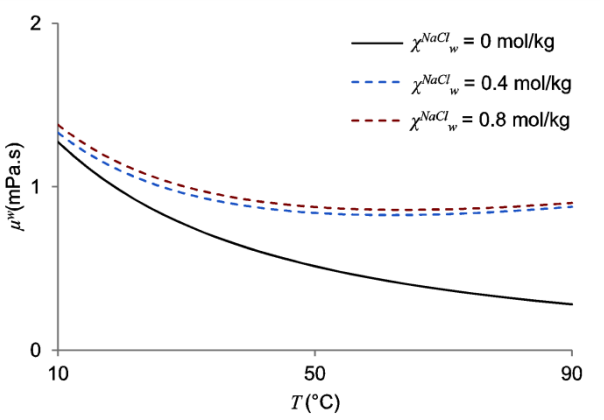

Fig. 1.10 Viscosity of pure water and brine versus temperature for different values of salinity.

1.2.3.3 Constitutive laws for air

The air is assumed to be always in a gaseous phase in the wellbore, and hence the ideal gas law is utilized to establish its constitutive equations.

1.2.3.3.1 air density

Based on the ideal gas theory, the relationship between density, pressure and temperature of air can be described as

$$\rho = \frac{p}{(R/M_{air})T} \tag{1.36}$$

where M_{air} is the molar mass of air ($= 28.97\times10^{-3}$ kg/mol).

1.2.3.3.2 air enthalpy

The enthalpy of air as an ideal gas is given by

$$h = c_p^{\text{air}} T \tag{1.37}$$

in which c_p^{air} is the specific isobaric heat capacity ($=1006$ J/(kg K)).

1.2.3.3.3 air viscosity

The viscosity of air is given by Sutherland's relation (Rathakrishnan 2012), as

$$\mu = 1.46\left(\frac{T^{3/2}}{T+111}\right) \tag{1.38}$$

where T is in Kelvin and μ is in μPa.s.

1.3 Numerical solution method

Apparently, the involved conceptual model and the mathematical formulations are beyond standard routine models. Any attempt to include the proposed geometry and physical processes is put in the category of detailed modeling. This inevitably entails the use of parallel computing, hundreds of computer processors, and days or weeks of CPU time. The main reason for this computational inefficiency is that in almost all existing numerical simulators, which are designed for detailed modeling, standard numerical procedures are utilized to solve the problems.

One of the primary objectives of this thesis is the development of a computational tool, which can be run on a normal PC. This objective inevitably entails employing innovative computational solutions capable of achieving two main features: geometry-independence and mesh-independence. The geometry-independence feature indicates that the computational grid does not necessarily have to conform to certain geometrical details, such as layer boundaries or crack trajectories. This allows for the utilization of a fixed, structured mesh to deal with irregular geometries, as well as propagating

discontinuities. The mesh-independence feature indicates that the mesh size does not affect the accuracy of the result. However, due to the existence of multiple discontinuities as well as the involved multiphysics phenomena, it is almost impossible to achieve an ideally mesh independent model. Consequently, this work aims at an effectively mesh-independent model, by which a relatively coarse mesh can lead to a sufficiently accurate result. Together, these two features allow for the use of fixed, structured and relatively coarse meshes that make the computational processes efficient. To achieve this, a mixed discretization scheme and a multidomain coupling technique are employed.

1.3.1 Mixed discretization scheme

The proposed numerical solution method incorporates a mixed finite element discretization scheme. In this scheme, state variables exhibiting different physical nature are treated using different numerical discretization techniques. The standard Galerkin finite element method (SG) and the partition of unity finite element method (PUM) are integrated in a single numerical scheme. SG is utilized to discretize the diffusive dominant field equations, and PUM, within the framework of the extended finite element method (XFEM), is utilized to discretize the stationary or moving discontinuous fields, such as layer boundaries or advancing fluid interfaces. The proposed mixed discretization scheme differs from the well-known mixed FEM (Arbogast and Wheeler 1995; Masud and Hughes 2002) such that in the mixed FEM, different state variables are utilized, but a single discretization technique is adopted; whereas in the mixed discretization scheme, different state variables are utilized and different discretization techniques, depending on the physical nature of the state variables and the associated balance equations, are adopted. Specifically, the standard Galerkin method is utilized to model continuous and diffusive fields.

The partition of unity method is utilized to model solid displacement discontinuities due to crack propagation, and fluid saturation discontinuities at the boundary between layers, and together with the level set method, to model discontinuities at the front between CO_2 and air in the wellbore.

1.3.2 Multidomain coupling

Modeling CO_2 geosequestration requires coupling multiphase flow domains exhibiting significant difference in their physical processes, governing equations and flow velocities. Multiphase flow in a porous medium is dominated by Darcy laminar flow, whereas multiphase flow in wellbores and fractures is dominated by Navier Stokes viscous, compressible flow.

Two coupling schemes are proposed in this work:

- Reservoir-wellbore coupling: For this, a staggered-multiple time-stepping technique is utilized. This enables the use of different time step sizes and separate mathematical and numerical formulations for the two subdomains, and facilitates the implementation of a standard finite element computer code. See Chapter 4.

- Matrix-fracture coupling: For this, a leakage criterion is introduced to deal with the coupling between the porous matrix zone and the fracture zone. See Chapter 5.

The proposed multidomain coupling, together with the mixed discretization scheme, is essential in making the proposed numerical model geometry- and mesh-independent, and computationally efficient.

1.4 Objectives

The main objective of this research work is the development of a computational model for describing CO_2 leakage mechanisms and crack propagation due to regionally induced thermo-hydrodynamic-mechanical forces, and the establishment of innovative numerical procedures for solving the resulting governing equations. The conceptual model, the mathematical formulations and the numerical procedures are designed to bridge the gap between events occurring at a microscopic level with those occurring at macroscopic levels, using minimal computational requirements.

The proposed computational model is meant to be computationally efficient and geometry- and mesh-independent such that it can be incorporated in numerical tools for evaluation and monitoring of short- and long-term environmental and structural impact of CO_2 sequestration projects at regional levels.

1.5 Thesis outline

This thesis consists of six chapters describing four computational models. The four models are presented in four chapters: Chapters 2 – 5. They are copies of peer reviewed journal papers, two of which have already been published and two are under review.

Chapter 2 deals with CO_2 leakage via formation layer boundaries. A computational model for the simulation of multiphase flow in rigid heterogeneous layered media is introduced, with particular emphasis on modeling CO_2 leakage at the boundary between two layers constituting different physical properties. Chapter 2 is based on Arzanfudi et al. (2014), a paper published in Advances in Water Resources.

Chapter 3 deals with CO_2 leakage via abandoned wellbores. It introduces an effectively mesh-independent and computationally efficient model for CO_2 leakage through wellbores. All important physical phenomena and processes occurring along the wellbore path, including fluid dynamics, buoyancy, phase change, compressibility, thermal interaction, wall friction and slip between phases, together with a jump in density and enthalpy between the air and the CO_2, are considered. Chapter 3 is based on Arzanfudi and Al-Khoury (2015), a paper published in the International Journal for Numerical Methods in Fluids.

Chapter 4 introduces an integrated wellbore-reservoir numerical tool for the simulation of sequestrated CO_2 leakage through heterogeneous geological formation layers and abandoned wellbores. The two models of chapters 2 and 3 are integrated in a single simulator designed to simultaneously model multiple path leakage of sequestered

CO_2. Chapter 4 is based on Arzanfudi et al. (2016), a paper published in Finite Elements in Analysis and Design.

Chapter 5 focuses on fracturing and leakage through cracks. It presents a fully coupled thermo-hydrodynamic-mechanical computational model for multiphase flow in a deformable and fracturing porous solid. Chapter 5 is based on Arzanfudi and Al-Khoury (2016), a paper submitted for publication.

Chapter 6 concludes the work of this thesis, and highlights the challenges of the problem, as well as the adopted solutions. It also gives recommendations for future work.

2

CO_2 Leakage via Formation Layers

This chapter is based on Arzanfudi et al. (2014), a paper published in Advances in Water Resources.

This chapter introduces a new and computationally efficient model for the simulation of non-wetting phase leakage in a rigid heterogeneous layered medium domain constituting layers of different physical properties. Such a leakage exhibits a discontinuity in the saturation field at the interface between layers. The governing field equations are derived based on the averaging theory and solved numerically using a mixed finite element discretization scheme. This scheme entails solving different balance equations using different discretization techniques, which are tailored to accurately simulate the physical behavior of the primary state variables. A discontinuous non-wetting phase saturation – continuous water pressure formulation is adopted. The standard Galerkin finite element method is utilized to discretize the water phase pressure field, and the partition of unity finite element method is utilized to discretize the non-wetting phase saturation field. This mixed discretization scheme leads to a locally conservative system, giving accurate simulation of the saturation jump. The boundary between layers is embedded within the finite elements, alleviating the need to use the typical interface elements, and allowing for the use of structured, geometry-independent and relatively coarse meshes. The accuracy and capability of the proposed model are evaluated by verification and numerical examples covering water, DNAPL and CO_2 leakage through layers of different hydraulic properties.

2.1 Introduction

Leakage of a non-wetting phase through a porous medium domain constituting heterogeneous layers can have a significant consequence on the environment and life on earth. Leakage of contaminants, infiltration of dense oil and Leakage of CO_2 to the ground surface or layers containing ground water, among many others, are currently considered one of the main concerns of exploiting the earth space to cope with the current technological advancement.

Designing oil and gas fields, planning contaminant storages and selection of an appropriate geological formation for CO_2 sequestration require a good estimate of the amount of leakage that might take place in time. It is therefore vital to acquire computational tools capable of modeling this phenomenon. Modeling the leakage phenomenon accurately would not only give a good estimate of the amount of the leakage, but also an accurate approximation of the pore pressure distribution in the ground, and hence an accurate estimation of the mechanical behavior of the region surrounding such projects.

Computational modeling of multiphase flow in geological formations often requires modeling heterogeneous porous medium domains of regional scales with irregular and complicated geometry. Discretization of such a geometry is rather demanding. It requires finite element meshes (finite difference or finite volume grids), which are relatively fine and aligned along the boundaries between the layers. As the layers usually differ in porosity, permeability, and capillary entry pressure, fields generated by the fluid flow exhibit a jump at the boundary between them. This effect, in many cases, cannot be captured by standard numerical discretization schemes.

The physics of fluid leakage at boundaries between layers with different hydraulic properties has been intensively studied by several researchers, including Van Duijn et al. (1995), Helmig and Huber (1998), Van Duijn et al. (2002), and Fučík and Mikyška (2011). The capillary pressure plays an important role in the amount of leakage between two layers. Neighboring layers in a heterogeneous layered medium have different capillary pressure-saturation relationships. Fig. 2.1 shows typical Brooks and Corey capillary pressure-saturation relationships (Brooks and Corey 1964) for two layers having different permeability.

To illustrate the effect of capillary pressure on fluid flow in heterogeneous layered domain, a layered porous medium occupied by a wetting phase (water) that is being displaced by a non-wetting phase (CO_2, for example) is considered. In such a medium, according to Brooks and Corey capillary pressure-saturation relationships, the following conditions exist at the boundary between two layers:

- The non-wetting phase does not leak from a layer of high permeability to a layer of low permeability unless the capillary pressure of the first layer exceeds a threshold pressure, known as the entry pressure (also called bubbling pressure), of the second layer. B^+ in Fig. 2.1 indicates the entry pressure of the high permeability layer, and

B^- indicates that of the low permeability layer. This condition gives rise to mass accumulation of the non-wetting phase at the boundary between the two layers.

- Accumulation of the non-wetting phase continues to occur for all capillary pressures between point B^+ and point A in Fig. 2.1. In this region the capillary pressure at the boundary between the two layers exhibits a discontinuity.
- Above point A, the non-wetting phase starts to infiltrate into the second layer. In this region, the capillary pressure is continuous, and as a result, the saturation field exhibits a discontinuity. The capillary pressure crossing points C and D, in Fig. 2.1 is an example of this condition. It can be seen that these two points correspond to water saturations S_w^+ and S_w^-, respectively.
- If the non-wetting phase flow occurs from the low permeability layer to the high permeability layer, the saturation field also exhibits a jump, but in this case in the form of suction. Initially, at $S_w = 1$, the entry pressure of the low permeability layer (B^-) is readily higher than that of the high permeability layer (B^+). Due to this, upon the arrival of the non-wetting phase to the boundary between the two layers, leakage (suction) immediately occurs, maintaining $S_w = 1$ in the low permeability layer and decreasing in the high permeability layer.

Note that the van Genuchten capillary pressure –saturation relationship (van Genuchten 1980) exhibits continuous capillary pressure at all times. However, as for Brooks and Corey, the van Genuchten relationship exhibits the saturation discontinuity at the boundary between layers. In this chapter, we utilize the Brooks and Corey relationship, though extension to van Genuchten is straightforward.

The presence of these complicated physical conditions at the boundary between heterogeneous layers exerts sever difficulties on the numerical solution procedure. The standard Galerkin finite element method (SG), for instance, is not able to simulate this problem accurately, even if a fine mesh is utilized. Helmig and Huber (1998) intensively studied this problem and found that using SG to solve the infiltration of a Dense Non-Aqueous Phase Liquid (DNAPL) into a heterogeneous layered domain produces erroneous results. It fails to capture the discontinuity in the saturation field at the boundary between two layers, giving an incorrect impression of the amount of leakage.

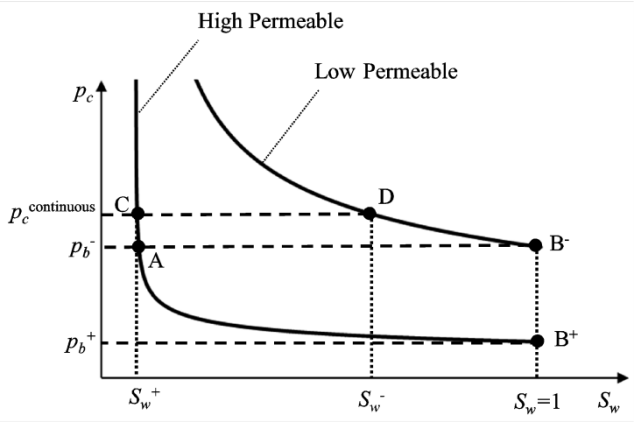

Fig. 2.1 Brooks and Corey capillary pressure-saturation relationships for two layers.

Therefore, in order to solve such a problem, the numerical scheme must be able to capture the discontinuity in the capillary pressure and saturation fields. In literature, several solution techniques with different discretization complexities have been proposed. Friis and Evje (2011), Brenner et al. (2013), Cances (2009) and Szymkiewicz et al. (2011) used the finite volume method for this purpose. Helmig and Huber (1998) used the subdomain collocation finite volume method (Box Method) to solve the problem. This method comprises coupling between the finite element method and the finite volume method. Fučík and Mikyška (2011) utilized a mixed hybrid finite element-discontinuous Galerkin discretization procedure (MHFE-DG).

Here, we solve this problem using a mixed finite element discretization scheme. This scheme differs from the well-known mixed FEM, such that in the mixed FEM, different state variables are utilized but a single discretization technique is adopted. However, in the mixed discretization scheme, we utilize different state variables and adopt different discretization techniques, depending on the nature of the state variable and the associated balance equations. We use the Partition of Unity finite element method (PUM) (Babuška and Melenk 1997) to discretize the discontinuity in the non-wetting phase saturation field, and the standard Galerkin method (SG) to discretize the continuous water (wetting phase) pressure. We adopt the partition of unity property within the framework of the extended finite element method (XFEM), which entails decomposing the saturation field into a continuous part and a discontinuous part, where the latter is enhanced by use of a function which closely describes the nature of the jump in the field (the Heaviside function in case of strong discontinuity, for instance). The main advantage of this method is two-fold. First, it captures the discontinuity accurately. Second, the discontinuity at the boundary between layers can be modelled regardless of the finite element mesh. Therefore, the mesh is not restricted to be aligned

with the discontinuity, enabling the use of structured, geometry-independent and relatively coarse meshes.

This chapter is organized as follows. In Section 2.2, governing equations based on a wetting pressure – non-wetting saturation formulation are derived. In Section 2.3, a detailed finite element formulation of the proposed PUM-SG model is given. In Section 2.4, a verification example and two numerical examples describing a DNAPL infiltration problem, and a 2D heterogeneous layered domain subjected to a CO_2 source are presented.

2.2 Governing Equations

The continuity equations of the wetting phase (formation water) and the non-wetting phase for isothermal, immiscible, incompressible two-phase flow in a rigid porous medium domain can be expressed as (Lewis and Schrefler 1998)

Water phase

$$\phi \frac{\partial S_w}{\partial t} + \frac{1}{\rho_w} \nabla \cdot \left[\rho_w \frac{\mathbf{k} k_{rw}}{\mu_w} \left(-\nabla p_w + \rho_w \mathbf{g} \right) \right] = Q_w \tag{2.1}$$

Non-wetting phase

$$\phi \frac{\partial S_n}{\partial t} + \frac{1}{\rho_n} \nabla \cdot \left[\rho_n \frac{\mathbf{k} k_{rn}}{\mu_n} \left(-\nabla p_n + \rho_n \mathbf{g} \right) \right] = Q_n \tag{2.2}$$

in which $\mathbf{g}$ is the gravity force vector, ρ_w is the water density, ρ_n is the non-wetting density, S_w is water saturation, S_n is non-wetting saturation, ϕ is the porosity, p_w and p_n are water and non-wetting pressure, $\mathbf{k}$ is the absolute permeability, k_{rw} and k_{rn} are water and non-wetting relative permeability (functions of saturation), μ_w and μ_n are water and non-wetting viscosity, and Q_w and Q_n are the volumetric source or sink terms. Note that subscript *n* is utilized to describe a non-wetting phase which can be oil, gas, or supercritical CO_2, among others.

We adopt a water phase pressure – non-wetting phase saturation formulation. In a porous domain, water and non-wetting phase are jointly occupying the pores, implying:

$$S_w + S_n = 1 \tag{2.3}$$

and

$$p_c(S_n) = p_n - p_w \tag{2.4}$$

where $p_c(S_n)$ is the capillary pressure, a function of non-wetting phase saturation.

Applying the chain rule to Eq. (2.4), the non-wetting phase pressure gradient can be described as

$$\nabla p_n = \nabla p_w + \nabla p_c = \nabla p_w + \frac{dp_c}{dS_n}\nabla S_n \tag{2.5}$$

Substituting Eqs. (2.3) and (2.5) into Eqs. (2.1) and (2.2), in the absence of volumetric sources/sinks, the continuity balance equations can be described as

Water phase

$$-\phi\frac{\partial S_n}{\partial t} - \nabla\cdot\left[\mathbf{k}\lambda_w\left(\nabla p_w - \rho_w\mathbf{g}\right)\right] = 0 \tag{2.6}$$

Non-wetting phase

$$\phi\frac{\partial S_n}{\partial t} - \nabla\cdot\left[\mathbf{k}\lambda_n\left(\nabla p_w + \frac{dp_c}{dS_n}\nabla S_n - \rho_n\mathbf{g}\right)\right] = 0 \tag{2.7}$$

in which $\lambda_w = k_{rw}/\mu_w$ and $\lambda_n = k_{rn}/\mu_n$ are the water and non-wetting phase mobility. The advantage of this formulation is that the non-wetting phase saturation is made a primary variable, and hence can be explicitly discretized taking into account its discontinuity at the boundary between layers.

2.2.1 Constitutive relationships

In literature, there are several empirical formulations correlating the capillary pressure and relative permeability to saturation, such as van Genuchten (1980) and Brooks and Corey (1964). Here, the Brooks and Corey formulation is adopted. Accordingly, the capillary pressure-saturation relationship is described as

$$p_c = p_b S_e^{-1/\hat{\theta}} \tag{2.8}$$

with

$$S_e = \frac{S_w - S_{rw}}{1 - S_{rw} - S_{rn}} \tag{2.9}$$

and the relative permeability-saturation relationships for the water and the non-wetting phases are described as

$$k_{rw} = S_e^{(2+3\hat{\theta})/\hat{\theta}} \tag{2.10}$$

$$k_{rn} = \left(1 - S_e\right)^2\left(1 - S_e^{(2+\hat{\theta})/\hat{\theta}}\right) \tag{2.11}$$

where S_e is the effective saturation, S_{rw} is the irreducible water saturation, S_{rn} is the residual non-wetting phase saturation, $\hat{\theta}$ is the pore size distribution index and p_b is the entry pressure, corresponding to the capillary pressure needed to displace the water phase from the largest pore.

2.2.2 Initial and boundary conditions

Initially, the water pressure and the non-wetting phase saturation are set to

$$\begin{aligned} p_w &= p_{w0}(\mathbf{x}) \\ S_n &= S_{n0}(\mathbf{x}) \end{aligned} \quad \text{at } t = 0 \tag{2.12}$$

The Dirichlet boundary conditions are prescribed as

$$\begin{aligned} p_w &= \hat{p}_w \quad \text{on } \Gamma_w \\ S_n &= \hat{S}_n \quad \text{on } \Gamma_n \end{aligned} \tag{2.13}$$

in which $\Gamma = \Gamma_w \cup \Gamma_n$ is the Dirichlet boundary surface.

The relevant Neumann boundary conditions are:

Water flux

$$\mathbf{k}\lambda_w\rho_w\left(-\nabla p_w + \rho_w \mathbf{g}\right)\cdot\mathbf{n} = \hat{q}_w \text{ on } \Gamma_w^q \tag{2.14}$$

Non-wetting phase flux

$$\mathbf{k}\lambda_n\rho_n\left(-\nabla p_w - \nabla S_n \frac{dp_c}{dS_n} + \rho_n \mathbf{g}\right)\cdot\mathbf{n} = \hat{q}_n \text{ on } \Gamma_n^q \tag{2.15}$$

in which $\mathbf{n}$ is the outward normal to the boundary and $\Gamma^q = \Gamma_w^q \cup \Gamma_n^q$ is the Neumann boundary surface. The boundaries Γ and Γ^q are shown in Fig. 2.2.

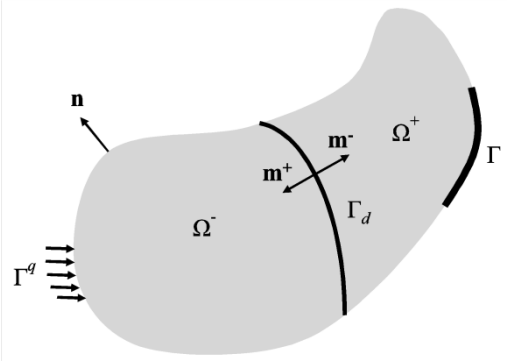

Fig. 2.2 Domain definition.

2.3 Mixed Finite Element Discretization

Eqs. (2.6)-(2.11), together with the initial and boundary conditions, Eqs. (2.12)-(2.15), represent an initial and boundary value problem of isothermal incompressible immiscible two-phase flow. This problem is solved here using a mixed finite element discretization scheme. This scheme entails solving different balance equations using different discretization schemes, which are tailored to accurately describe the nature of the primary state variables.

2.3.1 PUM-SG Formulation

Eqs. (2.6) and (2.7) are utilized here to describe multiphase flow in an initially saturated domain injected by a non-wetting phase. The water pressure is continuous even at the boundaries between layers, but the non-wetting phase saturation and capillary pressure (under certain conditions, described in the Introduction) exhibit a jump across the boundaries between layers. Considering this mixed nature of the involved variables, we utilize the standard Galerkin finite element method to discretize the water pressure field, and the partition of unity finite element method to discretize the saturation field. This kind of a mixed finite element discretization has been introduced by Al-Khoury and Sluys (2007) to model fluid flow in fracturing porous media, and employed by (Talebian et al. 2013b; Talebian et al. 2013a) to model coupled electrokinetic–hydromechanic processes in CO_2 geo-sequestration in single and double porosity porous medium domains. The difference, however, is that in this scheme a geometrical discontinuity is modelled, whereas in the previous ones either a discontinuity across a crack in the solid phase or a moving front of fluid phase were modelled.

Accordingly, using the Galerkin finite element method, the water pressure can be discretized as

$$p_w(\mathbf{x},t) = \sum_{i\in I} N_i(\mathbf{x})\, p_{wi}(t) = \mathbf{N}(\mathbf{x})\mathbf{p}_w(t) \tag{2.16}$$

in which I is the set of all nodes in the domain, $N_i(\mathbf{x})$ is the shape function of node i evaluated at $\mathbf{x}$, $p_{wi}(t)$ is the nodal value of water pressure for node i evaluated at time t, $\mathbf{N}(\mathbf{x})$ is the nodal vector of shape functions, and $\mathbf{p}_w(t)$ is the nodal vector of water pressure.

Using the partition of unity finite element method, the non-wetting phase saturation field can be discretized as

$$\begin{aligned} S_n(\mathbf{x},t) &= \sum_{i\in I} N_i(\mathbf{x})\, S_{ni}(t) + \sum_{i\in I^*} N_i^{eh}(\mathbf{x})\, \bar{S}_{ni}(t) \\ &= \mathbf{N}(\mathbf{x})\mathbf{S}_n(t) + \mathbf{N}^{eh}(\mathbf{x})\tilde{\mathbf{S}}_n(t) \end{aligned} \tag{2.17}$$

where I^* is the subset of enriched nodes, Fig. 2.3, $S_{ni}(t)$ and $\tilde{S}_{ni}(t)$ are the conventional and additional (extended) nodal values associated with the non-wetting phase saturation for node i, $N_i^{eh}(\mathbf{x})$ is an enriched shape function for node i, and $\mathbf{S}_n(t)$, $\tilde{\mathbf{S}}_n(t)$ and $\mathbf{N}^{eh}(\mathbf{x})$ are the associated nodal vectors. $\mathbf{N}^{eh}(\mathbf{x})$ is defined as

$$\mathbf{N}^{eh}(\mathbf{x}) = \mathbf{N}(\mathbf{x})H(\mathbf{x}) \tag{2.18}$$

where $H(\mathbf{x})$ is any function that can closely describe the profile of the field within an element. Here, the Heaviside function is utilized, that reads

$$H(\mathbf{x}) = \begin{cases} 0 & \mathbf{x} \in \Omega^- \\ 1 & \mathbf{x} \in \Omega^+ \end{cases} \tag{2.19}$$

in which Ω^+ and Ω^- represent subdomains occupied by two different layers, schematically illustrated in Fig. 2.2.

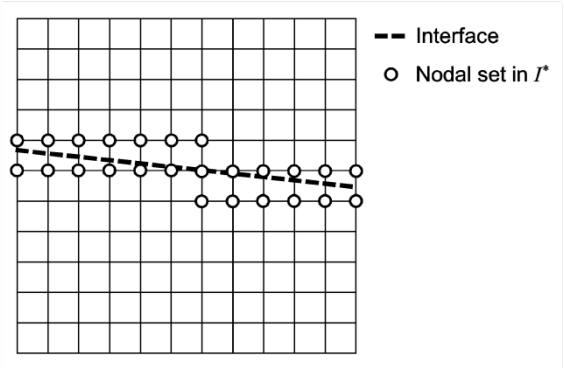

Fig. 2.3 Subset of enriched nodes.

The weak form of Eqs. (2.6) and (2.7) can be obtained using the weighted residual method. To compensate for the extra degrees of freedom introduced by PUM in Eq. (2.17), two different weight functions are necessary. A continuous weight function w is utilized for the water mass continuity equation, Eq. (2.6); and a discontinuous weight function w' is utilized for the non-wetting phase mass continuity equation, Eq. (2.7); giving

Water phase

$$\int_\Omega w\left\{-\phi\frac{\partial S_n}{\partial t} - \nabla\cdot\left[\mathbf{k}\lambda_w\left(\nabla p_w - \rho_w\mathbf{g}\right)\right]\right\}d\Omega = 0 \tag{2.20}$$

Non-wetting phase

$$\int_\Omega w'\left\{\phi\frac{\partial S_n}{\partial t} - \nabla\cdot\left[\mathbf{k}\lambda_n\left(\nabla p_w + \frac{dp_c}{dS_n}\nabla S_n - \rho_n\mathbf{g}\right)\right]\right\}d\Omega = 0 \tag{2.21}$$

where

$$w = \mathbf{N} \tag{2.22}$$

$$w' = \mathbf{N} + \mathbf{N}^{eh} \tag{2.23}$$

in which the dependencies on the spatial and temporal coordinates are discarded for simplicity of notation.

Substituting Eqs. (2.22) into Eqs. (2.20) and applying Green's theorem yields

$$-\int_{\Omega}\mathbf{N}^T\phi\left(\mathbf{N}\dot{\mathbf{S}}_n+\mathbf{N}^{eh}\dot{\tilde{\mathbf{S}}}_n\right)d\Omega+\int_{\Omega}\nabla\mathbf{N}^T\mathbf{k}\lambda_w\nabla\mathbf{N}\mathbf{p}_w d\Omega$$
$$-\int_{\Omega}\nabla\mathbf{N}^T\mathbf{k}\lambda_w\rho_w\mathbf{g}d\Omega+\frac{1}{\rho_w}\int_{\Gamma_w^q}\mathbf{N}^T\hat{q}_w d\Gamma=0 \tag{2.24}$$

Substituting Eq. (2.23) into Eq. (2.21) and applying Green's theorem yields two equations: one representing the continuous field and another the discontinuous field, as

$$\int_{\Omega}\mathbf{N}^T\phi\left(\mathbf{N}\dot{\mathbf{S}}_n+\mathbf{N}^{eh}\dot{\tilde{\mathbf{S}}}_n\right)d\Omega+\int_{\Omega}\nabla\mathbf{N}^T\mathbf{k}\lambda_n\nabla\mathbf{N}\mathbf{p}_w d\Omega$$
$$+\int_{\Omega}\nabla\mathbf{N}^T\mathbf{k}\lambda_n\frac{dp_c}{dS_n}\nabla\mathbf{N}\mathbf{S}_n\,d\Omega+\int_{\Omega^+}\nabla\mathbf{N}^T\mathbf{k}\lambda_n\frac{dp_c}{dS_n}\nabla\mathbf{N}^{eh}\tilde{\mathbf{S}}_n\,d\Omega$$
$$-\int_{\Omega}\nabla\mathbf{N}^T\mathbf{k}\lambda_n\rho_n\mathbf{g}d\Omega+\frac{1}{\rho_n}\int_{\Gamma_n^q}\mathbf{N}^T\hat{q}_n d\Gamma=0 \tag{2.25}$$

$$\int_{\Omega^+}\left(\mathbf{N}^{eh}\right)^T\phi\left(\mathbf{N}\dot{\mathbf{S}}_n+\mathbf{N}^{eh}\dot{\tilde{\mathbf{S}}}_n\right)d\Omega+\int_{\Omega^+}\left(\nabla\mathbf{N}^{eh}\right)^T\mathbf{k}\lambda_n\nabla\mathbf{N}\mathbf{p}_w d\Omega$$
$$+\int_{\Omega^+}\left(\nabla\mathbf{N}^{eh}\right)^T\mathbf{k}\lambda_n\frac{dp_c}{dS_n}\left(\nabla\mathbf{N}\mathbf{S}_n+\nabla\mathbf{N}^{eh}\tilde{\mathbf{S}}_n\right)d\Omega$$
$$-\int_{\Omega^+}\left(\nabla\mathbf{N}^{eh}\right)^T\mathbf{k}\lambda_n\rho_n\mathbf{g}d\Omega+\frac{1}{\rho_n}\int_{\Gamma_n^{q+}}\left(\mathbf{N}^{eh}\right)^T\hat{q}_n d\Gamma \tag{2.26}$$
$$-\frac{1}{\rho_n}\int_{\Gamma_d}\left(\mathbf{N}^{eh}\right)^T q_n^{\Gamma d}\,d\Gamma=0$$

where Γ_d is the boundary between layers as shown in Fig. 2.2, Γ_n^{q+} is the part of Γ_n^q which acts on the boundary of Ω^+, and $q_n^{\Gamma d}$ is the non-wetting phase flow rate across the boundary between layers, describing the leakage between layers; defined as

$$q_n^{\Gamma d}=\mathbf{q}_n^{\Gamma d}\cdot\mathbf{m} \tag{2.27}$$

where $\mathbf{q}_n^{\Gamma d}$ is the associated flux vector, and $\mathbf{m}$ is the unit normal vector to the interface. This leakage term is treated in details in Section 3.3.

2.3.2 Linearization

The resulting weak formulations, Eqs. (2.24)-(2.26), represent a set of semi-discrete nonlinear equations, where the nonlinearity arises from the constitutive relationships between the relative permeability and water saturation, and between the capillary pressure and water saturation, described in Eqs. (2.8)-(2.11). A fully implicit approach is adopted to solve the resulting nonlinear system of equations. Since the nonlinearity is due to scalar coefficients (i.e. λ_w, λ_n, dp_c/dS_n, etc.), and as the constitutive relationships are continuous, it is convenient to linearize these equations using Taylor

series expansions up to the first order (equivalent to the standard Newton-Raphson). The Taylor series expansion of a function $g(x)$ around a point $\overline{x}$ is given by

$$g(x) = g(\overline{x}) + \left.\frac{dg}{dx}\right|_{x=\overline{x}} (x - \overline{x}) + \text{higher order terms} \tag{2.28}$$

For example, the mobility parameter λ_w at the current iteration $r+1$, can be linearized as

$$\lambda_w^{r+1} = \lambda_w(S_n^r) + \frac{d\lambda_w(S_n^r)}{dS_n}\delta S_n \tag{2.29}$$

with

$$\delta S_n = S_n^{r+1} - S_n^r \tag{2.30}$$

where the superscript r denotes the iteration number and the prefix δ denotes the increment of the state vector. Other nonlinear parameters can be linearized in the same manner.

The primary variables and their time derivatives can be written as

$$\begin{aligned} \mathbf{p}_w^{r+1} &= \mathbf{p}_w^r + \delta\mathbf{p}_w \qquad \mathbf{S}_n^{r+1} = \mathbf{S}_n^r + \delta\mathbf{S}_n \qquad \tilde{\mathbf{S}}_n^{r+1} = \tilde{\mathbf{S}}_n^r + \delta\tilde{\mathbf{S}}_n \\ \dot{\mathbf{p}}_w^{r+1} &= \dot{\mathbf{p}}_w^r + \delta\dot{\mathbf{p}}_w \qquad \dot{\mathbf{S}}_n^{r+1} = \dot{\mathbf{S}}_n^r + \delta\dot{\mathbf{S}}_n \qquad \dot{\tilde{\mathbf{S}}}_n^{r+1} = \dot{\tilde{\mathbf{S}}}_n^r + \delta\dot{\tilde{\mathbf{S}}}_n \end{aligned} \tag{2.31}$$

Using Brooks and Corey model given in Eqs. (2.8)-(2.11), and assuming a constant viscosity, the mobility gradients can be calculated analytically according to

$$\frac{d\lambda_w}{dS_n} = \frac{1}{\mu_w}\frac{dk_{rw}}{dS_e}\frac{dS_e}{dS_n} \tag{2.32}$$

$$\frac{d\lambda_n}{dS_n} = \frac{1}{\mu_n}\frac{dk_{rn}}{dS_e}\frac{dS_e}{dS_n} \tag{2.33}$$

$$\frac{d\eta_n}{dS_n} = \frac{d\lambda_n}{dS_n}\frac{dp_c}{dS_n} + \lambda_n\frac{d^2p_c}{dS_n{}^2} \tag{2.34}$$

where $\eta_n = \lambda_n \dfrac{dp_c}{dS_n}$.

It is worth mentioning that when the wetting phase vanishes, the term dp_c / dS_n, goes to infinity. To avoid this situation, we follow a regularization technique proposed in (OPM (Open Porous Media) initiative, DuMux documentation). In this technique, the marginal values of capillary pressure are regularized. This means, instead of following Brooks-Corey relationships for very low wetting phase values, a linear approximation is used. However, more advanced regularization techniques can be found in (Barrett and Knabner 1997; Pop et al. 2004; Qin et al. 2002).

Inserting Eqs. (2.29) and (2.31) into Eqs. (2.24)-(2.26), after rearrangements, gives

Water continuity equation: continuous field

$$
\begin{aligned}
&-\int_{\Omega}\mathbf{N}^{T}\phi\mathbf{N}\dot{\mathbf{S}}_{n}^{r}d\Omega-\int_{\Omega}\mathbf{N}^{T}\phi\mathbf{N}\,\delta\dot{\mathbf{S}}_{n}d\Omega-\int_{\Omega}\mathbf{N}^{T}\phi\mathbf{N}^{eh}\dot{\tilde{\mathbf{S}}}_{n}^{r}d\Omega-\int_{\Omega}\mathbf{N}^{T}\phi\mathbf{N}^{eh}\delta\dot{\tilde{\mathbf{S}}}_{n}d\Omega\\
&\quad+\int_{\Omega}\nabla\mathbf{N}^{T}\mathbf{k}\lambda_{w}^{r}\nabla\mathbf{N}\mathbf{p}_{w}^{r}d\Omega+\int_{\Omega}\nabla\mathbf{N}^{T}\mathbf{k}\lambda_{w}^{r}\nabla\mathbf{N}\,\delta\mathbf{p}_{w}d\Omega\\
&\quad+\int_{\Omega}\nabla\mathbf{N}^{T}\mathbf{k}\nabla\mathbf{N}\,\mathbf{p}_{w}^{r}\left(\frac{d\lambda_{w}}{dS_{n}}\mathbf{N}\delta\mathbf{S}_{n}\right)d\Omega+\int_{\Omega}\nabla\mathbf{N}^{T}\mathbf{k}\nabla\mathbf{N}\,\mathbf{p}_{w}^{r}\left(\frac{d\lambda_{w}}{dS_{n}}\mathbf{N}^{eh}\delta\tilde{\mathbf{S}}_{n}\right)d\Omega\\
&\quad-\int_{\Omega}\nabla\mathbf{N}^{T}\mathbf{k}\lambda_{w}^{r}\rho_{w}\mathbf{g}d\Omega-\int_{\Omega}\nabla\mathbf{N}^{T}\mathbf{k}\rho_{w}\mathbf{g}\left(\frac{d\lambda_{w}}{dS_{n}}\mathbf{N}\delta\mathbf{S}_{n}\right)d\Omega\\
&\quad-\int_{\Omega}\nabla\mathbf{N}^{T}\mathbf{k}\rho_{w}\mathbf{g}\left(\frac{d\lambda_{w}}{dS_{n}}\mathbf{N}^{eh}\delta\tilde{\mathbf{S}}_{n}\right)d\Omega+\frac{1}{\rho_{w}}\int_{\Gamma_{w}^{q}}\mathbf{N}^{T}\hat{q}_{w}d\Gamma=0
\end{aligned}
\tag{2.35}
$$

Non-wetting phase continuity equation: continuous field

$$\begin{aligned}
&\int_\Omega \mathbf{N}^T \phi \mathbf{N} \dot{\mathbf{S}}_n^r d\Omega + \int_\Omega \mathbf{N}^T \phi \mathbf{N} \delta \dot{\mathbf{S}}_n d\Omega + \int_\Omega \mathbf{N}^T \phi \mathbf{N}^{eh} \dot{\tilde{\mathbf{S}}}_n^r d\Omega + \int_\Omega \mathbf{N}^T \phi \mathbf{N}^{eh} \delta \dot{\tilde{\mathbf{S}}}_n d\Omega \\
&+ \int_\Omega \nabla \mathbf{N}^T \mathbf{k} \lambda_n^r \nabla \mathbf{N} \mathbf{p}_w^r d\Omega + \int_\Omega \nabla \mathbf{N}^T \mathbf{k} \lambda_n^r \nabla \mathbf{N} \delta \mathbf{p}_w d\Omega \\
&+ \int_\Omega \nabla \mathbf{N}^T \mathbf{k} \nabla \mathbf{N} \mathbf{p}_w^r \left(\frac{d\lambda_n}{dS_n} \mathbf{N} \delta \mathbf{S}_n \right) d\Omega + \int_\Omega \nabla \mathbf{N}^T \mathbf{k} \nabla \mathbf{N} \mathbf{p}_w^r \left(\frac{d\lambda_n}{dS_n} \mathbf{N}^{eh} \delta \tilde{\mathbf{S}}_n \right) d\Omega \\
&+ \int_\Omega \nabla \mathbf{N}^T \mathbf{k} \eta_n^r \nabla \mathbf{N} \mathbf{S}_n^r \, d\Omega + \int_\Omega \nabla \mathbf{N}^T \mathbf{k} \eta_n^r \nabla \mathbf{N} \delta \mathbf{S}_n \, d\Omega \\
&+ \int_\Omega \nabla \mathbf{N}^T \mathbf{k} \nabla \mathbf{N} \mathbf{S}_n^r \left(\frac{d\eta_n}{dS_n} \mathbf{N} \delta \mathbf{S}_n \right) d\Omega + \int_\Omega \nabla \mathbf{N}^T \mathbf{k} \nabla \mathbf{N} \mathbf{S}_n^r \left(\frac{d\eta_n}{dS_n} \mathbf{N}^{eh} \delta \tilde{\mathbf{S}}_n \right) d\Omega \\
&+ \int_\Omega \nabla \mathbf{N}^T \mathbf{k} \eta_n^r \nabla \mathbf{N}^{eh} \tilde{\mathbf{S}}_n^r \, d\Omega + \int_\Omega \nabla \mathbf{N}^T \mathbf{k} \eta_n^r \nabla \mathbf{N}^{eh} \delta \tilde{\mathbf{S}}_n \, d\Omega \\
&+ \int_\Omega \nabla \mathbf{N}^T \mathbf{k} \nabla \mathbf{N}^{eh} \tilde{\mathbf{S}}_n^r \left(\frac{d\eta_n}{dS_n} \mathbf{N} \delta \mathbf{S}_n \right) d\Omega + \int_\Omega \nabla \mathbf{N}^T \mathbf{k} \nabla \mathbf{N}^{eh} \tilde{\mathbf{S}}_n^r \left(\frac{d\eta_n}{dS_n} \mathbf{N}^{eh} \delta \tilde{\mathbf{S}}_n \right) d\Omega \\
&- \int_\Omega \nabla \mathbf{N}^T \mathbf{k} \lambda_n^r \rho_n \mathbf{g} d\Omega - \int_\Omega \nabla \mathbf{N}^T \mathbf{k} \rho_n \mathbf{g} \left(\frac{d\lambda_n}{dS_n} \mathbf{N} \delta \mathbf{S}_n \right) d\Omega \\
&- \int_\Omega \nabla \mathbf{N}^T \mathbf{k} \rho_n \mathbf{g} \left(\frac{d\lambda_n}{dS_n} \mathbf{N}^{eh} \delta \tilde{\mathbf{S}}_n \right) d\Omega + \frac{1}{\rho_n} \int_{\Gamma_n^q} \mathbf{N}^T \hat{q}_n d\Gamma = 0
\end{aligned} \tag{2.36}$$

Non-wetting phase continuity equation: discontinuous field

$$\begin{aligned}
&\int_{\Omega^+}\left(\mathbf{N}^{eh}\right)^T\phi\mathbf{N}\dot{\mathbf{S}}_n^r d\Omega+\int_{\Omega^+}\left(\mathbf{N}^{eh}\right)^T\phi\mathbf{N}\delta\dot{\mathbf{S}}_n d\Omega\\
&+\int_{\Omega^+}\left(\mathbf{N}^{eh}\right)^T\phi\mathbf{N}^{eh}\dot{\tilde{\mathbf{S}}}_n^r d\Omega+\int_{\Omega^+}\left(\mathbf{N}^{eh}\right)^T\phi\mathbf{N}^{eh}\delta\dot{\tilde{\mathbf{S}}}_n d\Omega\\
&+\int_{\Omega^+}\left(\nabla\mathbf{N}^{eh}\right)^T\mathbf{k}\lambda_n^r\nabla\mathbf{N}\mathbf{p}_w^r d\Omega+\int_{\Omega^+}\left(\nabla\mathbf{N}^{eh}\right)^T\mathbf{k}\lambda_n^r\nabla\mathbf{N}\delta\mathbf{p}_w d\Omega\\
&+\int_{\Omega^+}\left(\nabla\mathbf{N}^{eh}\right)^T\mathbf{k}\nabla\mathbf{N}\mathbf{p}_w^r\left(\frac{d\lambda_n}{dS_n}\mathbf{N}\delta\mathbf{S}_n\right)d\Omega\\
&+\int_{\Omega^+}\left(\nabla\mathbf{N}^{eh}\right)^T\mathbf{k}\nabla\mathbf{N}\mathbf{p}_w^r\left(\frac{d\lambda_n}{dS_n}\mathbf{N}^{eh}\delta\tilde{\mathbf{S}}_n\right)d\Omega\\
&+\int_{\Omega^+}\left(\nabla\mathbf{N}^{eh}\right)^T\mathbf{k}\eta_n^r\nabla\mathbf{N}\mathbf{S}_n^r\, d\Omega+\int_{\Omega^+}\left(\nabla\mathbf{N}^{eh}\right)^T\mathbf{k}\eta_n^r\nabla\mathbf{N}\delta\mathbf{S}_n\, d\Omega\\
&+\int_{\Omega^+}\left(\nabla\mathbf{N}^{eh}\right)^T\mathbf{k}\nabla\mathbf{N}\mathbf{S}_n^r\left(\frac{d\eta_n}{dS_n}\mathbf{N}\delta\mathbf{S}_n\right)d\Omega\\
&+\int_{\Omega^+}\left(\nabla\mathbf{N}^{eh}\right)^T\mathbf{k}\nabla\mathbf{N}\mathbf{S}_n^r\left(\frac{d\eta_n}{dS_n}\mathbf{N}^{eh}\delta\tilde{\mathbf{S}}_n\right)d\Omega\\
&+\int_{\Omega^+}\left(\nabla\mathbf{N}^{eh}\right)^T\mathbf{k}\eta_n^r\nabla\mathbf{N}^{eh}\tilde{\mathbf{S}}_n^r\, d\Omega+\int_{\Omega^+}\left(\nabla\mathbf{N}^{eh}\right)^T\mathbf{k}\eta_n^r\nabla\mathbf{N}^{eh}\delta\tilde{\mathbf{S}}_n\, d\Omega\\
&+\int_{\Omega^+}\left(\nabla\mathbf{N}^{eh}\right)^T\mathbf{k}\nabla\mathbf{N}^{eh}\tilde{\mathbf{S}}_n^r\left(\frac{d\eta_n}{dS_n}\mathbf{N}\delta\mathbf{S}_n\right)d\Omega\\
&+\int_{\Omega^+}\left(\nabla\mathbf{N}^{eh}\right)^T\mathbf{k}\nabla\mathbf{N}^{eh}\tilde{\mathbf{S}}_n^r\left(\frac{d\eta_n}{dS_n}\mathbf{N}^{eh}\delta\tilde{\mathbf{S}}_n\right)d\Omega\\
&-\int_{\Omega^+}\left(\nabla\mathbf{N}^{eh}\right)^T\mathbf{k}\lambda_n^r\rho_n\mathbf{g}d\Omega-\int_{\Omega^+}\left(\nabla\mathbf{N}^{eh}\right)^T\mathbf{k}\rho_n\mathbf{g}\left(\frac{d\lambda_n}{dS_n}\mathbf{N}\delta\mathbf{S}_n\right)d\Omega\\
&-\int_{\Omega^+}\left(\nabla\mathbf{N}^{eh}\right)^T\mathbf{k}\rho_n\mathbf{g}\left(\frac{d\lambda_n}{dS_n}\mathbf{N}^{eh}\delta\tilde{\mathbf{S}}_n\right)d\Omega+\frac{1}{\rho_n}\int_{\Gamma_n^{q+}}\left(\mathbf{N}^{eh}\right)^T\hat{q}_n d\Gamma\\
&-\frac{1}{\rho_n}\int_{\Gamma_d}\left(\mathbf{N}^{eh}\right)^T q_n^{\Gamma d}\, d\Gamma=0
\end{aligned}\tag{2.37}$$

In a concise form, Eq. (2.35) can be written as

$$\mathbf{K}_{11}\,\delta\mathbf{p}_w + \mathbf{K}_{12}\,\delta\mathbf{S}_n + \mathbf{K}_{13}\,\delta\tilde{\mathbf{S}}_n + \mathbf{C}_{12}\,\delta\dot{\mathbf{S}}_n + \mathbf{C}_{13}\,\delta\dot{\tilde{\mathbf{S}}}_n = \mathbf{f}_1 - (\mathbf{K}_{11}^0\,\mathbf{p}_w^r + \mathbf{C}_{12}^0\,\dot{\mathbf{S}}_n^r + \mathbf{C}_{13}^0\,\dot{\tilde{\mathbf{S}}}_n^r) \tag{2.38}$$

Similarly, Eqs. (2.36) and (2.37) can be written as

$$\mathbf{K}_{21}\,\delta\mathbf{p}_w + \mathbf{K}_{22}\,\delta\mathbf{S}_n + \mathbf{K}_{23}\,\delta\tilde{\mathbf{S}}_n + \mathbf{C}_{22}\,\delta\dot{\mathbf{S}}_n + \mathbf{C}_{23}\,\delta\dot{\tilde{\mathbf{S}}}_n = \mathbf{f}_2 - (\mathbf{K}_{21}^0\,\mathbf{p}_w^r + \mathbf{K}_{22}^0\,\mathbf{S}_n^r + \mathbf{K}_{23}^0\,\tilde{\mathbf{S}}_n^r + \mathbf{C}_{22}^0\,\dot{\mathbf{S}}_n^r + \mathbf{C}_{23}^0\,\dot{\tilde{\mathbf{S}}}_n^r) \tag{2.39}$$

$$\mathbf{K}_{31}\,\delta\mathbf{p}_w + \mathbf{K}_{32}\,\delta\mathbf{S}_n + \mathbf{K}_{33}\,\delta\tilde{\mathbf{S}}_n + \mathbf{C}_{32}\,\delta\dot{\mathbf{S}}_n + \mathbf{C}_{33}\,\delta\dot{\tilde{\mathbf{S}}}_n = \mathbf{f}_3 - (\mathbf{K}_{31}^0\,\mathbf{p}_w^r + \mathbf{K}_{32}^0\,\mathbf{S}_n^r + \mathbf{K}_{33}^0\,\tilde{\mathbf{S}}_n^r + \mathbf{C}_{32}^0\,\dot{\mathbf{S}}_n^r + \mathbf{C}_{33}^0\,\dot{\tilde{\mathbf{S}}}_n^r) \tag{2.40}$$

Collecting Eqs. (2.38)-(2.40) in a matrix form, yields

$$\begin{pmatrix}\mathbf{K}_{11} & \mathbf{K}_{12} & \mathbf{K}_{13}\\ \mathbf{K}_{21} & \mathbf{K}_{22} & \mathbf{K}_{23}\\ \mathbf{K}_{31} & \mathbf{K}_{32} & \mathbf{K}_{33}\end{pmatrix}\begin{Bmatrix}\delta\mathbf{p}_w\\ \delta\mathbf{S}_n\\ \delta\tilde{\mathbf{S}}_n\end{Bmatrix} + \begin{pmatrix}0 & \mathbf{C}_{12} & \mathbf{C}_{13}\\ 0 & \mathbf{C}_{22} & \mathbf{C}_{23}\\ 0 & \mathbf{C}_{32} & \mathbf{C}_{33}\end{pmatrix}\begin{Bmatrix}\delta\dot{\mathbf{p}}_w\\ \delta\dot{\mathbf{S}}_n\\ \delta\dot{\tilde{\mathbf{S}}}_n\end{Bmatrix} = \begin{Bmatrix}\mathbf{f}_1\\ \mathbf{f}_2\\ \mathbf{f}_3\end{Bmatrix} - \begin{pmatrix}\mathbf{K}_{11}^0 & 0 & 0\\ \mathbf{K}_{21}^0 & \mathbf{K}_{22}^0 & \mathbf{K}_{23}^0\\ \mathbf{K}_{31}^0 & \mathbf{K}_{32}^0 & \mathbf{K}_{33}^0\end{pmatrix}\begin{Bmatrix}\mathbf{p}_w^r\\ \mathbf{S}_n^r\\ \tilde{\mathbf{S}}_n^r\end{Bmatrix} - \begin{pmatrix}0 & \mathbf{C}_{12}^0 & \mathbf{C}_{13}^0\\ 0 & \mathbf{C}_{22}^0 & \mathbf{C}_{23}^0\\ 0 & \mathbf{C}_{32}^0 & \mathbf{C}_{33}^0\end{pmatrix}\begin{Bmatrix}\dot{\mathbf{p}}_w^r\\ \dot{\mathbf{S}}_n^r\\ \dot{\tilde{\mathbf{S}}}_n^r\end{Bmatrix} \tag{2.41}$$

The matrix entries of this equation are given in Appendix A.

Eq. (2.41) contains an extra degree of freedom as compared to that if the standard Galerkin method is utilized to discretize all variables. This entails that the system of equations that needs to be solved is larger. However, this increase is minor, as the extra degree of freedom is only added to the nodes where the element intersects the boundary between layers. This increase in the system size is compensated by the advantages of the partition of unity method. This method is effectively mesh-independent, allowing thus for the utilization of relatively coarse meshes. Also, as the boundary between the layers is described within the element, the mesh can be independent of the alignment of the involved layers, allowing thus the use of structured meshes.

Time discretization of the semi-discrete equation, Eq. (2.41), can be done using a standard time discretization algorithm. Here, the theta-method (Lewis and Schrefler 1998) is utilized. A direct sparse linear solver is utilized to solve the linearized algebraic set of equations.

2.3.3 Leakage term

The leakage term $q_n^{\Gamma_d}$ in Eq. (2.26) is the mass flux, which describes the rate of mass flow per unit area of the interface between two layers. At the interface between two layers, the following conditions exist (Helmig and Huber 1998; Van Duijn et al. 1995; Fučík and Mikyška 2011) (see Fig. 2.1):

1. Immobile non-wetting phase:

$$\begin{aligned} q_n^{\Gamma d} &= 0 \\ p_c^+ &\neq p_c^- \end{aligned} \tag{2.42}$$

2. Mobile non-wetting phase:

$$\begin{aligned} q_n^{\Gamma d} &> 0 \\ p_c^+ &= p_c^- \end{aligned} \tag{2.43}$$

in which the superscripts ($^+$) and ($^-$) indicate the field values at the Ω^+ side and the Ω^- side of the interface, respectively (see Fig. 2.2).

Substituting Eqs. (2.3), (2.8), and (10) into the second equation of Eq. (2.43) leads to

$$p_b^+ \left(\frac{1-\left(S_n^{i+1}\right)^+ - S_{rw}^+}{1-S_{rw}^+ - S_{rn}^+} \right)^{-1/\hat{\theta}^+} = p_b^- \left(\frac{1-\left(S_n^{i+1}\right)^- - S_{rw}^-}{1-S_{rw}^- - S_{rn}^-} \right)^{-1/\hat{\theta}^-} \tag{2.44}$$

where $\left(S_n^{i+1}\right)^+$ and $\left(S_n^{i+1}\right)^-$ are the non-wetting phase saturations corresponding to the current time step i+1, that can be delineated as

$$\left(S_n^{i+1}\right)^+ = \left(S_n^i\right)^+ + \Delta S_n^+ \tag{2.45}$$

$$\left(S_n^{i+1}\right)^- = \left(S_n^i\right)^- + \Delta S_n^- \tag{2.46}$$

in which ΔS_n^+ and ΔS_n^- are the current saturation changes that are necessary to satisfy the capillary pressure field condition given in the second equation of Eq. (2.43).

Substituting Eqs. (2.45) and (2.46) into Eq. (2.44) gives

$$\begin{aligned} p_b^+ \left(\frac{1-\left(S_n^i\right)^+ - \Delta S_n^+ - S_{rw}^+}{1-S_{rw}^+ - S_{rn}^+} \right)^{-1/\hat{\theta}^+} \\ - p_b^- \left(\frac{1-\left(S_n^i\right)^- - \Delta S_n^- - S_{rw}^-}{1-S_{rw}^- - S_{rn}^-} \right)^{-1/\hat{\theta}^-} = 0 \end{aligned} \tag{2.47}$$

where all parameters are known, except ΔS_n^+ and ΔS_n^-. Since Eq. (2.47) contains two unknowns, another equation is necessary.

Following the conservation of mass, the mass entering the interface should be equal to the mass leaving, implying that the mass flow rate of the non-wetting phase is equal at both sides of the interface, as

$$\mathbf{q}_n^{\Gamma d+} \cdot \mathbf{m}^+ = \mathbf{q}_n^{\Gamma d-} \cdot \mathbf{m}^- \tag{2.48}$$

where $\mathbf{m}^+$ is the unit vector pointing out of Ω^+ zone into Ω^- zone, and $\mathbf{m}^-$ is the unit vector pointing out of Ω^- zone into Ω^+ zone, with

$$\mathbf{m}^{+} = -\mathbf{m}^{-} \tag{2.49}$$

giving

$$q_n^{\Gamma d+} = -q_n^{\Gamma d-} \tag{2.50}$$

where these mass fluxes can be described as

$$q_n^{\Gamma d+} = -\frac{\phi^{+}\Delta S_n^{+}\rho_n V^{+}}{A\Delta t} \tag{2.51}$$

$$q_n^{\Gamma d-} = -\frac{\phi^{-}\Delta S_n^{-}\rho_n V^{-}}{A\Delta t} \tag{2.52}$$

in which A is the interface surface area and V^{+} and V^{-} are the volumes of the non-wetting phase mass accumulating just before and after the interface, respectively. Assuming $V^{+} = V^{-}$ and substituting Eqs. (2.51) and (2.52) into Eq. (2.50) gives

$$\Delta S_n^{-} = -\frac{\phi^{+}}{\phi^{-}}\Delta S_n^{+} \tag{2.53}$$

Substituting Eq. (2.53) into Eq. (2.47) would eliminate ΔS_n^{-}, giving an algebraic equation with one unknown (ΔS_n^{+}), as

$$p_b^{+}\left(\frac{1-\left(S_n^{i}\right)^{+}-\Delta S_n^{+}-S_{rw}^{+}}{1-S_{rw}^{+}-S_{rn}^{+}}\right)^{-1/\hat{\theta}^{+}} - p_b^{-}\left(\frac{1-\left(S_n^{i}\right)^{-}+\frac{\phi^{+}}{\phi^{-}}\Delta S_n^{+}-S_{rw}^{-}}{1-S_{rw}^{-}-S_{rn}^{-}}\right)^{-1/\hat{\theta}^{-}} = 0 \tag{2.54}$$

Having ΔS_n^{+}, the mass flux across the boundary between two layers can then be calculated using Eq. (2.51). This equation can be written as

$$q_n^{\Gamma d+} = -\frac{\phi^{+}\Delta S_n^{+}\rho_n V}{A\Delta t} = -\frac{\phi^{+}\Delta S_n^{+}\rho_n Z}{\Delta t} \tag{2.55}$$

where Z is the thickness of the non-wetting mass accumulating before the interface (in case of fluid flow from a high to a low permeability domain) or the thickness of the suction zone (in case of fluid flow from a low to a high permeability domain). This parameter depends on the physics of the problem, mainly on the contrast between the entry pressures of the neighboring layers, permeability of the involved materials and the applied fluid flux. Formulating an exact constitutive relationship for Z is beyond the scope of this work. Alternatively, we employed an iterative scheme for its determination

such that the conservation of mass between the two sides of the boundary between two layers is maintained. The algorithm of this iterative scheme is:

0. **Do loop** over *i* (time steps)
1. $\left(S_n^i\right)^+ \leftarrow \left(S_n^{i+1}\right)^+$
2. **Do loop** over *Z*
3. Initialize *Z*
4. Calculate ΔS_n^+, Eq. (2.54)
5. Calculate $q_n^{\Gamma d+}$, Eq. (2.55)
6. **Do loop** over *r* (nonlinear iterations)
7. Compute state vector increments, Eq. (2.41)
8. **End Do loop** over *r*.
9. If the conditions in Eqs. (2.42) and (2.43), for immobile and mobile non-wetting phase, are not satisfied, modify *Z* and go back to step 4. Otherwise exit the loop.
10. **End Do loop** over *Z*.
11. Calculate $\left(S_n^{i+1}\right)^+$
12. **End Do loop** over *i*.

2.4 Verification and Numerical Examples

In this section, a verification example comparing the PUM-SG computational result to that obtained from a semi-analytical solution is studied. Additionally, two numerical examples evaluating the numerical capabilities of the model for simulating layered medium domains exhibiting leakages are presented.

2.4.1 Model Verification

Van Duijn and De Neef (1998) provided a semi-analytical solution based on the similarity solution technique to solve fluid flow in a two-layer system. The geometry constitutes two semi-infinite porous medium domains in-contact, as shown in Fig. 2.4. The left-hand side domain is initially saturated with a wetting phase, and the right-hand side domain is initially saturated with a non-wetting phase. With time, due to the capillary pressure, the wetting phase starts to infiltrate into the non-wetting phase domain. As expected, a jump in the saturation field occurs at the boundary between the two layers.

Fig. 2.4 Van Duijn and De Neef (1998) domain and initial condition.

We solve this problem using the proposed PUM-SG model. The computational domain and boundary conditions are shown in Fig. 2.5. To compare to the semi-analytical solution, the following dimensionless parameters are utilized:

$$x^* = \frac{1}{L}x \; ; \; t^* = \frac{\sigma\sqrt{k^*}}{\mu_w L^2}t \; ; \; h^* = \left(\frac{k}{k^*\phi}\right)^{\frac{1}{2}} \; ; \; M = \frac{\mu_n}{\mu_w} \; ; \; F = \frac{\phi_r}{\phi_l} \tag{2.56}$$

in which x^* is a dimensionless distance from the interface, L is a reference quantity for length, x is the distance from the interface, t^* is a dimensionless time, σ is the interfacial tension, and k^* is a reference permeability. We implemented $h_l^* = 1$, $h_r^* = 0.5$, $M = 1$, $F = 1$, pore size distribution index ($\hat{\theta}$) = 2, entry pressure at the left-hand side domain = $\sigma\sqrt{\phi_l / k_l}$, and entry pressure at the right-hand side = $\sigma\sqrt{\phi_r / k_r}$, as given by Van Duijn and De Neef (1998).

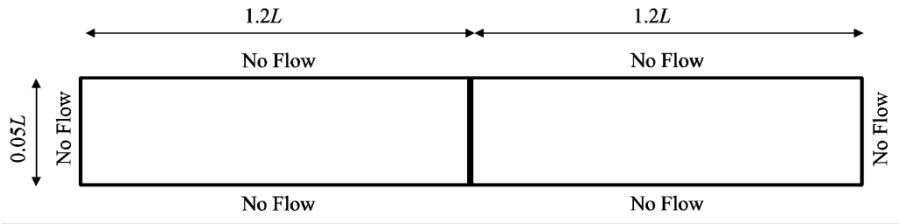

Fig. 2.5 Computational domain and boundary conditions.

Finite element meshes with different sizes are utilized: 75, 125 and 300 linear elements along the length of the domain (*x*-direction). Fig. 2.6 shows the computed results for the three mesh sizes, together with the semi-analytical solution of Van Duijn and De Neef (1998). The figure clearly shows that there is a good match between the two solutions, whereas the results obtained from the fine mesh is almost identical to the semi-analytical solution.

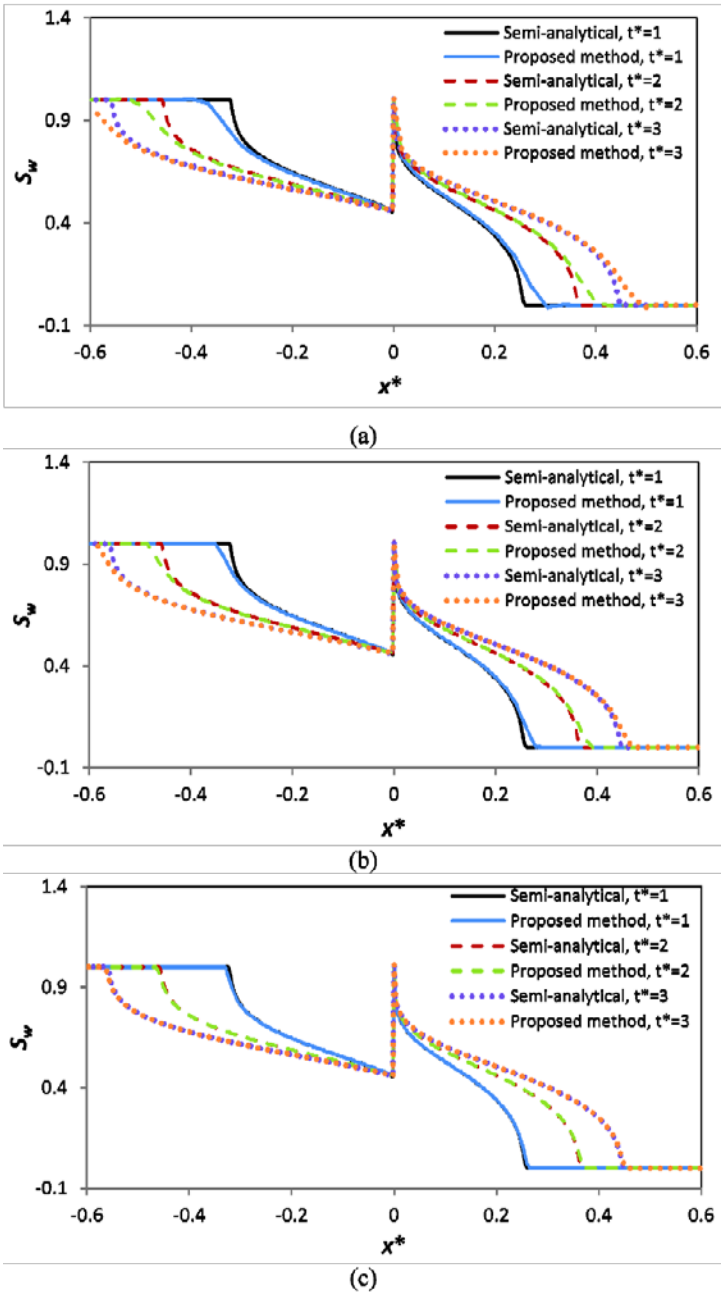

Fig. 2.6 PUM-SG versus Van Duijn and De Neef semi-analytical solution using: (a) 75 elements, (b) 125 elements, and (c) 300 elements.

A convergence study is conducted to investigate the rate of convergence of the proposed model. The L_1 error norm is utilized, defined as

$$L_{1-\text{error}} = \int_{\Omega} \left| S_w - S_w^{ref} \right| d\Omega \tag{2.57}$$

where S_w^{ref} is the reference value calculated from the semi-analytical solution of Van Duijn and De Neef (1998). The error norms for three different points in time using four mesh sizes, 25, 75, 125, and 300 elements have been calculated. The results are plotted in Fig. 2.7 along with those reported by Friis and Evje (2011), who solved the problem using the finite volume method with two different permeability averaging techniques: harmonic averaging and arithmetic averaging. The figure shows that the convergence rate of the proposed model is relatively high, several times higher than that based on the finite volume method.

Table 2.1 shows the error in jump in saturation versus mesh sizes for three points in time. The table clearly exhibits that with finer meshes, the error becomes smaller. Nevertheless, all mesh sizes give a reasonable error, which suggests that the method is mesh-independent.

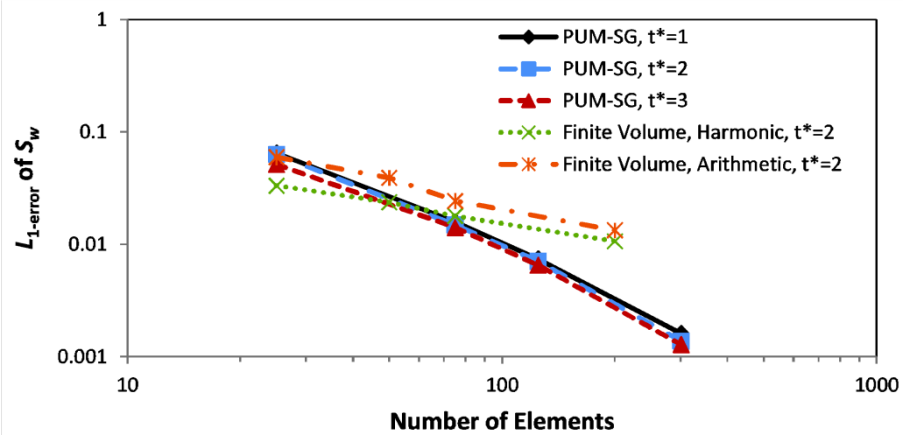

Fig. 2.7 Model convergence rate.

Table 2.1 Error in saturation discontinuity at three points in time.

Number of elements	Error (%)		
	t^*=1	t^*=2	t^*=3
25	0.74	3.74	3.62
75	3.69	0.88	0.24
125	1.44	0.15	0.99
300	1.12	0.15	0.18

2.4.2 DNAPL Infiltration

Helmig and Huber (1998) and Fučík and Mikyška (2011), among others, numerically examined the infiltration of a Dense Non-Aqueous Phase Liquid (DNAPL) in a multilayer system. The geometry constitutes a three-layer soil column, with a relatively high permeability (k_1) at the upper and lower layers, and a relatively low permeability (k_2) in the middle layer. The geometry of this problem together with the dimensions and boundary conditions are shown in Fig. 2.8.

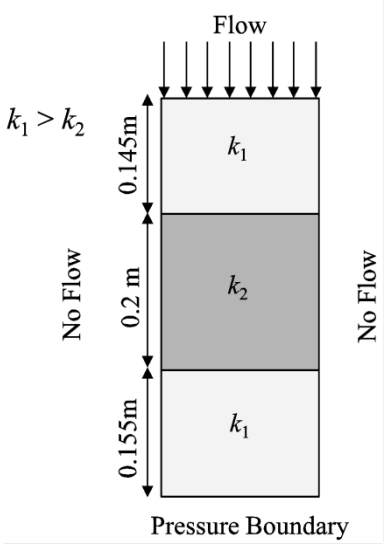

Fig. 2.8 DNAPL infiltration problem.

Initially, the domain is saturated with water. Then, DNAPL was injected from the upper boundary at a constant flow rate of 0.05 kg/s. The left- and right-hand side boundaries are closed to the flow, and a pressure boundary condition is defined at the lower boundary so that the water and DNAPL can freely exit the domain. The gravitational force is taken into account, and the Brooks-Corey relationships are

utilized. Table 2.2 lists the fluid and layers properties, and Fig. 2.9 shows the corresponding Brooks and Corey diagrams.

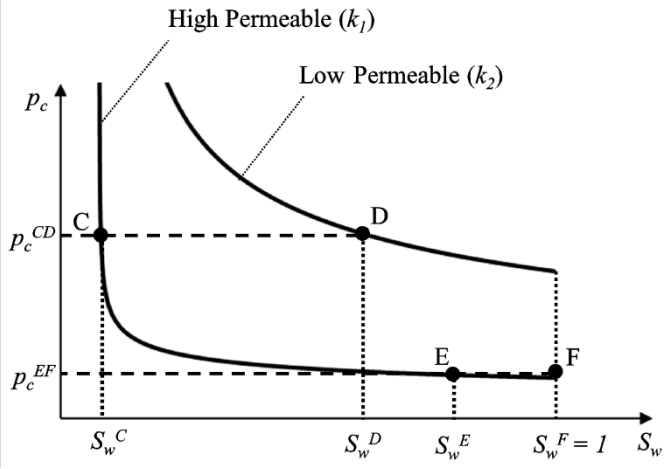

Fig. 2.9 Brooks and Corey diagrams for DNAPL infiltration example.

Table 2.2 Fluid and porous media properties for DNAPL infiltration problem.

Fluid properties	**Water**	**DNAPL**
Density [kg/m^3]	1000	1400
Viscosity [Pa.s]	0.001	0.001
Porous media properties	**Porous Medium #1 (high permeable)**	**Porous Medium #2 (low permeable)**
Permeability [m^2]	5.04×10^{-10}	5.26×10^{-11}
Porosity	0.4	0.39
Entry pressure (Brooks-Corey) [Pa]	370	1324
$\hat{\theta}$ (Brooks-Corey)	3.86	2.49
Water residual saturation	0.08	0.10
DNAPL residual saturation	0.00	0.00

We first utilized the standard Galerkin finite element method to solve the problem. Fig. 2.10 shows a DNAPL saturation distribution at time t = 1700 s using a relatively fine mesh (500 linear elements). It shows that there is a rise in the DNAPL saturation starting just before the boundary between the upper and middle layers and continuing in the middle layer. This behavior is physically not correct as there should be an accumulation of DNAPL at the boundary between the two layers, followed by a jump in the saturation field. This erroneous result is expected since the standard Galerkin method is not capable of modeling the jump in the saturation field between layers of

different hydraulic parameters. Helmig and Huber (1998) have shown similar results for the standard Galerkin finite element method.

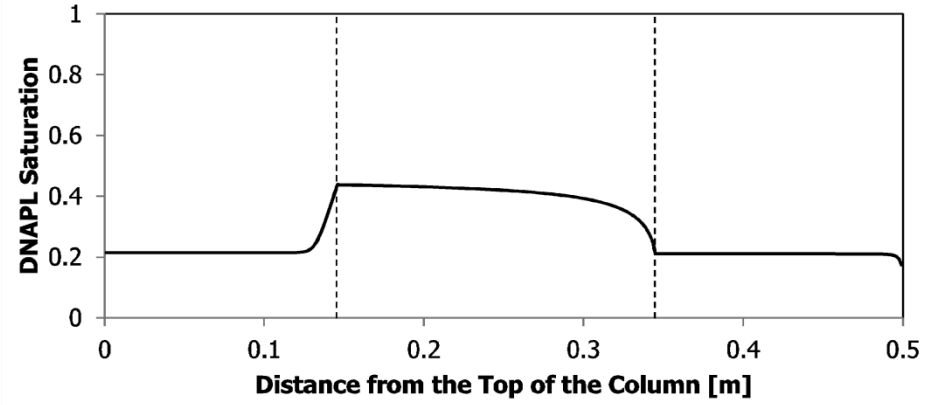

Fig. 2.10 Solution of DNAPL infiltration problem using standard Galerkin FEM method.

Fig. 2.11 shows the DNAPL saturation distribution at time t = 1700 s using the proposed PUM-SG model. Three finite element mesh sizes consisting of 25, 50 and 200 linear elements were utilized. The computational results show that the proposed model could capture accurately the saturation jump at the interfaces, even with the use of the relatively coarse mesh. However, the 25 elements mesh exhibits some errors before the jump, which is expected for such a coarse mesh. The 50 and 200 elements meshes exhibit accurate results in the whole domain. The computational results with 200 elements have been compared to the results given by Fučík and Mikyška (2011), as illustrated in Fig. 2.12. It can be seen that the results are very close, though the PUM-SG results are more accurate at the suction interface, where it predicts full suction, while Fučík and Mikyška's model does not. The difference at the front location, however, is due to that Fučík and Mikyška have stopped their analysis at 1650 s, and we have stopped at 1700 s.

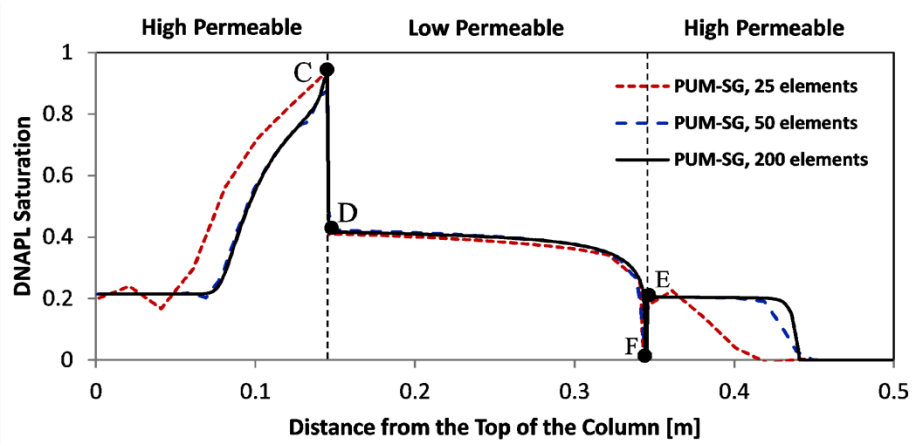

Fig. 2.11 Solution of DNAPL infiltration problem using PUM-SG model.

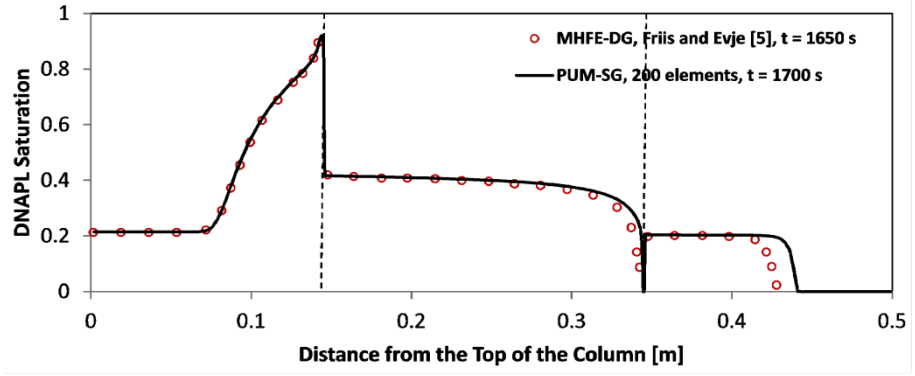

Fig. 2.12 PUM-SG versus Fučík and Mikyška model.

At the beginning, DNAPL accumulates at the boundary between the upper layer and the middle layer, on the upper layer side. In this case, the capillary pressure is discontinuous at the boundary. As the capillary pressure exceeds the entry pressure of the middle layer, DNAPL infiltrates into the middle layer. In this case, the capillary pressure is continuous and the saturation is discontinuous, as shown on points C and D on the Brooks and Corey diagram, Fig. 2.9.

On the boundary between the middle layer and the lower layer, suction occurs, appearing as a drop in the saturation profile before the boundary between the two layers and a sudden rise after the boundary. In this case, the entry pressure of the middle layer is initially higher than that of the lower layer, giving rise, upon the arrival of the DNAPL, to an immediate leakage. This behavior corresponds to points E and F on the

Brooks and Corey diagram in Fig. 2.9. Note that point F in Fig. 2.11 indicates $S_{DNAPL} = S_n = 0$, which corresponds to $S_w = 1$ in Fig. 2.9.

2.4.3 CO_2 Leakage

CO_2 geo-sequestration is currently utilized as a means to mitigate CO_2 emission to the atmosphere in an attempt to reduce the likely greenhouse effect. Selection of an appropriate geological formation for CO_2 sequestration requires a good estimate of the amount of leakage that might take place in time. Leakage of CO_2 to the ground surface or upper layers containing ground water is considered as one of the main concerns of applying this technology.

This example demonstrates the computational capability and efficiency of the proposed model to simulate the likely leakage of CO_2 in a two-dimensional non-horizontally layered domain. The geometry is assumed to describe an aquifer bounded by a cap-rock and subjected to CO_2 injection. Fig. 2.13 shows the geometry and boundary conditions, and Table 2.3 lists the material and physical properties of the domain. The fluid and the porous medium properties of the aquifer are taken from the well-known benchmark leakage problem, which is utilized in literature to compare between numerical simulators (Class et al. 2009). For the cap-rock layer, the entry pressure is made 1.156 times that of the aquifer, and the permeability is made 0.375 times that of the aquifer. The Brooks and Corey relationships are assumed. The CO_2 is injected at a constant flow rate of 12.5 kg/day from the lower left corner of the aquifer. The gravity is taken into consideration so that the buoyancy forces will lead the CO_2 to flow upwards, towards the cap-rock. Because leakage is the main interest here, this set of material properties and boundary conditions is imposed such that we observe a significant contrast in performance between the proposed model and models based on standard numerical schemes.

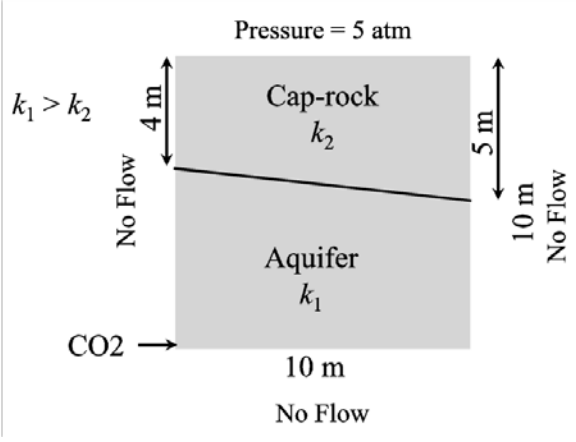

Fig. 2.13 Geometry and boundary conditions for the CO_2 injection problem.

This problem is solved using the standard Galerkin finite element method and the proposed PUM-SG model by means of five mesh sizes: 9, 25, 121, 225 and 400 linear elements. The finite element mesh for the SG must coincide with the boundary between the two layers, while for PUM-SG, this is not necessary. A structured mesh can be used for the PUM-SG model which enables the use of a standard simple mesh generator. Fig. 2.14 shows an example of these meshes.

Table 2.3 Fluid and domain properties for the problem of CO_2 injection.

Fluid properties	**Water**	**CO_2**
Density [kg/m^3]	1045	479
Viscosity [Pa.s]	2.535×10^{-4}	3.950×10^{-5}
Porous media properties	**Aquifer (high permeable)**	**Cap-rock (low permeable)**
Permeability [m^2]	2.0×10^{-14}	7.5×10^{-15}
Porosity	0.15	0.1
Entry pressure (Brooks-Corey) [kPa]	225	260
$\hat{\theta}$ (Brooks-Corey)	4.0	2.0
Water residual saturation	0.20	0.20
CO_2 residual saturation	0.00	0.00

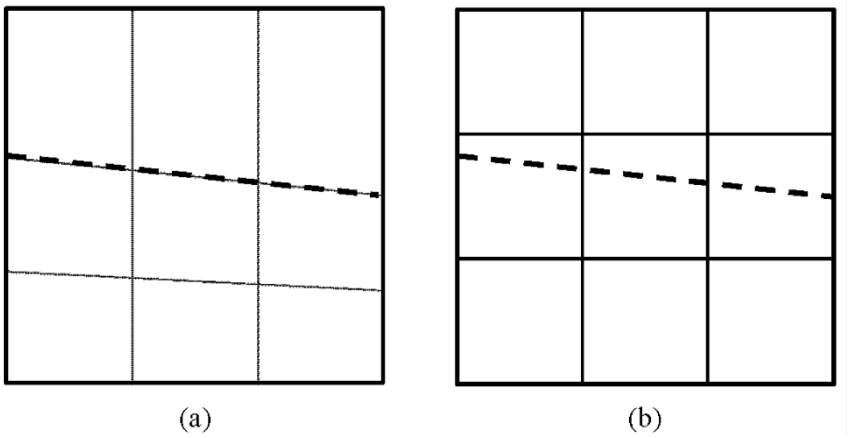

Fig. 2.14 Finite element meshes: (a) standard Galerkin model, and (b) PUM-SG model.

Fig. 2.15 shows the computational results of both models at time t = 82 days. Apparently, the standard Galerkin model, even for the relatively fine meshes, was not able to capture the jump in the saturation field at the boundary between the two layers, giving a false impression about the amount of leakage.

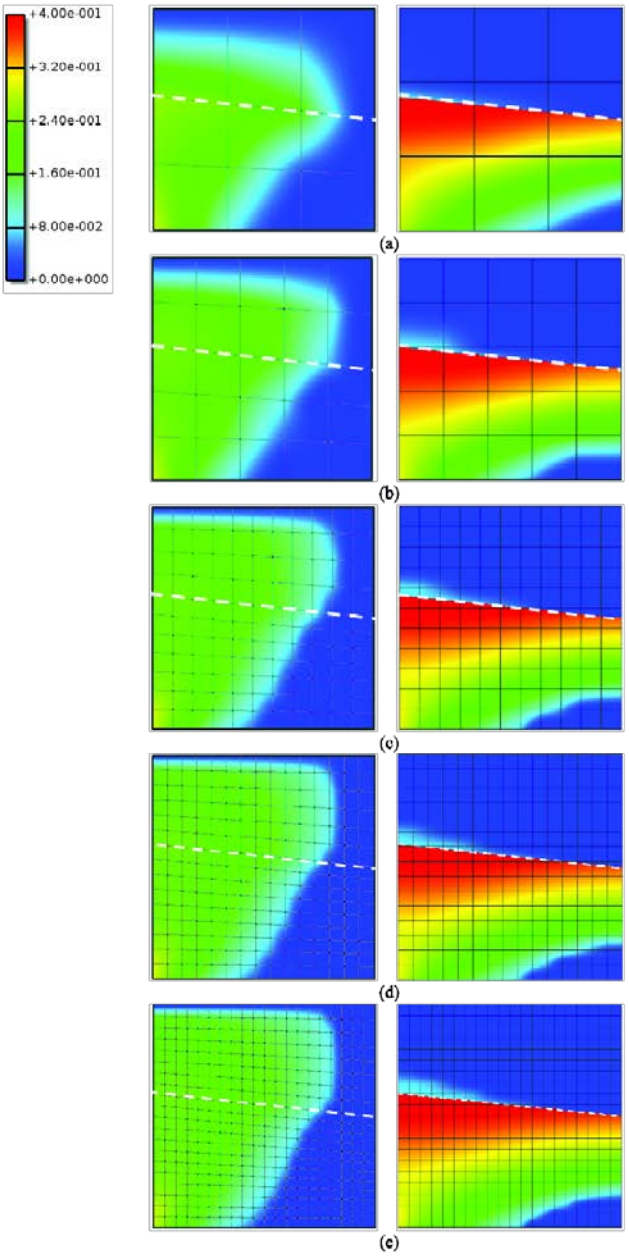

Fig. 2.15 CO_2 phase saturation distribution at t = 82 days. Left: standard Galerkin model; Right: PUM-SG model: (a) 9 elements, (b) 25 elements, (c) 121 elements, (d) 225 elements, (e) 400 elements.

On the other hand, the PUM-SG model could capture this phenomenon even with 9 elements, though the leakage was not as accurate. For 121 to 400 elements meshes, the computational results exhibit analogous accumulation and leakage, indicating that the model is effectively mesh-independent.

Fig. 2.16 shows the resulting pore pressure ($p = S_w p_w + S_n p_n$) obtained from the SG model and the PUM-SG model. Clearly, the figure shows a significant difference in the pore pressure distribution in the aquifer and the cap-rock layer between the two models. Failure to capture gas accumulation at the boundary between the aquifer and the cap-rock by the SG model leads to incorrect pore pressure distribution, and hence incorrect prediction of the mechanical behavior of the CO_2 sequestration region.

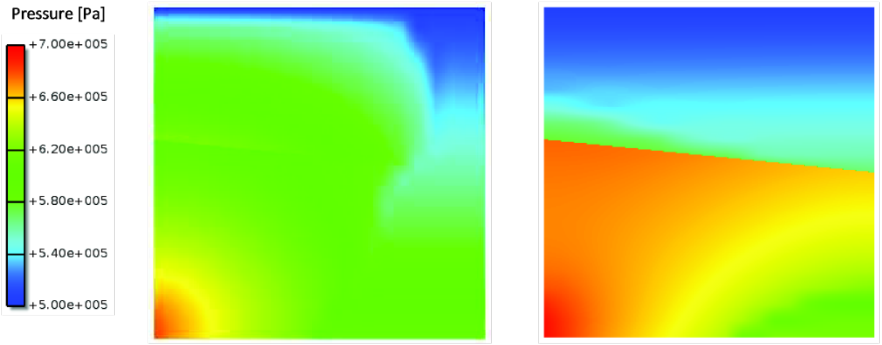

Fig. 2.16 Pore pressure distribution for the CO_2 leakage problem at t = 82 days (by using 400 elements): (a) SG model, and (b) PUM-SG model.

2.5 Conclusions

Leakage of fluids into underground formations is in many cases unwanted. Among others, contaminants, DNAPL and CO_2 leakage to the groundwater layers or to the ground surface is considered as one of the main concerns of applying geoenvironmental engineering technologies. This necessitates the development of computational tools capable of simulating this phenomenon accurately and efficiently.

In this work, we introduced a computationally efficient model capable of capturing a non-wetting phase leakage at the boundary between heterogeneous layers. A mixed discretization scheme is utilized. This scheme entails solving coupled balance equations using different discretization schemes, which are tailored to accurately describe the physics of the primary state variables. We utilized the standard Galerkin finite element method to discretize the continuous water pressure field, and the partition of unity finite element method to discretize the discontinuous saturation field. The finite element formulation is three-dimensional (3D) but the computer implementation is two-

dimensional (2D). The focus here is on the computational scheme which requires an intensive verification and validation study, that necessitates relatively short CPU time and small computer capacity. However, extension to 3D can be made using the usual finite element implementation practice.

The advantages of the proposed model is, in addition to its accuracy and robustness, its ability to embed the boundary between layers within the elements, allowing for the use of structured and geometry-independent meshes.

2.6 Appendix A. Components of the finite element matrices

$$\mathbf{K}_{11} = \int_{\Omega} \nabla \mathbf{N}^T \mathbf{k} \lambda_w^r \nabla \mathbf{N} \, d\Omega \tag{2.58}$$

$$\mathbf{K}_{12} = \int_{\Omega} \nabla \mathbf{N}^T \mathbf{k} \nabla \mathbf{N} \mathbf{p}_w^r \left(\frac{d\lambda_w}{dS_n} \mathbf{N} \right) d\Omega - \int_{\Omega} \nabla \mathbf{N}^T \mathbf{k} \rho_w \mathbf{g} \left(\frac{d\lambda_w}{dS_n} \mathbf{N} \right) d\Omega \tag{2.59}$$

$$\mathbf{K}_{13} = \int_{\Omega} \nabla \mathbf{N}^T \mathbf{k} \nabla \mathbf{N} \mathbf{p}_w^r \left(\frac{d\lambda_w}{dS_n} \mathbf{N}^{eh} \right) d\Omega - \int_{\Omega} \nabla \mathbf{N}^T \mathbf{k} \rho_w \mathbf{g} \left(\frac{d\lambda_w}{dS_n} \mathbf{N}^{eh} \right) d\Omega \tag{2.60}$$

$$\mathbf{K}_{21} = \int_{\Omega} \nabla \mathbf{N}^T \mathbf{k} \lambda_n^r \nabla \mathbf{N} \, d\Omega \tag{2.61}$$

$$\begin{aligned} \mathbf{K}_{22} = & \int_{\Omega} \nabla \mathbf{N}^T \mathbf{k} \nabla \mathbf{N} \mathbf{p}_w^r \left(\frac{d\lambda_n}{dS_n} \mathbf{N} \right) d\Omega + \int_{\Omega} \nabla \mathbf{N}^T \mathbf{k} \eta_n^r \nabla \mathbf{N} \, d\Omega \\ & + \int_{\Omega} \nabla \mathbf{N}^T \mathbf{k} \nabla \mathbf{N} \mathbf{S}_n^r \left(\frac{d\eta_n}{dS_n} \mathbf{N} \right) d\Omega + \int_{\Omega^+} \nabla \mathbf{N}^T \mathbf{k} \nabla \mathbf{N}^{eh} \tilde{\mathbf{S}}_n^r \left(\frac{d\eta_n}{dS_n} \mathbf{N} \right) d\Omega \\ & - \int_{\Omega} \nabla \mathbf{N}^T \mathbf{k} \rho_n \mathbf{g} \left(\frac{d\lambda_n}{dS_n} \mathbf{N} \right) d\Omega \end{aligned} \tag{2.62}$$

$$\begin{aligned} \mathbf{K}_{23} = & \int_{\Omega} \nabla \mathbf{N}^T \mathbf{k} \nabla \mathbf{N} \mathbf{p}_w^r \left(\frac{d\lambda_n}{dS_n} \mathbf{N}^{eh} \right) d\Omega + \int_{\Omega^+} \nabla \mathbf{N}^T \mathbf{k} \eta_n^r \nabla \mathbf{N}^{eh} \, d\Omega \\ & + \int_{\Omega+} \nabla \mathbf{N}^T \mathbf{k} \nabla \mathbf{N}^{eh} \tilde{\mathbf{S}}_n^r \left(\frac{d\eta_n}{dS_n} \mathbf{N}^{eh} \right) d\Omega + \int_{\Omega} \nabla \mathbf{N}^T \mathbf{k} \nabla \mathbf{N} \mathbf{S}_n^r \left(\frac{d\eta_n}{dS_n} \mathbf{N}^{eh} \right) d\Omega \\ & - \int_{\Omega} \nabla \mathbf{N}^T \mathbf{k} \rho_n \mathbf{g} \left(\frac{d\lambda_n}{dS_n} \mathbf{N}^{eh} \right) d\Omega \end{aligned} \tag{2.63}$$

$$\mathbf{K}_{31} = \int_{\Omega^+} \left(\nabla \mathbf{N}^{eh} \right)^T \mathbf{k} \lambda_n^r \nabla \mathbf{N} \, d\Omega \tag{2.64}$$

$$\mathbf{K}_{32} = \int_{\Omega^+} \left(\nabla \mathbf{N}^{eh}\right)^T \mathbf{k} \nabla \mathbf{N} \mathbf{p}_w^r \left(\frac{d\lambda_n}{dS_n} \mathbf{N}\right) d\Omega + \int_{\Omega^+} \left(\nabla \mathbf{N}^{eh}\right)^T \mathbf{k} \eta_n^r \nabla \mathbf{N} \, d\Omega + \int_{\Omega^+} \left(\nabla \mathbf{N}^{eh}\right)^T \mathbf{k} \nabla \mathbf{N} \mathbf{S}_n^r \left(\frac{d\eta_n}{dS_n} \mathbf{N}\right) d\Omega + \int_{\Omega^+} \left(\nabla \mathbf{N}^{eh}\right)^T \mathbf{k} \nabla \mathbf{N}^{eh} \tilde{\mathbf{S}}_n^r \left(\frac{d\eta_n}{dS_n} \mathbf{N}\right) d\Omega - \int_{\Omega^+} \left(\nabla \mathbf{N}^{eh}\right)^T \mathbf{k} \rho_n \mathbf{g} \left(\frac{d\lambda_n}{dS_n} \mathbf{N}\right) d\Omega \tag{2.65}$$

$$\mathbf{K}_{33} = \int_{\Omega^+} \left(\nabla \mathbf{N}^{eh}\right)^T \mathbf{k} \nabla \mathbf{N} \mathbf{p}_w^r \left(\frac{d\lambda_n}{dS_n} \mathbf{N}^{eh}\right) d\Omega + \int_{\Omega^+} \left(\nabla \mathbf{N}^{eh}\right)^T \mathbf{k} \nabla \mathbf{N} \mathbf{S}_n^r \left(\frac{d\eta_n}{dS_n} \mathbf{N}^{eh}\right) d\Omega + \int_{\Omega^+} \left(\nabla \mathbf{N}^{eh}\right)^T \mathbf{k} \eta_n^r \nabla \mathbf{N}^{eh} \, d\Omega + \int_{\Omega^+} \left(\nabla \mathbf{N}^{eh}\right)^T \mathbf{k} \nabla \mathbf{N}^{eh} \tilde{\mathbf{S}}_n^r \left(\frac{d\eta_n}{dS_n} \mathbf{N}^{eh}\right) d\Omega - \int_{\Omega^+} \left(\nabla \mathbf{N}^{eh}\right)^T \mathbf{k} \rho_n \mathbf{g} \left(\frac{d\lambda_n}{dS_n} \mathbf{N}^{eh}\right) d\Omega \tag{2.66}$$

$$\mathbf{C}_{12} = -\int_{\Omega} \mathbf{N}^T \phi \mathbf{N} \delta d\Omega \tag{2.67}$$

$$\mathbf{C}_{13} = -\int_{\Omega} \mathbf{N}^T \phi \mathbf{N}^{eh} d\Omega \tag{2.68}$$

$$\mathbf{C}_{22} = \int_{\Omega} \mathbf{N}^T \phi \mathbf{N} \, d\Omega \tag{2.69}$$

$$\mathbf{C}_{23} = \int_{\Omega} \mathbf{N}^T \phi \mathbf{N}^{eh} d\Omega \tag{2.70}$$

$$\mathbf{C}_{32} = \int_{\Omega^+} \left(\mathbf{N}^{eh}\right)^T \phi \mathbf{N} \, d\Omega \tag{2.71}$$

$$\mathbf{C}_{33} = \int_{\Omega^+} \left(\mathbf{N}^{eh}\right)^T \phi \mathbf{N}^{eh} d\Omega \tag{2.72}$$

$$\mathbf{K}_{11}^0 = \int_{\Omega} \nabla \mathbf{N}^T \mathbf{k} \lambda_w^r \nabla \mathbf{N} \, d\Omega \tag{2.73}$$

$$\mathbf{K}_{21}^0 = \int_{\Omega} \nabla \mathbf{N}^T \mathbf{k} \lambda_n^r \nabla \mathbf{N} \, d\Omega \tag{2.74}$$

$$\mathbf{K}_{22}^0 = \int_{\Omega} \nabla \mathbf{N}^T \mathbf{k} \eta_n^r \nabla \mathbf{N} \, d\Omega \tag{2.75}$$

$$\mathbf{K}_{23}^0 = \int_{\Omega} \nabla \mathbf{N}^T \mathbf{k} \eta_n^r \nabla \mathbf{N}^{eh} \, d\Omega \tag{2.76}$$

$$\mathbf{K}_{31}^{0} = \int_{\Omega^+} \left(\nabla \mathbf{N}^{eh}\right)^T \mathbf{k} \lambda_n^r \nabla \mathbf{N}\, d\Omega \tag{2.77}$$

$$\mathbf{K}_{32}^{0} = \int_{\Omega^+} \left(\nabla \mathbf{N}^{eh}\right)^T \mathbf{k} \eta_n^r \nabla \mathbf{N}\, d\Omega \tag{2.78}$$

$$\mathbf{K}_{33}^{0} = \int_{\Omega^+} \left(\nabla \mathbf{N}^{eh}\right)^T \mathbf{k} \eta_n^r \nabla \mathbf{N}^{eh}\, d\Omega \tag{2.79}$$

$$\mathbf{C}_{12}^{0} = -\int_{\Omega} \mathbf{N}^T \phi \mathbf{N}\, d\Omega \tag{2.80}$$

$$\mathbf{C}_{13}^{0} = -\int_{\Omega} \mathbf{N}^T \phi \mathbf{N}^{eh} d\Omega \tag{2.81}$$

$$\mathbf{C}_{22}^{0} = \int_{\Omega} \mathbf{N}^T \phi \mathbf{N}\, d\Omega \tag{2.82}$$

$$\mathbf{C}_{23}^{0} = \int_{\Omega} \mathbf{N}^T \phi \mathbf{N}^{eh} d\Omega \tag{2.83}$$

$$\mathbf{C}_{32}^{0} = \int_{\Omega^+} \left(\mathbf{N}^{eh}\right)^T \phi \mathbf{N} d\Omega \tag{2.84}$$

$$\mathbf{C}_{33}^{0} = \int_{\Omega^+} \left(\mathbf{N}^{eh}\right)^T \phi \mathbf{N}^{eh} d\Omega \tag{2.85}$$

$$\mathbf{f}_1 = \int_{\Omega} \nabla \mathbf{N}^T \mathbf{k} \lambda_w^r \rho_w \mathbf{g} d\Omega - \frac{1}{\rho_w} \int_{\Gamma_w^q} \mathbf{N}^T \hat{q}_w d\Gamma \tag{2.86}$$

$$\mathbf{f}_2 = \int_{\Omega} \nabla \mathbf{N}^T \mathbf{k} \lambda_n^r \rho_n \mathbf{g} d\Omega - \frac{1}{\rho_n} \int_{\Gamma_n^q} \mathbf{N}^T \hat{q}_n d\Gamma \tag{2.87}$$

$$\mathbf{f}_3 = \int_{\Omega^+} \left(\nabla \mathbf{N}^{eh}\right)^T \mathbf{k} \lambda_n^r \rho_n \mathbf{g} d\Omega - \frac{1}{\rho_n} \int_{\Gamma_n^{q+}} \left(\mathbf{N}^{eh}\right)^T \hat{q}_n d\Gamma + \frac{1}{\rho_n} \int_{\Gamma_d} \left(\mathbf{N}^{eh}\right)^T q_n^{\Gamma_d} d\Gamma \tag{2.88}$$

3

CO_2 Leakage via Abandoned Wellbores

This chapter is based on Arzanfudi and Al-Khoury (2015), a paper published in International Journal for Numerical Methods in Fluids.

This chapter introduces an effectively mesh-independent and computationally efficient model for CO_2 leakage through wellbores. A one dimensional compressible two-fluid domain, representing a homogeneous air gas and a multiphase CO_2 with a jump at the interface between them, is modeled.
The physical domain is modeled using the drift-flux model, and the governing equations are solved using a mixed finite element discretization scheme. The standard Galerkin finite element method, the partition of unity method and the level-set method are integrated to solve the problem. All important physical phenomena and processes occurring along the wellbore path, including fluid dynamics, buoyancy, phase change, compressibility, thermal interaction, wall friction and slip between phases, together with the jump in density and enthalpy between air and CO_2, are considered. Two numerical examples illustrating the computational capability and efficiency of the model are presented.

3.1 Introduction

CO_2 geo-sequestration is currently utilized as a means to mitigate CO_2 emission into the earth atmosphere in an attempt to reduce the likely greenhouse effect. Selection of an

appropriate geological formation for CO_2 sequestration requires a good estimate of the amount of leakage that might take place in time. Leakage of CO_2 to the ground surface or upper layers containing ground water is hazardous and considered as one of the major concerns of applying this technology. It is therefore vital to develop computational tools capable of modeling the leakage processes and phenomena. Two kinds of CO_2 leakage can be identified: leakage via heterogeneous layered domains, for which the theory of multiphase flow in porous medium domains is applicable; and leakage via faults and abandoned wells, for which the theory of fluid dynamics is applicable. The focus in this chapter is placed on leakage via abandoned wellbores.

The physical processes of CO_2 leakage via a wellbore and the involved flow mechanisms are rather complicated. They involve movement of multiple fluids comprising multiple phases which can be dispersed, mixed and have no distinct interfaces between them. Several coupled mechanisms including buoyancy, heat transfer, phase change, compressibility, wall friction and slip between phases are involved. Computational modeling of such a physical combination occurring in a wellbore, hundreds of meters long, is challenging.

Modeling fluid flow in wellbores has been a field of wide interest in oil and gas industry. A detailed review of the relevant physical processes and mathematical formulations can be found in Brill and Mukherjee (1999) and Hasan et al. (2002). A review on the earlier wellbore models and codes can be found in Freeston and Hadgu (1988) and Probst et al. (1992). An excellent overview of transport phenomena in multiphase systems is given by Faghri and Zhang (2006).

As the computational modeling of fluid flow is challenging and time and capacity demanding, different models deal with different aspects of the involved processes and geometry. Some treat CO_2 as a single phase and others treat it as a mixture; while many models simulate leakage in the wells only, and others are coupled with the reservoir. Some consider steady-state flow with no phase change, whereas several others consider transient flow with phase change. Stone et al. (1989) proposed a finite volume model for coupled wellbore-reservoir transient two-fluid (oil-water), three-phase flow in the wellbore with phase change of water only (water/steam). Hadgu et al. (1995) modeled transient two-fluid flow in a coupled wellbore-reservoir domain without phase change, using the coupled WFSA-TOUGH code. Livescu et al. (2010) introduced a finite volume model for coupled wellbore-reservoir transient three-fluid, three-phase flow with phase change for oil and gas applications. Hasan and Kabir (2010) presented a steady-state model for single-fluid (water) flow with phase change (water/steam). Recently, Pan and Oldenburg (2014) developed a transient finite volume model for coupled wellbore-reservoir for compressed air energy storage applications that include a two-fluid domain consisting of water and air but no phase change.

Regarding CO_2 flow in a wellbore, Cronshaw and Bolling (1982) developed a finite volume numerical model for transient two-fluid (CO_2-water), three-phase flow in the wellbore with phase change of CO_2 only. Lu and Connell (2008) and Lindeberg (2011) introduced models based on Runge–Kutta finite difference method to simulate steady-

state two-phase, single-fluid flow of CO_2 with phase change in the wellbore. Paterson et al. (2008) modeled a transient two-phase, single-fluid flow of CO_2 with phase change in the wellbore. Pan et al. (2009) presented a finite volume model for transient flow in wellbores of two-fluid (CO_2-brine) with phase change of CO_2 only. Remoroza et al. (2011) utilized TOUGH2 to study the coupled wellbore-reservoir steady-state two-fluid flow (CO_2 and water) with no phase change for geothermal heat flow applications.

In these models, while providing very useful basis for developing computational tools for fluid flow in wellbores, the focus is placed on modeling the physical processes, rather than the numerical solutions. Mostly, standard numerical discretization schemes are utilized. This normally requires the use of excessively fine meshes (grids) with adaptive meshing, or some other appropriate approaches. As a consequence, these models suffer from two main shortcomings: 1. computational inefficiency, and 2. mesh size dependency. This chapter intensively addresses a solution to these two issues.
The objective of this work is to develop an accurate, mesh-independent and computationally efficient transient model for CO_2 leakage through wellbores. A detailed modeling approach is given hereafter.

3.2 Modeling approach

Deriving an accurate, mesh-independent and computationally efficient transient model for CO_2 leakage from a geo-sequestration site via an abandoned wellbore requires a well-designed formulation of the mathematical model and the numerical model.

Regarding the mathematical model, it is apparent that the model should take into consideration all important physical phenomena and processes occurring along the wellbore. Fluid dynamics, buoyancy, phase change, compressibility, thermal interactions, wall friction, slip between phases, together with all relevant thermodynamic relationships must be considered. Initially, the wellbore is filled with air and the CO_2 in the reservoir is, most probably, in a supercritical state. Upon leakage, the CO_2 changes phase and starts displacing the air. This gives rise to having two fluids in the domain: air and CO_2. The air is a homogeneous gas, and the CO_2 is a multiphase fluid constituting supercritical liquid, liquid and gas, which are, in general, dispersed, mixed and having no distinct interfaces. The physical processes of such a domain are governed by the conservation laws of transport of mass, momentum and energy given by the Navier-Stokes equations. As the size of the engineering system that we are dealing with is huge and the CO_2 phases are dispersed and mixed, relying on an averaging approach is indispensable. Here, we model the air and the CO_2 as two separate fluids. The air is modeled as a homogenous gas, and the CO_2 is modeled as a homogeneous mixture. The jump condition at the interface between the air and the CO_2 is considered. We utilize the one-dimensional drift-flux model to simulate the transport of air and CO_2 in the wellbore. This model adopts the area-averaged approach, where detailed analysis of the local behavior of the involved phases is averaged over the cross-sectional area of the wellbore. Important aspects of fluid dynamics such as the inertia

force, buoyancy, wall friction, drift velocity, flow profile are considered in the drift-flux model.

To model two fluids, two sets of governing equations representing the two fluids are needed, together with a constraint condition at the interface between them. In literature, however, many models utilized for CO_2 flow in a wellbore, or similar applications, consider single phase with no phase change. The primary state variables usually utilized in such models are velocity, pressure and temperature. For a single phase, such primary variables are sufficient, as the variation of enthalpy is directly related to the variations of temperature and pressure. However, for a multiphase, the fluid temperature is not directly related to the enthalpy, and additional constitutive equations relating the variation of enthalpy to the variations of pressure, temperature, entropy and molar fraction are necessary (see Lu and Connell (2008)).

Here, we utilize a set of drift-flux model equations to represent the two fluids, but impose a jump at the interface between them. This necessitates adopting the mass density as a primary state variable instead of the temperature to clearly distinguish between the two fluids. The set of the primary state variables in this chapter is thus: velocity, pressure and density. In such a set, there is a fundamental thermodynamic relationship relating the fluid mass density to the gas/liquid volume fraction, that allows for a distinct separation between the liquid and gas phases, and avoids the additional constitutive relationships mentioned above. However, this should be supplemented with a proper numerical scheme capable of modeling the jump between the two fluids.

Regarding the numerical model, it is obvious that the model should take into consideration the local and global conservative nature of the system and its nonlinear hyperbolic characteristics. Using standard numerical discretization methods such as the finite difference, the finite volume or the finite element necessitate excessively fine grids and small time steps. Therefore, in order to obtain a computationally efficient model, adopting an advanced discretization procedure is indispensable. Here, we adopt a mixed discretization scheme. In this scheme, state variables exhibiting different physical nature are treated using different numerical discretization techniques. Techniques such as the standard Galerkin finite element method (SG), the partition of unity finite element method (PUM), and the level-set method (LS) are integrated in a single numerical scheme. SG is utilized to discretize the diffusive dominant field equations, and PUM, within the framework of the extended finite element method (XFEM), together with LS are utilized to discretize the advective dominant field equations. The level-set method is employed to trace and locate the CO_2 front, and the extended finite element method is employed to model the associated jump in the mass density field. The use of LS and XFEM for the advective field leads to a globally and locally conservative discretization, giving a stable and effectively mesh-independent scheme. The proposed mixed discretization scheme differs from the well-known mixed FEM such that in the mixed FEM, different state variables are utilized but adopt a single discretization technique; whereas in the mixed discretization scheme, we utilize

different state variables and adopt different discretization techniques, depending on the physical nature of the state variable and the associated balance equations.

Compressible fluid dynamic equations inevitably involve acoustic waves. Numerically, this requires fine grids and small time steps. However, for CO_2 leakage in a wellbore, the time scale of interest is dominated by the time scale of the fluid advection, and hence, the acoustic waves pose no significance on the analysis. Therefore it is desirable to remove the acoustic wave from the system of equations. This is done by decoupling the pressure term of the balance momentum equation from the mass and energy equations.

3.3 Governing equations

The governing equations of the drift-flux model are described in many literature, including Shi et al. (2005), Ishii and Hibiki (2006) and Pan and Oldenburg (2014). Here, a listing of the governing equations of this model and its associated thermodynamic and engineering constitutive relationships is given. We utilize a set of governing equations to describe both, the air and the CO_2, but impose a jump at the interface between them. The fluids are allowed to exist at any state or mixture composition, depending on their thermodynamic conditions along the wellbore. However, no mass exchange at the interface is allowed. This assumption is justified because CO_2 leakage via a wellbore is advection-dominant and the rate of dissolution and diffusion between the two fluids is negligible. This inevitably entails that the fluids velocities and pressures at the interface are continuous, but discontinuous in the their mass density and enthalpy, giving:

$$\begin{aligned} v_{\mathrm{co}_2} &= v_{\mathrm{air}} \\ p_{\mathrm{co}_2} &= p_{\mathrm{air}} \qquad \text{at}\,\Gamma_d \\ [\![\rho_m]\!] &= \rho_{\mathrm{co}_2} - \rho_{\mathrm{air}} \\ [\![h_m]\!] &= h_{\mathrm{co}_2} - h_{\mathrm{air}} \end{aligned} \tag{3.1}$$

3.3.1 Drift-flux balance equations with discontinuity

Based on the drift-flux model, the balance equations of fluid mixture flow in one dimension with a jump condition at the interface between two separate fluids (air and CO_2) can be described as

Mass balance

$$\frac{\partial \rho_m}{\partial t} + \frac{\partial}{\partial z}(\rho_m v_m) + [\![\rho_m]\!] v_m \cdot n\,\delta(z - z_d) = 0 \tag{3.2}$$

Momentum balance

$$\frac{\partial}{\partial t}(\rho_m v_m)+\frac{\partial}{\partial z}\left(\rho_m v_m^2+\gamma\right)+[\![\rho_m]\!]v_m^2\cdot n\,\delta(z-z_d) = -\frac{\partial p}{\partial z}-\frac{f\rho_m|v_m|v_m}{4r_i}-\rho_m g\sin\theta \tag{3.3}$$

Energy balance

$$\frac{\partial}{\partial t}\left[\rho_m\left(h_m+\frac{1}{2}v_m^2\right)-p\right]+\frac{\partial}{\partial z}\left[\rho_m v_m\left(h_m+\frac{v_m^2}{2}\right)\right] +[\![\rho_m]\!]v_m\left([\![h_m]\!]+\frac{v_m^2}{2}\right)\cdot n\,\delta(z-z_d)=\rho_m v_m g\sin\theta-\frac{Q}{\pi r_i^2} \tag{3.4}$$

where δ is the Dirac delta function (unit= m^{-1}), z_d is the coordinate of interface between CO_2 and air, shown in Fig. 3.1, n is the unit normal vector, r_i is the inner radius of the wellbore, ρ_m is the mixture density, v_m is the mixture velocity, p is the pressure, f is the wall friction coefficient, g is the gravitational constant, θ is the inclination angle of the well, h_m is the specific enthalpy of the mixture, Q is the heat exchange between the well and its surrounding formation, and γ describes the slip between two phases. The definitions of the drift flux model parameters are listed in Appendix A.

Fig. 3.1 Definitions of domains, interface, coordinate and unit normal vector to the boundary

3.3.2 Constitutive equations

A comprehensive treatment of the CO_2 constitutive equations is given in Arzanfudi and Al-Khoury (2014). The relevant constitutive equations for the CO_2, together with those for air, are given in Appendix B.

3.3.3 Initial and boundary conditions

Initially, the primary state variables might be described as

$$G(z,0)=G_0(z) \quad \text{at } t=0 \tag{3.5}$$

where G can be v_m, p, or ρ_m.

The Dirichlet boundary conditions might be described as

$$G(t) = \hat{G}(t) \quad \text{on } \Gamma_u \tag{3.6}$$

in which Γ_u is the Dirichlet boundary.

The Neumann boundary conditions are defined as

$$\begin{aligned} \hat{q}_\rho &= (\hat{\rho}_m \hat{v}_m) \cdot n \\ \hat{q}_v &= \left(\hat{\rho}_m \hat{v}_m^2 + \hat{\gamma}\right) \cdot n \qquad \text{on } \Gamma_q \\ \hat{q}_e &= \left[\hat{\rho}_m \hat{v}_m \left(\hat{h}_m + \frac{\hat{v}_m^2}{2}\right)\right] \cdot n \end{aligned} \tag{3.7}$$

where Γ_q is the Neumann boundary, and the subscripts ρ, v and e refer to mass, momentum and energy, respectively.

At an outflow boundary, the Neumann boundary conditions are defined as

$$\begin{aligned} q_\rho &= (\rho_m v_m) \cdot n \\ q_v &= \left(\rho_m v_m^2 + \gamma\right) \cdot n \qquad \text{on } \Gamma_o \\ q_e &= \left[\rho_m v_m \left(h_m + \frac{v_m^2}{2}\right)\right] \cdot n \end{aligned} \tag{3.8}$$

where Γ_o is the outflow boundary. Note that the primary state variables at this boundary are not known and have to be calculated. Otherwise, this boundary becomes by definition close, or has to be assigned a typical Dirichlet or Neumann boundary conditions. As it will be shown later, the discretization of this kind of boundary conditions will add up terms to the finite element matrices, including the left-hand side.

3.4 Modeling the discontinuity between air and CO_2

At the front of the CO_2 plume, a discontinuity in the density field, together with other thermodynamic properties differentiating air from CO_2, exists. This discontinuity is traced using the level-set method.

3.4.1 Tracing the front: level-set method

The level-set method is a numerical technique usually utilized to trace a moving interface, Γ_d, between two zones, for instance, Ω^+ and Ω^-. A level-set function is defined as a signed distance function, $\phi(z)$, which is positive in Ω^+, negative in Ω^-, and zero at the interface between them. For a one-dimensional domain, it can be described as

$$\phi(z)=\begin{cases}|z-z_d| & z\in\Omega^+\\ -|z-z_d| & z\in\Omega^-\end{cases}\qquad \phi(z)\in\Re,\ z\in\Omega \tag{3.9}$$

where z_d is the coordinate of the interface. The sign indicates different domains, and the magnitude represents the distance to the interface. The level-set function is advected by a field motion equation of the form

$$\frac{\partial\phi}{\partial t}+v\frac{d\phi}{dz}=0 \tag{3.10}$$

where v represents the interface (front) velocity, taken here as the average of the two fluids velocities at the vicinity of the interface.

3.4.2 Thermodynamic properties

The thermodynamic properties of the two fluids exhibit a jump at the interface between them. For instance, the temperature can be calculated as a function of pressure and mixture density as

$$T(z,p,\rho_m)=\begin{cases}T_{\mathrm{co}_2}(p,\rho_m) & z\in\Omega^+\\ T_{\mathrm{air}}(p,\rho_m) & z\in\Omega^-\end{cases} \tag{3.11}$$

where T_{co_2} is the CO_2 temperature in Ω^+ zone, and T_{air} is the air temperature in Ω^- zone. In terms of the level-set function, Eq. (3.11) can be described as

$$T(\phi,p,\rho_m)=\begin{cases}T_{\mathrm{co}_2}(p,\rho_m) & \phi>0\\ T_{\mathrm{air}}(p,\rho_m) & \phi\le 0\end{cases} \tag{3.12}$$

This can be equivalently written as

$$T(\phi,p,\rho_m)=H(\phi)T_{\mathrm{co}_2}(p,\rho_m)+(1-H(\phi))T_{\mathrm{air}}(p,\rho_m) \tag{3.13}$$

where $H(\phi)$ is the Heaviside function, that reads

$$H(\phi)=\begin{cases}1 & \phi>0\\ 0 & \phi\le 0\end{cases} \tag{3.14}$$

Similar equations can be derived for the enthalpy, h_m, gas volume fraction, f_G, gas density, ρ_G, and liquid density, ρ_L.

3.5 Acoustic filtration

The fully compressible fluid flow equations given above are not exactly suited to the type of fluid flow in wellbores because of the inevitable generation of acoustic waves. The mean velocity flow of the CO_2 plume is much slower than that of the acoustic wave. Therefore, it is useful to filter out the unwanted acoustic modes. These modes can be filtered out by decoupling the pressure in the momentum equation from that arising from the density-temperature-pressure equations of state.

An early work in this field was introduced by Rehm and Baum (1978), for inviscid flow; and Paolucci (1982), for viscous flow. An in-depth analysis of this problem is given by Principe and Codina (2009) and Reddy and Gartling (2010).

The general approach is that the fluid pressure is decomposed into two terms: a spatially uniform, time-dependent background (thermodynamic) pressure $p_0(t)$; and a dynamical (mechanical) pressure, $p'(z,t)$; such that

$$p(z,t) = p_0(t) + p'(z,t) \tag{3.15}$$

The background pressure, $p_0(t)$, is utilized in the thermodynamic properties formulations, e.g. Eq. (3.13), such that

$$T(\phi, p_0, \rho_m) = H(\phi)T^c(p_0, \rho_m) + (1 - H(\phi))T^a(p_0, \rho_m) \tag{3.16}$$

Other properties follow suite.

The dynamical pressure $p'(z,t)$ is utilized instead of the total pressure, p, which appears on the right-hand side of the momentum balance equations, Eq. (3.3).

The common practice of assuming $p_0(t)$ as spatially uniform can be in many cases realistic, especially those dealing with relatively small geometry constituting fluids with an insignificant pressure variation. However, for a CO_2 leakage case, which involves long wellbores with a huge pressure variation along its length, this assumption is not realistic. To circumvent this, we assume this pressure to have a linear variation between the pressure at the bottom boundary and that at the top boundary of the wellbore. This is done at every time step, giving

$$p(z,t) = p_0(z,t) + p'(z,t) \tag{3.17}$$

Following this, and since the background pressure is a function of space as well, the original momentum balance equation, Eq. (3.3), can be utilized. The use of acoustic filtration allows for using larger time step sizes while preserving the accuracy of the results (Reddy and Gartling 2010), which will obviously result in a more efficient computational model.

3.6 Mixed discretization finite element scheme (PUM-SG)

The governing drift-flux equations, together with the initial and boundary conditions, form an initial and boundary value problem that is dynamic, advective, nonlinear and involves a jump condition. Solving such a problem using standard finite element procedures entails utilization of excessively fine and adaptive meshes and small time steps, but nevertheless, the model can be unstable and the results are very likely mesh-dependent. Above all, standard finite element discretization procedure is not locally convergent, a feature necessary to model the jump condition at the interface between the two fluids. To tackle this, we solve the problem using a mixed finite element discretization scheme. This scheme entails solving different balance equations using different discretization schemes, which are tailored to accurately describe the nature of

the involved primary state variables v_m, p, and ρ_m. The discontinuity at the interface is modeled using the level-set method to trace the interface; and the partition of unity to discretize the mass density.

3.6.1 Level-set discretization

Applying the weighted residual finite element discretization procedure to Eq. (3.10) gives

$$\int_\Omega w\frac{\partial\phi}{\partial t}d\Omega+\int_\Omega wv\frac{d\phi}{dz}d\Omega=0 \tag{3.18}$$

Approximating ϕ as $\phi=\mathbf{N}(z)\mathbf{\Phi}(t)$, with $\mathbf{N}(z)$ a vector of shape functions and $\mathbf{\Phi}(t)$ a vector of nodal values of the level-set function at time t, and assuming $w=\mathbf{N}$ yields

$$\int_\Omega \mathbf{N}^T\mathbf{N}\frac{\partial\mathbf{\Phi}}{\partial t}d\Omega+\int_\Omega \mathbf{N}^T v\frac{d\mathbf{N}}{dz}\mathbf{\Phi}\,d\Omega=0 \tag{3.19}$$

Utilizing the level-set method to trace a moving front requires re-distancing (re-initialization) at every time step. This is necessary because otherwise the distance property of the level-set function is no longer maintained after advection. We utilize the direct distancing approach proposed by Cho et al. (2010) for this purpose. In this approach, the re-distancing is performed by geometrical updating of the advective front instead of solving a re-initialization equation.

3.6.2 PUM-SG formulation

The standard Galerkin finite element method (SG) and the partition of unity method (PUM), within the framework of the extended finite element method, are integrated to discretize the problem. The first is, in general, accurate and computationally efficient for solving continuous problems, and the second is accurate and effective in solving discontinuous problems.

As stated above, the mixture velocity and pressure are continuous at the interface between CO_2 and air, and thus SG suffices, entailing

$$v_m(z,t)=\sum_{i\in I}N_i(z)v_{mi}(t)=\mathbf{N}(z)\mathbf{v}_m(t) \tag{3.20}$$

$$p=\sum_{i\in I}N_i(z)p_i(t)=\mathbf{N}(z)\mathbf{p}(t) \tag{3.21}$$

in which I is the set of all nodes in the domain, $N_i(z)$ is the shape function of node i, $v_{mi}(t)$ and $p_i(t)$ are the nodal values of the mixture velocity and pressure for node i, respectively, and $\mathbf{N}(z)$, $\mathbf{v}_m(t)$, and $\mathbf{p}(t)$ are the associated nodal vectors.

On the other hand, the mixture mass density is discontinuous at the interface between CO_2 and air, and for this PUM suffices, entailing

$$\begin{aligned}\rho_m(z,t) &= \sum_{i\in I} N_i(z)\rho_{mi}(t) + \sum_{i\in I^*} N_i^{eh}(z)\tilde{\rho}_{mi}(t) \\ &= \mathbf{N}(z)\boldsymbol{\rho}_m(t) + \mathbf{N}^{eh}(z)\tilde{\boldsymbol{\rho}}_m(t)\end{aligned} \tag{3.22}$$

where I^* is the subset of enriched nodes, $\rho_{mi}(t)$ and $\tilde{\rho}_{mi}(t)$ are the conventional and additional (extended) nodal values of the mixture density at node i, and $N_i^{eh}(z)$ is an enriched shape function at node i, and $\boldsymbol{\rho}_m(t)$, $\tilde{\boldsymbol{\rho}}_m(t)$ and $\mathbf{N}^{eh}(z)$ are the associated nodal vectors. $N_i^{eh}(z)$ is defined as

$$N_i^{eh}(z) = N_i(z)\psi_i(\phi) \tag{3.23}$$

in which $\psi_i(\phi)$ is the shifted enrichment function (Zi and Belytschko 2003) at node i, defined as

$$\psi_i(\phi) = H(\phi) - H(\phi_i) \tag{3.24}$$

where ϕ_i is the value of level-set function at node i. Using the shifted PUM leads to the existence of a non-zero enriched shape function over both sides of the discontinuity. Consequently, the density of each fluid across the discontinuity is calculated as

$$\begin{aligned}\rho_{\mathrm{co_2}}(z_d,t) &= \mathbf{N}(z_d)\boldsymbol{\rho}_m(t) + \mathbf{N}^{eh+}(z_d)\tilde{\boldsymbol{\rho}}_m(t) \\ \rho_{\mathrm{air}}(z_d,t) &= \mathbf{N}(z_d)\boldsymbol{\rho}_m(t) + \mathbf{N}^{eh-}(z_d)\tilde{\boldsymbol{\rho}}_m(t)\end{aligned} \tag{3.25}$$

in which $\mathbf{N}^{eh+}$ and $\mathbf{N}^{eh-}$ are the enriched shape functions at the neighborhood of the discontinuity on Ω^+ and Ω^-, respectively. Note that we utilized the shifted enrichment approximation because the conventional un-shifted PUM does not, in general, have the Kronecker-δ property of the standard FEM, rendering the imposition of essential boundary conditions difficult. A comprehensive treatment of this issue is given by Fries and Belytschko (2010).

Using the weighted residual method, the finite element formulation of the governing equations; Eqs. (3.2), (3.3) and (3.4); can be described as

Mass balance

$$\int_\Omega w\frac{\partial \rho_m}{\partial t}d\Omega + \int_\Omega w\frac{\partial}{\partial z}(\rho_m v_m)d\Omega + \int_{\Gamma_d} w[\![\rho_m]\!]v_m \cdot n\, d\Gamma = 0 \tag{3.26}$$

Momentum balance

$$\begin{aligned}&\int_\Omega w'\frac{\partial}{\partial t}(\rho_m v_m)d\Omega+\int_\Omega w'\frac{\partial}{\partial z}\left(\rho_m v_m^2+\gamma\right)d\Omega+\int_{\Gamma_d} w'[\![\rho_m]\!]v_m^2\cdot n\,d\Gamma\\&=-\int_\Omega w'\frac{\partial p}{\partial z}d\Omega-\int_\Omega w'\frac{f\rho_m|v_m|v_m}{4r_i}d\Omega-\int_\Omega w'\rho_m g\sin\theta d\Omega\end{aligned}\tag{3.27}$$

Energy balance

$$\begin{aligned}&\int_\Omega w''\frac{\partial}{\partial t}\left[\rho_m\left(h_m+\frac{1}{2}v_m^2\right)-p\right]d\Omega+\int_\Omega w''\frac{\partial}{\partial z}\left[\rho_m v_m\left(h_m+\frac{v_m^2}{2}\right)\right]d\Omega\\&+\int_{\Gamma_d} w''[\![\rho_m]\!]v_m\left([\![h_m]\!]+\frac{v_m^2}{2}\right)\cdot n\,d\Gamma=\int_\Omega w''\rho_m v_m g\sin\theta d\Omega-\int_\Omega w''\frac{Q}{\pi r_i^2}d\Omega\end{aligned}\tag{3.28}$$

in which w, w' and w'' are the weighting functions of the mass, momentum and energy balance equations respectively.

As the discontinuity occurs in one primary state variable, only one balance equation is needed to be partitioned. For this, we chose the energy balance equation since its jump term contains the specific enthalpy term, which is a function of density, and accordingly exhibiting a discontinuity at the interface between air and CO_2. Thus, for the mass and momentum balance equations, a continuous weighting function is utilized; whereas for the energy balance equation, a discontinuous weighting function is utilized, i.e.

$$w=w'=\mathbf{N}\tag{3.29}$$

$$w''=\mathbf{N}+\mathbf{N}^{eh}\tag{3.30}$$

where the dependency on the spatial coordinates are ignored for simplicity of notation.

Substituting Eq. (3.29) into Eqs. (3.26) and (3.27), and applying Green's theorem, yields

Mass balance

$$\begin{aligned}&\int_\Omega \mathbf{N}^T\mathbf{N}\dot{\boldsymbol{\rho}}_m d\Omega+\int_\Omega \mathbf{N}^T\mathbf{N}^{eh}\dot{\tilde{\boldsymbol{\rho}}}_m d\Omega-\int_\Omega \mathbf{B}^T v_m\mathbf{N}\boldsymbol{\rho}_m d\Omega-\int_\Omega \mathbf{B}^T v_m\mathbf{N}^{eh}\tilde{\boldsymbol{\rho}}_m d\Omega\\&+\int_{\Gamma_q}\mathbf{N}^T\hat{q}_\rho d\Gamma+\int_{\Gamma_o}\mathbf{N}^T\left(\rho_m v_m\right)\cdot n\,d\Gamma+\int_{\Gamma_d}\mathbf{N}^T[\![\rho_m]\!]v_m\cdot n\,d\Gamma=0\end{aligned}\tag{3.31}$$

in which $\mathbf{B}=\partial\mathbf{N}/\partial z$.

Momentum balance

$$\begin{aligned}&\int_\Omega \mathbf{N}^T\left(v_m\mathbf{N}\dot{\boldsymbol{\rho}}_m+v_m\mathbf{N}^{eh}\dot{\tilde{\boldsymbol{\rho}}}_m+\rho_m\mathbf{N}\dot{\mathbf{v}}_m\right)d\Omega-\int_\Omega \mathbf{B}^T\left(\rho_m v_m\mathbf{N}\mathbf{v}_m+\gamma\right)d\Omega\\&+\int_{\Gamma_q}\mathbf{N}^T\hat{q}_v d\Gamma+\int_{\Gamma_o}\mathbf{N}^T\left(\rho_m v_m^2+\gamma\right)\cdot n\,d\Gamma+\int_{\Gamma_d}\mathbf{N}^T[\![\rho_m]\!]v_m^2\cdot n\,d\Gamma\\&=-\int_\Omega\mathbf{N}^T\mathbf{B}\,\mathbf{p}d\Omega-\int_\Omega\mathbf{N}^T\frac{f\rho_m|v_m|}{4r_i}\mathbf{N}\mathbf{v}_m d\Omega-\int_\Omega\mathbf{N}^T\rho_m g\sin\theta\,d\Omega\end{aligned}\tag{3.32}$$

Substituting Eq. (3.30) into Eq. (3.28) and applying Green's theorem yields two equations: one representing a continuously weighted field and a discontinuously weighted field, as

Energy balance

continuously weighted:

$$\begin{aligned}&\int_\Omega\mathbf{N}^T\left[\left(h_m+\frac{1}{2}v_m^2\right)\mathbf{N}\dot{\boldsymbol{\rho}}_m+\left(h_m+\frac{1}{2}v_m^2\right)\mathbf{N}^{eh}\dot{\tilde{\boldsymbol{\rho}}}_m\right]d\Omega\\&+\int_\Omega\mathbf{N}^T\left[\dot{h}_m\mathbf{N}\boldsymbol{\rho}_m+\dot{h}_m\mathbf{N}^{eh}\tilde{\boldsymbol{\rho}}_m+\rho_m v_m\mathbf{N}\dot{\mathbf{v}}_m-\mathbf{N}\dot{\mathbf{p}}\right]d\Omega\\&-\int_\Omega\mathbf{B}^T\left[\rho_m\left(h_m+\frac{v_m^2}{2}\right)\mathbf{N}\mathbf{v}_m\right]d\Omega+\int_{\Gamma_q}\mathbf{N}^T\hat{q}_e d\Gamma+\int_{\Gamma_o}\mathbf{N}^T\left[\rho_m v_m\left(h_m+\frac{v_m^2}{2}\right)\right]\cdot n\,d\Gamma\\&+\int_{\Gamma_d}\mathbf{N}^T\left[[\![\rho_m]\!]v_m\left([\![h_m]\!]+\frac{{v_m}^2}{2}\right)\right]\cdot n\,d\Gamma=\int_\Omega\mathbf{N}^T\rho_m v_m g\sin\theta\,d\Omega-\int_\Omega\mathbf{N}^T\frac{Q}{\pi {r_i}^2}d\Omega\end{aligned}\tag{3.33}$$

discontinuously weighted:

$$\begin{aligned}&\int_\Omega\left(\mathbf{N}^{eh}\right)^T\left[\left(h_m+\frac{1}{2}v_m^2\right)\mathbf{N}\dot{\boldsymbol{\rho}}_m+\left(h_m+\frac{1}{2}v_m^2\right)\mathbf{N}^{eh}\dot{\tilde{\boldsymbol{\rho}}}_m\right]d\Omega\\&+\int_\Omega\left(\mathbf{N}^{eh}\right)^T\left[\dot{h}_m\mathbf{N}\boldsymbol{\rho}_m+\dot{h}_m\mathbf{N}^{eh}\tilde{\boldsymbol{\rho}}_m+\rho_m v_m\mathbf{N}\dot{\mathbf{v}}_m-\mathbf{N}\dot{\mathbf{p}}\right]d\Omega\\&-\int_\Omega\left(\mathbf{B}^{eh}\right)^T\left[\rho_m\left(h_m+\frac{v_m^2}{2}\right)\mathbf{N}\mathbf{v}_m\right]d\Omega+\int_{\Gamma_q}\left(\mathbf{N}^{eh}\right)^T\hat{q}_e d\Gamma\\&+\int_{\Gamma_d}\left(\mathbf{N}^{eh}\right)^T\left[[\![\rho_m]\!]v_m\left([\![h_m]\!]+\frac{{v_m}^2}{2}\right)\right]\cdot n\,d\Gamma\\&=\int_\Omega\left(\mathbf{N}^{eh}\right)^T\rho_m v_m g\sin\theta d\Omega-\int_\Omega\left(\mathbf{N}^{eh}\right)^T\frac{Q}{\pi {r_i}^2}d\Omega\end{aligned}\tag{3.34}$$

where $\mathbf{B}^{eh} = \partial \mathbf{N}^{eh} / \partial z$. Note that, unlike conventional PUM formulation, the integral of Eq. (3.34) is evaluated over $\Omega^+ \cup \Omega^- \equiv \Omega$ because the shifted enrichment function is non-zero over both sides of the discontinuity.
It is worth mentioning that the Neumann boundary conditions appearing in the finite element equations are a natural outcome of the Green's theorem. In other numerical schemes, such as the finite difference and finite volume, they have to be imposed a priori.

3.6.3 Linearization

The resulting weak formulations, Eqs. (3.31)-(3.34), represent a set of semi-discrete nonlinear equations, where the nonlinearity arises due to the constitutive relationships between the pressure and mixture density and other thermodynamic variables. Since the nonlinearity is due to scalar coefficients (i.e. v_m, ρ_m, h_m, etc.), and as the constitutive relationships are continuous (within a domain), it is convenient to linearize these equations using Taylor series expansions up to the first order (standard Newton-Raphson scheme).
The Taylor series expansion of the temperature T at the current iteration $r+1$, gives

$$T^{r+1} = T\left(p_0^r, \rho_m^r\right) + \frac{\partial T\left(p_0^r, \rho_m^r\right)}{\partial p_0}\delta p_0 + \frac{\partial T\left(p_0^r, \rho_m^r\right)}{\partial \rho_m}\delta \rho_m \tag{3.35}$$

or in a more concise form

$$T^{r+1} = T^r + \frac{\partial T^r}{\partial p_0}\delta p_0 + \frac{\partial T^r}{\partial \rho_m}\delta \rho_m \tag{3.36}$$

with

$$\begin{aligned} \delta p_0 &= p_0^{r+1} - p_0^r \\ \delta \rho_m &= \rho_m^{r+1} - \rho_m^r \end{aligned} \tag{3.37}$$

where the superscript r denotes the iteration number and the prefix δ denotes the increment of the state vector.

Since the background pressure is treated explicitly, as described in Section 3.5, its increment over a time step is set to zero, i.e. $\delta p_0 = 0$, and henceforth

$$T^{r+1} = T^r + \frac{\partial T^r}{\partial \rho_m}\delta \rho_m \tag{3.38}$$

Following this, the primary state variables and their time derivatives can be written as

$$\begin{aligned} &\rho_m^{r+1} = \rho_m^r + \delta\rho_m \quad v_m^{r+1} = v_m^r + \delta v_m \quad p^{r+1} = p^r + \delta p \\ &\dot{\rho}_m^{r+1} = \dot{\rho}_m^r + \delta\dot{\rho}_m \quad \dot{v}_m^{r+1} = \dot{v}_m^r + \delta\dot{v}_m \quad \dot{p}^{r+1} = \dot{p}^r + \delta\dot{p} \end{aligned} \tag{3.39}$$

The other variables and their time derivatives can be written as follows:

Specific enthalpy

$$h_m^{r+1} = h_m\left(p_0^r, \rho_m^r\right) + \frac{\partial h_m\left(p_0^r, \rho_m^r\right)}{\partial p_0}\delta p_0 + \frac{\partial h_m\left(p_0^r, \rho_m^r\right)}{\partial \rho_m}\delta\rho_m \tag{3.40}$$

$$\dot{h}_m = \frac{\partial h_m\left(p_0, \rho_m\right)}{\partial p_0}\dot{p}_0 + \frac{\partial h_m\left(p_0, \rho_m\right)}{\partial \rho_m}\dot{\rho}_m \tag{3.41}$$

which after linearization, neglecting the dependency terms, reads

$$\begin{aligned}\dot{h}_m^{r+1} = &\left(\frac{\partial h_m^r}{\partial p_0} + \frac{\partial^2 h_m^r}{\partial p_0^2}\delta p_0 + \frac{\partial^2 h_m^r}{\partial p_0 \partial \rho_m}\delta\rho_m\right)\left(\dot{p}_0^r + \delta\dot{p}_0\right) \\ &+ \left(\frac{\partial h_m^r}{\partial \rho_m} + \frac{\partial^2 h_m^r}{\partial p_0 \partial \rho_m}\delta p_0 + \frac{\partial^2 h_m^r}{\partial \rho_m^2}\delta\rho_m\right)\left(\dot{\rho}_m^r + \delta\dot{\rho}_m\right)\end{aligned} \tag{3.42}$$

As for temperature, the increment due to the background pressure is eliminated, yielding

$$\begin{aligned}h_m^{r+1} &= h_m^r + \frac{\partial h_m^r}{\partial \rho_m}\delta\rho_m^r \\ \dot{h}_m^{r+1} &= \left(\frac{\partial h_m^r}{\partial \rho_m} + \frac{\partial^2 h_m^r}{\partial \rho_m^2}\delta\rho_m\right)\left(\dot{\rho}_m^r + \delta\dot{\rho}_m\right)\end{aligned} \tag{3.43}$$

Slip term

$$\begin{aligned}\gamma^{r+1} = \gamma\left(v_m^r, p_0^r, \rho_m^r\right) &+ \frac{\partial\gamma\left(v_m^r, p_0^r, \rho_m^r\right)}{\partial v_m}\delta v_m \\ &+ \frac{\partial\gamma\left(v_m^r, p_0^r, \rho_m^r\right)}{\partial p_0}\delta p_0 + \frac{\partial\gamma\left(v_m^r, p_0^r, \rho_m^r\right)}{\partial \rho_m}\delta\rho_m\end{aligned} \tag{3.44}$$

Similarly, eliminating the background pressure, gives

$$\gamma^{r+1} = \gamma^r + \frac{\partial\gamma^r}{\partial v_m}\delta v_m + \frac{\partial\gamma^r}{\partial \rho_m}\delta\rho_m \tag{3.45}$$

Heat transfer

$$Q^{r+1} = Q\left(T\left(p_0^r, \rho_m^r\right)\right) + \frac{dQ}{dT}\delta T \tag{3.46}$$

$$Q^{r+1} = Q\left(T\left(p_0^r, \rho_m^r\right)\right) + \frac{dQ\left(T\left(p_0^r, \rho_m^r\right)\right)}{dT}\left(\frac{\partial T\left(p_0^r, \rho_m^r\right)}{\partial p_0}\delta p_0 + \frac{\partial T\left(p_0^r, \rho_m^r\right)}{\partial \rho_m}\delta\rho_m\right) \tag{3.47}$$

Eliminating the background pressure, gives

$$Q^{r+1} = Q^r + \frac{dQ^r}{dT}\frac{\partial T^r}{\partial \rho_m}\delta\rho_m \tag{3.48}$$

Reynolds number

$$\delta \mathrm{Re} = \frac{\partial \mathrm{Re}^r}{\partial v_m}\delta v_m + \frac{\partial \mathrm{Re}^r}{\partial p_0}\delta p_0 + \frac{\partial \mathrm{Re}^r}{\partial \rho_m}\delta\rho_m \tag{3.49}$$

Using Eq. (3.66), gives

$$\begin{aligned}\delta \mathrm{Re} = {} & \frac{\rho_m^r \mathrm{sign}\left(v_m^r\right)(2r_i)}{\mu_m^r}\delta v_m - \frac{\rho_m^r\left|v_m^r\right|(2r_i)}{\left(\mu_m^r\right)^2}\frac{\partial \mu_m^r}{\partial p_0}\delta p_0 \\ & + \left(\frac{\left|v_m^r\right|(2r_i)}{\mu_m^r} - \frac{\rho_m^r\left|v_m^r\right|(2r_i)}{\left(\mu_m^r\right)^2}\frac{\partial \mu_m^r}{\partial \rho_m}\right)\delta\rho_m\end{aligned} \tag{3.50}$$

Eliminating the background pressure, gives

$$\delta \mathrm{Re} = \frac{\rho_m^r \mathrm{sign}\left(v_m^r\right)(2r_i)}{\mu_m^r}\delta v_m + \left(\frac{\left|v_m^r\right|(2r_i)}{\mu_m^r} - \frac{\rho_m^r\left|v_m^r\right|(2r_i)}{\left(\mu_m^r\right)^2}\frac{\partial \mu_m^r}{\partial \rho_m}\right)\delta\rho_m \tag{3.51}$$

Wall friction

$$f^{r+1} = f^r + \frac{\partial f^r}{\partial \mathrm{Re}}\delta \mathrm{Re} \tag{3.52}$$

Using Eq. (3.51), gives

$$\begin{aligned}f^{r+1} = {} & f^r + \frac{\rho_m^r \mathrm{sign}\left(v_m^r\right)(2r_i)}{\mu_m^r}\frac{\partial f^r}{\partial \mathrm{Re}}\delta v_m - \frac{\rho_m^r\left|v_m^r\right|(2r_i)}{\left(\mu_m^r\right)^2}\frac{\partial f^r}{\partial \mathrm{Re}}\frac{\partial \mu_m^r}{\partial p_0}\delta p_0 \\ & + \left(\frac{\left|v_m^r\right|(2r_i)}{\mu_m^r} - \frac{\rho_m^r\left|v_m^r\right|(2r_i)}{\left(\mu_m^r\right)^2}\frac{\partial \mu_m^r}{\partial \rho_m}\right)\frac{\partial f^r}{\partial \mathrm{Re}}\delta\rho_m\end{aligned} \tag{3.53}$$

Eliminating the background pressure, gives

$$f^{r+1} = f^r + \frac{\rho_m^r \text{sign}\left(v_m^r\right)(2r_i)}{\mu_m^r}\frac{\partial f^r}{\partial \text{Re}}\delta v_m + \left(\frac{\left|v_m^r\right|(2r_i)}{\mu_m^r} - \frac{\rho_m^r\left|v_m^r\right|(2r_i)}{\left(\mu_m^r\right)^2}\frac{\partial \mu_m^r}{\partial \rho_m}\right)\frac{\partial f^r}{\partial \text{Re}}\delta\rho_m \tag{3.54}$$

3.6.4 Finite element equations

Inserting Eqs. (3.38)-(3.54) into Eqs. (3.31)-(3.34) and using Eq. (3.1), after rearrangements, gives:

Mass field equations

$$\begin{aligned}
&\int_\Omega \mathbf{N}^T\mathbf{N}\dot{\boldsymbol{\rho}}_m^r d\Omega + \int_\Omega \mathbf{N}^T\mathbf{N}\delta\dot{\boldsymbol{\rho}}_m d\Omega + \int_\Omega \mathbf{N}^T\mathbf{N}^{eh}\dot{\tilde{\boldsymbol{\rho}}}_m^r d\Omega + \int_\Omega \mathbf{N}^T\mathbf{N}^{eh}\delta\dot{\tilde{\boldsymbol{\rho}}}_m d\Omega \\
&- \int_\Omega \mathbf{B}^T\rho_m^r\mathbf{N}\mathbf{v}_m^r d\Omega - \int_\Omega \mathbf{B}^T v_m^r\mathbf{N}\delta\boldsymbol{\rho}_m d\Omega - \int_\Omega \mathbf{B}^T v_m^r\mathbf{N}^{eh}\delta\tilde{\boldsymbol{\rho}}_m d\Omega \\
&- \int_\Omega \mathbf{B}^T\rho_m^r\mathbf{N}\delta\mathbf{v}_m d\Omega + \int_{\Gamma_d} \mathbf{N}^T\rho_{\text{co}_2}^r\mathbf{N}\mathbf{v}_m^r\cdot n\, d\Gamma + \int_{\Gamma_d} \mathbf{N}^T\rho_{\text{co}_2}^r\mathbf{N}\delta\mathbf{v}_m\cdot n\, d\Gamma \\
&+ \int_{\Gamma_d} \mathbf{N}^T v_m^r\mathbf{N}\delta\boldsymbol{\rho}_m^r\cdot n\, d\Gamma + \int_{\Gamma_d} \mathbf{N}^T v_m^r\mathbf{N}^{eh+}\delta\tilde{\boldsymbol{\rho}}_m\cdot n\, d\Gamma - \int_{\Gamma_d} \mathbf{N}^T\rho_{\text{air}}^r\mathbf{N}\mathbf{v}_m^r\cdot n\, d\Gamma \\
&- \int_{\Gamma_d} \mathbf{N}^T\rho_{\text{air}}^r\mathbf{N}\delta\mathbf{v}_m\cdot n\, d\Gamma - \int_{\Gamma_d} \mathbf{N}^T v_m^r\mathbf{N}\delta\boldsymbol{\rho}_m\cdot n\, d\Gamma - \int_{\Gamma_d} \mathbf{N}^T v_m^r\mathbf{N}^{eh-}\delta\tilde{\boldsymbol{\rho}}_m\cdot n\, d\Gamma \\
&+ \int_{\Gamma_o} \mathbf{N}^T\rho_m^r\mathbf{N}\mathbf{v}_m^r\cdot n\, d\Gamma + \int_{\Gamma_o} \mathbf{N}^T\rho_m^r\mathbf{N}\delta\mathbf{v}_m\cdot n\, d\Gamma + \int_{\Gamma_o} \mathbf{N}^T v_m^r\mathbf{N}\delta\boldsymbol{\rho}_m\cdot n\, d\Gamma \\
&+ \int_{\Gamma_o} \mathbf{N}^T v_m^r\mathbf{N}^{eh}\delta\tilde{\boldsymbol{\rho}}_m\cdot n\, d\Gamma + \int_{\Gamma_q} \mathbf{N}^T\hat{q}_\rho d\Gamma = 0
\end{aligned} \tag{3.55}$$

in which $\rho_{\text{co}_2}^r$ and ρ_{air}^r are the CO_2 and air mass densities at the vicinity of the interface between them, known from the previous iteration, *r*.

Similar discretization can be made for the momentum and energy field equations, that upon putting them together in a concise form, leads to

Mass field equations

$$\mathbf{K}_{11}\delta\mathbf{v}_m+\mathbf{K}_{13}\delta\boldsymbol{\rho}_m+\mathbf{K}_{14}\delta\tilde{\boldsymbol{\rho}}_m+\mathbf{C}_{13}\delta\dot{\boldsymbol{\rho}}_m+\mathbf{C}_{14}\delta\dot{\tilde{\boldsymbol{\rho}}}_m=\mathbf{f}_1-\left(\mathbf{K}_{11}^0\mathbf{v}_m^r+\mathbf{C}_{13}^0\dot{\boldsymbol{\rho}}_m^r+\mathbf{C}_{14}^0\dot{\tilde{\boldsymbol{\rho}}}_m^r\right) \tag{3.56}$$

Momentum field equations

$$\begin{aligned}&\mathbf{K}_{21}\delta\mathbf{v}_m+\mathbf{K}_{22}\delta\mathbf{p}\ +\mathbf{K}_{23}\delta\boldsymbol{\rho}_m+\mathbf{K}_{24}\delta\tilde{\boldsymbol{\rho}}_m+\mathbf{C}_{21}\delta\dot{\mathbf{v}}_m+\mathbf{C}_{23}\delta\dot{\boldsymbol{\rho}}_m+\mathbf{C}_{24}\delta\dot{\tilde{\boldsymbol{\rho}}}_m\\&=\mathbf{f}_2-\left(\mathbf{K}_{21}^0\mathbf{v}_m^r+\mathbf{K}_{22}^0\mathbf{p}^r+\mathbf{K}_{23}^0\boldsymbol{\rho}_m^r+\mathbf{K}_{24}^0\tilde{\boldsymbol{\rho}}_m^r+\mathbf{C}_{21}^0\dot{\mathbf{v}}_m^r+\mathbf{C}_{23}^0\dot{\boldsymbol{\rho}}_m^r+\mathbf{C}_{24}^0\dot{\tilde{\boldsymbol{\rho}}}_m^r\right)\end{aligned} \tag{3.57}$$

Energy field equations

$$\begin{aligned}&\mathbf{K}_{31}\delta\mathbf{v}_m+\mathbf{K}_{33}\delta\boldsymbol{\rho}_m+\mathbf{K}_{34}\delta\tilde{\boldsymbol{\rho}}_m+\mathbf{C}_{31}\delta\dot{\mathbf{v}}_m+\mathbf{C}_{32}\delta\dot{\mathbf{p}}\ +\mathbf{C}_{33}\delta\dot{\boldsymbol{\rho}}_m+\mathbf{C}_{34}\delta\dot{\tilde{\boldsymbol{\rho}}}_m\\&=\mathbf{f}_3-\left(\mathbf{K}_{31}^0\mathbf{v}_m^r+\mathbf{K}_{33}^0\boldsymbol{\rho}_m^r+\mathbf{K}_{34}^0\tilde{\boldsymbol{\rho}}_m^r+\mathbf{C}_{31}^0\dot{\mathbf{v}}_m^r+\mathbf{C}_{32}^0\dot{\mathbf{p}}^r+\mathbf{C}_{33}^0\dot{\boldsymbol{\rho}}_m^r+\mathbf{C}_{34}^0\dot{\tilde{\boldsymbol{\rho}}}_m^r\right)\end{aligned} \tag{3.58}$$

$$\begin{aligned}&\mathbf{K}_{41}\delta\mathbf{v}_m+\mathbf{K}_{43}\delta\boldsymbol{\rho}_m+\mathbf{K}_{44}\delta\tilde{\boldsymbol{\rho}}_m+\mathbf{C}_{41}\delta\dot{\mathbf{v}}_m+\mathbf{C}_{42}\delta\dot{\mathbf{p}}\ +\mathbf{C}_{43}\delta\dot{\boldsymbol{\rho}}_m+\mathbf{C}_{44}\delta\dot{\tilde{\boldsymbol{\rho}}}_m\\&=\mathbf{f}_4-\left(\mathbf{K}_{41}^0\mathbf{v}_m^r+\mathbf{K}_{43}^0\boldsymbol{\rho}_m^r+\mathbf{K}_{44}^0\tilde{\boldsymbol{\rho}}_m^r+\mathbf{C}_{41}^0\dot{\mathbf{v}}_m^r+\mathbf{C}_{42}^0\dot{\mathbf{p}}^r+\mathbf{C}_{43}^0\dot{\boldsymbol{\rho}}_m^r+\mathbf{C}_{44}^0\dot{\tilde{\boldsymbol{\rho}}}_m^r\right)\end{aligned} \tag{3.59}$$

In a matrix form, these equations can be described as

$$\begin{aligned}&\begin{pmatrix}\mathbf{K}_{11}&0&\mathbf{K}_{13}&\mathbf{K}_{14}\\\mathbf{K}_{21}&\mathbf{K}_{22}&\mathbf{K}_{23}&\mathbf{K}_{24}\\\mathbf{K}_{31}&0&\mathbf{K}_{33}&\mathbf{K}_{34}\\\mathbf{K}_{41}&0&\mathbf{K}_{43}&\mathbf{K}_{44}\end{pmatrix}\begin{Bmatrix}\delta\mathbf{v}_m\\\delta\mathbf{p}\\\delta\boldsymbol{\rho}_m\\\delta\tilde{\boldsymbol{\rho}}_m\end{Bmatrix}+\begin{pmatrix}0&0&\mathbf{C}_{13}&\mathbf{C}_{14}\\\mathbf{C}_{21}&0&\mathbf{C}_{23}&\mathbf{C}_{24}\\\mathbf{C}_{31}&\mathbf{C}_{32}&\mathbf{C}_{33}&\mathbf{C}_{34}\\\mathbf{C}_{41}&\mathbf{C}_{42}&\mathbf{C}_{43}&\mathbf{C}_{44}\end{pmatrix}\begin{Bmatrix}\delta\dot{\mathbf{v}}_m\\\delta\dot{\mathbf{p}}\\\delta\dot{\boldsymbol{\rho}}_m\\\delta\dot{\tilde{\boldsymbol{\rho}}}_m\end{Bmatrix}\\&=\begin{Bmatrix}\mathbf{f}_1\\\mathbf{f}_2\\\mathbf{f}_3\\\mathbf{f}_4\end{Bmatrix}-\begin{pmatrix}\mathbf{K}_{11}^0&0&0&0\\\mathbf{K}_{21}^0&\mathbf{K}_{22}^0&\mathbf{K}_{23}^0&\mathbf{K}_{24}^0\\\mathbf{K}_{31}^0&0&\mathbf{K}_{33}^0&\mathbf{K}_{34}^0\\\mathbf{K}_{41}^0&0&\mathbf{K}_{43}^0&\mathbf{K}_{44}^0\end{pmatrix}\begin{Bmatrix}\mathbf{v}_m^r\\\mathbf{p}^r\\\boldsymbol{\rho}_m^r\\\tilde{\boldsymbol{\rho}}_m^r\end{Bmatrix}-\begin{pmatrix}0&0&\mathbf{C}_{13}^0&\mathbf{C}_{14}^0\\\mathbf{C}_{21}^0&0&\mathbf{C}_{23}^0&\mathbf{C}_{24}^0\\\mathbf{C}_{31}^0&\mathbf{C}_{32}^0&\mathbf{C}_{33}^0&\mathbf{C}_{34}^0\\\mathbf{C}_{41}^0&\mathbf{C}_{42}^0&\mathbf{C}_{43}^0&\mathbf{C}_{44}^0\end{pmatrix}\begin{Bmatrix}\dot{\mathbf{v}}_m^r\\\dot{\mathbf{p}}^r\\\dot{\boldsymbol{\rho}}_m^r\\\dot{\tilde{\boldsymbol{\rho}}}_m^r\end{Bmatrix}\end{aligned} \tag{3.60}$$

The matrix entries of this equation are given in Appendix C.

Eq. (3.60) contains an extra degree of freedom as compared to that if the standard Galerkin method is utilized to discretize all variables. This entails that the system of

equations that needs to be solved is larger. However, this increase is minor, as the extra degree of freedom is only added to the nodes where the element is intersected by the interface between air and CO_2. Moreover, this increase in the system size is compensated by the advantages of the partition of unity method, which is effectively mesh-independent that allows for the utilization of relatively coarse meshes.
Eq. (3.60) is solved using fully implicit time integration scheme.

3.7 Numerical examples

Two numerical examples simulating CO_2 leakage through an abandoned wellbores are solved using the proposed PUM-SG model. The first numerical example is designed to simulate initial and boundary conditions normally existing in typical CO_2 geosequestration sites, and the second numerical example is designed to simulate an extreme boundary condition that results to phase changes and a complicated mixture of fluids through the wellbore. The computational efficiency of the model and its capability to simulate phase changes are highlighted.

3.7.1 CO_2 leakage: normal boundary conditions

This example simulates CO_2 leakage through an abandoned wellbore subjected to initial and boundary conditions typically existing in CO_2 geosequestration sites. Fig. 3.2 shows the wellbore geometry and its boundary conditions, and Table 3.1 shows its properties, together with the properties of the surrounding formation. The objective of this example is to examine the model computational efficiency and its mesh-independency.

$$\text{Mixed boundary: } \begin{cases} \Gamma_u : & \hat{p} = 1.01325\times10^5 \text{ Pa (1 atm)} \\ \Gamma_o : & q_\rho \text{ excluded; } q_v \text{ and } q_e \text{ included} \end{cases}$$

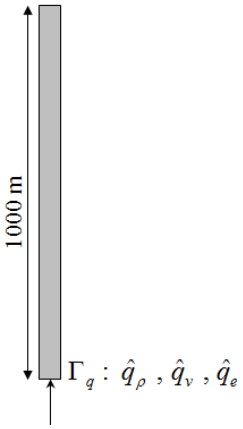

Fig. 3.2 Geometry and boundary conditions for the CO_2 blowout example.

Table 3.1 Wellbore and formation data.

Well Data	
Deviation angle [degree]	90
Well inner radius [m]	0.1
Well casing thickness [m]	0.02
Casing thermal conductivity [W m^{-1} K^{-1}]	0.6
Roughness of the wellbore [-]	5.0×10^{-6}
Formation Data	
Surface temperature [K]	275.15
Geothermal Gradient [K/m]	0.058

Initially, the wellbore is filled with air, which is under mechanical equilibrium with the atmosphere on the top, and in thermal equilibrium with the surrounding formation. The thermodynamic state of CO_2 in the reservoir is supercritical with $p = 7.5$ MPa and $\rho = 250$ kg/m^3. The CO_2 leakage rate at the bottom-hole is a function of the reservoir pressure, as

$$v_m = \frac{k_p}{\mu_{co_2}}\left(p_R - p\big|_{z=z_b}\right) \tag{3.61}$$

where p_R is the local reservoir pressure, and z_b is the coordinate of the bottom-hole, and k_p is the effective permeability of the defective cement plug, assumed 4×10^{-13} m^2.

This problem is solved using four mesh sizes: 4, 10, 20 and 100, 1D linear finite elements.

Fig. 3.3 shows the computational results of the mixture density at four different points of time before the CO_2 front reaches the top of the wellbore. Apparently, the results are very close to each other, especially those of the 20 elements mesh and the 100 elements mesh. Additionally, the model is capable of capturing the sharp front between the CO_2 and air, even with relatively coarse meshes. This clearly implies that the model is computationally efficient and effectively mesh-independent.

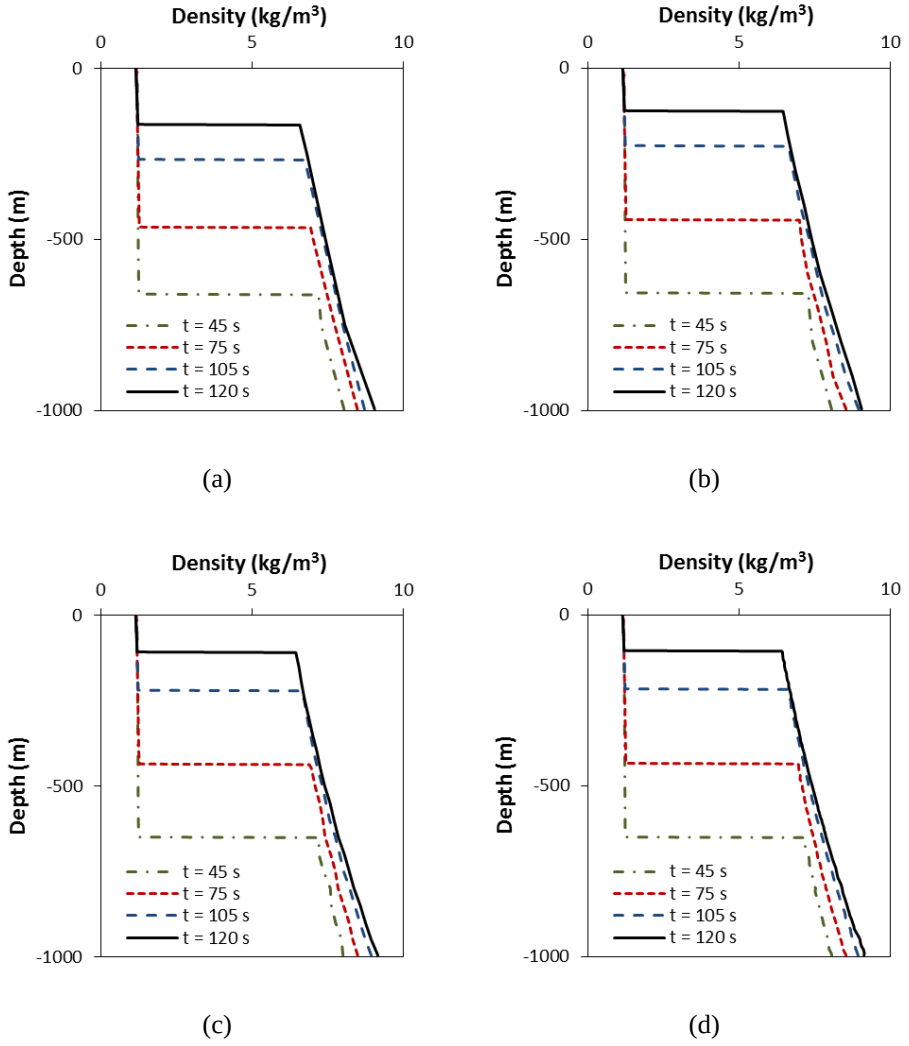

Fig. 3.3 Mixture density at four different points of time: (a) 4 elements, (b) 10 elements, (c) 20 elements, (d) 100 elements.

Fig. 3.4 shows the velocity, pressure and temperature distributions along the wellbore for the 20 elements mesh. The figure clearly shows that the velocity and pressure fields are continuous over the domain, as stated in Eq. (3.1), but the temperature field is discontinues due its direct relationship to the fluid density, as stated in Section 3.4.2. The plot of temperature shows that the temperature drops as low as 271 K (-2.15 ºC) which is 62.15 degrees less than the reservoir temperature. This drop in

temperature is attributed to that, upon leaking of a supercritical CO_2, an immediate expansion of CO_2 takes place, giving rise to a sudden reduction of temperature due to the Joule–Thomson effect.

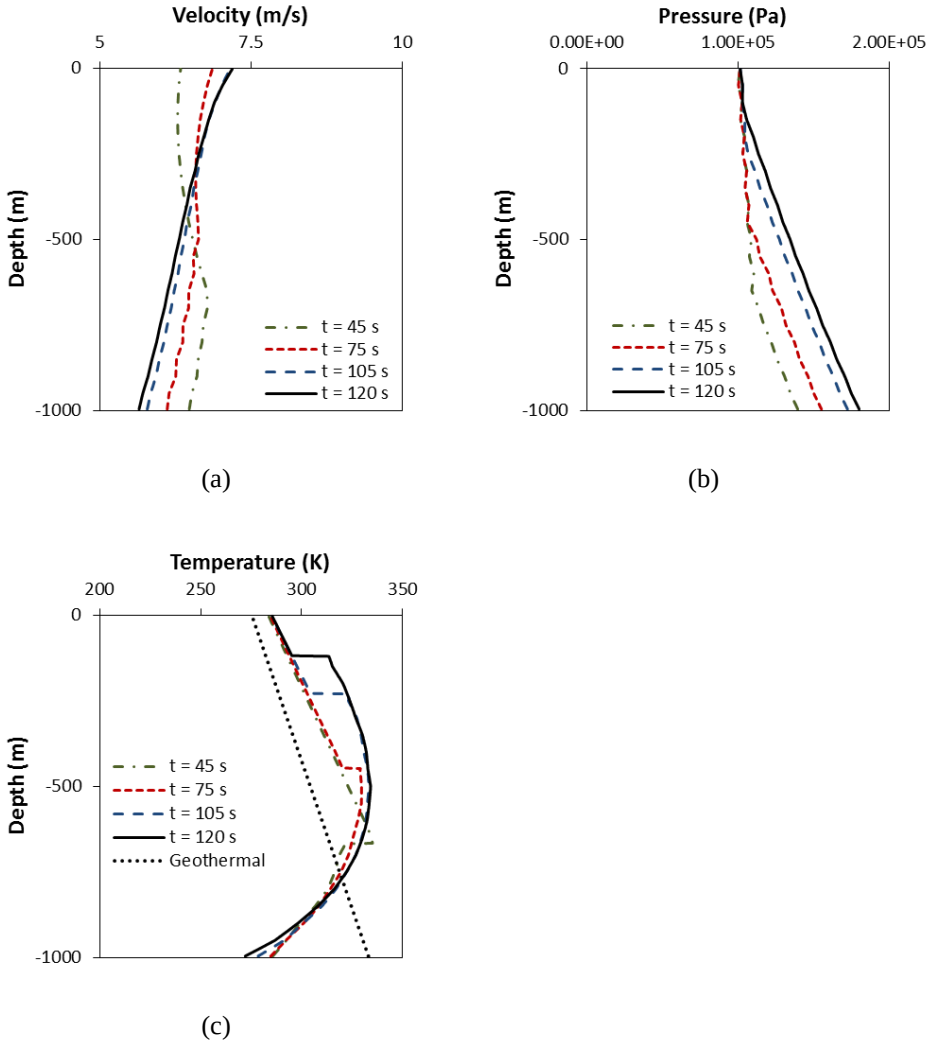

Fig. 3.4 Computational results using 20 elements: (a) mixture velocity, (b) pressure, (c) temperature.

3.7.2 CO_2 leakage: extreme boundary conditions

This example simulates CO_2 leakage through an abandoned wellbore subjected to extreme boundary conditions. Fig. 3.5 shows the wellbore geometry and its boundary

conditions. The properties of the wellbore and the surrounding formation are as those given in Table 3.1. The initial conditions are similar to that of the previous numerical example. The objective of this example is to examine the model computational capability to simulate extreme boundary conditions, which lead to phase changes and complicated flow pattern along the wellbore.

The CO_2 leakage rate at the bottom-hole is assumed to have a constant velocity, but exhibiting an increasing pressure and density, as

$$\hat{v}_m = 1 \text{ m/s} \tag{3.62}$$

$$\hat{p} = \begin{cases} 1.114575\times10^5 + 4.44427125\times10^3 t & t < 2000 \text{ s} \\ 9\times10^6 & t \geq 2000 \text{ s} \end{cases} \text{ Pa} \tag{3.63}$$

$$\hat{\rho}_m = \begin{cases} 10 + 0.27t & t < 2000 \text{ s} \\ 550 & t \geq 2000 \text{ s} \end{cases} \text{ kg/m}^3 \tag{3.64}$$

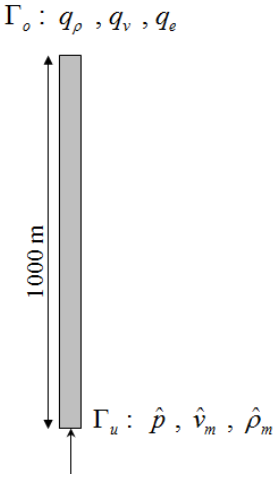

Fig. 3.5 Geometry and boundary conditions for the CO_2 leakage problem with extreme boundary conditions.

This problem is solved using 100, 1D linear elements.

Fig. 3.6 shows the CO_2 gas/liquid phase distribution along the wellbore versus time. The figure shows that, immediately, after the start of leakage, the CO_2 gas displaces the air and a gas/liquid mixture starts to form at the bottom of the wellbore. Until approximately 750 s, the wellbore is occupied by air, gas CO_2 and gas/liquid mixture CO_2. After 1500 s, a liquid CO_2 starts to form at the wellbore bottom, shortly followed by a supercritical CO_2. After approximately 2000 s, the pure gas state disappears and the wellbore becomes occupied by CO_2 liquid/gas mixture, liquid CO_2 and supercritical CO_2.

Fig. 3.7 shows the projection of the CO_2 states on the CO_2 phase diagram over the length of wellbore at four different times marked by dashed-lines in Fig. 3.6. The phase

diagram is plotted using Eq. (1.18). At times t = 1000 s and t = 1500 s, the computed $p-\rho$ curve goes through liquid/gas mixture to pure gas zone. At t = 1750 s, the p-ρ curve goes through supercritical CO_2, liquid CO_2, liquid/gas mixture and pure gas zones. At t = 4500 s, the $p-\rho$ curve goes through supercritical CO_2, liquid CO_2 and liquid/gas CO_2 zones. The pure gas in this interval has already disappeared.

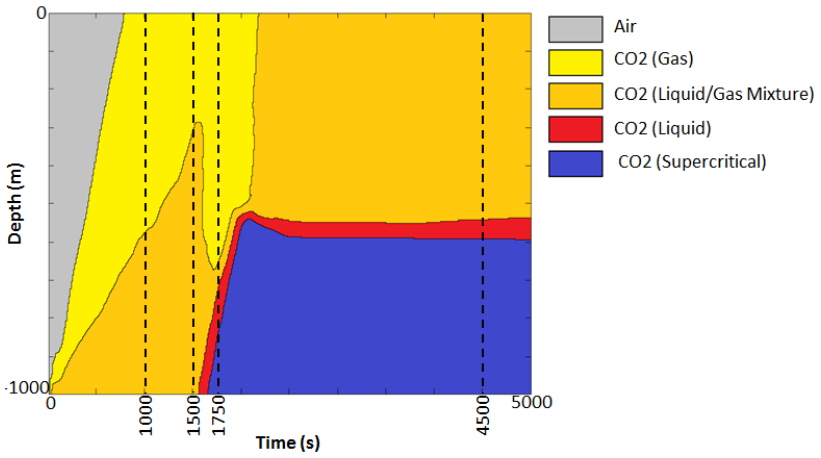

Fig. 3.6 Fluid and phase distribution over time.

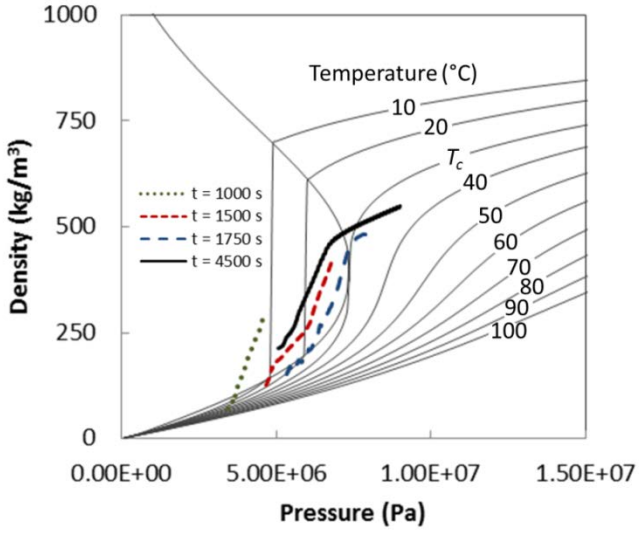

Fig. 3.7 Projections of the CO_2 state into the phase diagram of CO_2 over the length of wellbore.

3.8 Conclusions

Leakage of CO_2 to the ground surface via abandoned wellbores is hazardous and considered as one of the main concerns of applying CO_2 geosequestration technology. It is therefore vital to develop accurate computational tools capable of modeling this kind of leakage. As the problem occurs at a regional level, it is also vital that the tool be computationally efficient and mesh-independent. Solving this problem constitutes the focal point of this chapter.

Developing an accurate, mesh-independent and computationally efficient transient model for such a problem is challenging due to the presence of fluid dynamics, buoyancy, phase change, compressibility, thermal interactions, wall friction and slip between phases along the wellbore. In this chapter, we show that solving this problem requires an innovative coupling between the theoretical formulation and the numerical procedure. Both, averaging techniques and tailored numerical discretization procedures are necessary. The drift-flux model is utilized to formulate the problem, and a mixed discretization scheme, integrating the standard Galerkin finite element method, the partition of unity method, and the level-set method, is utilized to solve the problem. A one dimensional compressible two-fluid domain, representing a homogeneous air gas and a mixture CO_2 with a jump at the interface between them, is modeled. All important physical phenomena and processes are considered.

The computational model is tested by solving two numerical examples with different boundary conditions. The computational results clearly exhibit the occurrence of phase change along the wellbore, the extent of which depends on the boundary conditions and the thermodynamic properties of CO_2. The chapter shows that the proposed computational model is computationally efficient and effectively mesh-independent.

3.9 Appendix A: Drift flux model parameters

The drift flux model parameters are defined as follows:

The wall friction coefficient can be defined as (Brill and Mukherjee 1999):

$$f = \begin{cases} \dfrac{16}{\mathrm{Re}} & \mathrm{Re} < 2400 \\ \dfrac{1}{16}\left\{\log\left[\dfrac{\varepsilon}{3.7 r_i} - \dfrac{5.02}{\mathrm{Re}}\log\left(\dfrac{\varepsilon}{3.7 r_i} + \dfrac{13}{\mathrm{Re}}\right)\right]\right\}^{-2} & \mathrm{Re} \geq 2400 \end{cases} \tag{3.65}$$

where ε is the roughness of the wellbore, and Re is the Reynolds number given by

$$\mathrm{Re} = \frac{\rho_m |v_m| (2 r_i)}{\mu_m} \tag{3.66}$$

The heat exchange between the well and the surrounding formation can be described as

$$Q = 2\pi r_w U \left(T - T_e(z)\right) \tag{3.67}$$

in which $T_e(z)$ is the formation temperature, and U is the overall thermal interaction coefficient of the wellbore, which can be described as (Al-Khoury et al. 2010):

$$U = \frac{1}{R_{\text{conv}} + R_{\text{cond}}} \tag{3.68}$$

where R_{conv} and R_{cond} are the thermal resistances of the fluid and casing material, respectively, described as

$$R_{\text{conv}} = r_o / (r_w \bar{h}) \tag{3.69}$$

$$R_{\text{cond}} = r_o \ln(r_o / r_w) / \lambda_p \tag{3.70}$$

in which r_o is the outer radius of the wellbore, λ_p is the thermal conductivity of the casing material, and $\bar{h}$ is the convective heat transfer coefficient, described as

$$\bar{h} = \text{Nu}\, \lambda_m / (2 r_i) \tag{3.71}$$

where Nu is the Nusselt number, defined as

$$\text{Nu} = \begin{cases} 0.664\, \text{Re}^{1/2}\, \text{Pr}^{1/3} & \text{Re} \le 2000 \\ 0.023\, \text{Re}^{0.8}\, \text{Pr}^{0.4} & \text{Re} > 2000 \end{cases} \tag{3.72}$$

in which Pr is the Prandtl number given by

$$\text{Pr} = \frac{\nu}{\alpha} = \frac{\mu_m / \rho_m}{\lambda_m / (\rho_m c_{pm})} = \frac{\mu_m c_{pm}}{\lambda_m} \tag{3.73}$$

where c_{pm} and λ_m are the specific isobaric heat capacity and thermal conductivity of the mixture, respectively.

The slip parameter γ is defined as (Pan et al. 2011b)

$$\gamma(v_m, p, \rho_m) = \frac{f_G}{1 - f_G} \frac{\rho_G \rho_L \rho_m}{\rho_m^{*2}} \left[(C_0 - 1) v_m + v_d \right]^2 \tag{3.74}$$

in which f_G is the gas volume fraction, ρ_G is the gas density, ρ_L is the liquid density, v_d is the drift velocity, and

$$\rho_m^* = f_G C_0 \rho_G + (1 - f_G C_0) \rho_L \tag{3.75}$$

The drift velocity describes the variance in velocities between phases of a mixture. It can be described as (Shi et al. 2005):

$$v_d(v_m, p, \rho_m) = \frac{(1 - C_0 f_G) v_c K(f_G, K_u, C_0) m(\theta)}{C_0 f_G \sqrt{\rho_G / \rho_L} + 1 - C_0 f_G} \tag{3.76}$$

where:

- $m(\theta)$ is an inclination adjusting function, described as

$$m(\theta) = m_0 (\cos\theta)^{n1} (1 + \sin\theta)^{n2} \tag{3.77}$$

in which m_0, n_1, and n_2 are fitting parameters.

- K_u is the Kutateladze number, described as

$$K_u = \left[\frac{C_{ku}}{\sqrt{N_B}}\left(\sqrt{1+\frac{N_B}{C_{ku}^2 C_w}}-1\right)\right]^{\frac{1}{2}} \tag{3.78}$$

in which $C_w = 0.008$ and $C_{ku} = 142$ (Pan and Oldenburg 2014), and N_B is the Bond number, defined as

$$N_B = 4r_i^2\left[\frac{g(\rho_L-\rho_G)}{\sigma_{GL}}\right] \tag{3.79}$$

where σ_{GL} is the gas-liquid surface tension.

- v_c is the characteristic velocity, given by

$$v_c = \left[\frac{g\sigma_{GL}(\rho_L-\rho_G)}{\rho_L^2}\right]^{\frac{1}{4}} \tag{3.80}$$

- K is a smooth transition function, introduced to make a smooth transition of the drift velocity between the bubble rise and the film flooding flow regimes, described as (Pan and Oldenburg 2014):

$$K = \begin{cases} 1.53 & f_G \le a_1 \\ 1.53+\dfrac{C_0K_u-1.53}{2}\left[1-\cos\left(\pi\dfrac{f_G-a_1}{a_2-a_1}\right)\right] & a_1 \le f_G \le a_2 \\ C_0K_u & f_G \ge a_2 \end{cases} \tag{3.81}$$

in which a_1 and a_2 are two transitional gas volume fractions corresponding to the bubble rise and the film flooding flow regimes, respectively.

- C_0 is a profile parameter, calculated as (Shi et al. 2005):

$$C_0 = \frac{C_{\max}}{1+(C_{\max}-1)\eta^2} \tag{3.82}$$

in which $C_{\max}$ is the profile parameter for low gas fraction and η is a parameter reflecting the effect of the flow status on the profile parameter, given by:

$$\eta = \frac{\beta-B}{1-B} \tag{3.83}$$

where B is the threshold parameter above which C_0 starts to drop below $C_{\max}$, described as (Pan and Oldenburg 2014):

$$B = \frac{2}{C_{\max}} - 1.0667 \tag{3.84}$$

and β is calculated as

$$\beta = \max\left(f_G, F_V \frac{f_G |v_m|}{v_{sgf}} \right) \ , \quad 0 \le \beta \le 1 \tag{3.85}$$

in which F_V is a multiplier to adjust the sensitivity of the profile flattening to the gas velocity, and v_{sgf} is a gas superficial velocity at which flooding occurs. F_V is equal to 1, according to Shi et al. (2005), and v_{sgf} is calculated as:

$$v_{sgf} = K_u \left(\frac{\rho_L}{\rho_G} \right)^{\frac{1}{2}} v_c \tag{3.86}$$

Since there is no experimental data to determine the fitting parameters $C_{\max}$, m_0, n_1, n_2, a_1 and a_2, the available values for water-gas mixture is used instead, that read: $C_{\max} = 1$, $m_0 = 1.85$ $n_1 = 0.21$, $n_2 = 0.95$, $a_1 = 0.06$, and $a_2 = 0.21$ (Shi et al. 2005).

3.10 Appendix B: Constitutive equations

3.10.1 Appendix B.1 CO_2 constitutive equations

See chapter 1, Section 1.2.3.1.

3.10.2 Appendix B.2 Air constitutive equations

See chapter 1, Section 1.2.3.3.

3.11 Appendix C. Components of the finite element matrices

$$\mathbf{K}_{11} = -\int_{\Omega} \mathbf{B}^T \rho_m^r \mathbf{N} d\Omega + \int_{\Gamma_d} \mathbf{N}^T \rho_{\mathrm{co}_2}^r \mathbf{N} \cdot n \, d\Gamma - \int_{\Gamma_d} \mathbf{N}^T \rho_{\mathrm{air}}^r \mathbf{N} \cdot n \, d\Gamma + \int_{\Gamma_o} \mathbf{N}^T \rho_m^r \mathbf{N} \cdot n \, d\Gamma \tag{3.87}$$

$$\mathbf{K}_{13} = -\int_{\Omega} \mathbf{B}^T v_m^r \mathbf{N} d\Omega + \int_{\Gamma_o} \mathbf{N}^T v_m^r \mathbf{N} \cdot n \, d\Gamma \tag{3.88}$$

$$\mathbf{K}_{14} = -\int_{\Omega} \mathbf{B}^T v_m^r \mathbf{N}^{eh} d\Omega + \int_{\Gamma_d} \mathbf{N}^T v_m^r \mathbf{N}^{eh+} \cdot n \, d\Gamma - \int_{\Gamma_d} \mathbf{N}^T v_m^r \mathbf{N}^{eh-} \cdot n \, d\Gamma + \int_{\Gamma_o} \mathbf{N}^T v_m^r \mathbf{N}^{eh} \cdot n \, d\Gamma \tag{3.89}$$

$$\mathbf{C}_{13} = \int_{\Omega} \mathbf{N}^T \mathbf{N} d\Omega \tag{3.90}$$

$$\mathbf{C}_{14} = \int_{\Omega} \mathbf{N}^T \mathbf{N}^{eh} d\Omega \tag{3.91}$$

$$\mathbf{K}_{11}^0 = -\int_{\Omega} \mathbf{B}^T \rho_m^r \mathbf{N} d\Omega + \int_{\Gamma_d} \mathbf{N}^T \rho_{\mathrm{co}_2}^r \mathbf{N} \cdot n \, d\Gamma - \int_{\Gamma_d} \mathbf{N}^T \rho_{\mathrm{air}}^r \mathbf{N} \cdot n \, d\Gamma + \int_{\Gamma_o} \mathbf{N}^T \rho_m^r \mathbf{N} \cdot n \, d\Gamma \tag{3.92}$$

$$\mathbf{C}_{13}^0 = \int_{\Omega} \mathbf{N}^T \mathbf{N} d\Omega \tag{3.93}$$

$$\mathbf{C}_{14}^0 = \int_{\Omega} \mathbf{N}^T \mathbf{N}^{eh} d\Omega \tag{3.94}$$

$$\mathbf{f}_1 = -\int_{\Gamma_q} \mathbf{N}^T \hat{q}_\rho d\Gamma \tag{3.95}$$

$$\mathbf{K}_{21} = \int_{\Omega} \mathbf{N}^T \dot{\rho}_m^r \mathbf{N} d\Omega - \int_{\Omega} 2\mathbf{B}^T \rho_m^r v_m^r \mathbf{N} d\Omega - \int_{\Omega} \mathbf{B}^T \frac{\partial \gamma^r}{\partial v_m} \mathbf{N} d\Omega + \int_{\Omega} \mathbf{N}^T \frac{f^r}{2r_i} \rho_m^r \mathrm{sign}\left(v_m^r\right) v_m^r \mathbf{N} d\Omega + \int_{\Omega} \mathbf{N}^T \frac{1}{4r_i} \frac{\rho_m^r \mathrm{sign}\left(v_m^r\right)(2r_i)}{\mu_m^r} \frac{\partial f^r}{\partial \mathrm{Re}} \rho_m^r \mathrm{sign}\left(v_m^r\right)\left(v_m^r\right)^2 \mathbf{N} d\Omega + \int_{\Gamma_d} 2\mathbf{N}^T \rho_{\mathrm{co}_2}^r v_m^r \mathbf{N} \cdot n \, d\Gamma - \int_{\Gamma_d} 2\mathbf{N}^T \rho_{\mathrm{air}}^r v_m^r \mathbf{N} \cdot n \, d\Gamma + \int_{\Gamma_o} 2\mathbf{N}^T \rho_m^r v_m^r \mathbf{N} \cdot n \, d\Gamma + \int_{\Gamma_o} \mathbf{N}^T \frac{\partial \gamma^r}{\partial v_m} \mathbf{N} \cdot n \, d\Gamma \tag{3.96}$$

$$\mathbf{K}_{22} = \int_{\Omega} \mathbf{N}^T \mathbf{B} d\Omega \tag{3.97}$$

$$\mathbf{K}_{23} = \int_{\Omega} \mathbf{N}^T \dot{v}_m^r \mathbf{N} d\Omega - \int_{\Omega} \mathbf{B}^T \left(v_m^r\right)^2 \mathbf{N} d\Omega - \int_{\Omega} \mathbf{B}^T \frac{\partial \gamma^r}{\partial \rho_m} \mathbf{N} d\Omega$$
$$+ \int_{\Omega} \mathbf{N}^T \frac{f^r}{4r_i} \text{sign}\left(v_m^r\right)\left(v_m^r\right)^2 \mathbf{N} d\Omega + \int_{\Omega} \mathbf{N}^T \mathbf{N} g \sin\theta d\Omega$$
$$+ \int_{\Omega} \mathbf{N}^T \frac{1}{4r_i} \left(\frac{\left|v_m^r\right|(2r_i)}{\mu_m^r} - \frac{\rho_m^r \left|v_m^r\right|(2r_i)}{\left(\mu_m^r\right)^2} \frac{\partial \mu_m^r}{\partial \rho_m} \right) \frac{\partial f^r}{\partial \text{Re}} \rho_m^r \text{sign}\left(v_m^r\right)\left(v_m^r\right)^2 \mathbf{N} d\Omega \tag{3.98}$$
$$+ \int_{\Gamma_o} \mathbf{N}^T \left(v_m^r\right)^2 \mathbf{N} \cdot n \, d\Gamma + \int_{\Gamma_o} \mathbf{N}^T \frac{\partial \gamma^r}{\partial \rho_m} \mathbf{N} \cdot n \, d\Gamma$$

$$\mathbf{K}_{24} = \int_{\Omega} \mathbf{N}^T \dot{v}_m^r \mathbf{N}^{eh} d\Omega - \int_{\Omega} \mathbf{B}^T \left(v_m^r\right)^2 \mathbf{N}^{eh} d\Omega - \int_{\Omega} \mathbf{B}^T \frac{\partial \gamma^r}{\partial \rho_m} \mathbf{N}^{eh} d\Omega$$
$$+ \int_{\Omega} \mathbf{N}^T \frac{f^r}{4r_i} \text{sign}\left(v_m^r\right)\left(v_m^r\right)^2 \mathbf{N}^{eh} d\Omega + \int_{\Omega} \mathbf{N}^T \mathbf{N}^{eh} g \sin\theta d\Omega$$
$$+ \int_{\Omega} \mathbf{N}^T \frac{1}{4r_i} \left(\frac{\left|v_m^r\right|(2r_i)}{\mu_m^r} - \frac{\rho_m^r \left|v_m^r\right|(2r_i)}{\left(\mu_m^r\right)^2} \frac{\partial \mu_m^r}{\partial \rho_m} \right) \frac{\partial f^r}{\partial \text{Re}} \rho_m^r \text{sign}\left(v_m^r\right)\left(v_m^r\right)^2 \mathbf{N}^{eh} d\Omega$$
$$+ \int_{\Gamma_d} \mathbf{N}^T \left(v_m^r\right)^2 \mathbf{N}^{eh+} \cdot n \, d\Gamma - \int_{\Gamma_d} \mathbf{N}^T \left(v_m^r\right)^2 \mathbf{N}^{eh-} \cdot n \, d\Gamma$$
$$+ \int_{\Gamma_o} \mathbf{N}^T \left(v_m^r\right)^2 \mathbf{N}^{eh} \cdot n \, d\Gamma + \int_{\Gamma_o} \mathbf{N}^T \frac{\partial \gamma^r}{\partial \rho_m} \mathbf{N}^{eh} \cdot n \, d\Gamma \tag{3.99}$$

$$\mathbf{C}_{21} = \int_{\Omega} \mathbf{N}^T \rho_m^r \mathbf{N} d\Omega \tag{3.100}$$

$$\mathbf{C}_{23} = \int_{\Omega} \mathbf{N}^T v_m^r \mathbf{N} d\Omega \tag{3.101}$$

$$\mathbf{C}_{24} = \int_{\Omega} \mathbf{N}^T v_m^r \mathbf{N}^{eh} d\Omega \tag{3.102}$$

$$\mathbf{K}_{21}^0 = -\int_{\Omega} \mathbf{B}^T \rho_m^r v_m^r \mathbf{N} d\Omega + \int_{\Omega} \mathbf{N}^T \frac{f^r}{4r_i} \rho_m^r \text{sign}\left(v_m^r\right) v_m^r \mathbf{N} d\Omega \tag{3.103}$$

$$\mathbf{K}_{22}^0 = \int_{\Omega} \mathbf{N}^T \mathbf{B} \; d\Omega \tag{3.104}$$

$$\mathbf{K}_{23}^0 = \int_{\Omega} \mathbf{N}^T \mathbf{N} g \sin\theta d\Omega \tag{3.105}$$

$$\mathbf{K}_{24}^{0} = \int_{\Omega} \mathbf{N}^{T} \mathbf{N}^{eh} g \sin\theta d\Omega \tag{3.106}$$

$$\mathbf{C}_{21}^{0} = \int_{\Omega} \mathbf{N}^{T} \rho_{m}^{r} \mathbf{N} d\Omega \tag{3.107}$$

$$\mathbf{C}_{23}^{0} = \int_{\Omega} \mathbf{N}^{T} v_{m}^{r} \mathbf{N} d\Omega \tag{3.108}$$

$$\mathbf{C}_{24}^{0} = \int_{\Omega} \mathbf{N}^{T} v_{m}^{r} \mathbf{N}^{eh} d\Omega \tag{3.109}$$

$$\begin{aligned}\mathbf{f}_{2} = & \int_{\Omega} \mathbf{B}^{T} \gamma^{r} d\Omega - \int_{\Gamma_{d}} \mathbf{N}^{T} \rho_{\mathrm{co}_2}^{r} \left(v_{m}^{r}\right)^{2} \cdot n \, d\Gamma + \int_{\Gamma_{d}} \mathbf{N}^{T} \rho_{\mathrm{air}}^{r} \left(v_{m}^{r}\right)^{2} \cdot n \, d\Gamma \\ & - \int_{\Gamma_{o}} \mathbf{N}^{T} \rho_{m}^{r} \left(v_{m}^{r}\right)^{2} \cdot n \, d\Gamma - \int_{\Gamma_{o}} \mathbf{N}^{T} \gamma^{r} \cdot n \, d\Gamma - \int_{\Gamma_{q}} \mathbf{N}^{T} \hat{q}_{v} d\Gamma\end{aligned} \tag{3.110}$$

$$\begin{aligned}\mathbf{K}_{31} = & \int_{\Omega} \mathbf{N}^{T} v_{m}^{r} \dot{\rho}_{m}^{r} \mathbf{N} d\Omega + \int_{\Omega} \mathbf{N}^{T} \rho_{m}^{r} \dot{v}_{m}^{r} \mathbf{N} d\Omega - \int_{\Omega} \mathbf{B}^{T} \rho_{m}^{r} \left(v_{m}^{r}\right)^{2} \mathbf{N} d\Omega \\ & - \int_{\Omega} \mathbf{B}^{T} \rho_{m}^{r} \left(h_{m}^{r} + \frac{1}{2}\left(v_{m}^{r}\right)^{2}\right) \mathbf{N} d\Omega - \int_{\Omega} \mathbf{N}^{T} \rho_{m}^{r} \mathbf{N} g \sin\theta d\Omega \\ & + \int_{\Gamma_{d}} \mathbf{N}^{T} \rho_{\mathrm{co}_2}^{r} \left(h_{\mathrm{co}_2}^{r} + \frac{1}{2}\left(v_{m}^{r}\right)^{2}\right) \mathbf{N} \cdot n \, d\Gamma + \int_{\Gamma_{d}} \mathbf{N}^{T} \rho_{\mathrm{co}_2}^{r} \left(v_{m}^{r}\right)^{2} \mathbf{N} \cdot n \, d\Gamma \\ & - \int_{\Gamma_{d}} \mathbf{N}^{T} \rho_{\mathrm{air}}^{r} \left(h_{\mathrm{air}}^{r} + \frac{1}{2}\left(v_{m}^{r}\right)^{2}\right) \mathbf{N} \cdot n \, d\Gamma - \int_{\Gamma_{d}} \mathbf{N}^{T} \rho_{\mathrm{air}}^{r} \left(v_{m}^{r}\right)^{2} \mathbf{N} \cdot n \, d\Gamma \\ & + \int_{\Gamma_{o}} \mathbf{N}^{T} \rho_{m}^{r} \left(h_{m}^{r} + \frac{1}{2}\left(v_{m}^{r}\right)^{2}\right) \mathbf{N} \cdot n \, d\Gamma + \int_{\Gamma_{o}} \mathbf{N}^{T} \rho_{m}^{r} \left(v_{m}^{r}\right)^{2} \mathbf{N} \cdot n \, d\Gamma\end{aligned} \tag{3.111}$$

$$\mathbf{K}_{33} = \int_\Omega \mathbf{N}^T \frac{\partial h_m^r}{\partial \rho_m} \dot{\rho}_m^r \mathbf{N} d\Omega + \int_\Omega \mathbf{N}^T \frac{\partial^2 h_m^r}{\partial \rho_m^2} \dot{\rho}_m^r \rho_m^r \mathbf{N} d\Omega - \int_\Omega \mathbf{N}^T v_m^r \mathbf{N} g \sin\theta d\Omega$$
$$+ \int_\Omega \mathbf{N}^T \frac{\partial h_m^r}{\partial \rho_m} \dot{\rho}_m^r \mathbf{N} d\Omega + \int_\Omega \mathbf{N}^T v_m^r \dot{v}_m^r \mathbf{N} d\Omega - \int_\Omega \mathbf{B}^T \left(h_m^r + \frac{1}{2}\left(v_m^r\right)^2 \right) v_m^r \mathbf{N} d\Omega$$
$$- \int_\Omega \mathbf{B}^T \rho_m^r \frac{\partial h_m^r}{\partial \rho_m} v_m^r \mathbf{N} d\Omega + \int_\Omega \mathbf{N}^T \frac{1}{\pi r_i^2} \frac{dQ^r}{dT} \frac{\partial T^r}{\partial \rho_m} \mathbf{N} d\Omega$$
$$+ \int_{\Gamma_d} \mathbf{N}^T v_m^r \left(h_{\mathrm{co}_2}^r + \frac{1}{2}\left(v_m^r\right)^2 \right) \mathbf{N} \cdot n \, d\Gamma - \int_{\Gamma_d} \mathbf{N}^T v_m^r \left(h_{\mathrm{air}}^r + \frac{1}{2}\left(v_m^r\right)^2 \right) \mathbf{N} \cdot n \, d\Gamma$$
$$+ \int_{\Gamma_d} \mathbf{N}^T \rho_{\mathrm{co}_2}^r v_m^r \frac{\partial h_{\mathrm{co}_2}^r}{\partial \rho_m} \mathbf{N} \cdot n \, d\Gamma - \int_{\Gamma_d} \mathbf{N}^T \rho_{\mathrm{air}}^r v_m^r \frac{\partial h_{\mathrm{air}}^r}{\partial \rho_m} \mathbf{N} \cdot n \, d\Gamma$$
$$+ \int_{\Gamma_o} \mathbf{N}^T v_m^r \left(h_m^r + \frac{1}{2}\left(v_m^r\right)^2 \right) \mathbf{N} \cdot n \, d\Gamma + \int_{\Gamma_o} \mathbf{N}^T \rho_m^r v_m^r \frac{\partial h_m^r}{\partial \rho_m} \mathbf{N} \cdot n \, d\Gamma \tag{3.112}$$

$$\mathbf{K}_{34} = \int_\Omega \mathbf{N}^T \frac{\partial h_m^r}{\partial \rho_m} \dot{\rho}_m^r \mathbf{N}^{eh} d\Omega + \int_\Omega \mathbf{N}^T \frac{\partial^2 h_m^r}{\partial \rho_m^2} \dot{\rho}_m^r \rho_m^r \mathbf{N}^{eh} d\Omega - \int_\Omega \mathbf{N}^T v_m^r \mathbf{N}^{eh} g \sin\theta d\Omega$$
$$+ \int_\Omega \mathbf{N}^T \frac{\partial h_m^r}{\partial \rho_m} \dot{\rho}_m^r \mathbf{N}^{eh} d\Omega + \int_\Omega \mathbf{N}^T v_m^r \dot{v}_m^r \mathbf{N}^{eh} d\Omega + \int_\Omega \mathbf{N}^T \frac{1}{\pi r_i^2} \frac{dQ^r}{dT} \frac{\partial T^r}{\partial \rho_m} \mathbf{N}^{eh} d\Omega$$
$$- \int_\Omega \mathbf{B}^T \left(h_m^r + \frac{1}{2}\left(v_m^r\right)^2 \right) v_m^r \mathbf{N}^{eh} d\Omega - \int_\Omega \mathbf{B}^T \rho_m^r \frac{\partial h_m^r}{\partial \rho_m} v_m^r \mathbf{N}^{eh} d\Omega$$
$$+ \int_{\Gamma_d} \mathbf{N}^T v_m^r \left(h_{\mathrm{co}_2}^r + \frac{1}{2}\left(v_m^r\right)^2 \right) \mathbf{N}^{eh+} \cdot n \, d\Gamma - \int_{\Gamma_d} \mathbf{N}^T v_{\mathrm{m}}^r \left(h_{\mathrm{air}}^r + \frac{1}{2}\left(v_{\mathrm{m}}^r\right)^2 \right) \mathbf{N}^{eh-} \cdot n \, d\Gamma$$
$$+ \int_{\Gamma_d} \mathbf{N}^T \rho_{\mathrm{co}_2}^r v_m^r \frac{\partial h_{\mathrm{co}_2}^r}{\partial \rho_m} \mathbf{N}^{eh+} \cdot n \, d\Gamma - \int_{\Gamma_d} \mathbf{N}^T \rho_{\mathrm{air}}^r v_{\mathrm{m}}^r \frac{\partial h_{\mathrm{air}}^r}{\partial \rho_m} \mathbf{N}^{eh-} \cdot n \, d\Gamma$$
$$+ \int_{\Gamma_o} \mathbf{N}^T v_m^r \left(h_m^r + \frac{1}{2}\left(v_m^r\right)^2 \right) \mathbf{N}^{eh} \cdot n \, d\Gamma + \int_{\Gamma_o} \mathbf{N}^T \rho_m^r v_m^r \frac{\partial h_m^r}{\partial \rho_m} \mathbf{N}^{eh} \cdot n \, d\Gamma \tag{3.113}$$

$$\mathbf{C}_{31} = \int_\Omega \mathbf{N}^T \rho_m^r v_m^r \mathbf{N} d\Omega \tag{3.114}$$

$$\mathbf{C}_{32} = -\int_\Omega \mathbf{N}^T \mathbf{N} d\Omega \tag{3.115}$$

$$\mathbf{C}_{33} = \int_{\Omega} \mathbf{N}^T h_m^r \mathbf{N} d\Omega + \int_{\Omega} \frac{1}{2} \mathbf{N}^T \left(v_m^r\right)^2 \mathbf{N} d\Omega + \int_{\Omega} \mathbf{N}^T \frac{\partial h_m^r}{\partial \rho_m} \rho_m^r \mathbf{N} d\Omega \tag{3.116}$$

$$\mathbf{C}_{34} = \int_{\Omega} \mathbf{N}^T h_m^r \mathbf{N}^{eh} d\Omega + \int_{\Omega} \frac{1}{2} \mathbf{N}^T \left(v_m^r\right)^2 \mathbf{N}^{eh} d\Omega + \int_{\Omega} \mathbf{N}^T \frac{\partial h_m^r}{\partial \rho_m} \rho_m^r \mathbf{N}^{eh} d\Omega \tag{3.117}$$

$$\mathbf{K}_{31}^0 = -\int_{\Omega} \mathbf{B}^T \rho_m^r \left(h_m^r + \frac{1}{2}\left(v_m^r\right)^2 \right) \mathbf{N} d\Omega - \int_{\Omega} \mathbf{N}^T \rho_m^r \mathbf{N} g \sin\theta d\Omega \tag{3.118}$$

$$\mathbf{K}_{33}^0 = \int_{\Omega} \mathbf{N}^T \frac{\partial h_m^r}{\partial \rho_m} \dot{\rho}_m^r \mathbf{N} d\Omega \tag{3.119}$$

$$\mathbf{K}_{34}^0 = \int_{\Omega} \mathbf{N}^T \frac{\partial h_m^r}{\partial \rho_m} \dot{\rho}_m^r \mathbf{N}^{eh} d\Omega \tag{3.120}$$

$$\mathbf{C}_{31}^0 = \int_{\Omega} \mathbf{N}^T \rho_m^r v_m^r \mathbf{N} d\Omega \tag{3.121}$$

$$\mathbf{C}_{32}^0 = -\int_{\Omega} \mathbf{N}^T \mathbf{N} d\Omega \tag{3.122}$$

$$\mathbf{C}_{33}^0 = \int_{\Omega} \mathbf{N}^T h_m^r \mathbf{N} d\Omega + \int_{\Omega} \frac{1}{2} \mathbf{N}^T \left(v_m^r\right)^2 \mathbf{N} d\Omega \tag{3.123}$$

$$\mathbf{C}_{34}^0 = \int_{\Omega} \mathbf{N}^T h_m^r \mathbf{N}^{eh} d\Omega + \int_{\Omega} \frac{1}{2} \mathbf{N}^T \left(v_m^r\right)^2 \mathbf{N}^{eh} d\Omega \tag{3.124}$$

$$\begin{aligned} \mathbf{f}_3 = & -\int_{\Omega} \mathbf{N}^T \frac{1}{\pi r_i^2} Q^r d\Omega - \int_{\Gamma_d} \mathbf{N}^T \rho_{\mathrm{co}_2}^r v_m^r \left(h_{\mathrm{co}_2}^r + \frac{1}{2}\left(v_m^r\right)^2 \right) \cdot n \, d\Gamma \\ & + \int_{\Gamma_d} \mathbf{N}^T \rho_{\mathrm{air}}^r v_m^r \left(h_{\mathrm{air}}^r + \frac{1}{2}\left(v_m^r\right)^2 \right) \cdot n \, d\Gamma - \int_{\Gamma_o} \mathbf{N}^T \rho_m^r v_m^r \left(h_m^r + \frac{1}{2}\left(v_m^r\right)^2 \right) \cdot n \, d\Gamma \\ & - \int_{\Gamma_q} \mathbf{N}^T \hat{q}_e d\Gamma \end{aligned} \tag{3.125}$$

$$\begin{aligned}\mathbf{K}_{41} &= \int_{\Omega}\left(\mathbf{N}^{eh}\right)^{T} v_m^r \dot{\rho}_m^r \mathbf{N} d\Omega + \int_{\Omega}\left(\mathbf{N}^{eh}\right)^{T} \rho_m^r \dot{v}_m^r \mathbf{N} d\Omega - \int_{\Omega}\left(\mathbf{B}^{eh}\right)^{T} \rho_m^r \left(v_m^r\right)^2 \mathbf{N} d\Omega \\ &- \int_{\Omega}\left(\mathbf{B}^{eh}\right)^{T} \rho_m^r \left(h_m^r + \frac{1}{2}\left(v_m^r\right)^2\right)\mathbf{N} d\Omega - \int_{\Omega}\left(\mathbf{N}^{eh}\right)^{T} \rho_m^r \mathbf{N} g \sin\theta d\Omega \\ &+ \int_{\Gamma_d}\left(\mathbf{N}^{eh}\right)^{T} \rho_{\mathrm{co}_2}^r \left(h_{\mathrm{co}_2}^r + \frac{1}{2}\left(v_m^r\right)^2\right)\mathbf{N}\cdot n\, d\Gamma + \int_{\Gamma_d}\left(\mathbf{N}^{eh}\right)^{T} \rho_{\mathrm{co}_2}^r \left(v_m^r\right)^2 \mathbf{N}\cdot n\, d\Gamma \\ &- \int_{\Gamma_d}\left(\mathbf{N}^{eh}\right)^{T} \rho_{\mathrm{air}}^r \left(h_{\mathrm{air}}^r + \frac{1}{2}\left(v_m^r\right)^2\right)\mathbf{N}\cdot n\, d\Gamma - \int_{\Gamma_d}\left(\mathbf{N}^{eh}\right)^{T} \rho_{\mathrm{air}}^r \left(v_m^r\right)^2 \mathbf{N}\cdot n\, d\Gamma \\ &+ \int_{\Gamma_o}\left(\mathbf{N}^{eh}\right)^{T} \rho_m^r \left(h_m^r + \frac{1}{2}\left(v_m^r\right)^2\right)\mathbf{N}\cdot n\, d\Gamma + \int_{\Gamma_o}\left(\mathbf{N}^{eh}\right)^{T} \rho_m^r \left(v_m^r\right)^2 \mathbf{N}\cdot n\, d\Gamma \end{aligned} \tag{3.126}$$

$$\begin{aligned}\mathbf{K}_{42} &= \int_{\Omega}\left(\mathbf{N}^{eh}\right)^{T} \frac{\partial h_m^r}{\partial p}\dot{\rho}_m^r \mathbf{N} d\Omega + \int_{\Omega}\left(\mathbf{N}^{eh}\right)^{T} \frac{\partial^2 h_m^r}{\partial p^2}\dot{p}^r \rho_m^r \mathbf{N} d\Omega \\ &+ \int_{\Omega}\left(\mathbf{N}^{eh}\right)^{T} \frac{\partial^2 h_m^r}{\partial p \partial \rho_m}\dot{\rho}_m^r \rho_m^r \mathbf{N} d\Omega - \int_{\Omega}\left(\mathbf{B}^{eh}\right)^{T} \rho_m^r \frac{\partial h_m^r}{\partial p} v_m^r \mathbf{N} d\Omega \\ &+ \int_{\Omega}\left(\mathbf{N}^{eh}\right)^{T} \frac{1}{\pi r_i^2}\frac{dQ^r}{dT}\frac{\partial T^r}{\partial p}\mathbf{N} d\Omega + \int_{\Gamma_d}\left(\mathbf{N}^{eh}\right)^{T} \rho_{\mathrm{co}_2}^r v_m^r \frac{\partial h_{\mathrm{co}_2}^r}{\partial p}\mathbf{N}\cdot n\, d\Gamma \\ &- \int_{\Gamma_d}\left(\mathbf{N}^{eh}\right)^{T} \rho_{\mathrm{air}}^r v_m^r \frac{\partial h_{\mathrm{air}}^r}{\partial p}\mathbf{N}\cdot n\, d\Gamma + \int_{\Gamma_o}\left(\mathbf{N}^{eh}\right)^{T} \rho_m^r v_m^r \frac{\partial h_m^r}{\partial p}\mathbf{N}\cdot n\, d\Gamma \end{aligned} \tag{3.127}$$

$$
\begin{aligned}
\mathbf{K}_{43} = & \int_{\Omega}\left(\mathbf{N}^{eh}\right)^{T}\frac{\partial h_m^r}{\partial \rho_m}\dot{\rho}_m^r\mathbf{N}d\Omega+\int_{\Omega}\left(\mathbf{N}^{eh}\right)^{T}\frac{\partial^2 h_m^r}{\partial p\partial \rho_m}\dot{p}^r\rho_m^r\mathbf{N}d\Omega \\
& +\int_{\Omega}\left(\mathbf{N}^{eh}\right)^{T}\frac{\partial h_m^r}{\partial p}\dot{p}^r\mathbf{N}d\Omega+\int_{\Omega}\left(\mathbf{N}^{eh}\right)^{T}\frac{\partial^2 h_m^r}{\partial \rho_m^2}\dot{\rho}_m^r\rho_m^r\mathbf{N}d\Omega \\
& -\int_{\Omega}\left(\mathbf{N}^{eh}\right)^{T}v_m^r\mathbf{N}g\sin\theta d\Omega+\int_{\Omega}\left(\mathbf{N}^{eh}\right)^{T}\frac{\partial h_m^r}{\partial \rho_m}\dot{\rho}_m^r\mathbf{N}d\Omega \\
& +\int_{\Omega}\left(\mathbf{N}^{eh}\right)^{T}v_m^r\dot{v}_m^r\mathbf{N}d\Omega-\int_{\Omega}\left(\mathbf{B}^{eh}\right)^{T}\left(h_m^r+\frac{1}{2}\left(v_m^r\right)^2\right)v_m^r\mathbf{N}d\Omega \\
& -\int_{\Omega}\left(\mathbf{B}^{eh}\right)^{T}\rho_m^r\frac{\partial h_m^r}{\partial \rho_m}v_m^r\mathbf{N}d\Omega+\int_{\Omega}\left(\mathbf{N}^{eh}\right)^{T}\frac{1}{\pi r_i^2}\frac{dQ^r}{dT}\frac{\partial T^r}{\partial \rho_m}\mathbf{N}d\Omega \\
& +\int_{\Gamma_d}\left(\mathbf{N}^{eh}\right)^{T}v_m^r\left(h_{\mathrm{co}_2}^r+\frac{1}{2}\left(v_m^r\right)^2\right)\mathbf{N}\cdot n\,d\Gamma+\int_{\Gamma_d}\left(\mathbf{N}^{eh}\right)^{T}\rho_{\mathrm{co}_2}^r v_m^r\frac{\partial h_{\mathrm{co}_2}^r}{\partial \rho_m}\mathbf{N}\cdot n\,d\Gamma \\
& -\int_{\Gamma_d}\left(\mathbf{N}^{eh}\right)^{T}v_m^r\left(h_{\mathrm{air}}^r+\frac{1}{2}\left(v_m^r\right)^2\right)\mathbf{N}\cdot n\,d\Gamma-\int_{\Gamma_d}\left(\mathbf{N}^{eh}\right)^{T}\rho_{\mathrm{air}}^r v_m^r\frac{\partial h_{\mathrm{air}}^r}{\partial \rho_m}\mathbf{N}\cdot n\,d\Gamma \\
& +\int_{\Gamma_o}\left(\mathbf{N}^{eh}\right)^{T}v_m^r\left(h_m^r+\frac{1}{2}\left(v_m^r\right)^2\right)\mathbf{N}\cdot n\,d\Gamma+\int_{\Gamma_o}\left(\mathbf{N}^{eh}\right)^{T}\rho_m^r v_m^r\frac{\partial h_m^r}{\partial \rho_m}\mathbf{N}\cdot n\,d\Gamma
\end{aligned}
\tag{3.128}
$$

$$\begin{aligned}\mathbf{K}_{44} &= \int_\Omega \left(\mathbf{N}^{eh}\right)^T \frac{\partial h_m^r}{\partial \rho_m}\dot{\rho}_m^r \mathbf{N}^{eh} d\Omega + \int_\Omega \left(\mathbf{N}^{eh}\right)^T \frac{\partial^2 h_m^r}{\partial p \partial \rho_m}\dot{p}^r \rho_m^r \mathbf{N}^{eh} d\Omega \\ &+ \int_\Omega \left(\mathbf{N}^{eh}\right)^T \frac{\partial h_m^r}{\partial p}\dot{p}^r \mathbf{N}^{eh} d\Omega + \int_\Omega \left(\mathbf{N}^{eh}\right)^T \frac{\partial^2 h_m^r}{\partial \rho_m^2}\dot{\rho}_m^r \rho_m^r \mathbf{N}^{eh} d\Omega \\ &- \int_\Omega \left(\mathbf{N}^{eh}\right)^T v_m^r \mathbf{N}^{eh} g \sin\theta d\Omega + \int_\Omega \left(\mathbf{N}^{eh}\right)^T \frac{\partial h_m^r}{\partial \rho_m}\dot{\rho}_m^r \mathbf{N}^{eh} d\Omega \\ &+ \int_\Omega \left(\mathbf{N}^{eh}\right)^T v_m^r \dot{v}_m^r \mathbf{N}^{eh} d\Omega - \int_\Omega \left(\mathbf{B}^{eh}\right)^T \left(h_m^r + \frac{1}{2}\left(v_m^r\right)^2\right) v_m^r \mathbf{N}^{eh} d\Omega \\ &- \int_\Omega \left(\mathbf{B}^{eh}\right)^T \rho_m^r \frac{\partial h_m^r}{\partial \rho_m} v_m^r \mathbf{N}^{eh} d\Omega + \int_\Omega \left(\mathbf{N}^{eh}\right)^T \frac{1}{\pi r_i^2}\frac{dQ^r}{dT}\frac{\partial T^r}{\partial \rho_m}\mathbf{N}^{eh} d\Omega \\ &+ \int_{\Gamma_d} \left(\mathbf{N}^{eh}\right)^T v_m^r \left(h_{\mathrm{co}_2}^r + \frac{1}{2}\left(v_m^r\right)^2\right)\mathbf{N}^{eh+} \cdot n\, d\Gamma \\ &+ \int_{\Gamma_d} \left(\mathbf{N}^{eh}\right)^T \rho_{\mathrm{co}_2}^r v_m^r \frac{\partial h_{\mathrm{co}_2}^r}{\partial \rho_m}\mathbf{N}^{eh+} \cdot n\, d\Gamma \\ &- \int_{\Gamma_d} \left(\mathbf{N}^{eh}\right)^T v_m^r \left(h_{\mathrm{air}}^r + \frac{1}{2}\left(v_m^r\right)^2\right)\mathbf{N}^{eh-} \cdot n\, d\Gamma - \int_{\Gamma_d} \left(\mathbf{N}^{eh}\right)^T \rho_{\mathrm{air}}^r v_m^r \frac{\partial h_{\mathrm{air}}^r}{\partial \rho_m}\mathbf{N}^{eh-} \cdot n\, d\Gamma \\ &+ \int_{\Gamma_o} \left(\mathbf{N}^{eh}\right)^T v_m^r \left(h_m^r + \frac{1}{2}\left(v_m^r\right)^2\right)\mathbf{N}^{eh} \cdot n\, d\Gamma + \int_{\Gamma_o} \left(\mathbf{N}^{eh}\right)^T \rho_m^r v_m^r \frac{\partial h_m^r}{\partial \rho_m}\mathbf{N}^{eh} \cdot n\, d\Gamma \end{aligned} \tag{3.129}$$

$$\mathbf{C}_{41} = \int_\Omega \left(\mathbf{N}^{eh}\right)^T \rho_m^r v_m^r \mathbf{N} d\Omega \tag{3.130}$$

$$\mathbf{C}_{42} = -\int_\Omega \left(\mathbf{N}^{eh}\right)^T \mathbf{N} d\Omega \tag{3.131}$$

$$\begin{aligned}\mathbf{C}_{43} &= \int_\Omega \left(\mathbf{N}^{eh}\right)^T h_m^r \mathbf{N} d\Omega + \int_\Omega \frac{1}{2}\left(\mathbf{N}^{eh}\right)^T \left(v_m^r\right)^2 \mathbf{N} d\Omega \\ &+ \int_\Omega \left(\mathbf{N}^{eh}\right)^T \frac{\partial h_m^r}{\partial \rho_m}\rho_m^r \mathbf{N} d\Omega \end{aligned} \tag{3.132}$$

$$\begin{aligned}\mathbf{C}_{44} &= \int_\Omega \left(\mathbf{N}^{eh}\right)^T h_m^r \mathbf{N}^{eh} d\Omega + \int_\Omega \frac{1}{2}\left(\mathbf{N}^{eh}\right)^T \left(v_m^r\right)^2 \mathbf{N}^{eh} d\Omega \\ &+ \int_\Omega \left(\mathbf{N}^{eh}\right)^T \frac{\partial h_m^r}{\partial \rho_m}\rho_m^r \mathbf{N}^{eh} d\Omega \end{aligned} \tag{3.133}$$

$$\mathbf{K}_{41}^{0} = -\int_{\Omega}\left(\mathbf{B}^{eh}\right)^{T}\rho_{m}^{r}\left(h_{m}^{r}+\frac{1}{2}\left(v_{m}^{r}\right)^{2}\right)\mathbf{N}d\Omega-\int_{\Omega}\left(\mathbf{N}^{eh}\right)^{T}\rho_{m}^{r}\mathbf{N}g\sin\theta d\Omega \tag{3.134}$$

$$\mathbf{K}_{43}^{0} = \int_{\Omega}\left(\mathbf{N}^{eh}\right)^{T}\frac{\partial h_{m}^{r}}{\partial\rho_{m}}\dot{\rho}_{m}^{r}\mathbf{N}d\Omega \tag{3.135}$$

$$\mathbf{K}_{44}^{0} = \int_{\Omega}\left(\mathbf{N}^{eh}\right)^{T}\frac{\partial h_{m}^{r}}{\partial\rho_{m}}\dot{\rho}_{m}^{r}\mathbf{N}^{eh}d\Omega \tag{3.136}$$

$$\mathbf{C}_{41}^{0} = \int_{\Omega}\left(\mathbf{N}^{eh}\right)^{T}\rho_{m}^{r}v_{m}^{r}\mathbf{N}d\Omega \tag{3.137}$$

$$\mathbf{C}_{42}^{0} = -\int_{\Omega}\left(\mathbf{N}^{eh}\right)^{T}\mathbf{N}d\Omega \tag{3.138}$$

$$\mathbf{C}_{43}^{0} = \int_{\Omega}\left(\mathbf{N}^{eh}\right)^{T}h_{m}^{r}\mathbf{N}d\Omega+\int_{\Omega}\frac{1}{2}\left(\mathbf{N}^{eh}\right)^{T}\left(v_{m}^{r}\right)^{2}\mathbf{N}d\Omega \tag{3.139}$$

$$\mathbf{C}_{44}^{0} = \int_{\Omega}\left(\mathbf{N}^{eh}\right)^{T}h_{m}^{r}\mathbf{N}^{eh}d\Omega+\int_{\Omega}\frac{1}{2}\left(\mathbf{N}^{eh}\right)^{T}\left(v_{m}^{r}\right)^{2}\mathbf{N}^{eh}d\Omega \tag{3.140}$$

$$\begin{aligned}\mathbf{f}_{4} = &-\int_{\Omega}\left(\mathbf{N}^{eh}\right)^{T}\frac{1}{\pi r_{i}^{2}}Q^{r}d\Omega-\int_{\Gamma_{d}}\left(\mathbf{N}^{eh+}\right)^{T}\rho_{\mathrm{co}_2}^{r}v_{m}^{r}\left(h_{\mathrm{co}_2}^{r}+\frac{1}{2}\left(v_{m}^{r}\right)^{2}\right)\cdot n\,d\Gamma\\ &+\int_{\Gamma_{d}}\left(\mathbf{N}^{eh-}\right)^{T}\rho_{\mathrm{air}}^{r}v_{m}^{r}\left(h_{\mathrm{air}}^{r}+\frac{1}{2}\left(v_{m}^{r}\right)^{2}\right)\cdot n\,d\Gamma\\ &-\int_{\Gamma_{o}}\left(\mathbf{N}^{eh}\right)^{T}\rho_{m}^{r}v_{m}^{r}\left(h_{m}^{r}+\frac{1}{2}\left(v_{m}^{r}\right)^{2}\right)\cdot n\,d\Gamma-\int_{\Gamma_{q}}\left(\mathbf{N}^{eh}\right)^{T}\hat{q}_{e}d\Gamma\end{aligned} \tag{3.141}$$

4

Coupled Layer-Wellbore Leakage

This chapter is based on Arzanfudi et al. (2016), a paper published in Finite Elements in Analysis and Design.

This chapter introduces a multidomain-staggered technique for coupling multiphase flow in a porous medium, dominated by the Darcy laminar flow, with multiphase flow in a wellbore, dominated by the Navier Stokes viscous, compressible flow. The Darcy flow in the porous medium is formulated using the averaging theory, and the Navier Stokes flow in the wellbore is formulated using the drift-flux model. The governing equations are discretized using a mixed discretization finite element scheme, in which the partition of unity finite element method, the level set method and the standard Galerkin finite element method are combined in an integrated numerical scheme. A multidomain technique is utilized to uncouple the physical system into two subdomains, coupled back by enforcing flow constraints at their interaction boundaries. The resulting system of equations is solved using an iterative staggered technique and a multiple time-stepping scheme. This combination between the multidomain technique and the staggered-multiple time-stepping technique enables the use of different mathematical and numerical formulations for the two subdomains, and facilitates the implementation of a standard finite element computer code. The proposed model is tailored to simulate sequestered CO_2 leakage through heterogeneous geological formation layers and abandoned wellbores. A numerical example describing different leakage scenarios is given to demonstrate the computational capability of the model. The numerical results are compared to those obtained from a commercial simulator.

4.1 Introduction

Coupling multiphase flow domains exhibiting significant difference in their velocity fields using standard numerical discretization schemes is computationally nuisance and can cause severe numerical oscillations. Fluid flow in porous media related to most geoscience applications is relatively slow, and the use of Darcy's law is practically valid. Whereas, fluid flow in pipes, such as wellbores, is relatively fast and can only be described using the Navier-Stokes equations, or some of their derivatives.

In reservoir engineering, the underground reservoirs can be useful and functional only if they are connected to the ground surface. The connection is usually made using wellbores, which are utilized for injection of fluids, such as water or supercritical CO_2, or pumping of fluids, such as geothermal water or fossil fuels. Despite this intimate link between reservoirs and wellbores, numerical simulators utilized for design and analysis of projects related to reservoir engineering, are mostly separated. The main reason for this separation is the difficulty in treating the distinct fluid flow characteristics between the reservoirs and the wellbores.

In general, there are three main techniques utilized for reservoir-wellbore integration. In one technique, the wellbore is assumed to constitute a porous domain with Darcy flow (Pruess 2004; Réveillère and Rohmer 2011; Zeng et al. 2011). This assumption is, in many cases, not valid, since the wellbore is in reality a hollow space filled with fluid, where, upon flowing, the Navier-Stokes flow is physically occurring. In the other technique, the wellbore and the reservoir are modeled using separate simulators, which are linked externally as a post-processing. This is the most common technique in reservoir engineering (Ebigbo et al. 2007; Pawar et al. 2009). In the third one, there is a full coupling between the two domains (Nordbotten et al. 2004; Pan et al. 2011a). Yet only few simulators are of this type, and mostly, standard numerical procedures are utilized to discretize the governing equations, entailing the need for fine grids and large CPU time and capacity.

Here, we develop a coupling technique for multiphase flow in a reservoir, connected to a wellbore. The fluid in the reservoir is governed by Darcy laminar flow, and in the wellbore by Navier-Stokes viscous, compressible flow. The two subdomains are spatially and temporally coupled, using a multidomain-staggered technique. The multidomain technique is utilized to uncouple and re-couple the physical system, and the staggered technique is utilized to solve the system of equations. The physical domain is divided into two subdomains representing the reservoir (and other rock formations), and the wellbore. At the contact points between the two subdomains, constraint conditions, controlling the fluid flow between them, are enforced. This multidomain-staggered combination allows for the use of different discretization schemes for the two subdomains, and more importantly, different time integration schemes, which count for the slow fluid motion in the porous domain and the fast fluid motion in the wellbore.

The proposed model is tailored to simulate sequestered CO_2 leakage through heterogeneous geological formation layers and abandoned wellbores. CO_2 geosequestration is a technology designed to mitigate the amount of CO_2 emitted into the earth atmosphere in an attempt to reduce the likely greenhouse effect. Selection of an appropriate geological formation and a proper design of a CO_2 sequestration plant require a good assessment of the risks of leakage. Leakage of CO_2 to the ground surface or upper layers containing underground water is hazardous and is considered as one of the major concerns of applying this technology. There are two major CO_2 leakage mechanisms: leakage through geological layers, for which the theory of multiphase flow in heterogeneous layered porous medium is applicable; and leakage through faults and abandoned wellbores, for which the theory of fluid dynamics is applicable.

In an earlier work, Arzanfudi et al. (2014 and 2015) introduced two numerical models describing these two CO_2 leakage mechanisms. A mixed discretization scheme has been utilized to solve these two leakage mechanisms. For the first, a stationary partition of unity finite element method (PUM) was utilized to model the discontinuity between layers of different physical properties, and the standard Galerkin finite element method (SG) was utilized to model the continuous fields. For the second, the drift flux model was utilized, taking into consideration all relevant phenomena occurring along the wellbore, including advection, buoyancy, phase change, compressibility, thermal interaction, wall friction and slip between phases. In this, the level-set method (LS) was utilized to trace the movement of the CO_2 front, the partition of unity to model the front and the standard Galerkin to model the continuous fields. In both cases, the implementation of the mixed PUM-LS-SG discretization scheme has enabled the use of structured, fixed meshes, regardless of the complexity of the layer geometries and the fluid front movement, and resulted in an effectively mesh-independent finite element solution. In this paper, these two models will be spatially and temporally coupled. A brief description of these models is given hereafter.

4.2 Two-phase flow in a heterogeneous layered domain

The physical domain is assumed two-dimensional multilayer, rigid, isotropic, homogeneous within a layer and isothermal with local thermal equilibrium. Two fluids can simultaneously exist in the reservoir: a wetting phase, represented by the formation water; and a non-wetting phase, represented by the injected CO_2. The fluids in the reservoir are incompressible, immiscible and do not exhibit phase change.

For CO_2 geosequestration, these assumptions might not be accurate in the area immediately surrounding the injection point, but further away, they are valid. Typically, CO_2 leakage occurs via upper layers and abandoned wellbores, which are usually far from the injection point. Additionally, the CO_2 in the reservoir is usually in a supercritical state, which is significantly less compressible than its gas state. Moreover, the focus here is on the numerical coupling between the two domains, which can readily be applied to more detailed conceptual models.

4.2.1 Governing equations

The continuity equations of an isothermal, immiscible and incompressible flow of a wetting phase (formation water) and a non-wetting phase (CO_2) in a rigid porous medium domain can be expressed as:

Wetting phase

$$-\phi\frac{\partial S_n}{\partial t}-\nabla\cdot\left[\mathbf{k}\lambda_w\left(\nabla p_w-\rho_w\mathbf{g}\right)\right]=0 \tag{4.1}$$

Non-wetting phase

$$\phi\frac{\partial S_n}{\partial t}-\nabla\cdot\left[\mathbf{k}\lambda_n\left(\nabla p_w+\frac{dp_c}{dS_n}\nabla S_n-\rho_n\mathbf{g}\right)\right]=0 \tag{4.2}$$

in which $\lambda_w=k_{rw}/\mu_w$ and $\lambda_n=k_{rn}/\mu_n$ are the wetting and non-wetting phase mobility, $\mathbf{g}$ is the gravity force vector, ρ_w is the wetting phase mass density, ρ_n is the non-wetting phase mass density, S_w is the wetting phase saturation, S_n is the non-wetting phase saturation, ϕ is the porosity, p_w is the wetting phase pressure, p_c is the capillary pressure, $\mathbf{k}$ is the absolute permeability, k_{rw} and k_{rn} are the wetting and non-wetting phase relative permeability (functions of saturation), and μ_w and μ_n are the wetting and non-wetting phase viscosity. The capillary pressure-saturation and relative permeability-saturation are described by Brooks and Corey (1964) relationships.

4.2.2 Numerical discretization

We adopt the wetting phase pressure – non-wetting phase saturation formulation. The wetting phase pressure in Eqs. (2.6) and (2.7) is continuous across the boundaries between heterogeneous layers, but the non-wetting phase saturation (and the capillary pressure under certain conditions) exhibits a jump. The presence of these complicated physical conditions at the boundary between layers exerts severe difficulties on the numerical solution procedure. The standard Galerkin finite element method, for instance, is not capable of simulating this problem accurately, even if a fine mesh is utilized. To tackle this, we employ a mixed discretization scheme, in which we use the standard Galerkin method (SG) to discretize the continuous wetting phase pressure, and the partition of unity finite element method (PUM) (Babuška and Melenk 1997) to discretize the discontinuity in the non-wetting phase saturation field, such that

$$p_w(\mathbf{x},t)=\mathbf{N}(\mathbf{x})\mathbf{p}_w(t) \tag{4.3}$$

and

$$S_n(\mathbf{x},t)=\mathbf{N}(\mathbf{x})\mathbf{S}_n(t)+\mathbf{N}^{eh}(\mathbf{x})\tilde{\mathbf{S}}_n(t) \tag{4.4}$$

in which $\mathbf{N}(\mathbf{x})$ is the nodal vector of shape functions, and $\mathbf{p}_w(t)$ is the nodal vector of water pressure, $\mathbf{S}_n(t)$ and $\tilde{\mathbf{S}}_n(t)$ are the conventional and extended nodal vectors of the non-wetting phase saturation, and $\mathbf{N}^{eh}(\mathbf{x})$ is an enriched shape function, defined as

$$\mathbf{N}^{eh}(\mathbf{x}) = \mathbf{N}(\mathbf{x})H(\mathbf{x}) \tag{4.5}$$

where H(x) is any function that can accurately describe the jump profile of the field within the element, which contains the discontinuity. The use of the partition of unity entails decomposing the saturation field into a continuous part and a discontinuous part, where the latter is enhanced by use of a function which closely describes the nature of the jump in the field (the Heaviside function in case of a strong discontinuity, for instance).

The weighted residual method, together with the mixed discretization scheme highlighted in Eqs. (2.16)-(4.5), are utilized to solve Eqs. (2.6) and (2.7). A detailed description of the discretization procedure and the finite element matrices is given in Arzanfudi et al. (2014).

The advantage of this model is mainly two-fold. First, it is capable of accurately capturing multiphase flow fields discontinuities between layers. Second, the physical discontinuity between layers is modelled regardless of the finite element mesh. Therefore, the mesh is not restricted to be aligned with the boundary between layers, and it can be structured, geometry-independent and relatively coarse. Fig. 4.1 shows the possible use of a structured mesh to model a multilayer system.

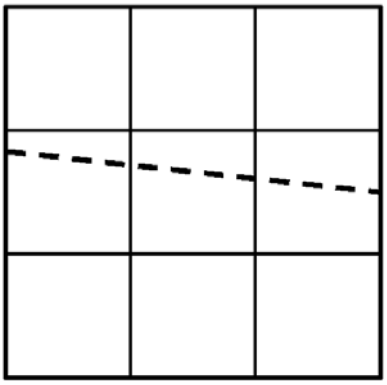

Fig. 4.1. Structured and geometry-independent mesh in two-phase flow in a heterogeneous layered domain model

4.3 Multiphase flow in a wellbore

The physical domain is assumed one-dimensional, multiphase, and constituting two compressible fluids: air and CO_2. The air is a homogeneous gas, and the CO_2 is a multiphase mixture exhibiting phase change. The physical process of such a domain is governed by the Navier-Stokes equations.

4.3.1 Governing equations

We utilize the one-dimensional drift-flux model to simulate the transport of air and CO_2 in the wellbore. This model adopts the area-averaged approach, where detailed analysis of the local behavior of the involved phases is averaged over the cross-sectional area of the wellbore (Faghri and Zhang 2006; Ishii and Hibiki 2006; Pan and Oldenburg 2014; Wallis 1969; Zuber and Findlay 1965). Important aspects of fluid dynamics, such as the inertia force, buoyancy, compressibility, wall friction, drift velocity, and flow profile are considered.

The fluid velocities and pressures at the interface between the two fluids are continuous, but the mass density and specific enthalpy exhibit discontinuity, such that:

$$\begin{aligned} &v_{\mathrm{co}_2} = v_{\mathrm{air}} \\ &p_{\mathrm{co}_2} = p_{\mathrm{air}} \qquad \text{at}\,\Gamma_d \\ &[\![\rho_m]\!] = \rho_{\mathrm{co}_2} - \rho_{\mathrm{air}} \\ &[\![h_m]\!] = h_{\mathrm{co}_2} - h_{\mathrm{air}} \end{aligned} \tag{4.6}$$

in which v_{co_2} and v_{air} are the velocities of CO_2 and air, and h_{co_2} and h_{air} are their specific enthalpies, respectively.

Taking the interface conditions, Eq. (3.1), into consideration, the drift-flux model is modified and expressed as:

Mass balance

$$\frac{\partial \rho_m}{\partial t} + \frac{\partial}{\partial z}(\rho_m v_m) + [\![\rho_m]\!] v_m \cdot n\,\delta(z - z_d) = 0 \tag{4.7}$$

Momentum balance

$$\frac{\partial}{\partial t}(\rho_m v_m) + \frac{\partial}{\partial z}\left(\rho_m v_m^2 + \gamma\right) + [\![\rho_m]\!] v_m^2 \cdot n\,\delta(z - z_d) = -\frac{\partial p}{\partial z} - \frac{f\,\rho_m |v_m| v_m}{4 r_i} - \rho_m g \sin\theta \tag{4.8}$$

Energy balance

$$\frac{\partial}{\partial t}\left[\rho_m\left(h_m+\frac{1}{2}v_m^2\right)-p\right]+\frac{\partial}{\partial z}\left[\rho_m v_m\left(h_m+\frac{v_m^2}{2}\right)\right] + [\![\rho_m]\!]v_m\left([\![h_m]\!]+\frac{v_m^2}{2}\right)\cdot n\,\delta(z-z_d)=\rho_m v_m g\sin\theta-\frac{Q}{\pi r_i^2} \tag{4.9}$$

where δ is the Dirac delta function, z_d is the coordinate of the interface between CO_2 and air, n is the unit normal vector (here equal to ±1), r_i is the inner radius of the wellbore, ρ_m is the mixture mass density, v_m is the mixture velocity, p is the pressure, f is the wall friction coefficient, g is the gravitational constant, θ is the inclination angle of the well, h_m is the specific enthalpy of the mixture, Q is the heat exchange between the well and its surrounding formation, and γ describes the slip between phases.

4.3.2 Numerical discretization

We adopt the velocity – pressure – density formulation. Following Eq.(3.1), the velocity and pressure are continuous at the interface between CO_2 and air, and thus the standard Galerkin finite element method suffices, entailing

$$v_m(z,t)=\mathbf{N}(z)\mathbf{v}_m(t) \tag{4.10}$$

$$p=\mathbf{N}(z)\mathbf{p}(t) \tag{4.11}$$

in which $\mathbf{N}(z)$ is the shape functions vector, $\mathbf{v}_m(t)$ and $\mathbf{p}(t)$ are the nodal values of the mixture velocity and pressure, respectively.

On the other hand, the mass density is discontinuous at the interface between CO_2 and air, and for this, the partition of unity method is utilized, entailing

$$\rho_m(z,t)=\mathbf{N}(z)\boldsymbol{\rho}_m(t)+\mathbf{N}^{eh}(z)\tilde{\boldsymbol{\rho}}_m(t) \tag{4.12}$$

where $\boldsymbol{\rho}_m(t)$ and $\tilde{\boldsymbol{\rho}}_m(t)$ are the conventional and extended nodal values of the mixture density, and $\mathbf{N}^{eh}(z)$ is an enriched shape function.

The level-set method is utilized to trace the moving interface, Γ_d, between the air and the CO_2 zones.

The weighted residual finite element method, together with the mixed discretization scheme highlighted in Eqs. (4.10)-(4.12), are employed to solve Eqs. (3.2), (3.3) and (3.4). A comprehensive description of the discretization procedure and the finite element matrices is given in Arzanfudi and Al-Khoury (2015).

As for the heterogeneous layered domain model, the main advantage of this model is two-fold. First, it is capable of capturing the discontinuity between the initial fluid (air, in this case) and the leaked CO_2 accurately. Second, the discontinuity at the boundary

between the two fluids is modelled regardless of the finite element mesh. It allows the use of a fixed, structured, and relatively coarse mesh.

4.4 Multidomain-staggered coupling scheme

As it can readily be noticed, the mathematical formulations of the fluid flow in the reservoir and the wellbore, given respectively in Sections 4.2 and 4.3, are considerably different. In the reservoir, the flow is relatively slow, dominated by Darcy flow; and in the wellbore, it is relatively fast, dominated by Navier-Stokes flow. The time scales of events in the two domains are significantly different. Accordingly, coupling them in a single domain using standard numerical discretization procedures and time integration schemes can cause numerical oscillations and requires an extensive CPU time and capacity. This may explain why most numerical simulators, which are in use in reservoir engineering, separate the two problems. Here we couple the two domains using a multidomain-staggered technique.

In solid mechanics, the multidomain mixed approximation is mainly conducted via domain decomposition and frame methods. In the first, the domain is divided into several smaller subdomains and linked together using the Lagrange multiplier, penalty method or Nitsche method (Zienkiewicz et al. 2005). They link the subdomains via the traction (the derivative of the primary variable). The difference between the Nitche method and the other two is that it includes the Dirichlet boundary condition between the divided domains. These three techniques necessitate modifying the finite element equations. The Lagrange multiplier adds an extra degree of freedom to the finite element equations, and the penalty method and Nitsche method modify the stiffness matrix by adding a constraint parameter. The frame method, on the other hand, links the subdomains via the displacement field (primary variable) at the boundaries between them. Accordingly, the link is made via standard stiffness matrix formulation, making it more suitable for computer implementation.

In most solid mechanics applications, for which the multidomain technique is adopted, the boundaries between subdomains are homogeneous, and the displacement field is essentially continuous. In the application which we are dealing with, however, there is a Cauchy type boundary condition between the reservoir and the wellbore bottom-hole, and between the wellbore and the rock formations. The first boundary condition describes the hydraulic pressure gradient between the two subdomains, and the second describes the temperature gradient. In CO_2 geosequestration, the hydraulic pressure gradient boundary condition is manifested by the possible leakage of CO_2 from the reservoir to the wellbore bottom. The pressure in both subdomains is a primary state variable. The gradient in pressure at the contact point between the reservoir and the wellbore determines the amount of CO_2 leakage to the wellbore. This sort of interactions makes the reservoir an external source to the wellbore, and the wellbore an external source to the reservoir. No homogeneous boundary conditions exist between them.

To solve this problem, we utilize a combination between a multidomain technique and a staggered technique. We utilize the concept of the frame method to link the two subdomains by their force vectors, and we enforce a Cauchy type constraint on their primary state variables at the boundary between them. The resulting system of equations is solved using a staggered technique and a multiple time-stepping scheme.

The staggered technique is essentially an iterative solution method, which can be employed to solve large, coupled sets of algebraic equations. It is conducted by partitioning the equations describing the coupled state variables, usually displacement and pressure, into two (or more) sets of equations, and relating them via their force vectors. Lewis and Schrefler (1998) gave an elegant overview of the standard staggered technique and its applications. The stability of the staggered algorithm has been thoroughly discussed and addressed for a broad range of coupled field problems in several literatures, including Park et al. (1977), Park (1980), Zienkiewicz et al. (1988) and Farhat et al. (1991).

The main advantage of using the sequential iterative scheme is that it allows for the use of different spatial discretization schemes, and, importantly, different time integration schemes, which efficiently, count for the significant difference in the fluid flow velocities in the two subdomains. This entails that the finite element matrices of the two subdomains are kept intact, and only the force vectors are modified.

4.4.1 Boundary condition between reservoir and wellbore

The coupling between the reservoir and the wellbore occurs at the location where the wellbore bottom hole is connected to the reservoir. We assume that the sealing plug at the wellbore bottom hole might deteriorate with time, giving rise to a leakage path to the wellbore.

The leakage velocity at the wellbore bottom hole can be described as:

Wetting

$$v_w = \frac{k_p k_{rw}}{\mu_w} \frac{1}{L} \left(p_{w/\mathrm{Res}} - p_{\mathrm{Wel}} \right) \tag{4.13}$$

Non-wetting

$$v_n = \frac{k_p k_{rn}}{\mu_n} \frac{1}{L} \left(p_{n/\mathrm{Res}} - p_{\mathrm{Well}} \right) \tag{4.14}$$

where $p_{n/\mathrm{Res}}$ and $p_{w/\mathrm{Res}}$ are the local reservoir CO_2 and water phases pressures, respectively, p_{Wel} is the wellbore bottom hole pressure, k_p is the effective permeability of the defective cement plug, and L is the thickness of the plug.

The proposed model is generic and the wellbore bottom hole pressure, p_{Wel}, might arise from the wetting phase or the non-wetting phase. But to study the worst case scenario that might occur during CO_2 geosequestration, we assume that the wellbore is

initially filled with air and allows only CO_2 to leak. The CO_2 in this case exhibits high advection and can rapidly reach to the top of the wellbore with large quantities.

4.4.2 Spatial Coupling

The physical domain is partitioned into two subdomains: the porous media and the wellbore. The porous media are represented by the reservoir and rock formation, where the Darcy flow is dominant; and the wellbore is represented by the borehole, where the Navier-Stokes flow is dominant. The two subdomains are coupled at the point where the wellbore and the reservoir are connected. Numerically, this implies that the wellbore acts as an external source to the reservoir, and the reservoir acts as an external source to the wellbore.

Recall the finite element system of equations of the multiphase flow in the reservoir from Arzanfudi et al. (2014). It reads:

$$\begin{aligned}\begin{pmatrix}\mathbf{K}_{11} & \mathbf{K}_{12} & \mathbf{K}_{13}\\ \mathbf{K}_{21} & \mathbf{K}_{22} & \mathbf{K}_{23}\\ \mathbf{K}_{31} & \mathbf{K}_{32} & \mathbf{K}_{33}\end{pmatrix}\begin{Bmatrix}\delta\mathbf{p}_w\\ \delta\mathbf{S}_n\\ \delta\tilde{\mathbf{S}}_n\end{Bmatrix}+\begin{pmatrix}0 & \mathbf{C}_{12} & \mathbf{C}_{13}\\ 0 & \mathbf{C}_{22} & \mathbf{C}_{23}\\ 0 & \mathbf{C}_{32} & \mathbf{C}_{32}\end{pmatrix}\begin{Bmatrix}\delta\dot{\mathbf{p}}_w\\ \delta\dot{\mathbf{S}}_n\\ \delta\dot{\tilde{\mathbf{S}}}_n\end{Bmatrix}\\ =\begin{Bmatrix}\mathbf{f}_1\\ \mathbf{f}_2\\ \mathbf{f}_3\end{Bmatrix}-\begin{pmatrix}\mathbf{K}^0_{11} & 0 & 0\\ \mathbf{K}^0_{21} & \mathbf{K}^0_{22} & \mathbf{K}^0_{23}\\ \mathbf{K}^0_{31} & \mathbf{K}^0_{32} & \mathbf{K}^0_{33}\end{pmatrix}\begin{Bmatrix}\mathbf{p}^r_w\\ \mathbf{S}^r_n\\ \tilde{\mathbf{S}}^r_n\end{Bmatrix}-\begin{pmatrix}0 & \mathbf{C}^0_{12} & \mathbf{C}^0_{13}\\ 0 & \mathbf{C}^0_{22} & \mathbf{C}^0_{23}\\ 0 & \mathbf{C}^0_{32} & \mathbf{C}^0_{33}\end{pmatrix}\begin{Bmatrix}\dot{\mathbf{p}}^r_w\\ \dot{\mathbf{S}}^r_n\\ \dot{\tilde{\mathbf{S}}}^r_n\end{Bmatrix}\end{aligned} \tag{4.15}$$

where $\mathbf{p}_w$ is the nodal vector of the wetting phase pressure; $\mathbf{S}_n$ is the nodal vector of the non-wetting phase saturation, which exhibits a jump at the boundary between layers of different physical properties, as outlined in Eq. (2.17); (~) represents the extended degrees of freedom due to the partition of unity, δ is the Newton-Raphson increment; and the superscript $(\cdot)^r$ is the Newton-Raphson iteration number. The first and second matrices on the left-hand side of this equation are the stiffness and the capacitance matrices, respectively. These, together with their corresponding matrices on the right-hand side, are obtained from the mixed PUM-SG discretization, outlined in Section 4.2. Details of the matrices are given in Arzanfudi et al. (2014).

Similarly, recall the finite element system of equations of the multiphase flow in the wellbore from Arzanfudi and Al-Khoury (2015). It reads:

$$\begin{pmatrix}\mathbf{K}_{11} & 0 & \mathbf{K}_{13} & \mathbf{K}_{14}\\ \mathbf{K}_{21} & \mathbf{K}_{22} & \mathbf{K}_{23} & \mathbf{K}_{24}\\ \mathbf{K}_{31} & 0 & \mathbf{K}_{33} & \mathbf{K}_{34}\\ \mathbf{K}_{41} & 0 & \mathbf{K}_{43} & \mathbf{K}_{44}\end{pmatrix}\begin{Bmatrix}\delta\mathbf{v}_m\\ \delta\mathbf{p}\\ \delta\boldsymbol{\rho}_m\\ \delta\tilde{\boldsymbol{\rho}}_m\end{Bmatrix}+\begin{pmatrix}0 & 0 & \mathbf{C}_{13} & \mathbf{C}_{14}\\ \mathbf{C}_{21} & 0 & \mathbf{C}_{23} & \mathbf{C}_{24}\\ \mathbf{C}_{31} & \mathbf{C}_{32} & \mathbf{C}_{33} & \mathbf{C}_{34}\\ \mathbf{C}_{41} & \mathbf{C}_{42} & \mathbf{C}_{43} & \mathbf{C}_{44}\end{pmatrix}\begin{Bmatrix}\delta\dot{\mathbf{v}}_m\\ \delta\dot{\mathbf{p}}\\ \delta\dot{\boldsymbol{\rho}}_m\\ \delta\dot{\tilde{\boldsymbol{\rho}}}_m\end{Bmatrix}$$

$$=\begin{Bmatrix}\mathbf{f}_1\\ \mathbf{f}_2\\ \mathbf{f}_3\\ \mathbf{f}_4\end{Bmatrix}-\begin{pmatrix}\mathbf{K}_{11}^0 & 0 & 0 & 0\\ \mathbf{K}_{21}^0 & \mathbf{K}_{22}^0 & \mathbf{K}_{23}^0 & \mathbf{K}_{24}^0\\ \mathbf{K}_{31}^0 & 0 & \mathbf{K}_{33}^0 & \mathbf{K}_{34}^0\\ \mathbf{K}_{41}^0 & 0 & \mathbf{K}_{43}^0 & \mathbf{K}_{44}^0\end{pmatrix}\begin{Bmatrix}\mathbf{v}_m^r\\ \mathbf{p}^r\\ \boldsymbol{\rho}_m^r\\ \tilde{\boldsymbol{\rho}}_m^r\end{Bmatrix}-\begin{pmatrix}0 & 0 & \mathbf{C}_{13}^0 & \mathbf{C}_{14}^0\\ \mathbf{C}_{21}^0 & 0 & \mathbf{C}_{23}^0 & \mathbf{C}_{24}^0\\ \mathbf{C}_{31}^0 & \mathbf{C}_{32}^0 & \mathbf{C}_{33}^0 & \mathbf{C}_{34}^0\\ \mathbf{C}_{41}^0 & \mathbf{C}_{42}^0 & \mathbf{C}_{43}^0 & \mathbf{C}_{44}^0\end{pmatrix}\begin{Bmatrix}\dot{\mathbf{v}}_m^r\\ \dot{\mathbf{p}}^r\\ \dot{\boldsymbol{\rho}}_m^r\\ \dot{\tilde{\boldsymbol{\rho}}}_m^r\end{Bmatrix} \tag{4.16}$$

where $\mathbf{v}_m$ is the nodal velocity vector of the mixture (CO_2 in our case), $\mathbf{p}$ is the nodal pressure vector of the mixture, and $\boldsymbol{\rho}_m$ is the nodal mass density vector, which exhibits a jump at the boundary between air and CO_2, as outlined in Eq. (4.12). The first and second matrices on the left-hand side of this equation are the stiffness and the capacitance matrices, respectively. These, together with their corresponding matrices on the right-hand side, are obtained from the mixed PUM-LS-SG discretization, outlined in Section 4.3. Details of the matrices are given in Arzanfudi and Al-Khoury (2015).

Coupling these two equations, Eq. (4.15) and (4.16), at their source vectors, and put them in a compact form, they can be written as

$$\mathbf{K}_{\text{Res}}\delta\mathbf{X}_{\text{Res}}+\mathbf{C}_{\text{Res}}\delta\dot{\mathbf{X}}_{\text{Res}}=\mathbf{f}_{\text{Res-Wel}}+\mathbf{f}_{\text{Res}} \tag{4.17}$$

$$\mathbf{K}_{\text{Wel}}\delta\mathbf{Y}_{\text{Wel}}+\mathbf{C}_{\text{Wel}}\delta\dot{\mathbf{Y}}_{\text{Wel}}=\mathbf{f}_{\text{Wel-Res}}+\mathbf{f}_{\text{Wel}} \tag{4.18}$$

in which all matrices and vectors terms are kept intact, except that the right-hand side of the equations is augmented with $\mathbf{f}_{\text{Res-Wel}}$ and $\mathbf{f}_{\text{Wel-Res}}$' which are the coupling source vectors that include the boundary forces at the contact node/surface between the wellbore and the reservoir. They are defined as

$$\mathbf{f}_{\text{Res-Wel}}=\begin{Bmatrix}\int_{\Gamma_q^{\text{Coupl}}}\mathbf{N}^T v_w d\Gamma\\ \int_{\Gamma_q^{\text{Coupl}}}\mathbf{N}^T v_n d\Gamma\\ \int_{\Gamma_q^{\text{Coupl}}}\left(\mathbf{N}^{eh}\right)^T v_n d\Gamma\end{Bmatrix} \tag{4.19}$$

and

$$\mathbf{f}_{\text{Wel-Res}} = \begin{Bmatrix} -\int_{\Gamma_q^{\text{Coupl}}} \mathbf{N}^T \rho_{n/\text{Res}} v_n d\Gamma \\ -\int_{\Gamma_q^{\text{Coupl}}} \mathbf{N}^T \rho_{n/\text{Res}} {v_n}^2 d\Gamma \\ -\int_{\Gamma_q^{\text{Coupl}}} \mathbf{N}^T \rho_{n/\text{Res}} v_n \left(h_{n/\text{Res}} + \frac{1}{2}\left(v_n\right)^2 \right) d\Gamma \\ -\int_{\Gamma_q^{\text{Coupl}}} \left(\mathbf{N}^{eh}\right)^T \rho_{n/\text{Res}} v_n \left(h_{n/\text{Res}} + \frac{1}{2}\left(v_n\right)^2 \right) d\Gamma \end{Bmatrix} \tag{4.20}$$

where Γ_q^{Coupl} is the boundary between the reservoir and the wellbore, v_w and v_n are the velocities of leaking water and CO_2, given in Eqs. (4.13) and (4.14), and $\rho_{n/\text{Res}}$ and $h_{n/\text{Res}}$ are the density and specific enthalpy of CO_2 at the reservoir, respectively. The first term in the $\mathbf{f}_{\text{Res-Wel}}$ vector belongs to the conservation of mass of the wetting phase, the second belongs to the conservation of mass of the non-wetting phase and the third is the enhanced part of the non-wetting phase, obtained by applying the partition of unity method on the saturation field. Similarly, the first term in the $\mathbf{f}_{\text{Wel-Res}}$ vector belongs to the conservation of mass of the non-wetting phase, the second belongs to the conservation of momentum, and the third and fourth belong to the conservation of energy obtained by applying the partition of unity method.

At the element level, and as the reservoir upper boundary with the cap layer is embedded inside the finite elements, the contact point between the wellbore bottom-hole and the reservoir does not need to conform to a node. Rather on a point inside the element, shown in Fig. 4.2. Using standard finite element procedure, the flux in this point is distributed at the element nodes. For a 4-node 2D element, the integral over the element length in Eq. (4.19) is distributed over the four nodes, and the integral in Eq. (4.20) reduces to a point, such that

$$\mathbf{f}_{\text{Res-Wel}} = \begin{Bmatrix} \sum_{i=1}^{4} N_{\text{R}i} v_w \\ \sum_{i=1}^{4} N_{\text{R}i} v_n \\ \sum_{i=1}^{4} N_{\text{R}i}^{eh} v_n \end{Bmatrix} \tag{4.21}$$

and

$$\mathbf{f}_{\text{Wel-Res}} = \begin{Bmatrix} -N_{\text{W1}}\rho_{n/\text{Res}}v_n \\ -N_{\text{W1}}\rho_{n/\text{Res}}{v_n}^2 \\ -N_{\text{W1}}\rho_{n/\text{Res}}v_n\left(h_{n/\text{Res}} + \frac{1}{2}{v_n}^2\right) \\ -N^{eh}_{\text{W1}}\rho_{n/\text{Res}}v_n\left(h_{n/\text{Res}} + \frac{1}{2}{v_n}^2\right) \end{Bmatrix} \tag{4.22}$$

in which the subscript W1 represents the 1D wellbore bottom-hole node, and R1-R4 are the 2D four nodes of the element where the coupling occurs (see Fig. 4.2). Consequently, the coupling is carried out without conforming with the mesh.

The coupling element shown in Fig. 4.2, has two overlapping functions: partitioning the heterogeneous layered domain, via the partition of unity method; and coupling the reservoir and wellbore subdomains, via the multidomain technique.

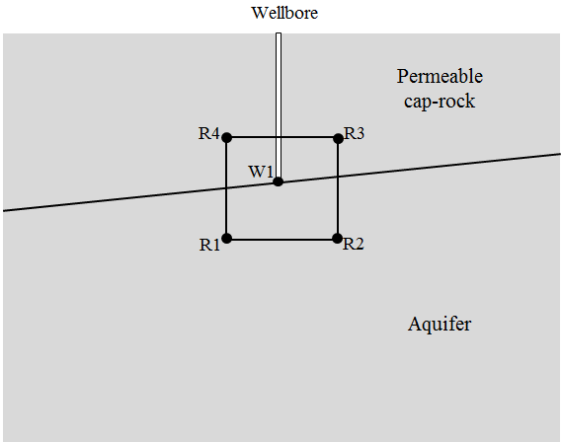

Fig. 4.2 Coupling element and nodes.

As described above, the two subdomains are coupled via their force vectors, without the use of Lagrange multiplier or penalty methods. This entails that no extra degree of freedom or other constraint parameters are added to the finite element stiffness matrix. However, in order to enforce the constraints at the boundaries between the subdomains, a staggered solution scheme is employed.

In the staggered scheme, an iterative solution between the reservoir and the wellbore is conducted sequentially, by solving the two systems of equations independently, but updating their force vectors, Eqs. (4.21) and (4.22). The iteration continues until fulfilling the coupling condition:

$$v_n - \frac{k_p k_{rn}}{\mu_n}\frac{1}{L}\left(p_{n/\text{Res}} - p_{\text{Wel}}\right) < \varepsilon \tag{4.23}$$

where ε is an allowable error.

Coding the staggered algorithm requires two nesting loops: an outer loop, to establish the coupling condition between the reservoir model and the wellbore model, Eq. (4.23); and an inner loop, for solving the reservoir and wellbore sets of equations. The simple Picard iterative scheme is sufficient to solve the resulting nonlinear scheme.

4.4.3 Temporal coupling

Sequestered CO_2 in saline formations is likely designed to remain in a supercritical state within the reservoir. Upon its leakage into the wellbore, the CO_2 is expected to undergo phase change from the supercritical state to the gaseous state, followed by a sudden expansion due to the relatively low pressure inside the wellbore. This results in a flow regime in the wellbore that is much faster than that inside the reservoir. This entails having a significantly different time scale in the system: one in the order of months or years and another in the order of minutes or hours.

This considerable contrast in the time scale necessitates the use of different time discretization schemes. We adopt a nested multiple time integration scheme, illustrated schematically in Fig. 4.3. Fluid flow in the wellbore is discretized using an adaptive time step size, Δt_{Wel}, which is considerably smaller than that used in the reservoir, Δt_{Res}. Exchange of data between the two subsystems takes place at the end of the reservoir time step.

We utilize the θ-finite difference time integration scheme to discretize Eqs. (4.17) and (4.18). Applying this scheme, for instance, on Eq. (4.17), yields:

$$\begin{aligned}\left(\mathbf{C}_{\text{Res}}+\theta\Delta t\mathbf{K}_{\text{Res}}\right)\delta\mathbf{X}_{\text{Res}}\big|_{n+1}&=\left(\mathbf{C}_{\text{Res}}-(1-\theta)\Delta t\mathbf{K}_{\text{Res}}\right)\delta\mathbf{X}_{\text{Res}}\big|_{n}\\&+\theta\Delta t\,\mathbf{f}_{\text{Res-Wel}}\big|_{n+1}+(1-\theta)\Delta t\,\mathbf{f}_{\text{Res-Wel}}\big|_{n}+\theta\Delta t\,\mathbf{f}_{\text{Res}}\big|_{n+1}+(1-\theta)\Delta t\,\mathbf{f}_{\text{Res}}\big|_{n}\end{aligned} \tag{4.24}$$

in which n is a time step, and $0\le\theta\le1$ is the time integration parameter. The equation is solved using a standard direct solver.

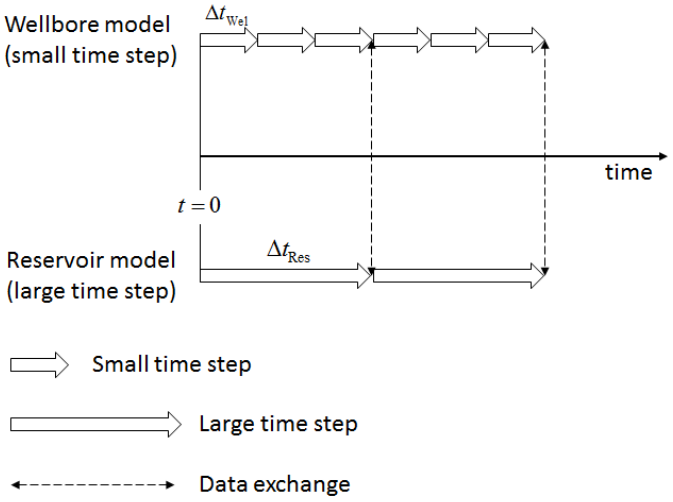

Fig. 4.3 Multiple time-stepping scheme.

Coding this multiple time-stepping scheme within the staggered solution requires an extra nested loop to take into account the small time stepping associated with the fluid flow in the wellbore. The coding algorithm is as follows:

0. Initialize p_{Wel} (wellbore bottom-hole pressure) and $p_{n/\mathrm{Res}}$ (local CO_2 phase pressure at reservoir)
1. Do loop over i (reservoir time steps Δt_{Res})
2. Do loop over v_n
3. Initialize v_n using Eq. (4.14)
4. Solve reservoir model, Eq. (4.17)
5. Calculate $p_{n/\mathrm{Res}}$
6. Do loop over j (wellbore time steps Δt_{Wel})
7. Solve wellbore model, Eq. (4.18)
8. End Do loop over j.
9. Calculate p_{Wel}
10. Calculate the wellbore leakage residual error, Eq. (4.23). If the conditions in Eq. (4.23) does not hold, modify v_n using Eq. (4.14), and go back to step 4. Otherwise exit the loop.
11. End Do loop over v_n.
12. Update p_{Wel} and $p_{n/\mathrm{Res}}$
13. End Do loop over i.

4.5 Numerical example and validation

We present a numerical example highlighting the computational capabilities of the proposed model to simulate possible leakage of sequestered CO_2 via the upper boundary of a reservoir and through an abandoned wellbore. Three cases describing different leakage scenarios are discussed: coupled leakage, leakage via the wellbore only, and leakage via the reservoir upper boundary only. A comparison between numerical results obtained from the proposed model and those from the Eclipse simulator (Schlumberger 2015) is also given.

4.5.1 Coupled leakage

A CO_2 sequestration reservoir undergoing a possible leakage through both an upper layer and a wellbore is assumed. The conceptual geometry is shown in Fig. 4.4. Supercritical CO_2 is injected at the lower left corner of the aquifer. On the top of the aquifer, a permeable upper layer exists, with a hydraulic conductivity smaller than that of the aquifer. A leaky wellbore is intersecting the aquifer at 90 m from the injection well. The properties of the aquifer and the permeable upper layer, as well as the fluid properties are given in Table 4.1. The layers are initially saturated with water. The properties of the wellbore and its surrounding formation are presented in

Table 4.2. The wellbore is initially filled with air, connected to the atmosphere at the wellbore head, and in thermodynamic equilibrium with the surrounding formation layers. The permeability of the leaky cement plug is assumed $k_p = 4 \times 10^{-13}\mathrm{m}^2$. The CO_2 is injected with a rate of 1.4 kg/s.

The relatively high permeability for the upper (cap) layer and the cement plug are chosen to emphasize the leakage mechanisms, which constitute the core subject of the proposed model. They represent the worst case scenarios that might occur in practice. The cap layers might be fissured due to natural causes, such as earthquakes or chemical reactions between CO_2 and the cap rocks. The same is valid for the wellbore sealing plug.

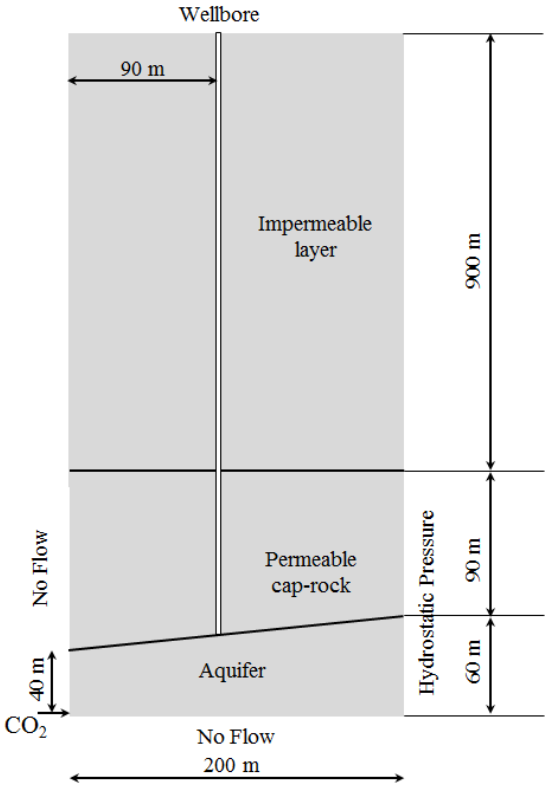

Fig. 4.4 Conceptual geometry.

Table 4.1 Fluid and domain properties.

Fluid properties inside the reservoir	**Water**	**CO_2**
Density [kg/m3]	1045	479
Viscosity [Pa.s]	2.535×10^{-4}	3.950×10^{-5}
Porous media properties	**Aquifer (high permeable)**	**Upper layer (low permeable)**
Permeability [m2]	2.0×10^{-12}	7.5×10^{-13}
Porosity	0.15	0.1
Entry pressure (Brooks-Corey) [kPa]	225	260
$\hat{\theta}$ (Brooks-Corey)	4.0	2.0
Water residual saturation	0.20	0.20
CO_2 residual saturation	0.00	0.00

Table 4.2 Wellbore and formation data.

Well Data	
Well inner radius [m]	0.1
Thickness of plug [m]	1
Heat transfer coefficient at the wellbore-formation interface (U) $[\mathrm{W\,m^{-1}\,K^{-1}}]$	1.5
Roughness of the wellbore [-]	5.0×10^{-6}
Formation Data	
Surface temperature [K]	275.15
Geothermal Gradient [K/m]	0.058

The computational domain is illustrated in Fig. 4.5. The overburden top layer is not modeled; instead, the upper layer is subjected to a pressure boundary condition equivalent to the pressure exerted by the overburden layer. Four mesh sizes were utilized: 80, 204, 792 and 999 four-node elements. The wellbore is modeled using only four, two-node 1D elements. The use of this highly coarse mesh to model the fluid flow in the wellbore is only possible due to the utilization of the mixed discretization scheme to solve the wellbore governing equations (Arzanfudi and Al-Khoury 2015).

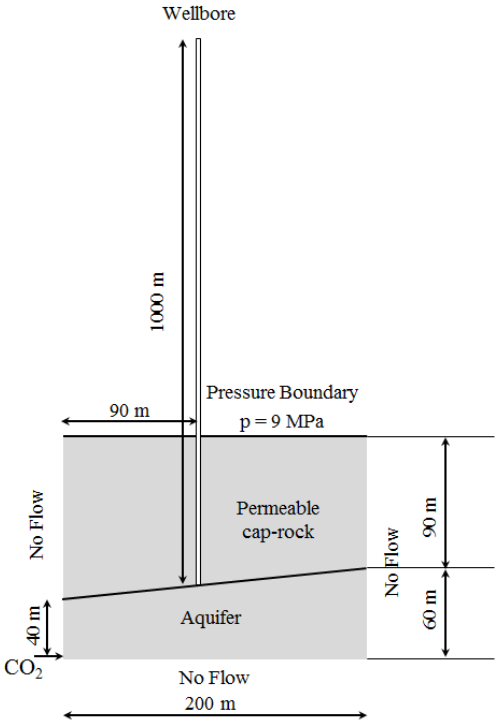

Fig. 4.5 Computational domain.

Fig. 4.6 shows the computed distribution of mass density, pressure, temperature and velocity along the wellbore. Despite that a very coarse mesh is utilized for the wellbore, the discontinuity in density and temperature fields between the air and the CO_2 is accurately captured.

Three important phenomena can be observed:

1. Once entering the wellbore, the CO_2 density reduces significantly, as compared to that in the reservoir,
2. with time, the CO_2 density starts to increase, and also
3. along the wellbore, it decreases.

Explaining these phenomena requires a closer examination of the pressure and temperature behavior along the wellbore. CO_2, upon entering the wellbore, expands and exhibits a significant reduction of pressure due to the Joule-Thomson effect (Green 2008). This results into a significant reduction of density. With more leakage, the CO_2 accumulates at the bottom of the wellbore, leading to an increase in pressure. This gives rise to an increase in density. Along the wellbore, and due to the hydrostatic pressure, there is a reduction of pressure, accompanied by a reduction of density.

The same happens to the temperature. Upon the expansion of CO_2, the temperature drops significantly. But after that, and due to the second Joule-Thomson mechanism,

there will be an increase in the kinetic energy of CO_2, which gives rise to an increase of temperature. Together with the thermal interaction with the neighboring formation, the temperature, first increases along the wellbore, and then follows a reduction trend similar to the geothermal gradient.

Regarding the velocity, at the beginning the velocity is relatively high, but due to the increase of pressure and density with time, the velocity decreases. However, along the wellbore, and due to the decrease of pressure and density, the velocity increases.

The CO_2 saturation fields in the reservoir and the upper layer are shown in Fig. 4.7 for different mesh sizes, at t = 1 day. The CO_2 breakthrough times, i.e. the times when the CO_2 starts to leak through the upper layer and through the wellbore, corresponding to the different mesh sizes, are given in Fig. 4.8. The amount of stored CO_2, as well as the amount of leaked CO_2 from the upper layer and the wellbore, at t = 1 day, are shown in Fig. 4.9. The figures show that the breakthrough times as well as the stored and leaked values computed from the 204 elements mesh give very close results to those from the finer meshes. However, results obtained from the 80 elements mesh are reasonably accurate. This indicates that the proposed model is effectively mesh-independent, and analyses using coarse meshes are feasible.

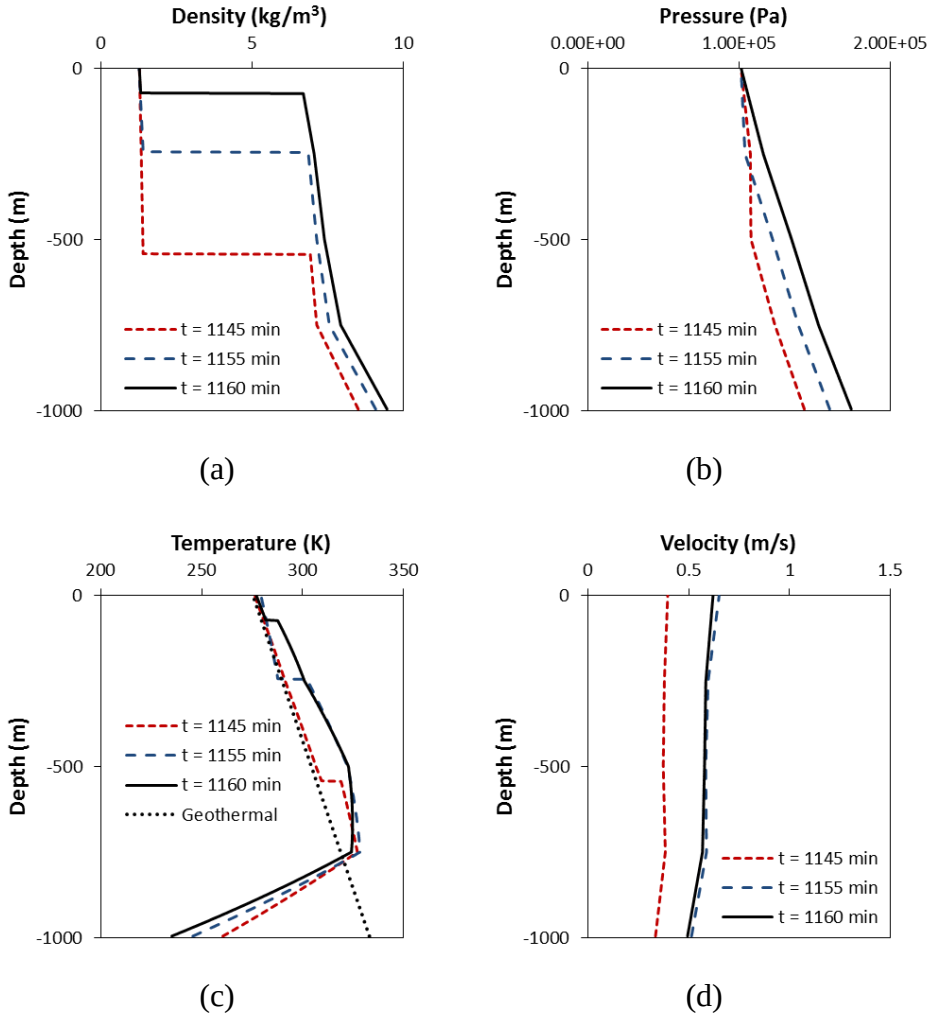

Fig. 4.6 Field variables in the wellbore for the coupled leakage problem: (a) density, (b) pressure, (c) temperature, and (d) velocity.

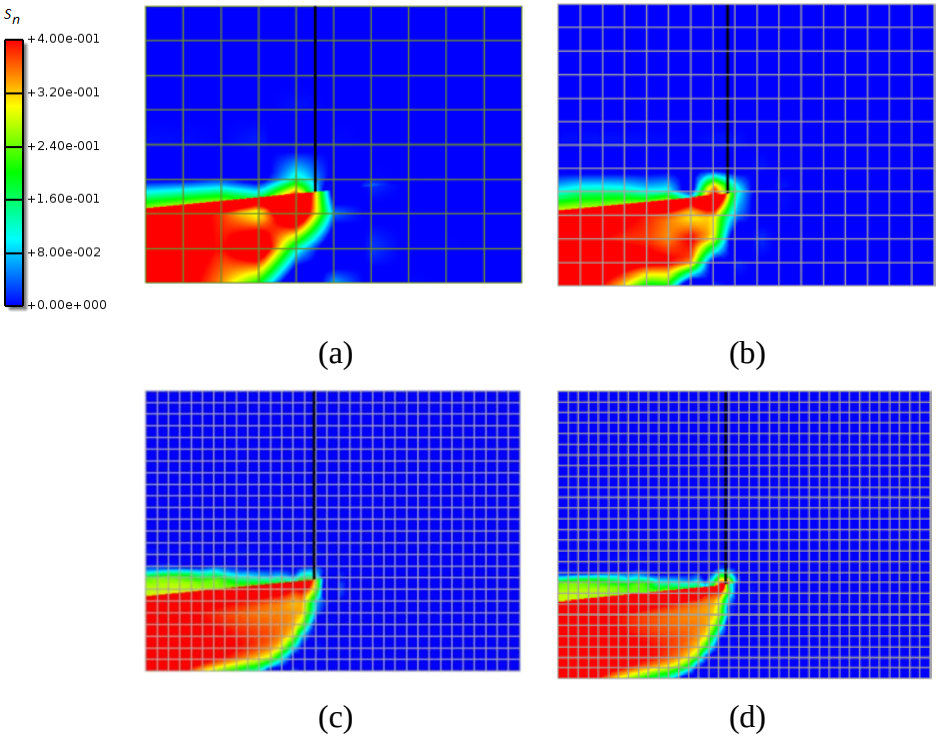

Fig. 4.7 CO_2 saturation in the reservoir for the coupled leakage problem: (a) 80 elements, (b) 204 elements, (c) 792 elements and (d) 999 elements.

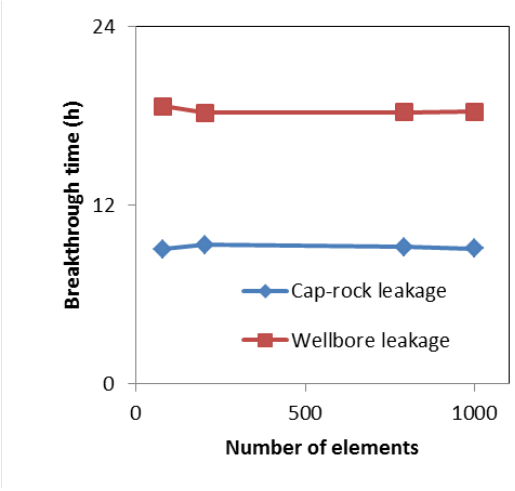

Fig. 4.8 Breakthrough times for the CO_2 leakage start-up through the upper layer and wellbore.

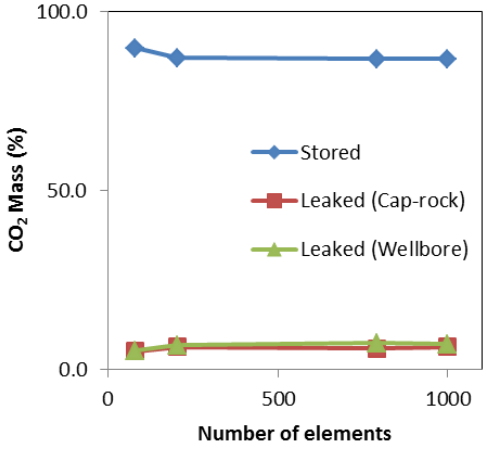

Fig. 4.9 Amount of leaked and stored CO_2 through the cap-layer and the leaky wellbore at time t = 1 day.

4.5.2 No layer leakage

The same problem is repeated, except that the entry pressure of the upper layer does not allow the CO_2 to leak from the aquifer, and the leakage can only occur through the wellbore. The same mesh sizes as for the previous example are utilized.

Fig. 4.10 shows the CO_2 saturation field in the reservoir for the different mesh sizes, at t = 1 day. The amount of stored and leaked CO_2 at t = 1 day are given in Fig. 4.11. The results again show that the stored and leaked values obtained from the analyses with the coarse meshes are close to those obtained from the finer meshes.

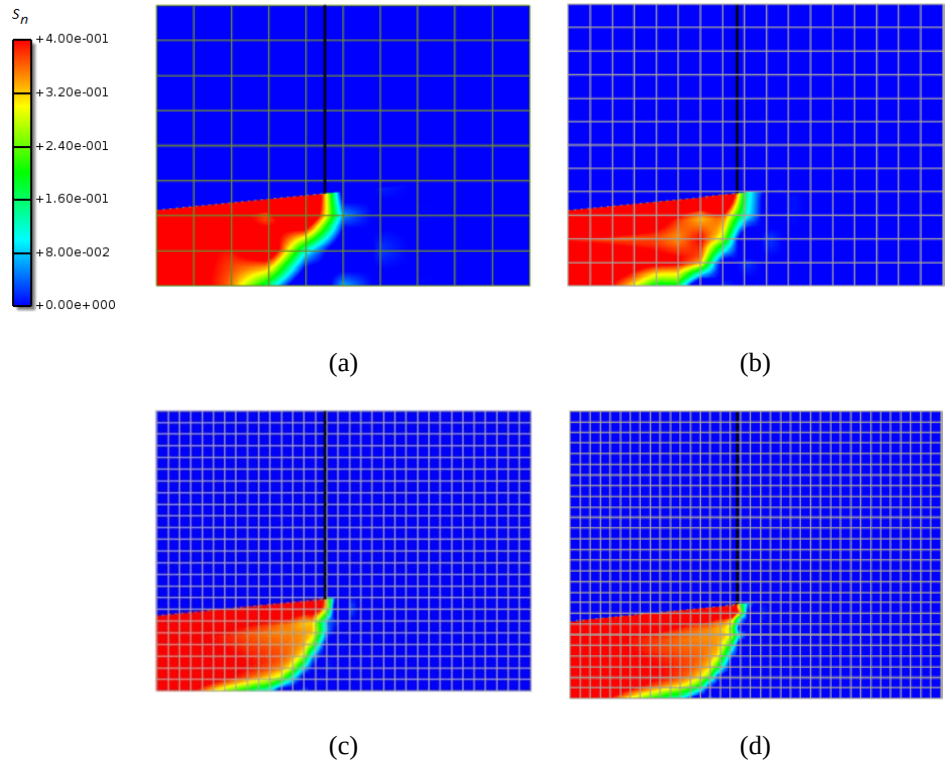

Fig. 4.10 CO_2 saturation in the reservoir for the "no layer leakage" problem: (a) 80 elements, (b) 204 elements, (c) 792 elements and (d) 999 elements.

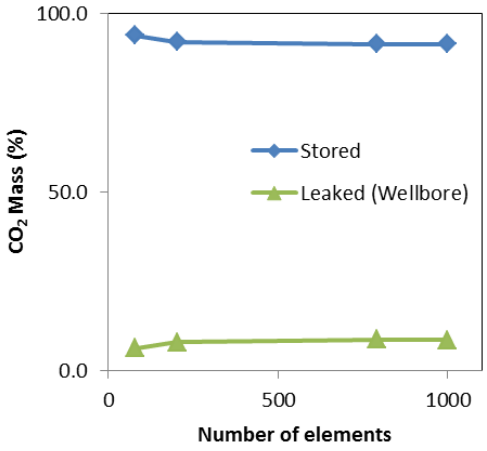

Fig. 4.11 Amount of leaked and stored CO_2 for the "no layer leakage" problem at time t = 1 day.

4.5.3 No wellbore leakage

A similar case is conducted, but now the leakage through the wellbore is blocked. The same mesh sizes as in the previous example are utilized.

Fig. 4.12 shows the CO_2 saturation field in the reservoir and the upper layer, for the different mesh sizes, at t = 1 day. The amount of stored and leaked CO_2 at t = 1 day are given in Fig. 4.13. The results again show that the stored and leaked values obtained from the coarse meshes are close to those obtained from the finer ones.

An interesting finding from these analyses can be deduced from the computed values of the leaked CO_2, as shown in Fig. 4.13. The amount of leakage to the upper layer occurring in the no-wellbore leakage case is more than the total amount of leakage occurring in the coupled leakage case, by a factor of 2. This can be attributed to the fact that the existence of a leaky wellbore leads to a significant change in the pressure and fluid distribution in the reservoir that eventually affect the mechanisms leading to the leakage through the upper layer. Nevertheless, leakage through the wellbore comes with a greater risk because it can rapidly reach to the surface.

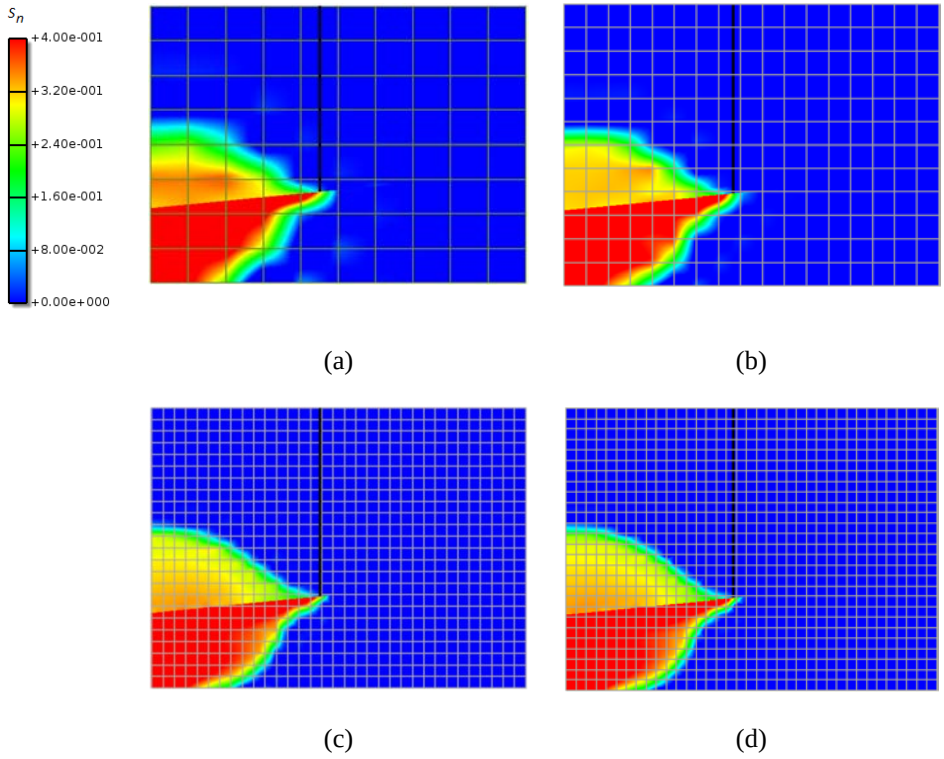

Fig. 4.12 CO_2 saturation in the reservoir for the "no wellbore leakage" problem: (a) 80 elements, (b) 204 elements, (c) 792 elements and (d) 999 elements.

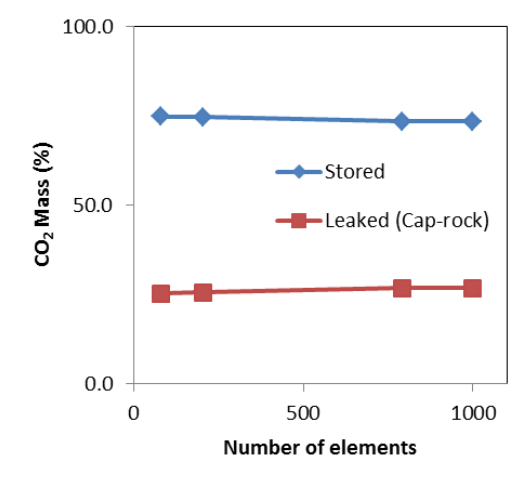

Fig. 4.13 Amount of leaked and stored CO_2 for the "no wellbore leakage" problem at time t=1 day.

4.5.4 Model validation

It is difficult to find in literature benchmark numerical examples including all features of the proposed model. As a consequence, we conducted a limited numerical validation comparing common computational aspects with Eclipse**,** a commercial simulator based on the finite difference method (Schlumberger 2015). This simulator is commonly utilized for the analysis of compressible, multiphase flow in geological formations.

We compared the computational results of the three leakage scenarios, given above, with those obtained from Eclipse. However, the comparison can only be applied to the multiphase flow in the heterogeneous porous formation. Two aspects are not possible to be compared: (i) fluid flow in the wellbore; Eclipse does not explicitly incorporate the transient fluid flow in wellbores, and (ii) compressibility in the reservoir; the proposed model assumes incompressible flow in the reservoir. To tackle these two limitations in both simulators, the numerical example is adjusted such that we make use of common features. The leakage via the wellbore in Eclipse is prescribed manually. Leakage flow rates computed by the proposed model at different time steps are imposed as a production history in Eclipse at the cell where the wellbore is connected to the reservoir. The reservoir in Eclipse is made nearly incompressible by making the variation of fluid density and viscosity, together with the formation volume factor, with pressure small.

A black oil two-phase flow model, built-in in Eclipse, is utilized for this purpose. The geometry of the reservoir and the surrounding formation, together with the initial and boundary conditions, as given in Fig. 4.5, are employed. The material properties and the Brook-Corey parameters are as given in Table 1.

The geometry is discretized in Eclipse using 30,000 finite difference grid cells, and in the proposed model using 999, four-node rectangular finite elements for the porous formation, and 4, two-node linear finite elements for the wellbore.

Fig. 4.14 shows the computational results of the three leakage scenarios computed by both simulators. The figure shows that there is a close match between the two results. The slight difference in the front shape, however, is due to the difference in the compressibility of the materials.

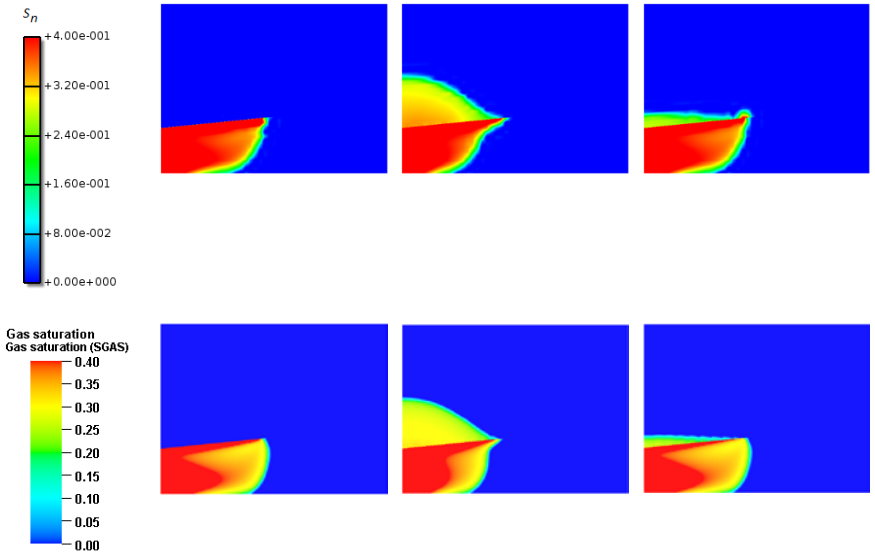

Fig. 4.14 Comparison of computed results obtained from the proposed model (top) and Eclipse (bottom): (a) no cap-layer leakage, (b) no wellbore leakage, and (c) coupled leakage

4.6 Conclusions

In this paper we introduce a coupling technique suitable for integrating multiphase flow in a porous medium, dominated by the Darcy laminar flow; with multiphase flow in a wellbore, dominated by the Navier Stokes viscous, compressible flow. The proposed technique is tailored to simulate sequestered CO_2 leakage mechanisms, which might occur via abandoned wellbores and underground formations. Leakage of CO_2 to the ground surface or upper layers containing ground water is hazardous and considered as one of the major concerns of applying CO_2 sequestration technology.

As the fluid flow in the porous medium is significantly different than that in the wellbore, it is essential to design a coupling scheme, which is capable of efficiently and

robustly solving the distinct mathematical formulations of the two subdomains. Here, the two subdomains are spatially and temporally coupled using a multidomain-staggered technique.

In the proposed multidomain-staggered technique, the multidomain technique is utilized to uncouple and re-couple the physical system, and the staggered technique is utilized to uncouple and solve the system of equations. The physical domain is divided into two subdomains representing the reservoir (and other rock formations), and the wellbore. At the contact points or surfaces between the two subdomains, constraint conditions are enforced. The governing equations describing the two subdomains are formulated separately, but augmented with the constraint conditions at the boundaries, where the two systems physically interact with each other. The use of the staggered technique alleviates the need for adding a Lagrange multiplier or other constraint parameters into the governing equations, normally needed in the multidomain discretization technique. Rather, the two subdomains are linked via their force (source) vector and, the boundary constraints at the contact surfaces/points are enforced iteratively. This eventually allows for the use of different time integration schemes, which count for the slow fluid motion in the porous domain and the fast fluid motion in the wellbore.

In contrast to the standard multidomain techniques, the proposed multidomain-staggered technique is essential for multiphase flow problems exhibiting significant differences in their fluid flow velocities for three main reasons:

1. It allows for the use of different mathematical and numerical formulations for the two subdomains, fostering innovative discretization schemes that can save significant computational capacity and CPU time. The computational efficiency of the proposed model is manifested by the use of structured and fixed meshes, and the gain of geometry- and effectively mesh-independent results.

2. The two subdomains are spatially coupled via their force (source) vectors, keeping their finite element matrices intact. This makes the computer implementation straightforward.

3. The two subdomains are temporally coupled using a multiple time-stepping scheme, which takes into consideration the significant difference in the fluid flow velocities. The time step of the wellbore is made small and nested in that of the reservoir.

5

CO_2 Leakage via Fracturing Porous Media

This chapter is based on Arzanfudi and Al-Khoury (2016), a paper submitted for publication.

In this chapter we introduce a fully coupled thermo-hydrodynamic-mechanical computational model for multiphase flow in a deformable porous solid, exhibiting crack propagation due to fluid dynamics. The geometry is described by a matrix domain, a fracture domain, and a matrix-fracture domain. The fluid flow in the matrix domain is governed by Darcy's law, and that in the crack is governed by the Navier-Stokes equations. At the matrix-fracture domain, the fluid flow is governed by a leakage term derived from Darcy's law. Upon crack propagation, the conservation of mass and energy of the crack fluid is constrained by the isentropic process. We utilize the representative elementary volume averaging theory to formulate the mathematical model of the porous matrix, and the drift-flux model to formulate the fluid dynamics in the fracture. The numerical solution is conducted using a mixed finite element discretization scheme. The standard Galerkin finite element method is utilized to discretize the diffusive dominant field equations, and the extended finite element method is utilized to discretize the crack propagation, and the fluid leakage at the boundaries between layers of different physical properties. A numerical example is given to demonstrate the computational capability of the model. It shows that the model, despite the relatively large number of degrees of freedom of different physical nature per node, is computationally efficient, and geometry- and effectively mesh-independent.

5.1 Introduction

Geoenvironmental applications involving multiphase flow in deformable porous media, undergoing fracturing and fluid flow inside the fractures, are abundant. Oil and gas extraction, geothermal energy mining, hydraulic fracturing, and CO_2 geosequestration are only few examples of these applications. Yet, despite the importance of these applications for the environment and economy, relatively few computational models are designed to simulate multiphase flow in fracturing porous media. Developing computational models for multiphase flow in such media is challenging because they exhibit significantly different fluid characteristics in the solid matrix and in the fractures, and have state variables of significantly different physical nature.

To circumvent the contrast in fluid flow characteristics in the matrix and in the fracture, the double porosity/permeability model (Barenblatt et al. 1960) has been introduced to simulate fluid flow in fractured porous media domains. This model assumes geometrical overlap between a continuum porous matrix and a continuum fracture zone, and allow for leakage to occur between them. The fracture zone is assumed to exist *a priori*; allowing no crack propagation. The double porosity/permeability model is utilized by, among others, Chen (1989), Zimmerman et al. (1993), Ghafouri and Lewis (Ghafouri and Lewis 1996; Lewis and Ghafouri 1997), Vogel et al. (2000), and Lewis and Pao (2002) for modeling single- and multiphase flow in rigid and deformable media. These models are valid for a wide range of engineering applications, but fall short in describing applications, in which the discrete crack behavior is important. Al-Khoury and Sluys (2007) extended the double porosity model to include the possible crack propagation in fully saturated porous media.

There are, however, several models explicitly treating the fluid flow inside the discrete fractures. Most of these models deal with single phase flow. They assume that fluid flow inside the fracture is governed by the Reynolds lubrication equation, which is a derivation of the Stokes equation and the Poiseuille law. The local fracture transmissivity is made directly proportional to the cube of local fracture aperture, known as the cubic law. Such formulations assume that the fluid is Newtonian and incompressible, with constant mass density and viscosity through film, and the flow is laminar, with negligible inertia and body forces, and exhibits a constant pressure through film. Schrefler et al. (2006), for instance, have utilized the Poiseuille law together with the cubic law to model the fluid flow in fractures. De Borst et al. (2007) have utilized the Stokes equation to describe fluid flow in a fluid-saturated and progressively fracturing porous medium. Kraaijeveld et al. (2013) have utilized the chemical potential driven Couette flow, which also relates the fracture fluid flow to the fracture width and pressure, to model the fluid flow in a fracturing, ionized porous medium.

A number of other models have been introduced dealing with multiphase flow in deformable and fracturing porous media, and including the fluid flow in fractures. Mohammadnejad and Khoei (2013), for instance, adopted a multiphase Darcy flow, with smeared fracture properties, to model fluid flow through a propagating crack. A noteworthy recently presented model is due to Salimzadeh and Khalili (2015), who introduced a multiphase hydro-mechanical model for hydraulic fracturing in porous media. The fluid flow in fracture is modeled using a mass balance equation for a slightly compressible Newtonian fluid, exhibiting leak-off at the boundary between the fracture and the porous matrix. They utilized the extended finite element method to discretize the crack propagation.

Despite the elegance of these models, which incorporate the Reynolds-like equations for formulating the fluid flow in fractures, the assumptions of laminar and incompressible fluid flow, together with negligible inertia and buoyancy forces, are not, in many applications, accurate. Studies conducted by Mourzenko et al. (1995), Brown et al. (1995), and Nicholl et al. (1999) have shown that fluid flow simulations based on the Reynolds equation result to flow rates, which can be several times greater than those obtained by the fundamental Navier-Stokes equations. Al-Yaarubi et al. (2004) compared results of fluid flow in a fracture obtained from the Reynolds equation to these obtained from the Navier-Stokes equations. They found that the Navier-Stokes simulations predicted transmissivities that are, depending on the relative roughness, 10%-50% lower than these predicted by the Reynolds equation. This range of discrepancy was earlier found by Yeo and Ge (2005) and by Nicholl et al. (1999), who compared the Reynolds equation results with experimental results. Accordingly, Al-Yaarubi et al. (2004) conclusively asserted that this would entail that the Navier-Stokes equations, with no-slip boundary conditions, does constitute the correct mathematical model for single phase flow through a rock fracture.

In this work, we adopt the Navier-Stokes equations in the form of the drift flux model to describe fluid flow in fractures. We introduce a coupled thermo-hydrodynamic-mechanical computational model for multiphase flow in a deformable porous solid, exhibiting crack propagation due to fluid dynamics. The fracture fluid is compressible and exhibits phase change, buoyancy, slip between phases and convective-conductive heat transfer. The model is advanced in mainly two aspects: (i) the mathematical formulation is highly descriptive of the physics, and (ii) the numerical solution is computationally efficient and geometry- and effectively mesh-independent. Description of the model is given in the following section. The model is designed to be applicable to a wide range of applications, but here, the focus is placed on modeling the possible leakage of sequestered CO_2 via the fractures. CO_2 geosequestration is a technology designed to mitigate the amount of CO_2 emitted into the earth atmosphere. Selection of an appropriate geological formation and a proper design of a CO_2 sequestration plant require a good estimation of the likely occurrence of leakage. CO_2

leakage to the ground surface or upper layers containing underground water is hazardous and is considered as one of the major concerns of applying this technology.

5.2 Model description

Deriving an accurate, geometry- and mesh-independent, and computationally efficient transient model for thermo-hydrodynamic-mechanical behavior of a multiphase domain, exhibiting deformation and crack propagation requires a well-designed conceptual model, a descriptive mathematical formulation and an innovative numerical method.

The conceptual model distinguishes three domains: a matrix domain, a fracture domain, and a matrix-fracture domain. The matrix domain comprises a porous solid phase and two fluid phases: a wetting phase and a non-wetting phase. The wetting phase represents formation brine water, and the non-wetting phase represents sequestered CO_2. The fluid phases are compressible and their mass density and dynamic viscosity may change, depending on pressure and temperature in the reservoir. Leakage of the non-wetting phase can occur due to saturation field discontinuity between layers of different hydraulic properties. The solid phase is deformable, fracturing linear elastic. It exhibits deformation due to the hydraulic pressure, which is exerted by the injection of the non-wetting phase. The fracture domain comprises a discrete crack, in which a non-wetting phase runs through. The fracture fluid is compressible and exhibits phase change, buoyancy, slip between phases and heat transfer. The crack propagates due to the fluid dynamic forces exerted by the fracture fluid. The matrix domain and the fracture domain interact with each other via leakage, which might occur via the crack aperture and the fracture-matrix boundaries.

The mathematical formulation takes into consideration all important physical phenomena and processes occurring in the porous matrix and the fracture. Solid and fluids compressibility, buoyancy, phase change, thermal interactions, wall friction, slip between phases are considered. The physical processes in the porous matrix are governed by the conservation laws of transport of mass, momentum and energy, within the framework of Darcy flow poromechanics. We utilize the representative elementary volume (REV) averaging theory (Lewis and Schrefler 1998) to formulate the mathematical model of the porous matrix. The physical processes in the fracture domain, on the other hand, are governed by the conservation laws of transport of mass, momentum and energy, within the framework of the Navier-Stokes fluid flow. We utilize the drift-flux model (Ishii and Hibiki 2006; Pan and Oldenburg 2014; Wallis 1969; Zuber and Findlay 1965) to formulate the mathematical model of the fluid flow in the fracture domain. This model adopts an area-averaged approach, where details of the local behavior of the involved phases are averaged over the cross-sectional area of the crack (Faghri and Zhang 2006). Important aspects of fluid dynamics such as inertia force, buoyancy, wall friction, drift velocity, and flow profile are considered in the drift-flux model. The interaction between the matrix domain and the fracture domain is described using a leakage term, which is a function of pressure, matrix permeability and

fluid density and viscosity. Upon crack propagation, the isentropic expansion process (Turns 2006) is constrained to conserve the mass and energy in the newly formed crack volume.

The numerical method incorporates a mixed finite element discretization scheme. In this scheme, state variables exhibiting different physical nature are treated using different numerical discretization techniques. The standard Galerkin finite element method (SG) and the partition of unity finite element method (PUM) are integrated in a single numerical scheme. SG is utilized to discretize the diffusive dominant field equations, and PUM, within the framework of the extended finite element method (XFEM), is utilized to discretize the saturation field discontinuity at the boundaries between layers of different physical properties, and the solid displacement discontinuity across the crack. The proposed mixed discretization scheme differs from the well-known mixed FEM (Arbogast and Wheeler 1995; Masud and Hughes 2002) such that in the mixed FEM, different state variables are utilized, but adopt a single discretization technique; whereas in the mixed discretization scheme, we utilize different state variables and adopt different discretization techniques, depending on the physical nature of the state variables and the associated balance equations.

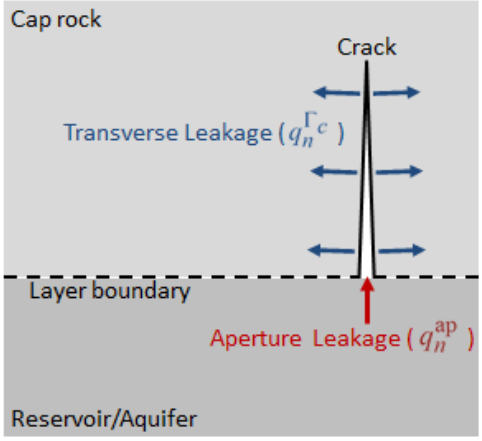

Fig. 5.1 A sketch of the conceptual model

5.3 Governing Equations

The physical domain is assumed homogeneous, isotropic and non-isothermal, constituting a porous solid phase, a wetting (formation water) phase and a non-wetting (CO_2) phase. The domain is subjected to thermo-hydrodynamic-mechanical and gravitational forces. The fluids can exhibit buoyancy and phase change, and the solid can exhibit deformation and crack propagation driven by fluid dynamic forces.

As stated earlier, the conceptual model distinguishes multiphase flow in three geometrical domains: a matrix domain, governed by Darcy's law; a fracture domain,

governed by the Navier-Stokes equations; and a matrix-fracture domain, governed by a leakage term.

5.3.1 Matrix domain

The REV averaging theory is utilized to formulate the governing equations. We adopt the displacement-pressure-saturation-temperature formulation with the primary variables: solid phase displacement u, wetting phase pressure p_w, non-wetting phase saturation S_n, and temperature T. A detailed mathematical derivation of the governing field equations for two phase flow in a porous medium, exhibiting solid deformation, non-isothermal heat flow and phase change is given by Arzanfudi and Al-Khoury (2014).

Consider the following identities and relationships:

$$\begin{aligned}
&S_w + S_n = 1; \quad p_n = p_w + p_c; \quad T_w = T_n = T_s = T; \quad \rho_w = \rho_w(p_w, T); \quad \rho_n = \rho_n(p_n, T) \\
&\frac{\partial p_n}{\partial t} = \frac{\partial p_w}{\partial t} + \frac{\partial p_c}{\partial S_n}\frac{\partial S_n}{\partial t}; \quad \nabla p_n = \nabla p_w + \frac{\partial p_c}{\partial S_n}\nabla S_n \\
&\boldsymbol{\sigma}' = \boldsymbol{\sigma} + \mathbf{I}\alpha(S_w p_w + S_n p_n)
\end{aligned} \tag{5.1}$$

where p_c is the capillary pressure; S_w and S_n are the wetting and non-wetting phase saturation, respectively; ρ_w and ρ_n are the wetting and non-wetting phase mass density, respectively; p_w and p_n are the wetting and non-wetting phase pressure, respectively; $\boldsymbol{\sigma}'$ is the effective stress; $\boldsymbol{\sigma}$ is the total stress; $\mathbf{I}$ is the identity tensor; α is Biot's constant; and T_w, T_n, and T_s are the wetting, non-wetting and solid phase temperatures, which are, following the local equilibrium assumption, equal (= T). Accordingly, the governing field equations for the momentum, the mass and the energy in the matrix domain can be derived, and expressed as:

Momentum balance

The averaged macroscopic linear momentum field equation for a multiphase porous medium is:

$$\mathrm{div}\left[\mathbf{D}(\mathbf{L}\mathbf{u} - \frac{1}{3}\mathbf{m}\beta_s T) - \mathbf{I}\alpha(S_w p_w + S_n p_n)\right] + \rho_{eff}\,\mathbf{g} = 0 \tag{5.2}$$

where

$$\rho_{eff} = (1-\phi)\rho_s + \phi S_w \rho_w + \phi S_n \rho_n \tag{5.3}$$

in which D is a stiffness matrix of the solid, which can be linear or non-linear; β_s is the thermal expansion coefficient of solid phase; $\mathbf{L}$ is the displacement-strain operator; $\mathbf{m} = [1 \quad 1 \quad 1 \quad 0 \quad 0 \quad 0]^T$; $\mathbf{u}$ is the displacement vector of the solid phase; $\mathbf{g}$ is the gravity force vector; and ϕ is the porosity.

For the wetting phase, the linear momentum is:

$$\phi S_w \bar{\mathbf{v}}_{w/s} = \frac{\mathbf{k} k_{rw}}{\mu_w}\left(-\nabla p_w + \rho_w \mathbf{g}\right) \tag{5.4}$$

and for the non-wetting phase, is:

$$\phi S_n \bar{\mathbf{v}}_{n/s} = \frac{\mathbf{k} k_{rn}}{\mu_n}\left(-\nabla p_n + \rho_n \mathbf{g}\right) \tag{5.5}$$

where $\mathbf{k}$ is the intrinsic permeability tensor; k_{rw} and k_{rn} are the wetting and non-wetting phases relative permeability (functions of saturation), respectively; μ_w and μ_n are the wetting and non-wetting phases viscosity, respectively; and $\bar{\mathbf{v}}_{w/s}$ and $\bar{\mathbf{v}}_{n/s}$ are the mass averaged values of the wetting and non-wetting phases relative to the solid phase, respectively.

Mass balance

The averaged macroscopic mass balance equations for the wetting phase and the non-wetting phase for a compressible, non-isothermal multiphase flow can be expressed as

Wetting phase

$$d_1 \frac{\partial p_w}{\partial t} + d_2 \frac{\partial S_n}{\partial t} + d_3 \frac{\partial T}{\partial t} + d_4 \mathbf{m}^T \mathbf{L} \frac{\partial \mathbf{u}}{\partial t} + \nabla \cdot \left(-\mathbf{c}_1 \nabla p_w\right) + \nabla \cdot \mathbf{G}_1 = 0 \tag{5.6}$$

in which

$$d_1 = \frac{\alpha - \phi}{K_s}\rho_w S_w + \frac{\phi}{K_w} S_w; \quad d_2 = \frac{\alpha - \phi}{K_s}\rho_w S_w \left(p_c + S_n \frac{\partial p_c}{\partial S_n}\right) - \phi \rho_w$$

$$d_3 = -\rho_w S_w \beta_s \left(\alpha - \phi\right) + \phi S_w \frac{\partial \rho_w}{\partial T}; \quad d_4 = \alpha \rho_w S_w; \quad \mathbf{c}_1 = \rho_w \frac{\mathbf{k} k_{rw}}{\mu_w} \tag{5.7}$$

$$\mathbf{G}_1 = \rho_w \frac{\mathbf{k} k_{rw}}{\mu_w} \rho_w \mathbf{g}$$

and K_s and K_w are the bulk moduli of solid and water phases, respectively.

Non-wetting phase

$$d_5 \frac{\partial p_w}{\partial t} + d_6 \frac{\partial S_n}{\partial t} + d_7 \frac{\partial T}{\partial t} + d_8 \mathbf{m}^T \mathbf{L} \frac{\partial \mathbf{u}}{\partial t} + \nabla \cdot \left(-\mathbf{c}_2 \nabla p_w\right) + \nabla \cdot \left(-\mathbf{c}_3 \nabla S_n\right) + \nabla \cdot \left(\mathbf{G}_2\right) = 0 \tag{5.8}$$

in which

$$
\begin{aligned}
d_5 &= \frac{\alpha-\phi}{K_s}\rho_n S_n + \frac{\phi}{K_n}S_n \\
d_6 &= \frac{\alpha-\phi}{K_s}\rho_n S_n\left(p_c + S_n\frac{\partial p_c}{\partial S_n}\right) + \phi\left(\rho_n - \frac{1}{K_n}S_n\frac{\partial p_c}{\partial S_n}\right)en \\
d_7 &= -\rho_n S_n\beta_s(\alpha-\phi) + \phi S_n\frac{\partial \rho_n}{\partial T};\quad d_8 = \alpha\rho_n S_n;\quad \mathbf{c}_2 = \rho_n\frac{\mathbf{k}k_{rn}}{\mu_n} \\
\mathbf{c}_3 &= \rho_n\frac{\mathbf{k}k_{rn}}{\mu_n}\frac{\partial p_c}{\partial S_n};\quad \mathbf{G}_2 = \rho_g\frac{\mathbf{k}k_{rn}}{\mu_n}\rho_n\mathbf{g}
\end{aligned}
\tag{5.9}
$$

and K_n is the bulk modulus of the non-wetting phase.

Energy balance

The averaged macroscopic energy balance equation for a multiphase domain exhibiting local thermal equilibrium, can be described as

$$
\begin{aligned}
d_9\frac{\partial T}{\partial t} + d_{10}\frac{\partial p_w}{\partial t} + d_{11}\frac{\partial S_n}{\partial t} + \nabla\cdot(\boldsymbol{\beta}_1 T) - \nabla\cdot(\boldsymbol{\beta}_2\nabla p_w T) \\
- \nabla\cdot(\boldsymbol{\beta}_3\nabla S_n T) + \nabla\cdot(-\mathbf{c}_4\nabla T) = 0
\end{aligned}
\tag{5.10}
$$

in which

$$
\begin{aligned}
d_9 &= (1-\phi)\rho_s C_s^p + \phi S_w\rho_w C_w^p + \phi S_n\rho_n C_n^p en \\
d_{10} &= \left((1-\phi)\frac{\partial \rho_s}{\partial p_w}C_s^p + \phi S_w\frac{\partial}{\partial p_w}\left(\rho_w C_w^p\right) + \phi S_n\frac{\partial}{\partial p_w}\left(\rho_n C_n^p\right)\right)T \\
d_{11} &= \left(-\phi\rho_w C_w^p + \phi\rho_n C_n^p\right)T;\quad \boldsymbol{\beta}_1 = \rho_w C_w^p\frac{\mathbf{k}k_{rw}}{\mu_w}\rho_w\mathbf{g} + \rho_n C_n^p\frac{\mathbf{k}k_{rn}}{\mu_n}\rho_n\mathbf{g} \\
\boldsymbol{\beta}_2 &= \rho_w C_w^p\frac{\mathbf{k}k_{rw}}{\mu_w} + \rho_n C_n^p\frac{\mathbf{k}k_{rn}}{\mu_n};\quad \boldsymbol{\beta}_3 = \rho_n C_n^p\frac{\mathbf{k}k_{rn}}{\mu_n}\frac{\partial p_c}{\partial S_n} \\
\mathbf{c}_4 &= \boldsymbol{\lambda}_{eff} = (1-\phi)\boldsymbol{\lambda}_s + \phi S_w\boldsymbol{\lambda}_w + \phi S_n\boldsymbol{\lambda}_n
\end{aligned}
\tag{5.11}
$$

where $\boldsymbol{\lambda}_w$, $\boldsymbol{\lambda}_n$, and $\boldsymbol{\lambda}_s$ are the thermal conductivity of the wetting, non-wetting and solid phases, respectively; $\boldsymbol{\lambda}_{eff}$ is the effective thermal conductivity of the multiphase medium; and C_w^p, C_n^p, and C_s^p are the isobaric specific heat capacity of the wetting, non-wetting and solid phases, respectively.

5.3.2 Fracture domain

The fracture domain is assumed to comprise discrete cracks, where the non-wetting phase can flow. We adopt the mixture velocity-mixture pressure-mixture mass density formulation. The primary variables are: mixture velocity v'_m, mixture pressure p', and mixture mass density ρ'_m.

In what follows, the terms for crack and fracture will be exchanged, but in particular, crack will be utilized to indicate a discrete crack, and fracture will be utilized to indicate general cracks, fissures and fractures.

Crack initiation is not considered in this work. Instead, an initial crack is assumed to exist a priori. Crack propagation occurs due to solid deformation and fluid dynamics. When the fluid pressure on the crack faces increases and stress ahead of the crack tip exceeds the rock material tensile strength, the crack opens and increases in length. The fluid can exhibit phase change, compressibility, wall friction, thermal interaction and buoyancy.

The fracture zone is described by a solid phase, describing the skeleton of the crack, and a fluid phase, describing the fluid inside the skeleton of the crack. The solid phase is assumed two-dimensional, described in terms of a local $x' - y'$ coordinate system, as shown in Fig. 5.2. The mechanism for crack opening is governed by the matrix domain formulation given in Section 5.3.1 above, and its propagation will be treated in Section 5.3.4. The fluid phase is assumed one-dimensional with a volume equal to the volume of the crack. The thermo-hydrodynamics of the crack fluid is treated in this section, using the drift-flux model.

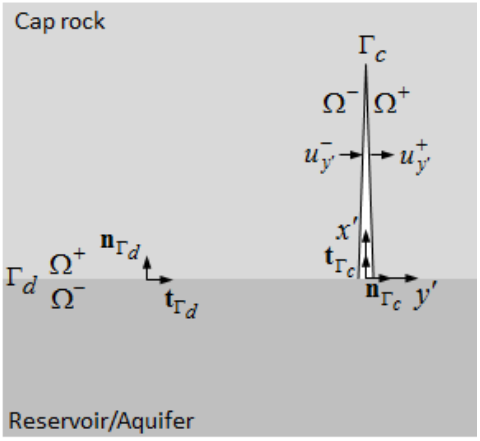

Fig. 5.2 Geometrical discontinuities: matrix-matrix discontinuity, and fracture-matrix discontinuity

Using the drift-flux model, the fluid mass, momentum and energy balance equations can be described as (Arzanfudi and Al-Khoury 2015):

Mass balance

$$\frac{\partial}{\partial t}\left(\rho'_m \left[\!\left[u_{y'}\right]\!\right]\right)+\frac{\partial}{\partial x'}\left(\rho'_m v'_m \left[\!\left[u_{y'}\right]\!\right]\right)=0 \tag{5.12}$$

Momentum balance

$$\begin{aligned}\frac{\partial}{\partial t}\left(\rho'_m v'_m \left[\!\left[u_{y'}\right]\!\right]\right)+\frac{\partial}{\partial x'}\left(\left(\rho'_m v'^2_m+\gamma'\right)\left[\!\left[u_{y'}\right]\!\right]\right)\\ =-\frac{\partial}{\partial x'}\left(p'\left[\!\left[u_{y'}\right]\!\right]\right)+\rho'_m \left[\!\left[u_{y'}\right]\!\right]\mathbf{g}\cdot\mathbf{t}_{\Gamma_c}-\frac{f'\rho'_m\left|v'_m\right|v'_m}{4}\end{aligned} \tag{5.13}$$

Energy balance

$$\frac{\partial}{\partial t}\left[\left(\rho'_m\left(h'_m+\frac{1}{2}v'^2_m\right)-p'\right)\left[\!\left[u_{y'}\right]\!\right]\right]+\frac{\partial}{\partial x'}\left[\rho'_m v'_m\left(h'_m+\frac{v'^2_m}{2}\right)\left[\!\left[u_{y'}\right]\!\right]\right]=\rho'_m v'_m\left[\!\left[u_{y'}\right]\!\right]\mathbf{g}\cdot\mathbf{t}_{\Gamma_c} \tag{5.14}$$

in which the subscript m indicates a fluid mixture; ρ'_m is the mixture mass density; v'_m is the mixture velocity; p' is the mixture pressure; h'_m is the mixture specific enthalpy; f' is the wall friction coefficient; γ' is the slip between phases; $\mathbf{t}_{\Gamma_c}$ is a unit tangent vector to the crack boundary, Fig. 5.2; and $\left[\!\left[u_{y'}\right]\!\right]=u^{+}_{y'}-u^{-}_{y'}$ is the crack opening size.

The wall friction coefficient is defined as (Brill and Mukherjee 1999):

$$f'=\begin{cases}\dfrac{16}{\mathrm{Re}'} & \mathrm{Re}'<2400\\ \dfrac{1}{16}\left\{\log\left[\dfrac{\varepsilon'}{3.7\left[\!\left[u_{y'}\right]\!\right]}-\dfrac{5.02}{\mathrm{Re}'}\log\left(\dfrac{\varepsilon'}{3.7\left[\!\left[u_{y'}\right]\!\right]}+\dfrac{13}{\mathrm{Re}'}\right)\right]\right\}^{-2} & \mathrm{Re}'\geq 2400\end{cases} \tag{5.15}$$

where ε' is the roughness of the crack, and Re' is the Reynolds number given by

$$\mathrm{Re}'=\frac{\rho'_m\left|v'_m\right|\left[\!\left[u_{y'}\right]\!\right]}{\mu'_m} \tag{5.16}$$

in which μ'_m is the mixture dynamic viscosity.

5.3.3 Matrix-Fracture domain

At the boundary between the fracture domain and the matrix domain, the fluid can leak from the matrix to the fracture, and from the fracture to the matrix, depending on the

pressure gradient and the physical properties of the matrix-fracture boundary. Two leakage mechanisms can occur: (1) leakage through the crack boundaries (transverse), and (2) leakage via the crack aperture, Fig. 5.1. They are described as:

Transverse leakage

$$q_n^{\Gamma_c} = \rho_n \frac{\bar{\alpha} k k_{rn}}{\mu_n} \left(p' - p_n \right) \tag{5.17}$$

where $\bar{\alpha}$ is a shape factor (m^{-1}).

Aperture leakage

$$q_n^{\mathrm{ap}} = \rho_n^{\mathrm{ap}} \frac{\bar{\beta} k^{\mathrm{ap}} k_{rn}^{\mathrm{ap}}}{\mu_n^{\mathrm{ap}}} \left(p_n - p' \right) \tag{5.18}$$

where $\bar{\beta}$ is a shape factor (m^{-1}).

5.3.4 Crack propagation mechanism

The traction at the crack boundaries arises from the fluid pressure and the cohesive traction between the crack faces, described as

$$\boldsymbol{\sigma} \cdot \mathbf{n}_{\Gamma_c} = \mathbf{t}_c - p' \mathbf{n}_{\Gamma_c} \tag{5.19}$$

where $\mathbf{n}_{\Gamma_c}$ is the unit normal vector to the crack boundary, Fig. 5.2; and $\mathbf{t}_c$ is the cohesive traction between crack edges, which is a function of the crack opening, such that

$$\mathbf{t}_c = \mathbf{t}_c \left(\left[\!\left[u_{y'} \right]\!\right] \right) \tag{5.20}$$

There are several formulations describing Eq. (5.20). Here, we utilize the exponential law given by van den Bosch et al. (2006).

The crack propagation is postulated to occur when the maximum principal stress ahead of the crack tip exceeds the tensile strength of the solid matrix. A nonlocal averaging of the stresses in a small region ahead of the crack tip is carried to evaluate the maximum principal stress (Wells and Sluys 2001). The direction of crack growth is perpendicular to the direction of the maximum principal stress.

By crack propagation, the fluid in the crack expands over the newly created crack volume. To ensure conservation of mass and energy in the crack, the isentropic process, describing a constant-entropy of an expanding fluid (Turns 2006), is assumed to prevail at the crack propagation moment. It is described as

$$dh'_m = v'_m dp' \tag{5.21}$$

which exerts a constraint on the pressure, specific volume, temperature and specific entropy of the fracture fluid. By expansion, the fluid volume increases, causing the pressure to drop, and the entropy to stay constant.

5.3.5 Constitutive relationships

The solid phase in the matrix domain is assumed linear elastic, governed by Hooke's law.

The non-wetting phase in the fracture domain is postulated to be compressible and exhibit phase change. The constitutive relationships are based on the equations of state of CO_2 (Arzanfudi and Al-Khoury 2014), and those describing the drift-flux model parameters (Arzanfudi and Al-Khoury 2015).

The wetting and non-wetting phases in the matrix domain are postulated to be compressible, but exhibit no phase change. The mass density and dynamic viscosity are described empirically in terms of pressure and temperature, as:

Matrix water mass density

$$\rho_w=\rho_w^0 e^{-\beta_w\left(T-T^0\right)+C_w\left(p-p^0\right)} \tag{5.22}$$

where $p^0=12\times10^6$ Pa, $T^0=333.15$ K, $\rho_w^0=1,045\,\text{kg/m}^3$, β_w=0.000522 K^{-1}, $C_w=1/K_w$, and $K_w=2.2$ GPa (Arzanfudi and Al-Khoury 2014).

Matrix water dynamic viscosity

$$\mu_w=\mu_{\text{w}}^0+a_w\left(T-T^0\right) \tag{5.23}$$

in which $\mu_{\text{w}}^0=4.32982\times10^{-4}$ Pa.s, and a_w = -7.057$\times10^{-6}$ Pa.s.K^{-1} (Arzanfudi and Al-Khoury 2014).

Matrix CO_2 mass density

$$\rho_n=\rho_{\text{co2}}^0 e^{-\beta_{\text{co2}}\left(T-T^0\right)+C_{\text{co2}}\left(p-p^0\right)} \tag{5.24}$$

where $\rho_{\text{co}_2}^0=479\,\text{kg/m}^3$, β_{co_2}=0.01866 K^{-1}, $C_{\text{co}_2}=1/K_{\text{co}_2}$, and $K_{\text{co}_2}=100$ MPa (Arzanfudi and Al-Khoury 2014).

Matrix CO_2 dynamic viscosity

$$\mu_n=\mu_{\text{co2}}^0+a_{\text{co2}}\left(T-T^0\right)+b_{\text{co2}}\left(p-p^0\right) \tag{5.25}$$

in which $\mu_{\text{co2}}^0=3.950\times10^{-5}$ Pa.s, $a_{\text{co2}}=-9.28913\times10^{-7}$ Pa.s.K^{-1} and $b_{\text{co2}}=1.9936\times10^{-12}$ s (Arzanfudi and Al-Khoury 2014).

The saturation-capillary pressure relationship, and the relative permeability-capillary pressure relationship in the matrix domain are based on Brooks and Corey (1964).

5.3.6 Initial and boundary conditions

Initially, the primary state variables might be described as

$$G(\mathbf{x},0) = G_0(\mathbf{x}) \quad \text{at } t = 0 \tag{5.26}$$

where G can be:

- $\mathbf{u}$, p_w, S_n, or T for the matrix domain
- v_m', p', or ρ_m' for the fracture domain

The Dirichlet boundary conditions might be described as

$$J(t) = \hat{J}(t) \quad \text{on } \Gamma_u \tag{5.27}$$

in which Γ_u is the Dirichlet boundary, and J can be $\mathbf{u}$, p_w, S_n, or T.

The Neumann boundary conditions are defined as

$$\begin{aligned}
&\hat{\mathbf{t}} = \boldsymbol{\sigma}\cdot\mathbf{n} \\
&\hat{q}_w = \left(-\mathbf{c}_1\nabla p_w + \mathbf{G}_1\right)\cdot\mathbf{n} \\
&\hat{q}_n = \left(-\mathbf{c}_2\nabla p_w - \mathbf{c}_3\nabla S_n + \mathbf{G}_2\right)\cdot\mathbf{n} \qquad \text{on } \Gamma_q \\
&\hat{Q}_{\text{cond}} = \left(-\mathbf{c}_4\nabla T\right)\cdot\mathbf{n} \\
&\hat{Q}_{\text{adv}} = \left(-\boldsymbol{\beta}_2\nabla p_w T - \boldsymbol{\beta}_3\nabla S_n T + \boldsymbol{\beta}_1 T\right)\cdot\mathbf{n}
\end{aligned} \tag{5.28}$$

where Γ_q is the Neumann boundary; $\hat{\mathbf{t}}$ is the prescribed traction; $\hat{q}_w$ and $\hat{q}_n$ are the prescribed mass flow rate of the wetting phase and the non-wetting phase, respectively; and $\hat{Q}_{\text{cond}}$ and $\hat{Q}_{\text{adv}}$ are the conductive and advective energy flux at Γ_q.

5.4 Finite element mixed discretization

The physical domain comprises coupled flow fields of significantly different nature. It comprises solid displacement, multiphase flow in the porous domain, and fluid dynamics in the fracture domain. The mass, momentum and energy balance equations of these fields are considerably different, but strongly coupled with each other. The flow mechanisms and velocities are significantly different. Discretizing such a system using standard numerical techniques is, if possible, computationally nuisance, can cause spurious oscillations, and requires extensive CPU time and capacity.

To tackle this problem, we utilize a mixed finite element discretization scheme. Primary state variables representing different fields are discretized using different discretization procedures, depending on their physical nature. Continuous fields are discretized using the standard Galerkin finite element method, whereas moving and stationary discontinuous fields are discretized using the partition of unity method. We adopt a fixed, structured and geometry-independent finite element discretization scheme.

We distinguish two types of discontinuities: a fluid discontinuity at the boundary between porous medium layers exhibiting different hydraulic properties, and a solid discontinuity due to crack existence and propagation.

5.4.1 Matrix domain discretization

In the matrix domain, a solid phase displacement-wetting phase pressure-non wetting phase saturation-temperature primary state variables formulation is employed. These state variables are continuous within the matrix, but at the boundary between layers, the non-wetting phase saturation is discontinuous. The physical condition at the boundaries between layers of different hydraulic properties is treated in details in Arzanfudi et al. (2014). In the matrix-fracture boundary, the displacement in the solid phase exhibits a jump, while other state variables are continuous.

5.4.1.1 Weak form formulation

We use the weighted residual method to formulate the finite element equations. The momentum balance equation, Eq. (5.2), and the non-wetting phase mass balance equation, Eq. (5.8), are discretized using a discontinuous weighting function; whereas the wetting phase mass balance equation, Eq. (5.6), and the energy balance equation, Eq. (5.10), are discretized using a continuous weighting function. Applying the weighted residual finite element discretization procedure to these equations yields:

Momentum balance

Continuously weighted:

$$-\int_{\Omega}\nabla w_1\left(\mathbf{D}(\mathbf{L}\mathbf{u}-\frac{1}{3}\mathbf{m}\beta_s T)\right)d\Omega+\int_{\Omega}\nabla w_1\left(\mathbf{I}\alpha(p_w+S_n p_c)\right)d\Omega + \int_{\Gamma_q} w_1\hat{\mathbf{t}}d\Gamma+\int_{\Omega} w_1\rho_{eff}\,\mathbf{g}d\Omega=0 \tag{5.29}$$

Discontinuously weighted:

$$-\int_{\Omega}\nabla w_1^*\left(\mathbf{D}(\mathbf{L}\mathbf{u}-\frac{1}{3}\mathbf{m}\beta_s T)\right)d\Omega+\int_{\Omega}\nabla w_1^*\left(\mathbf{I}\alpha(p_w+S_n p_c)\right)d\Omega + \int_{\Gamma_q} w_1^*\hat{\mathbf{t}}d\Gamma-\int_{\Gamma_c} w_1^*\left(\mathbf{t}_c-p'\mathbf{n}_{\Gamma_c}\right)d\Gamma+\int_{\Omega} w_1^*\rho_{eff}\,\mathbf{g}d\Omega=0 \tag{5.30}$$

Mass balance

Wetting phase:

$$\int_\Omega w_2 d_1 \frac{\partial p_w}{\partial t} d\Omega + \int_\Omega w_2 d_2 \frac{\partial S_n}{\partial t} d\Omega + \int_\Omega w_2 d_3 \frac{\partial T}{\partial t} d\Omega + \int_\Omega w_2 d_4 \mathbf{m}^T \mathbf{L} \frac{\partial \mathbf{u}}{\partial t} d\Omega + \int_\Omega \nabla w_2 \cdot (\mathbf{c}_1 \nabla p_w) d\Omega - \int_\Omega \nabla w_2 \cdot \mathbf{G}_1 d\Omega + \int_{\Gamma_q} w_2 \hat{q}_w d\Gamma = 0 \tag{5.31}$$

Non-wetting phase:

Continuously weighted:

$$\int_\Omega w_3 d_5 \frac{\partial p_w}{\partial t} d\Omega + \int_\Omega w_3 d_6 \frac{\partial S_n}{\partial t} d\Omega + \int_\Omega w_3 d_7 \frac{\partial T}{\partial t} d\Omega + \int_\Omega w_3 d_8 \mathbf{m}^T \mathbf{L} \frac{\partial \mathbf{u}}{\partial t} d\Omega + \int_\Omega \nabla w_3 \cdot (\mathbf{c}_2 \nabla p_w) d\Omega + \int_\Omega \nabla w_3 \cdot (\mathbf{c}_3 \nabla S_n) d\Omega - \int_\Omega \nabla w_3 \cdot \mathbf{G}_2 d\Omega + \int_{\Gamma_q} w_3 \hat{q}_n d\Gamma - \int_{\Gamma_c} w_3 q_n^{\Gamma_c} d\Gamma + \int_\Omega w_3 q_n^{\mathrm{ap}} d\Omega = 0 \tag{5.32}$$

Discontinuously weighted:

$$\int_\Omega w_3^* d_5 \frac{\partial p_w}{\partial t} d\Omega + \int_\Omega w_3^* d_6 \frac{\partial S_n}{\partial t} d\Omega + \int_\Omega w_3^* d_7 \frac{\partial T}{\partial t} d\Omega + \int_\Omega w_3^* d_8 \mathbf{m}^T \mathbf{L} \frac{\partial \mathbf{u}}{\partial t} d\Omega + \int_\Omega \nabla w_3^* \cdot (\mathbf{c}_2 \nabla p_w) d\Omega + \int_\Omega \nabla w_3^* \cdot (\mathbf{c}_3 \nabla S_n) d\Omega - \int_\Omega \nabla w_3^* \cdot \mathbf{G}_2 d\Omega + \int_{\Gamma_q} w_3^* \hat{q}_n d\Gamma - \int_{\Gamma_d} w_3^* q_n^{\Gamma_d} d\Gamma - \int_{\Gamma_c} w_3^* q_n^{\Gamma_c} d\Gamma + \int_\Omega w_3^* q_n^{\mathrm{ap}} d\Omega = 0 \tag{5.33}$$

Energy balance

$$\int_\Omega w_4 d_9 \frac{\partial T}{\partial t} d\Omega + \int_\Omega w_4 d_{10} \frac{\partial p_w}{\partial t} d\Omega + \int_\Omega w_4 d_{11} \frac{\partial S_n}{\partial t} d\Omega - \int_\Omega \nabla w_4 \boldsymbol{\beta}_1 T d\Omega + \int_\Omega \nabla w_4 \boldsymbol{\beta}_2 \nabla p_w T d\Omega + \int_\Omega \nabla w_4 \boldsymbol{\beta}_3 \nabla S_n T d\Omega + \int_\Omega \nabla w_4 \cdot (\mathbf{c}_4 \nabla T) d\Omega + \int_{\Gamma_q} w_4 \hat{Q}_{\mathrm{adv}} d\Gamma + \int_{\Gamma_q} w_4 \hat{Q}_{\mathrm{cond}} d\Gamma - \int_{\Gamma_c} w_4 \left(Q_{\mathrm{adv}}^{\Gamma_c} + Q_{\mathrm{conv}}^{\Gamma_c} \right) d\Gamma + \int_\Omega w_4 Q_{\mathrm{adv}}^{\mathrm{ap}} d\Omega = 0 \tag{5.34}$$

in which w_1, w_2, w_3 and w_4 are continuous weighting functions; w_1^* is a discontinuous weighting function exhibiting discontinuity across the crack edge; w_3^* is a discontinuous weighting function exhibiting discontinuity across layer boundaries; Γ_c and Γ_d are the crack and layer boundaries, shown in Fig. 5.2; $q_n^{\Gamma d}$ is the layer leakage term, explained in-details in Arzanfudi et al. (2014); $Q_{\text{adv}}^{\text{ap}}(q_n^{\text{ap}}, h_n)$ is the advective energy source to the crack aperture; and $Q_{\text{adv}}^{\Gamma_c}(q_n^{\Gamma c}, h_n)$ and $Q_{\text{conv}}^{\Gamma_c}(T, T')$ are the advective and convective heat fluxes at the crack faces, described as

$$Q_{\text{adv}}^{\Gamma_c} = h_n q_n^{\Gamma c} \quad ; \quad Q_{\text{conv}}^{\Gamma_c} = \alpha_c \left(T - T'\right) \quad ; \quad Q_{\text{adv}}^{\text{ap}} = h_n q_n^{\text{ap}} \tag{5.35}$$

where h_n is the non-wetting phase specific enthalpy, and α_c is the thermal interaction coefficient at the matrix-fracture interface (Arzanfudi and Al-Khoury 2015). The Darcy fluxes, $q_n^{\Gamma c}$ and q_n^{ap}, are related to the crack momentum fluxes, $Q_{\text{mo}}^{\Gamma_c}(q_n^{\Gamma c}, v_m')$ and $Q_{\text{mo}}^{\text{ap}}(q_n^{\text{ap}}, v_m')$, by

$$q_n^{\Gamma c} = Q_{\text{mo}}^{\Gamma_c} \big/ v_m' \quad ; \quad q_n^{\text{ap}} = Q_{\text{mo}}^{\text{ap}} \big/ v_m' \tag{5.36}$$

5.4.1.2 Linearization

The constitutive parameters in Eqs. (5.29)-(5.34) are functions of the primary state variables, making the problem strongly non-linear. We use the standard Newton-Raphson method to linearize the problem, such that:

$$\begin{aligned} &\mathbf{u}^{r+1} = \mathbf{u}^r + \delta\mathbf{u} \qquad p_w^{r+1} = p_w^r + \delta p_w \qquad S_n^{r+1} = S_n^r + \delta S_n \qquad T^{r+1} = T^r + \delta T \\ &\dot{\mathbf{u}}^{r+1} = \dot{\mathbf{u}}^r + \delta\dot{\mathbf{u}} \qquad \dot{p}_w^{r+1} = \dot{p}_w^r + \delta \dot{p}_w \qquad \dot{S}_n^{r+1} = \dot{S}_n^r + \delta \dot{S}_n \qquad \dot{T}^{r+1} = \dot{T}^r + \delta \dot{T} \end{aligned} \tag{5.37}$$

where r + 1 represents the current iteration, r is the previous iteration and, δ is the exerted difference in the variables magnitudes. The second line in Eq. (5.37) denotes the linearization of the time derivative of the state variables. The spatial derivatives are linearized as

$$\nabla p_w^{r+1} = \nabla p_w^r + \delta \nabla p_w \qquad \nabla S_n^{r+1} = \nabla S_n^r + \delta \nabla S_n \qquad \nabla T^{r+1} = \nabla T^r + \delta \nabla T \tag{5.38}$$

The capillary pressure and effective mass density are linearized as

$$p_c^{r+1} = p_c^r + \frac{\partial p_c^r}{\partial S_n} \delta S_n \tag{5.39}$$

$$\rho_{eff}^{r+1} = \rho_{eff}^{r} + \frac{\partial \rho_{eff}^{r}}{\partial p_w}\delta p_w + \frac{\partial \rho_{eff}^{r}}{\partial S_n}\delta S_n + \frac{\partial \rho_{eff}^{r}}{\partial T}\delta T \tag{5.40}$$

The balance equations coefficients in Eqs. (5.6)-(5.11) are linearized in terms of the state variables, as

$$d_i^{r+1} = d_i^{r} + \frac{\partial d_i^{r}}{\partial p_w}\delta p_w + \frac{\partial d_i^{r}}{\partial S_n}\delta S_n + \frac{\partial d_i^{r}}{\partial T}\delta T \ , \ i = 1,...,9 \tag{5.41}$$

$$\mathbf{c}_i^{r+1} = \mathbf{c}_i^{r} + \frac{\partial \mathbf{c}_i^{r}}{\partial p_w}\delta p_w + \frac{\partial \mathbf{c}_i^{r}}{\partial S_n}\delta S_n + \frac{\partial \mathbf{c}_i^{r}}{\partial T}\delta T \ , \ i = 1,...,3 \tag{5.42}$$

$$\mathbf{c}_4^{r+1} = \mathbf{c}_4^{r} + \frac{\partial \mathbf{c}_4^{r}}{\partial S_n}\delta S_n \tag{5.43}$$

$$\mathbf{G}_i^{r+1} = \mathbf{G}_i^{r} + \frac{\partial \mathbf{G}_i^{r}}{\partial p_w}\delta p_w + \frac{\partial \mathbf{G}_i^{r}}{\partial S_n}\delta S_n + \frac{\partial \mathbf{G}_i^{r}}{\partial T}\delta T \ , \ i = 1,2 \tag{5.44}$$

$$\boldsymbol{\beta}_i^{r+1} = \boldsymbol{\beta}_i^{r} + \frac{\partial \boldsymbol{\beta}_i^{r}}{\partial p_w}\delta p_w + \frac{\partial \boldsymbol{\beta}_i^{r}}{\partial S_n}\delta S_n + \frac{\partial \boldsymbol{\beta}_i^{r}}{\partial T}\delta T \ , \ i = 1,...,3 \tag{5.45}$$

The matrix-fracture leakage terms are linearized as

$$\left(q_n^{\Gamma c}\right)^{r+1} = \left(q_n^{\Gamma c}\right)^{r} + \delta q_n^{\Gamma c} \tag{5.46}$$

$$\left(q_n^{\mathrm{ap}}\right)^{r+1} = \left(q_n^{\mathrm{ap}}\right)^{r} + \delta q_n^{\mathrm{ap}} \tag{5.47}$$

$$\mathbf{t}_c^{r+1} = \mathbf{t}_c^{r} + \frac{\partial \mathbf{t}_c^{r}}{\partial \left[\!\left[u_{y'}\right]\!\right]}\delta\left[\!\left[u_{y'}\right]\!\right] \tag{5.48}$$

$$\begin{aligned}\left(Q_{\mathrm{adv}}^{\Gamma c}\right)^{r+1} = \left(Q_{\mathrm{adv}}^{\Gamma c}\right)^{r} &+ \frac{\partial\left(Q_{\mathrm{adv}}^{\Gamma c}\right)^{r}}{\partial T}\delta T + \frac{\partial\left(Q_{\mathrm{adv}}^{\Gamma c}\right)^{r}}{\partial q_n^{\Gamma c}}\delta q_n^{\Gamma c} \\ &+ \frac{\partial\left(Q_{\mathrm{adv}}^{\Gamma c}\right)^{r}}{\partial p'}\delta p' + \frac{\partial\left(Q_{\mathrm{adv}}^{\Gamma c}\right)^{r}}{\partial \rho_m'}\delta \rho_m'\end{aligned} \tag{5.49}$$

$$\left(Q_{\mathrm{conv}}^{\Gamma c}\right)^{r+1} = \left(Q_{\mathrm{conv}}^{\Gamma c}\right)^{r} + \frac{\partial\left(Q_{\mathrm{conv}}^{\Gamma c}\right)^{r}}{\partial T}\delta T + \frac{\partial\left(Q_{\mathrm{conv}}^{\Gamma c}\right)^{r}}{\partial T'}\delta T' \tag{5.50}$$

$$\left(Q_{\text{adv}}^{\text{ap}}\right)^{r+1} = \left(Q_{\text{adv}}^{\text{ap}}\right)^{r} + \frac{\partial\left(Q_{\text{adv}}^{\text{ap}}\right)^{r}}{\partial T}\delta T + \frac{\partial\left(Q_{\text{adv}}^{\text{ap}}\right)^{r}}{\partial q_n^{\text{ap}}}\delta q_n^{\text{ap}} + \frac{\partial\left(Q_{\text{adv}}^{\text{ap}}\right)^{r}}{\partial p'}\delta p' + \frac{\partial\left(Q_{\text{adv}}^{\text{ap}}\right)^{r}}{\partial \rho_m'}\delta\rho_m' \tag{5.51}$$

$$p'^{\,r+1} = p'^{\,r} + \delta p' \tag{5.52}$$

5.4.1.3 PUM-SG formulation

The standard Galerkin finite element method and the partition of unity method, within the framework of the extended finite element method (XFEM), are integrated to discretize the problem. The first is, in general, accurate and computationally efficient for solving continuous flow fields, and the second is accurate and effective in solving discontinuous fields. The primary state variables in the matrix domain are discretized as:

Discontinuous fields (PUM)

Displacement

$$\mathbf{u}(\mathbf{x},t) = \mathbf{N}_u(\mathbf{x})\bar{\mathbf{u}}(t) + \mathbf{N}_u^*(\mathbf{x})\tilde{\mathbf{u}}(t) \tag{5.53}$$

Non-wetting phase saturation

$$S_n(\mathbf{x},t) = \mathbf{N}(\mathbf{x})\bar{\mathbf{S}}_n(t) + \mathbf{N}_d^*(\mathbf{x})\tilde{\mathbf{S}}_n(t) \tag{5.54}$$

Continuous field (SG)

Wetting phase pressure

$$p_w(\mathbf{x},t) = \mathbf{N}(\mathbf{x})\bar{\mathbf{p}}_w(t) \tag{5.55}$$

Temperature

$$T(\mathbf{x},t) = \mathbf{N}(\mathbf{x})\bar{\mathbf{T}}(t) \tag{5.56}$$

in which $\bar{\mathbf{u}}(t)$, $\bar{\mathbf{S}}_n(t)$, $\bar{\mathbf{p}}_w(t)$, and $\bar{\mathbf{T}}(t)$ are the standard nodal vectors; $\tilde{\mathbf{u}}(t)$ and $\tilde{\mathbf{S}}_n(t)$ are the extended nodal vectors; $\mathbf{N}(\mathbf{x})$ and $\mathbf{N}_u(\mathbf{x})$ are the standard finite element shape functions; and $\mathbf{N}_u^*(\mathbf{x})$ and $\mathbf{N}_d^*(\mathbf{x})$ are enriched shape functions, with components $N_i^*(\mathbf{x})$ defined as

$$N_i^*(\mathbf{x}) = N_i(\mathbf{x})\psi_i(\mathbf{x}) \tag{5.57}$$

where $\psi_i(\mathbf{x})$ is the shifted enrichment function (Zi and Belytschko 2003) at node i, defined as

$$\psi_i(\mathbf{x}) = H(\mathbf{x}) - H(\mathbf{x}_i) \tag{5.58}$$

in which $\mathbf{x}_i$ is the coordinate vector of node i; and $H(\mathbf{x})$ is the Heaviside function, which reads

$$H(\mathbf{x}) = \begin{cases} 1 & \mathbf{x} \in \Omega^+ \\ 0 & \mathbf{x} \in \Omega^- \end{cases} \tag{5.59}$$

where Ω^+ and Ω^- are defined with respect to the unit normal vector to the discontinuity $\mathbf{n}_{\Gamma_c}$ or $\mathbf{n}_{\Gamma_d}$, as illustrated in Fig. 5.2.

The fracture fluid pressure is discretized as

$$p'(x',t) = \mathbf{N}'(x')\bar{\mathbf{p}}'(t) \tag{5.60}$$

where $\mathbf{N}'(x')$ is the standard finite element shape function; and $\bar{\mathbf{p}}'(t)$ is the associated standard nodal vector.

5.4.1.4 Matrix domain finite element equations

Substituting Eqs. (5.37)-(5.60) into Eqs. (5.29)-(5.34), together with the following assumptions for the weighting functions:

$$w_1 = \mathbf{N}_u \quad ; \quad w_2 = w_3 = w_4 = \mathbf{N} \quad ; \quad w_1^* = \mathbf{N}_u^* \quad ; \quad w_3^* = \mathbf{N}_d^* \tag{5.61}$$

the final finite element equations for the matrix domain can be formulated. For instance, the finite element equation of the momentum balance is:

Continuously weighted:

$$\begin{aligned}
&-\int_\Omega \mathbf{B}^T\mathbf{D}\left(\mathbf{B}\bar{\mathbf{u}}^r + \mathbf{B}_c^*\tilde{\mathbf{u}}^r\right)d\Omega - \int_\Omega \mathbf{B}^T\mathbf{D}\left(\mathbf{B}\delta\bar{\mathbf{u}} + \mathbf{B}_c^*\delta\tilde{\mathbf{u}}\right)d\Omega + \int_\Omega \mathbf{B}^T\mathbf{D}\frac{1}{3}\mathbf{m}\beta_s\mathbf{N}\bar{\mathbf{T}}^r d\Omega \\
&+ \int_\Omega \mathbf{B}^T\mathbf{D}\frac{1}{3}\mathbf{m}\beta_s\mathbf{N}\delta\bar{\mathbf{T}}d\Omega + \int_\Omega \mathbf{B}^T\mathbf{m}^T\alpha\mathbf{N}\bar{\mathbf{p}}_w^r d\Omega + \int_\Omega \mathbf{B}^T\mathbf{m}^T\alpha\mathbf{N}\delta\bar{\mathbf{p}}_w d\Omega \\
&+ \int_\Omega \mathbf{B}^T\mathbf{m}^T\alpha p_c^r\left(\mathbf{N}\bar{\mathbf{S}}_n^r + \mathbf{N}_d^*\tilde{\mathbf{S}}_n^r\right)d\Omega + \int_\Omega \mathbf{B}^T\mathbf{m}^T\alpha p_c^r\left(\mathbf{N}\delta\bar{\mathbf{S}}_n + \mathbf{N}_d^*\delta\tilde{\mathbf{S}}_n\right)d\Omega \\
&+ \int_\Omega \mathbf{B}^T\mathbf{m}^T\alpha S_n^r\frac{\partial p_c^r}{\partial S_n}\left(\mathbf{N}\delta\bar{\mathbf{S}}_n + \mathbf{N}_d^*\delta\tilde{\mathbf{S}}_n\right)d\Omega + \int_\Omega \mathbf{N}^T\rho_{eff}^r\mathbf{g}d\Omega \\
&+ \int_\Omega \mathbf{N}^T\frac{\partial\rho_{eff}^r}{\partial p_w}\mathbf{g}\mathbf{N}\delta\bar{\mathbf{p}}_w d\Omega + \int_\Omega \mathbf{N}^T\frac{\partial\rho_{eff}^r}{\partial S_n}\mathbf{g}\left(\mathbf{N}\delta\bar{\mathbf{S}}_n + \mathbf{N}_d^*\delta\tilde{\mathbf{S}}_n\right)d\Omega \\
&+ \int_\Omega \mathbf{N}^T\frac{\partial\rho_{eff}^r}{\partial T}\mathbf{g}\mathbf{N}\delta\bar{\mathbf{T}}d\Omega + \int_{\Gamma_t}\mathbf{N}^T\hat{\mathbf{t}}d\Gamma = 0
\end{aligned} \tag{5.62}$$

Discontinuously weighted:

$$
\begin{aligned}
&-\int_{\Omega}\mathbf{B}^{*T}\mathbf{D}\left(\mathbf{B}\bar{\mathbf{u}}^{r}+\mathbf{B}^{*}\tilde{\mathbf{u}}^{r}\right)d\Omega-\int_{\Omega}\mathbf{B}^{*T}\mathbf{D}\left(\mathbf{B}\delta\bar{\mathbf{u}}+\mathbf{B}^{*}\delta\tilde{\mathbf{u}}\right)d\Omega+\int_{\Omega}\mathbf{B}^{*T}\mathbf{D}\frac{1}{3}\mathbf{m}\beta_{s}\mathbf{N}\bar{\mathbf{T}}^{r}d\Omega\\
&+\int_{\Omega}\mathbf{B}^{*T}\mathbf{D}\frac{1}{3}\mathbf{m}\beta_{s}\mathbf{N}\delta\bar{\mathbf{T}}d\Omega+\int_{\Omega}\mathbf{B}^{*T}\mathbf{m}^{T}\alpha\mathbf{N}\bar{\mathbf{p}}_{w}^{r}d\Omega+\int_{\Omega}\mathbf{B}^{*T}\mathbf{m}^{T}\alpha\mathbf{N}\delta\bar{\mathbf{p}}_{w}d\Omega\\
&+\int_{\Omega}\mathbf{B}^{*T}\mathbf{m}^{T}\alpha p_{c}^{r}\left(\mathbf{N}\bar{\mathbf{S}}_{n}^{r}+\mathbf{N}_{d}^{*}\tilde{\mathbf{S}}_{n}^{r}\right)d\Omega+\int_{\Omega}\mathbf{B}^{*T}\mathbf{m}^{T}\alpha p_{c}^{r}\left(\mathbf{N}\delta\bar{\mathbf{S}}_{n}+\mathbf{N}_{d}^{*}\delta\tilde{\mathbf{S}}_{n}\right)d\Omega\\
&+\int_{\Omega}\mathbf{B}^{*T}\mathbf{m}^{T}\alpha S_{n}^{r}\frac{\partial p_{c}^{r}}{\partial S_{n}}\left(\mathbf{N}\delta\bar{\mathbf{S}}_{n}+\mathbf{N}_{d}^{*}\delta\tilde{\mathbf{S}}_{n}\right)d\Omega+\int_{\Omega}\mathbf{N}^{*T}\rho_{eff}^{r}\mathbf{g}d\Omega\\
&+\int_{\Omega}\mathbf{N}^{*T}\frac{\partial\rho_{eff}^{r}}{\partial p_{w}}\mathbf{g}\mathbf{N}\delta\bar{\mathbf{p}}_{w}d\Omega+\int_{\Omega}\mathbf{N}^{*T}\frac{\partial\rho_{eff}^{r}}{\partial S_{n}}\mathbf{g}\left(\mathbf{N}\delta\bar{\mathbf{S}}_{n}+\mathbf{N}_{d}^{*}\delta\tilde{\mathbf{S}}_{n}\right)d\Omega\\
&+\int_{\Omega}\mathbf{N}^{*T}\frac{\partial\rho_{eff}^{r}}{\partial T}\mathbf{g}\mathbf{N}\delta\bar{\mathbf{T}}d\Omega+\int_{\Gamma_{t}}\mathbf{N}^{*T}\hat{\mathbf{t}}d\Gamma-\int_{\Gamma_{c}}\mathbf{N}^{*T}\mathbf{t}_{c}^{r}d\Gamma\\
&-\int_{\Gamma_{c}}\mathbf{N}^{*T}\frac{\partial\mathbf{t}_{c}^{r}}{\partial\left[\!\left[u_{y'}\right]\!\right]}\mathbf{n}_{\Gamma_{c}}\cdot\left[\!\left[\mathbf{N}_{c}^{*}\right]\!\right]\delta\bar{\mathbf{u}}d\Gamma+\int_{\Gamma_{c}}\mathbf{N}^{*T}\mathbf{n}_{\Gamma_{c}}\mathbf{N}'\bar{\mathbf{p}}'^{r}d\Gamma\\
&+\int_{\Gamma_{c}}\mathbf{N}^{*T}\mathbf{n}_{\Gamma_{c}}\mathbf{N}'\delta\bar{\mathbf{p}}'d\Gamma=0
\end{aligned}
\tag{5.63}
$$

in which $\mathbf{B}=\mathbf{L}\mathbf{N}$.

Similar discretization can be made for the mass and energy field equations. They can readily be revealed from the system finite element equations, given in Section 5.4.4 and the Appendix.

5.4.2 Fracture domain discretization

In the fracture domain, a mixture velocity-mixture pressure-mixture mass density primary state variables formulation is employed. The term "mixture" is introduced here to differentiate the non-wetting phase in the fracture domain from that in the matrix domain. In the fracture domain, due to phase change, the non-wetting phase can be a mixture of gas, liquid and supercritical state. This is not the case in the matrix domain. Within the crack, the velocity, pressure and density state variables are continuous, but at the boundary with the matrix domain, the solid displacement state variable is discontinuous.

5.4.2.1 Weak form formulation

Applying the weighted residual finite element method, together with the Green's theorem, Eqs. (5.12)-(5.14) can be discretized to give:

Mass balance

$$\int_{\Gamma_c} w_1' \frac{\partial}{\partial t}\left(\rho_m' \left[\!\left[u_{y'}\right]\!\right]\right) d\Gamma - \int_{\Gamma_c} \frac{\partial w_1'}{\partial x'}\left(\rho_m' v_m' \left[\!\left[u_{y'}\right]\!\right]\right) d\Gamma = -\int_{\Gamma_c} w_1' q_n^{\Gamma_c} d\Gamma + q_n^{\mathrm{ap}} \tag{5.64}$$

Momentum balance

$$\begin{aligned}&\int_{\Gamma_c} w_2' \frac{\partial}{\partial t}\left(\rho_m' v_m' \left[\!\left[u_{y'}\right]\!\right]\right) d\Gamma - \int_{\Gamma_c} \frac{\partial w_2'}{\partial x'}\left(\left(\rho_m' v_m'^2 + \gamma'\right)\left[\!\left[u_{y'}\right]\!\right]\right) d\Gamma \\ &= -\int_{\Gamma_c} w_2' \left(\frac{\partial p'}{\partial x'}\left[\!\left[u_{y'}\right]\!\right] + p' \frac{\partial \left[\!\left[u_{y'}\right]\!\right]}{\partial x'}\right) d\Gamma + \int_{\Gamma_c} w_2' \rho_m' \left[\!\left[u_{y'}\right]\!\right] \mathbf{g}\cdot\mathbf{t}_{\Gamma_c} d\Gamma \\ &- \int_{\Gamma_c} w_2' \frac{f' \rho_m' \left|v_m'\right| v_m'}{4} d\Gamma - \int_{\Gamma_c} w_2' Q_{\mathrm{mo}}^{\Gamma_c} d\Gamma + Q_{\mathrm{mo}}^{\mathrm{ap}}\end{aligned} \tag{5.65}$$

Energy balance

$$\begin{aligned}&\int_{\Gamma_c} w_3' \frac{\partial}{\partial t}\left[\left(\rho_m' \left(h_m' + \frac{1}{2} v_m'^2\right) - p'\right)\left[\!\left[u_{y'}\right]\!\right]\right] d\Gamma - \int_{\Gamma_c} \frac{\partial w_3'}{\partial x'}\left[\rho_m' v_m' \left(h_m' + \frac{v_m'^2}{2}\right)\left[\!\left[u_{y'}\right]\!\right]\right] d\Gamma \\ &= \int_{\Gamma_c} w_3' \rho_m' v_m' \left[\!\left[u_{y'}\right]\!\right] \mathbf{g}\cdot\mathbf{t}_{\Gamma_c} d\Gamma - \int_{\Gamma_c} w_3' Q_{\mathrm{adv}}^{\Gamma_c} d\Gamma - \int_{\Gamma_c} w_3' Q_{\mathrm{conv}}^{\Gamma_c} d\Gamma + Q_{\mathrm{adv}}^{\mathrm{ap}}\end{aligned} \tag{5.66}$$

where w_1', w_2', and w_3' are the weighting functions, and the interaction terms $Q_{\mathrm{adv}}^{\mathrm{ap}}(q_n^{\mathrm{ap}}, h_n)$, $Q_{\mathrm{adv}}^{\Gamma_c}(q_n^{\Gamma_c}, h_n)$, $Q_{\mathrm{conv}}^{\Gamma_c}(T, T')$, $Q_{\mathrm{mo}}^{\Gamma_c}(q_n^{\Gamma_c}, v_m')$ and $Q_{\mathrm{mo}}^{\mathrm{ap}}(q_n^{\mathrm{ap}}, v_m')$ have been defined by Eqs. (5.35)-(5.36).

5.4.2.2 Linearization

The state variables and parameters related to the matrix-fracture domain were linearized in Section 5.4.1.2. The other state variables in Eqs. (5.64)-(5.66) and their time derivatives are linearized, as:

$$\begin{aligned}
&\rho_m'^{r+1} = \rho_m'^{r} + \delta\rho_m' \quad v_m'^{r+1} = v_m'^{r} + \delta v_m' \quad p'^{r+1} = p'^{r} + \delta p' \\
&\dot{\rho}_m'^{r+1} = \dot{\rho}_m'^{r} + \delta\dot{\rho}_m' \quad \dot{v}_m'^{r+1} = \dot{v}_m'^{r} + \delta\dot{v}_m' \quad \dot{p}'^{r+1} = \dot{p}'^{r} + \delta\dot{p}' \\
&\left[\!\left[u_{y'}\right]\!\right]^{r+1} = \left[\!\left[u_{y'}\right]\!\right]^{r} + \delta\left[\!\left[u_{y'}\right]\!\right] \\
&\left[\!\left[\dot{u}_{y'}\right]\!\right]^{r+1} = \left[\!\left[\dot{u}_{y'}\right]\!\right]^{r} + \delta\left[\!\left[\dot{u}_{y'}\right]\!\right]
\end{aligned} \tag{5.67}$$

The temperature and the specific enthalpy and its time derivative are linearized as

$$T'^{r+1} = T'^{r} + \frac{\partial T'^{r}}{\partial \rho_m'}\delta\rho_m' + \frac{\partial T'^{r}}{\partial p'}\delta p' \tag{5.68}$$

$$h_m'^{r+1} = h_m'^{r} + \frac{\partial h_m'^{r}}{\partial \rho_m'}\delta\rho_m'^{r} + \frac{\partial h_m'^{r}}{\partial p'}\delta p' \tag{5.69}$$

$$\begin{aligned}
\dot{h}_m'^{r+1} = &\left(\frac{\partial h_m'^{r}}{\partial \rho_m'} + \frac{\partial^2 h_m'^{r}}{\partial \rho_m'^2}\delta\rho_m' + \frac{\partial^2 h_m'^{r}}{\partial \rho_m' \partial p'}\delta p'\right)\left(\dot{\rho}_m'^{r} + \delta\dot{\rho}_m'\right) \\
&+ \left(\frac{\partial h_m'^{r}}{\partial p'} + \frac{\partial^2 h_m'^{r}}{\partial p'^2}\delta p' + \frac{\partial^2 h_m'^{r}}{\partial \rho_m' \partial p'}\delta\rho_m'\right)\left(\dot{p}'^{r} + \delta\dot{p}'\right)
\end{aligned} \tag{5.70}$$

The slip between phases and crack wall friction parameters are linearized as

$$\gamma'^{r+1} = \gamma'^{r} + \frac{\partial \gamma'^{r}}{\partial v_m'}\delta v_m' + \frac{\partial \gamma'^{r}}{\partial \rho_m'}\delta\rho_m' + \frac{\partial \gamma'^{r}}{\partial p'}\delta p' \tag{5.71}$$

$$f'^{r+1} = f'^{r} + \frac{\partial f'^{r}}{\partial \mathrm{Re}'}\delta\mathrm{Re}' \tag{5.72}$$

$$\begin{aligned}
f'^{r+1} = &f'^{r} + \frac{\partial f'^{r}}{\partial \mathrm{Re}'}\frac{\partial \mathrm{Re}'^{r}}{\partial v_m'}\delta v_m' + \frac{\partial f'^{r}}{\partial \mathrm{Re}'}\frac{\partial \mathrm{Re}'^{r}}{\partial \rho_m'}\delta\rho_m' \\
&+ \frac{\partial f'^{r}}{\partial \mathrm{Re}'}\frac{\partial \mathrm{Re}'^{r}}{\partial \mu_m'}\left(\frac{\partial \mu_m'^{r}}{\partial \rho_m'}\delta\rho_m' + \frac{\partial \mu_m'^{r}}{\partial p'}\delta p'\right)
\end{aligned} \tag{5.73}$$

At the boundary with the crack, the momentum flux terms, $Q_{\mathrm{mo}}^{\Gamma c}(q_n^{\Gamma c}, v_m')$ and $Q_{\mathrm{mo}}^{\mathrm{ap}}(q_n^{\mathrm{ap}}, v_m')$, are linearized using Eq. (5.36), as

$$\left(Q_{\mathrm{mo}}^{\Gamma c}\right)^{r+1} = \left(Q_{\mathrm{mo}}^{\Gamma c}\right)^{r} + \frac{\partial\left(Q_{\mathrm{mo}}^{\Gamma c}\right)^{r}}{\partial q_n^{\Gamma c}}\delta q_n^{\Gamma c} + \frac{\partial\left(Q_{\mathrm{mo}}^{\Gamma c}\right)^{r}}{\partial v_m'}\delta v_m' \tag{5.74}$$

$$\left(Q_{\mathrm{mo}}^{\mathrm{ap}}\right)^{r+1}=\left(Q_{\mathrm{mo}}^{\mathrm{ap}}\right)^{r}+\frac{\partial\left(Q_{\mathrm{mo}}^{\mathrm{ap}}\right)^{r}}{\partial q_{n}^{\mathrm{ap}}}\delta q_{n}^{\mathrm{ap}}+\frac{\partial\left(Q_{\mathrm{mo}}^{\mathrm{ap}}\right)^{r}}{\partial v_{m}'}\delta v_{m}' \tag{5.75}$$

5.4.2.3 PUM-SG formulation

The standard Galerkin finite element method and the partition of unity method are integrated to discretize the governing equations.

As stated earlier, the mixture velocity, pressure and density are continuous in the crack, but the displacement at the boundary with the matrix domain is discontinuous. Thus:

Continuous fields

Mixture velocity:

$$v_{m}'\left(x',t\right)=\mathbf{N}'\left(x'\right)\overline{\mathbf{v}}_{m}'\left(t\right) \tag{5.76}$$

Mixture pressure:

see Eq. (5.60)

Mixture mass density:

$$\rho_{m}'\left(x',t\right)=\mathbf{N}'\left(x'\right)\overline{\boldsymbol{\rho}}_{m}'\left(t\right) \tag{5.77}$$

Discontinuous field

Displacement:

see Eq. (5.53)

where $\overline{\mathbf{v}}_{m}'\left(t\right)$ and $\overline{\boldsymbol{\rho}}_{m}'\left(t\right)$ are the nodal vectors of the mixture velocity and density in the fracture domain.

5.4.2.4 Fracture domain finite element equations

Substituting Eqs. (5.53), (5.60) and (5.67)-(5.77) into Eqs. (5.64)-(5.66), together with the following assumptions for the weighting functions:

$$w_{1}'=w_{2}'=w_{3}'=\mathbf{N}' \tag{5.78}$$

the final finite element equations for the fracture domain can be formulated. For instance, the finite element equation of the mass balance is:

Mass balance

$$\int_{\Gamma_c} \mathbf{N}'^T \left[\!\left[u_{y'} \right]\!\right]^r \mathbf{N}' \dot{\overline{\boldsymbol{\rho}}}'^r_m d\Gamma + \int_{\Gamma_c} \mathbf{N}'^T \dot{\rho}'^r_m \mathbf{n}_{\Gamma_c} \cdot \left[\!\left[\mathbf{N}^*_u \right]\!\right] \delta\tilde{\mathbf{u}} d\Gamma + \int_{\Gamma_c} \mathbf{N}'^T \left[\!\left[u_{y'} \right]\!\right]^r \mathbf{N}' \delta \dot{\overline{\boldsymbol{\rho}}}'_m d\Gamma$$
$$+ \int_{\Gamma_c} \mathbf{N}'^T \rho'^r_m \mathbf{n}_{\Gamma_c} \cdot \left[\!\left[\mathbf{N}^*_u \right]\!\right] \dot{\tilde{\mathbf{u}}}^r d\Gamma + \int_{\Gamma_c} \mathbf{N}'^T \rho'^r_m \mathbf{n}_{\Gamma_c} \cdot \left[\!\left[\mathbf{N}^*_u \right]\!\right] \delta\dot{\tilde{\mathbf{u}}} d\Gamma$$
$$+ \int_{\Gamma_c} \mathbf{N}'^T \left[\!\left[\dot{u}_{y'} \right]\!\right]^r \mathbf{N}' \delta \overline{\boldsymbol{\rho}}'_m d\Gamma - \int_{\Gamma_c} \mathbf{A}'^T \rho'^r_m \left[\!\left[u_{y'} \right]\!\right]^r \mathbf{N}' \overline{\mathbf{v}}'^r_m d\Gamma$$
$$- \int_{\Gamma_c} \mathbf{A}'^T v'^r_m \left[\!\left[u_{y'} \right]\!\right]^r \mathbf{N}' \delta \overline{\boldsymbol{\rho}}'_m d\Gamma - \int_{\Gamma_c} \mathbf{A}'^T \rho'^r_m \left[\!\left[u_{y'} \right]\!\right]^r \mathbf{N}' \delta \overline{\mathbf{v}}'_m d\Gamma$$
$$- \int_{\Gamma_c} \mathbf{A}'^T \rho'^r_m v'^r_m \mathbf{n}_{\Gamma_c} \cdot \left[\!\left[\mathbf{N}^*_u \right]\!\right] \delta\tilde{\mathbf{u}} d\Gamma$$
$$= \mathbf{N}'^T \left(q^{\text{ap}}_n \right)^r + \mathbf{N}'^T \delta q^{\text{ap}}_n - \int_{\Gamma_c} \mathbf{N}'^T \mathbf{N}' \overline{\mathbf{q}}^{\Gamma_c r}_n d\Gamma - \int_{\Gamma_c} \mathbf{N}'^T \mathbf{N}' \delta \overline{\mathbf{q}}^{\Gamma_c}_n d\Gamma \tag{5.79}$$

in which $\mathbf{A}' = \partial \mathbf{N}' / \partial x'$.

Similar finite element equations can be derived for the momentum and energy balance equations. They can readily be revealed from the system finite element equations, given in Section 5.4.4 and the Appendix.

5.4.3 Matrix-Fracture domain discretization

As mentioned earlier, we distinguish two leakage paths: transverse, between the crack faces and the matrix domain; and longitudinal, between the matrix domain and the crack aperture.

5.4.3.1 Weak form formulation

Applying the weighted residual finite element discretization procedure to Eqs. (5.17)-(5.18) yields:

Transverse leakage

$$\int_{\Gamma_c} w'_1 \left(q^{\Gamma_c}_n - k\eta_n \left(p' - p_w - p_c \right) \right) d\Gamma = 0 \tag{5.80}$$

where $\eta_n = \rho_n \dfrac{\overline{\alpha} k_{rn}}{\mu_n}$.

Aperture leakage

This leakage is treated as a constraint at the contact point between the crack and the reservoir, calculated as

$$q_n^{\text{ap}} - k^{\text{ap}} \eta_n^{\text{ap}} \left(p_w + p_c - p' \right) = 0 \tag{5.81}$$

where $\eta_n^{\text{ap}} = \rho_n^{\text{ap}} \dfrac{\overline{\beta} k_{rn}^{\text{ap}}}{\mu_n^{\text{ap}}}$.

5.4.3.2 Linearization

The transverse and aperture leakage fluxes are linearized in Eqs. (5.46) and (5.47). The crack leakage parameters given in Eqs. (5.80)-(5.81) are linearized as

$$\eta_n^{r+1} = \eta_n^r + \frac{\partial \eta_n^r}{\partial p_w} \delta p_w + \frac{\partial \eta_n^r}{\partial S_n} \delta S_n + \frac{\partial \eta_n^r}{\partial T} \delta T \tag{5.82}$$

$$\left(\eta_n^{\text{ap}} \right)^{r+1} = \left(\eta_n^{\text{ap}} \right)^r + \frac{\partial \left(\eta_n^{\text{ap}} \right)^r}{\partial p_w} \delta p_w + \frac{\partial \left(\eta_n^{\text{ap}} \right)^r}{\partial S_n} \delta S_n + \frac{\partial \left(\eta_n^{\text{ap}} \right)^r}{\partial T} \delta T \tag{5.83}$$

5.4.3.3 Matrix-fracture domain finite element equations

Substituting Eqs. (5.46)-(5.47) and (5.82)-(5.83) into Eqs. (5.80)-(5.81), the final finite element equations for the matrix-fracture domain can be formulated as:

Transverse leakage

$$\begin{aligned}
&\int_{\Gamma_c} \mathbf{N}'^T \mathbf{N}' \overline{\mathbf{q}}_n^{\Gamma_c r} d\Gamma + \int_{\Gamma_c} \mathbf{N}'^T \mathbf{N}' \delta \overline{\mathbf{q}}_n^{\Gamma_c} d\Gamma + \int_{\Gamma_c} \mathbf{N}'^T \eta_n^r \mathbf{N} \overline{\mathbf{p}}_w^r d\Gamma + \int_{\Gamma_c} \mathbf{N}'^T \eta_n^r p_c^r d\Gamma \\
&- \int_{\Gamma_c} \mathbf{N}'^T \eta_n^r \mathbf{N}' \overline{\mathbf{p}}'^r d\Gamma + \int_{\Gamma_c} \mathbf{N}'^T \frac{\partial \eta_n^r}{\partial p_w} \left(p_w^r + p_c^r - p'^r \right) \mathbf{N} \delta \overline{\mathbf{p}}_w d\Gamma \\
&+ \int_{\Gamma_c} \mathbf{N}'^T \frac{\partial \eta_n^r}{\partial S_n} \left(p_w^r + p_c^r - p'^r \right) \left(\mathbf{N} \delta \overline{\mathbf{S}}_n + \mathbf{N}_d^* \delta \tilde{\mathbf{S}}_n \right) d\Gamma \\
&+ \int_{\Gamma_c} \mathbf{N}'^T \frac{\partial \eta_n^r}{\partial T} \left(p_w^r + p_c^r - p'^r \right) \left(\mathbf{N} \delta \overline{\mathbf{T}} + \mathbf{N}_c^* \delta \tilde{\mathbf{T}} \right) d\Gamma + \int_{\Gamma_c} \mathbf{N}'^T \eta_n^r \mathbf{N} \delta \overline{\mathbf{p}}_w d\Gamma \\
&+ \int_{\Gamma_c} \mathbf{N}'^T \eta_n^r \frac{\partial p_c^r}{\partial S_n} \left(\mathbf{N} \delta \overline{\mathbf{S}}_n + \mathbf{N}_d^* \delta \tilde{\mathbf{S}}_n \right) d\Gamma - \int_{\Gamma_c} \mathbf{N}'^T \eta_n^r \mathbf{N}' \delta \overline{\mathbf{p}}' \; d\Gamma = 0
\end{aligned} \tag{5.84}$$

Aperture leakage

$$
\begin{aligned}
&\left(q_n^{\mathrm{ap}}\right)^r + \delta q_n^{\mathrm{ap}} - k^{\mathrm{ap}}\left(\eta_n^{\mathrm{ap}}\right)^r \left(\mathbf{N}\big|_{\mathbf{x}_{\mathrm{ap}}}\,\overline{\mathbf{p}}_w^r + p_c\big|_{\mathbf{x}_{\mathrm{ap}}}^r - \mathbf{N}'\big|_{x'_{\mathrm{ap}}}\,\overline{\mathbf{p}}'^r\right) \\
&\quad - k^{\mathrm{ap}}\frac{\partial\left(\eta_n^{\mathrm{ap}}\right)^r}{\partial p_w}\left(p_w\big|_{\mathbf{x}_{\mathrm{ap}}}^r + p_c\big|_{\mathbf{x}_{\mathrm{ap}}}^r - p'\big|_{x'_{\mathrm{ap}}}^r\right)\mathbf{N}\big|_{\mathbf{x}_{\mathrm{ap}}}\,\delta\overline{\mathbf{p}}_w \\
&\quad - k^{\mathrm{ap}}\frac{\partial\left(\eta_n^{\mathrm{ap}}\right)^r}{\partial S_g}\left(p_w\big|_{\mathbf{x}_{\mathrm{ap}}}^r + p_c\big|_{\mathbf{x}_{\mathrm{ap}}}^r - p'\big|_{x'_{\mathrm{ap}}}^r\right)\left(\mathbf{N}\big|_{\mathbf{x}_{\mathrm{ap}}}\,\delta\overline{\mathbf{S}}_n + \mathbf{N}_d^*\big|_{\mathbf{x}_{\mathrm{ap}}}\,\delta\tilde{\mathbf{S}}_n\right) \\
&\quad - k^{\mathrm{ap}}\frac{\partial\left(\eta_n^{\mathrm{ap}}\right)^r}{\partial T}\left(p_w\big|_{\mathbf{x}_{\mathrm{ap}}}^r + p_c\big|_{\mathbf{x}_{\mathrm{ap}}}^r - p'\big|_{x'_{\mathrm{ap}}}^r\right)\left(\mathbf{N}\big|_{\mathbf{x}_{\mathrm{ap}}}\,\delta\overline{\mathbf{T}} + \mathbf{N}_c^*\big|_{\mathbf{x}_{\mathrm{ap}}}\,\delta\tilde{\mathbf{T}}\right) \\
&\quad - k^{\mathrm{ap}}\left(\eta_n^{\mathrm{ap}}\right)^r \mathbf{N}\big|_{\mathbf{x}_{\mathrm{ap}}}\,\delta\overline{\mathbf{p}}_w - k^{\mathrm{ap}}\left(\eta_n^{\mathrm{ap}}\right)^r \frac{\partial\, p_c\big|_{\mathbf{x}_{\mathrm{ap}}}^r}{\partial S_n}\left(\mathbf{N}\big|_{\mathbf{x}_{\mathrm{ap}}}\,\delta\overline{\mathbf{S}}_n + \mathbf{N}_d^*\big|_{\mathbf{x}_{\mathrm{ap}}}\,\delta\tilde{\mathbf{S}}_n\right) \\
&\quad + k^{\mathrm{ap}}\left(\eta_n^{\mathrm{ap}}\right)^r \mathbf{N}'\big|_{x'_{\mathrm{ap}}}\,\delta\overline{\mathbf{p}}' = 0
\end{aligned}
\tag{5.85}
$$

in which $\mathbf{x}_{\mathrm{ap}}$ and x'_{ap} are the coordinates of the crack aperture in the global and local coordinate systems, respectively.

5.4.4 System finite element equation

Putting the finite element equations of the three domains in a matrix form, gives the finite element equation of the entire system, which can be described as

$$
\mathbf{K}\delta\mathbf{X} + \mathbf{C}\delta\dot{\mathbf{X}} = \mathbf{f} - \mathbf{K}_0\mathbf{X}^r + \mathbf{C}_0\dot{\mathbf{X}}^r \tag{5.86}
$$

in which

$$
\begin{aligned}
\delta\mathbf{X} &= \left(\delta\overline{\mathbf{u}} \quad \delta\tilde{\mathbf{u}} \quad \delta\overline{\mathbf{p}}_w \quad \delta\overline{\mathbf{S}}_n \quad \delta\tilde{\mathbf{S}}_n \quad \delta\overline{\mathbf{T}} \quad \delta\overline{\mathbf{v}}'_m \quad \delta\overline{\mathbf{p}}' \quad \delta\overline{\boldsymbol{\rho}}'_m \quad \delta\overline{\mathbf{q}}_n^{\Gamma c} \quad \delta q_n^{\mathrm{ap}}\right)^T \\
\delta\dot{\mathbf{X}} &= \left(\delta\dot{\overline{\mathbf{u}}} \quad \delta\dot{\tilde{\mathbf{u}}} \quad \delta\dot{\overline{\mathbf{p}}}_w \quad \delta\dot{\overline{\mathbf{S}}}_n \quad \delta\dot{\tilde{\mathbf{S}}}_n \quad \delta\dot{\overline{\mathbf{T}}} \quad \delta\dot{\overline{\mathbf{v}}}'_m \quad \delta\dot{\overline{\mathbf{p}}}' \quad \delta\dot{\overline{\boldsymbol{\rho}}}'_m \quad \delta\dot{\overline{\mathbf{q}}}_n^{\Gamma c} \quad \delta\dot{q}_n^{\mathrm{ap}}\right)^T \\
\mathbf{X}^r &= \left(\overline{\mathbf{u}}^r \quad \tilde{\mathbf{u}}^r \quad \overline{\mathbf{p}}_w^r \quad \overline{\mathbf{S}}_n^r \quad \tilde{\mathbf{S}}_n^r \quad \overline{\mathbf{T}}^r \quad \overline{\mathbf{v}}_m'^r \quad \overline{\mathbf{p}}'^r \quad \overline{\boldsymbol{\rho}}_m'^r \quad \overline{\mathbf{q}}_n^{\Gamma c r} \quad q_n^{\mathrm{ap} r}\right)^T \\
\dot{\mathbf{X}}^r &= \left(\dot{\overline{\mathbf{u}}}^r \quad \dot{\tilde{\mathbf{u}}}^r \quad \dot{\overline{\mathbf{p}}}_w^r \quad \dot{\overline{\mathbf{S}}}_n^r \quad \dot{\tilde{\mathbf{S}}}_n^r \quad \dot{\overline{\mathbf{T}}}^r \quad \dot{\overline{\mathbf{v}}}_m'^r \quad \dot{\overline{\mathbf{p}}}'^r \quad \dot{\overline{\boldsymbol{\rho}}}_m'^r \quad \dot{\overline{\mathbf{q}}}_n^{\Gamma c r} \quad \dot{q}_n^{\mathrm{ap} r}\right)^T \\
\mathbf{f} &= \left(\mathbf{f}_1 \quad \cdots \quad \mathbf{f}_{11}\right)^T
\end{aligned}
\tag{5.87}
$$

Details of the matrices terms are given in the Appendix.

5.4.5 Time discretization

We utilize the θ-finite difference time integration scheme to discretize Eq. (5.86), giving

$$(\mathbf{C}+\theta\Delta t\mathbf{K})\delta\mathbf{X}_{n+1}=(\mathbf{C}-(1-\theta)\Delta t\mathbf{K})\delta\mathbf{X}_n+\theta\Delta t\mathbf{f}_{n+1}+(1-\theta)\Delta t\mathbf{f}_n \qquad (5.88)$$

in which n is a time step, and $0\le\theta\le1$ is a time integration parameter. Eq. (5.88) is solved using a standard direct solver.

5.5 Numerical example

A numerical example demonstrating the geometry- and the effectively mesh-independent computational capabilities of the proposed model to simulate thermo-hydrodynamic-mechanical multiphase flow in a fracturing porous medium is given here. The geometry, material parameters and initial and boundary conditions are designed to highlight the model features, including: multiphase flow with supercritical non-wetting fluid flow in the porous domain; phase change in the fracture domain; solid deformation; crack propagation due to fluid dynamics; leakage via the porous domain layers and via the fracture-matrix domain; and heat transfer. No crack initiation, neither slip between phases is considered. A plane strain condition is considered.

A 70 m x 70 m three layers porous medium, representing a CO_2 sequestration reservoir, a permeable cap rock, and a relatively stiff upper layer, is designed for this purpose. A permeable cap rock is designated to emphasize the CO_2 leakage via the reservoir upper boundary, and a relatively stiff upper layer is designated to stop crack propagation and emphasize the leakage via the fracture-matrix boundaries. Fig. 5.3 shows the geometry and the initial and boundary conditions. The fluids properties are given in Table 5.1, the matrix domain properties are given in Table 5.2, and the fracture-matrix domain properties are given in Table 5.3. The CO_2 is injected along a 10 m surface in the middle of the reservoir bottom boundary, with 1.437 kg/s flow rate. This injection projection and location is designated to emphasize the uplifting of the reservoir upper boundary.

The reservoir is initially saturated with water, i.e. $S_{w0}=1$, $S_{n0}=0$. The solid displacement, pore water pressure and temperature initial conditions are:

$$\mathbf{u}_0=0 \;\;;\;\; p_{w0}=8+0.01467z \text{ MPa} \;\;;\;\; T_0=313.15+0.0333z \text{ K} \qquad (5.89)$$

in which z is the depth, measured from the top boundary of the domain.

An initial crack is assumed to exist. The crack is 10 cm wide and extends for four finite elements (in this example 21.5 m). The crack is initially filled with a fluid with mass density equal to $1\ \mathrm{kg/m^3}$, pressure equal to 1 atm, and velocity equal to $0\ \mathrm{m/s}$.

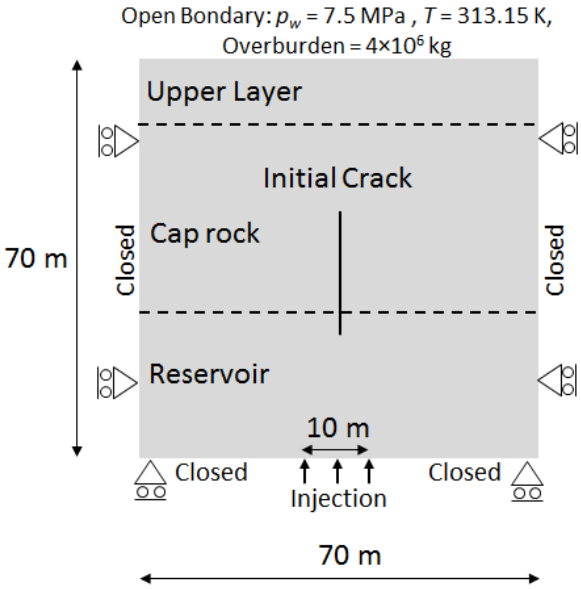

Fig. 5.3 Problem definition; geometry, and thermo-hydro-mechanical boundary conditions.

Table 5.1 Fluids properties

	Water	**CO_2**
Density Bulk modulus Thermal expansion coefficient	Section 5.3.5	
Thermal conductivity [$W \cdot m^{-1} \cdot K^{-1}$]	0.56	0.07
Isobaric specific heat capacity [kJ/kg]	4179	3500

Table 5.2 Matrix domain properties

	Reservoir (high permeable)	**Cap rock (low permeable)**	**Upper layer (low permeable)**
Permeability [m^2]	2.0×10^{-12}	5.0×10^{-14}	5.0×10^{-14}
Porosity [-]	0.15	0.1	0.1
Entry pressure (Brooks-Corey) [kPa]	60	80	80
Pore size distribution index (Brooks-Corey) $\hat{\theta}$ [-]	1.8	5.0	5.0
Water residual saturation [-]	0	0	0
CO_2 residual saturation [-]	0	0	0
Young's modulus [GPa]	75	95	95
Poisson's ratio [-]	0.4	0.4	0.4
Ultimate tensile strength [MPa]	12	15	25
Crack fracture energy [$N . m^{-1}$]	40.0	50.0	100.0
Density [kg/m^3]	2000	2000	2000
Thermal expansion coefficient [K^{-1}]	2×10^{-5}	1.5×10^{-5}	1.5×10^{-5}
Thermal conductivity [$W\cdot m^{-1}\cdot K^{-1}$]	4.5	3.5	3.5
Isobaric specific heat capacity [kJ/kg]	0.9	1.2	1.2

Table 5.3 Fracture-matrix domain properties

Crack transverse leakage shape factor ($\overline{\alpha}$) [m^{-1}]	0.1
Crack aperture leakage shape factor ($\overline{\beta}$ [m^{-1}]	0.1
Roughness of the crack surfaces [-]	5.0×10^{-6}

The finite element mesh is shown in Fig. 5.4. It consists of 169 linear quadrilateral elements. Such a mesh is quite coarse for such an analysis, but utilized here to demonstrate the computational capabilities of the model. Two important features can be seen from the discretization of the geometry: (i) the boundary between the reservoir and the cap rock is located inside the elements, and (ii) this boundary overlaps with the initial crack, which entails an overlap in the partition of unity procedure in the element which accommodates both discontinuities. As a result, the nodes of this element are enhanced twice; one due to saturation discontinuity and another due to displacement discontinuity.

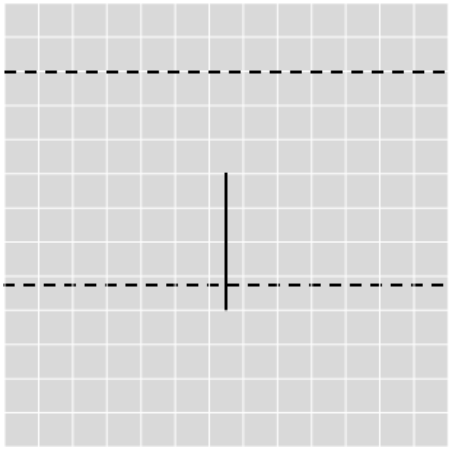

Fig. 5.4 Finite element mesh, 169 linear elements

The computational results are shown in Fig. 5.5. The figure consists of three columns showing different aspects of the thermo-hydrodynamic-mechanical behavior of the system, after: a) 25,850 s (around 7 hours), just before the first crack propagation starts; b) 26,900 s (around 8 hours), just before the third crack propagation starts; and c) 33,500 s (around 9.5 hours), almost one hour after the transverse leakage from the fracture-matrix domain starts. The interpretation of this figure will be overlapped with the interpretation of Fig. 5.6 and Fig. 5.7.

The first row in Fig. 5.5 shows the finite element mesh and the status of the three crack propagation stages.

The second row in Fig. 5.5 shows the CO_2 saturation distribution. The figure shows that due to buoyancy forces, the CO_2 accumulates at the upper boundary of the reservoir, followed by two leakage mechanisms. The first leakage occurs at the boundary between the reservoir and the cap rock. This kind of leakage typically occurs due to the discontinuity in the saturation field between layers with different hydraulic properties. In Arzanfudi et al. (2014) a detailed treatment for modeling such a boundary is given. The second leakage occurs through the crack aperture. This kind of leakage

occurs due to fluid dynamics, derived in this chapter. This leakage is clearly manifested in the tapering of the CO_2 plume at the fracture-reservoir zone.

Upon CO_2 arrival to the crack aperture, it leaks into the crack, causing a pressure built-up, followed by an increase in the solid phase stresses. When the maximum principal stress at the crack tip exceeds the tensile strength of the solid matrix, the crack propagates. Fig. 5.6 shows the progression of the maximum principal stress at the crack tip with time. It shows that when the maximum principal stress exceeds $\sigma_u = 15$ MPa, it suddenly decreases, indicating the occurrence of crack propagation and fluid expansion inside the crack. This process is repeated, in this example, three times. After the third propagation, the crack stops because it encounters the upper layer, which has a relatively high tensile strength, 25 MPa (see Table 5.2). This stage occurs after approximately 28,750 s, after which, the stress built-up at the crack tip continues. When the fluid pressure exceeds the entry pressure of the fracture-matrix zone, the transverse leakage via the crack boundaries starts. This phenomenon can be seen in the last part of the curve in Fig. 5.6, where the crack tip stress exhibits rate reduction. Physically, this leakage can be clearly seen in column c of the second row of Fig. 5.5. The leakage at the upper part of the crack is highest because the pressure gradient between the fracture fluid and the matrix fluid is highest.

The third row in Fig. 5.5 shows the vertical deformation in the porous domain. Two observations can be outlined from this figure: (i) heaving of the reservoir upper boundary occurs in the area above the injection zone, and (ii) heaving of the upper layer is more on the sides of the geometry as compared to the area above the crack (see column b). This figure is associated with Fig. 5.7, which shows the vertical displacement at the boundary between the reservoir and the cap rock at the three corresponding times. The figure shows that, due to the presence of the crack, there is a clear discontinuity in the deformation profile.

The fourth row in Fig. 5.5 shows the horizontal deformation, indicating the horizontal crack opening, which increases with crack propagation. The figure indicates that the crack has increased by approximately 8 mm from the initial crack opening.

The fifth row in Fig. 5.5 shows the temperature distribution. As expected, the heat flow front is slower than the fluid flow front. For the time span of this example, which is around 10 hours, the temperature seems to have little effect on the reservoir behavior. This indicates that the injected CO_2 arrives to the crack, with its original supercritical state.

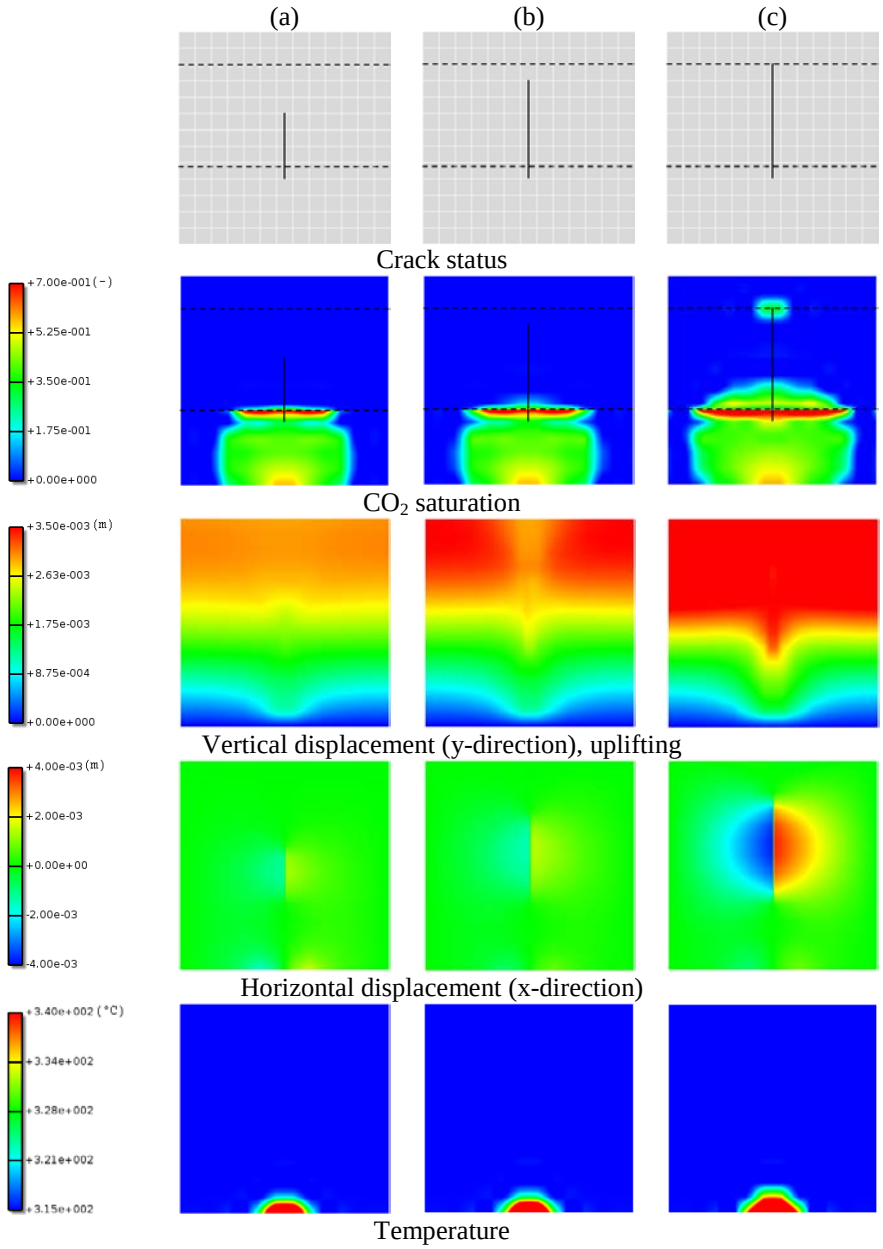

Fig. 5.5 Computational results at: (a) t = 25,850 s (just before the first crack propagation), (b) t = 26,900 s (just before the third crack propagation), and (c) t = 33,500 s (around one hour after the transverse leakage startup)

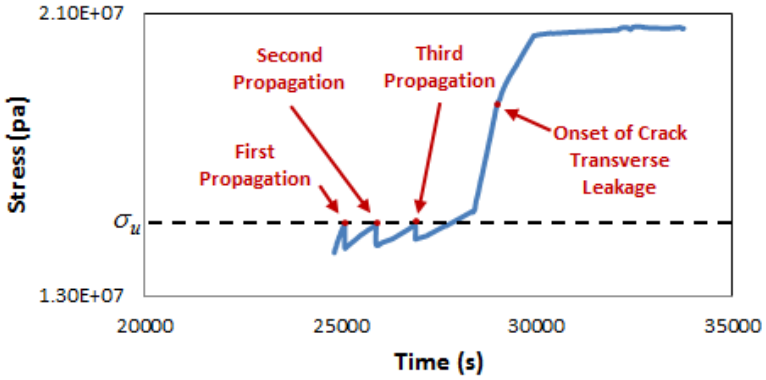

Fig. 5.6 Maximum principal effective stress at the crack tip

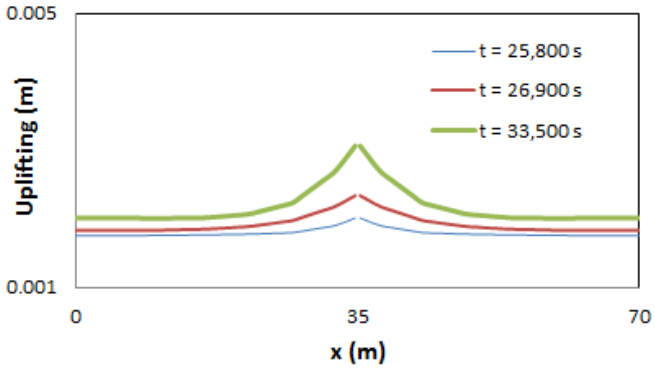

Fig. 5.7 Uplifting of reservoir-cap rock boundary

Fig. 5.8 and Fig. 5.9 illustrate the coupling effect of CO_2 leakage from the reservoir to the crack aperture, and from the fracture-matrix boundaries, respectively. Upon entering the initial crack, around 25,100 s, Fig. 5.8 shows a sudden increase in leakage flow rate through the crack aperture. By filling the crack volume, the flow rate decreases, while the CO_2 is still accumulating at the crack tip. At the first propagation, around 25,850 s, the isentropic process prevails by an immediate expansion of the CO_2 in the existing crack into the newly formed crack volume, causing a drop in pressure accompanied by a sharp increase in the CO_2 leakage from the reservoir to the crack aperture. Upon filling the crack volume, the flow rate decreases again, and this

condition holds until the second crack propagation takes place at around 26,950 s, giving rise to a sudden increase in the leakage rate. After this, as a result of CO_2 accumulation inside the crack, the flow rate starts to decrease again. By the halt of crack propagation, the pressure built-up in the crack continues, and at around 29,300 s the CO_2 starts to leak from the fracture-matrix boundaries, as shown in Fig. 5.9. The leakage from the crack boundaries is associated with an increment in flow rate into the crack aperture, as clearly shown in the last part of the curve in Fig. 5.8.

Fig. 5.10 shows the pressure distribution along the crack at the three corresponding times. The figure shows that the fluid pressure inside the crack increases with time, but spatially it is almost constant, due to the fact that the pressure builds-up is due to hydrodynamics rather than hydrostatic.

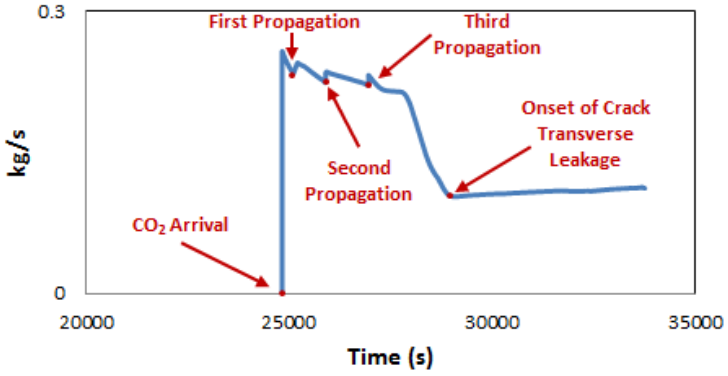

Fig. 5.8 CO_2 leakage rate from the reservoir to the crack aperture

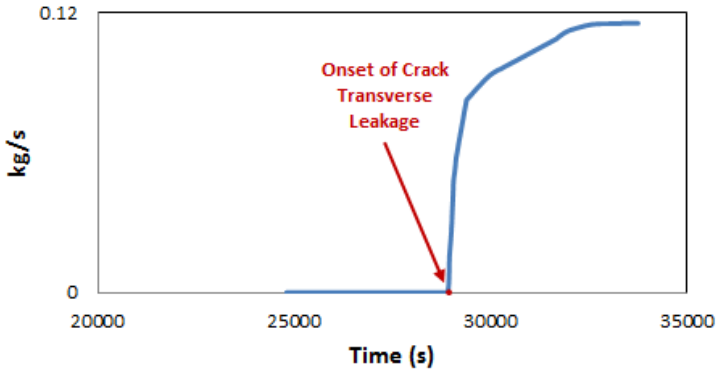

Fig. 5.9 CO_2 leakage rate from the fracture-matrix boundaries

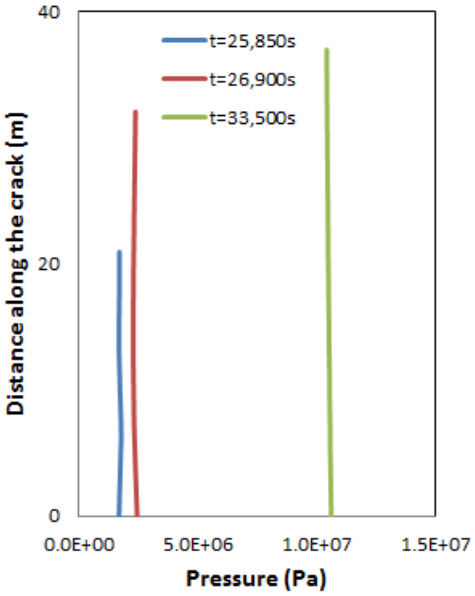

Fig. 5.10 Pressure distribution along the crack.

Fig. 5.11 illustrates the projection of CO_2 state into the CO_2 phase diagram, at a point in the middle of the crack. As mentioned earlier, initially, the crack is assumed to be filled with CO_2 with almost zero density and pressure. Upon leakage via the crack aperture, the CO_2 exhibits a sudden alteration in its pressure and density, giving rise to phase change from the supercritical state to the liquid-gas mixture state. Upon first crack propagation, as a result of the increase in crack volume and the associated isentropic fluid expansion process, a reduction in pressure and density occurs. After that, as a result of increasing the crack volume, more leakage takes place, associated with an increase in pressure and density. This continues until the occurrence of the second crack propagation, after which the same phenomenon takes place. By the halt of the crack propagation due to the encountering of the upper layer, more CO_2 enters into the crack, causing an increase in pressure and density, which gives rise to a second phase change; this time, from the mixture state to a liquid state, then back to its original supercritical state. After reaching a certain pressure-density level, the transverse leakage from the fracture-matrix boundaries starts, shown as a turning point in the pressure-density curve in Fig. 5.11.

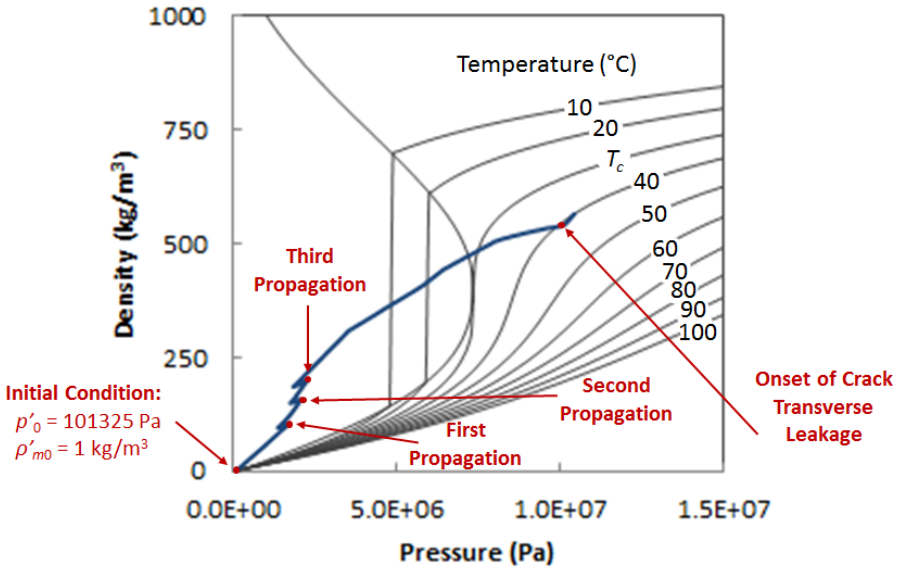

Fig. 5.11 Phase diagram projection of CO_2 state at a mid-point in the crack

To examine the computational efficiency and the effective mesh-independency of the model, the same numerical problem (base case) is solved using two more mesh sizes: a coarser mesh, 49 linear quadrilateral elements; and a finer mesh, 529 linear quadrilateral elements, shown in Fig. 5.12 and Fig. 5.13, the first row. The computational results are presented in Fig. 5.12 and Fig. 5.13, at the same time intervals as for the base case, i.e. at 25,850 s, 26,900 s, and 33,500 s.

The figures show that the computational results obtained from these mesh sizes are similar in trend and range of magnitudes to those computed by the base case mesh. In the coarser mesh, however, the magnitudes are smeared over larger elements, whereas the finer mesh gives a sharper field solution. This is apparent in the leakage at the matrix-fracture boundary, which is not clearly shown in the second row of Fig. 5.12.

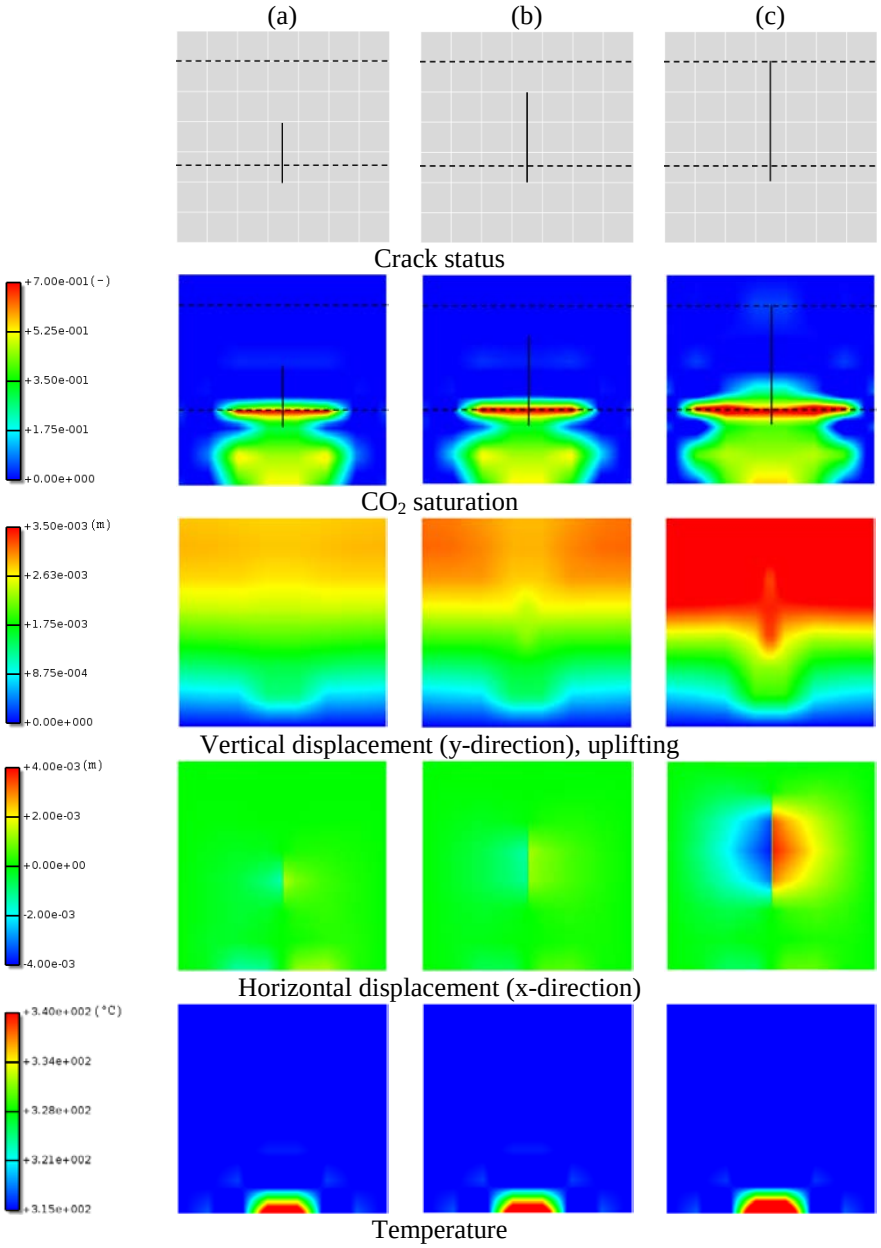

Fig. 5.12 Computational results at: (a) t = 25,850 s, (b) t = 26,900 s, and (c) t = 33,500 s

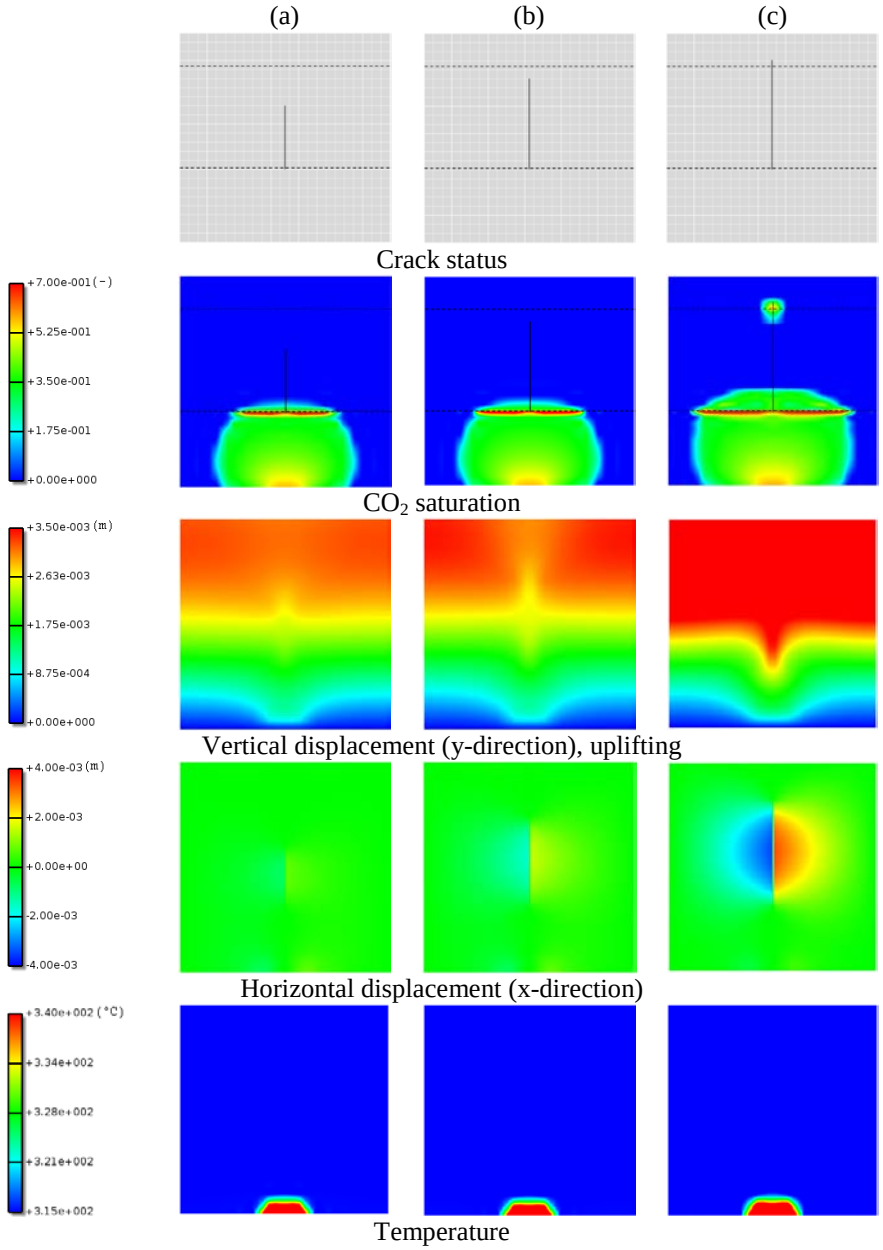

Fig. 5.13 Computational results at: (a) t = 25,850 s, (b) t = 26,900 s, and (c) t = 33,500 s

To emphasize the leakage at the fracture-matrix boundaries, we conducted an analysis, in which the CO_2 leakage at the reservoir-cap rock boundary is hindered by increasing the cap rock entry pressure. The initial crack is made off-center to emphasize skewed fluid flow. Fig. 5.14 shows the computed CO_2 saturation distribution. The figure clearly shows that as only leakage via the crack aperture is allowed, it gives rise to more CO_2 accumulation inside the crack, and hence, promoting more CO_2 leakage through the fracture-matrix boundaries.

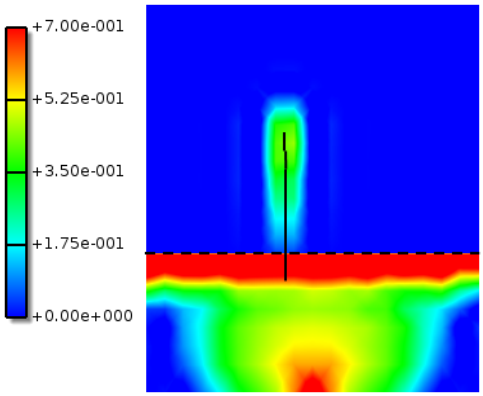

Fig. 5.14 CO_2 saturation for the no-layer-leakage case

5.6 Conclusions

A fully coupled thermo-hydrodynamic-mechanical computational model simulating multiphase flow in a deformable porous solid, exhibiting crack propagation and fluid dynamics inside the crack, is introduced. The geometry is described by a matrix domain, a fracture domain, and a matrix-fracture domain. The fluid flow in the matrix domain is governed by Darcy's law, in the fracture domain by the Navier-Stokes equations, and in the matrix-fracture domain by a leakage term derived from Darcy's law. We utilize the representative elementary volume averaging theory to formulate the multiphase phase flow in the porous matrix, and the drift-flux model to formulate the dynamic fluid flow in the fracture. The numerical solution is conducted using a mixed finite element discretization scheme, which integrates the standard Galerkin finite element method and the extended finite element method.

Several features characterize the originality of the proposed model:

1. Compared to models utilizing the Reynolds-like equations, the fluid flow in the fracture is modeled based on the Navier-Stokes equations, which are physically more representative. The fracture fluid is compressible and exhibits phase change, buoyancy, and convective heat transfer. The fluid transmissivity and leakage are computed as a natural result of the coupled balance equations in the matrix and in the fracture, unlike formulations, which are based on a cubic-like law.

2. Compared to models utilizing the Navier-Stokes equations, the fluid in the fracture is modeled as a multiphase, exhibiting phase change.

3. The mass and energy inside the crack are conserved due to the imposition of the isentropic expansion process. By expansion, the fluid volume increases, causing the pressure to drop, and the entropy to stay constant. This effect is not considered in literature dealing with crack propagation in porous media. Instead, they assume that the newly created volume is filled by the matrix fluid. However, physically, it is more likely that the fluid in the crack fills-in the newly created volume.

4. The numerical model, despite the relatively large number of coupled degrees of freedom describing state variables with significantly different physical nature per node, is computationally efficient, and geometry- and effectively mesh-independent. The use of the mixed discretization scheme made these features unique for this model.

5. The model is generic and can, with minor fine tuning, be applied to other applications, including hydraulic fracturing, high enthalpy geothermal systems, and compressed air or other gases energy storages.

The focus in this work, however, is placed on modeling the different physical processes involved in multiphase flow in deformable and fracturing porous media, with less emphasis on the constitutive behavior of the solid phase. The solid phase is assumed linear elastic, and no crack initiation is considered. The crack propagation is modeled by crossing a whole element per increment. In principle, the crack exhibits propagation velocity (Schrefler et al. 2006), and can stop anywhere in the element or cross more than one element. In a follow up work, emphasis will be placed on the solid phase constitutive behavior.

5.7 Appendix: Components of FEM matrices

K matrix terms

$$\mathbf{K}_{1-1} = -\int_{\Omega} \mathbf{B}^T \mathbf{D}\mathbf{B} d\Omega; \quad \mathbf{K}_{1-2} = -\int_{\Omega} \mathbf{B}^T \mathbf{D}\mathbf{B}^* d\Omega$$

$$\mathbf{K}_{1-3} = +\int_{\Omega} \mathbf{B}^T \mathbf{m}\alpha \mathbf{N} d\Omega + \int_{\Omega} \mathbf{N}_u^T \frac{\partial \rho_{eff}^r}{\partial p_w} \mathbf{g}\mathbf{N} d\Omega;$$

$$\mathbf{K}_{1-4} = \int_{\Omega} \mathbf{B}^T \mathbf{m}\alpha p_c^r \mathbf{N} d\Omega + \int_{\Omega} \mathbf{B}^T \mathbf{m}\alpha S_n^r \frac{\partial p_c^r}{\partial S_n} \mathbf{N} d\Omega + \int_{\Omega} \mathbf{N}_u^T \frac{\partial \rho_{eff}^r}{\partial S_n} \mathbf{g}\mathbf{N} d\Omega$$

$$\mathbf{K}_{1-5} = \int_{\Omega} \mathbf{B}^T \mathbf{m}\alpha p_c^r \mathbf{N}_d^* d\Omega + \int_{\Omega} \mathbf{B}^T \mathbf{m}\alpha S_n^r \frac{\partial p_c^r}{\partial S_n} \mathbf{N}_d^* d\Omega + \int_{\Omega} \mathbf{N}_u^T \frac{\partial \rho_{eff}^r}{\partial S_n} \mathbf{g}\mathbf{N}_d^* d\Omega$$

$$\mathbf{K}_{1-6} = \int_{\Omega} \mathbf{B}^T \mathbf{D} \frac{1}{3} \mathbf{m}\beta_s \mathbf{N} d\Omega + \int_{\Omega} \mathbf{N}_u^T \frac{\partial \rho_{eff}^r}{\partial T} \mathbf{g}\mathbf{N} d\Omega;$$

$$\mathbf{K}_{2-1} = -\int_{\Omega} \mathbf{B}^{*T} \mathbf{D}\mathbf{B} d\Omega; \quad \mathbf{K}_{2-2} = -\int_{\Omega} \mathbf{B}^{*T} \mathbf{D}\mathbf{B}^* d\Omega - \int_{\Gamma_c} \mathbf{N}_u^{*T} \frac{\partial \mathbf{t}_c^r}{\partial \left[\!\left[u_{y'} \right]\!\right]} \mathbf{n}_{\Gamma_c} \cdot \left[\!\left[\mathbf{N}_u^* \right]\!\right] d\Gamma;$$

$$\mathbf{K}_{2-3} = \int_{\Omega} \mathbf{B}^{*T} \mathbf{m}\alpha \mathbf{N} d\Omega + \int_{\Omega} \mathbf{N}_u^{*T} \frac{\partial \rho_{eff}^r}{\partial p_w} \mathbf{g}\mathbf{N} d\Omega;$$

$$\mathbf{K}_{2-4} = \int_{\Omega} \mathbf{B}^{*T} \mathbf{m}\alpha p_c^r \mathbf{N} d\Omega + \int_{\Omega} \mathbf{B}^{*T} \mathbf{m}\alpha S_n^r \frac{\partial p_c^r}{\partial S_n} \mathbf{N} d\Omega + \int_{\Omega} \mathbf{N}_u^{*T} \frac{\partial \rho_{eff}^r}{\partial S_n} \mathbf{g}\mathbf{N} d\Omega$$

$$\mathbf{K}_{2-5} = \int_{\Omega} \mathbf{B}^{*T} \mathbf{m}\alpha p_c^r \mathbf{N}_d^* d\Omega + \int_{\Omega} \mathbf{B}^{*T} \mathbf{m}\alpha S_n^r \frac{\partial p_c^r}{\partial S_n} \mathbf{N}_d^* d\Omega + \int_{\Omega} \mathbf{N}_u^{*T} \frac{\partial \rho_{eff}^r}{\partial S_n} \mathbf{g}\mathbf{N}_d^* d\Omega$$

$$\mathbf{K}_{2-6} = \int_{\Omega} \mathbf{B}^{*T} \mathbf{D} \frac{1}{3} \mathbf{m}\beta_s \mathbf{N} d\Omega + \int_{\Omega} \mathbf{N}_u^{*T} \frac{\partial \rho_{eff}^r}{\partial T} \mathbf{g}\mathbf{N} d\Omega; \quad \mathbf{K}_{2-8} = \int_{\Gamma_c} \left[\!\left[\mathbf{N}_u^{*T} \right]\!\right] \alpha \mathbf{n}_{\Gamma_c} \mathbf{N}' d\Gamma$$

$$\mathbf{K}_{3-3} = \int_\Omega \mathbf{N}^T \frac{\partial d_1^r}{\partial p_w} \dot{p}_w^r \mathbf{N} d\Omega + \int_\Omega \mathbf{N}^T \frac{\partial d_2^r}{\partial p_w} \dot{S}_n^r \mathbf{N} d\Omega + \int_\Omega \mathbf{N}^T \frac{\partial d_3^r}{\partial p_w} \dot{T}^r \mathbf{N} d\Omega$$
$$+ \int_\Omega \mathbf{N}^T \frac{\partial d_4^r}{\partial p_w} \mathbf{m}^T \mathbf{L} \dot{\mathbf{u}}^r \mathbf{N} d\Omega + \int_\Omega \nabla \mathbf{N}^T \cdot \mathbf{c}_1^r \nabla \mathbf{N} d\Omega + \int_\Omega \nabla \mathbf{N}^T \cdot \frac{\partial \mathbf{c}_1^r}{\partial p_w} \nabla p_w^r \mathbf{N} d\Omega$$
$$- \int_\Omega \nabla \mathbf{N}^T \cdot \frac{\partial \mathbf{G}_1^r}{\partial p_w} \mathbf{N} d\Omega$$

$$\mathbf{K}_{3-4} = \int_\Omega \mathbf{N}^T \frac{\partial d_1^r}{\partial S_n} \dot{p}_w^r \mathbf{N} d\Omega + \int_\Omega \mathbf{N}^T \frac{\partial d_2^r}{\partial S_n} \dot{S}_n^r \mathbf{N} d\Omega + \int_\Omega \mathbf{N}^T \frac{\partial d_3^r}{\partial S_n} \dot{T}^r \mathbf{N} d\Omega$$
$$+ \int_\Omega \mathbf{N}^T \frac{\partial d_4^r}{\partial S_n} \mathbf{m}^T \mathbf{L} \dot{\mathbf{u}}^r \mathbf{N} d\Omega + \int_\Omega \nabla \mathbf{N}^T \cdot \frac{\partial \mathbf{c}_1^r}{\partial S_n} \nabla p_w^r \mathbf{N} d\Omega - \int_\Omega \nabla \mathbf{N}^T \cdot \frac{\partial \mathbf{G}_1^r}{\partial S_n} \mathbf{N} d\Omega$$

$$\mathbf{K}_{3-5} = \int_\Omega \mathbf{N}^T \frac{\partial d_1^r}{\partial S_n} \dot{p}_w^r \mathbf{N}_d^* d\Omega + \int_\Omega \mathbf{N}^T \frac{\partial d_2^r}{\partial S_n} \dot{S}_n^r \mathbf{N}_d^* d\Omega + \int_\Omega \mathbf{N}^T \frac{\partial d_3^r}{\partial S_n} \dot{T}^r \mathbf{N}_d^* d\Omega$$
$$+ \int_\Omega \mathbf{N}^T \frac{\partial d_4^r}{\partial S_n} \mathbf{m}^T \mathbf{L} \dot{\mathbf{u}}^r \mathbf{N}_d^* d\Omega + \int_\Omega \nabla \mathbf{N}^T \cdot \frac{\partial \mathbf{c}_1^r}{\partial S_n} \nabla p_w^r \mathbf{N}_d^* d\Omega - \int_\Omega \nabla \mathbf{N}^T \cdot \frac{\partial \mathbf{G}_1^r}{\partial S_n} \mathbf{N}_d^* d\Omega$$

$$\mathbf{K}_{3-6} = \int_\Omega \mathbf{N}^T \frac{\partial d_1^r}{\partial T} \dot{p}_w^r \mathbf{N} d\Omega + \int_\Omega \mathbf{N}^T \frac{\partial d_2^r}{\partial T} \dot{S}_n^r \mathbf{N} d\Omega + \int_\Omega \mathbf{N}^T \frac{\partial d_3^r}{\partial T} \dot{T}^r \mathbf{N} d\Omega$$
$$+ \int_\Omega \mathbf{N}^T \frac{\partial d_4^r}{\partial T} \mathbf{m}^T \mathbf{L} \dot{\mathbf{u}}^r \mathbf{N} d\Omega + \int_\Omega \nabla \mathbf{N}^T \cdot \frac{\partial \mathbf{c}_1^r}{\partial T} \nabla p_w^r \mathbf{N} d\Omega - \int_\Omega \nabla \mathbf{N}^T \cdot \frac{\partial \mathbf{G}_1^r}{\partial T} \mathbf{N} d\Omega$$

$$\mathbf{K}_{4-3} = \int_\Omega \mathbf{N}^T \frac{\partial d_5^r}{\partial p_w} \dot{p}_w^r \mathbf{N} d\Omega + \int_\Omega \mathbf{N}^T \frac{\partial d_6^r}{\partial p_w} \dot{S}_n^r \mathbf{N} d\Omega + \int_\Omega \mathbf{N}^T \frac{\partial d_7^r}{\partial p_w} \dot{T}^r \mathbf{N} d\Omega$$
$$+ \int_\Omega \mathbf{N}^T \frac{\partial d_8^r}{\partial p_w} \mathbf{m}^T \mathbf{L} \dot{\mathbf{u}}^r \mathbf{N} d\Omega + \int_\Omega \nabla \mathbf{N}^T \cdot \mathbf{c}_2^r \nabla \mathbf{N} d\Omega + \int_\Omega \nabla \mathbf{N}^T \cdot \frac{\partial \mathbf{c}_2^r}{\partial p_w} \nabla p_w^r \mathbf{N} d\Omega$$
$$+ \int_\Omega \nabla \mathbf{N}^T \cdot \frac{\partial \mathbf{c}_3^r}{\partial p_w} \nabla S_n^r \mathbf{N} d\Omega - \int_\Omega \nabla \mathbf{N}^T \cdot \frac{\partial \mathbf{G}_2^r}{\partial p_w} \mathbf{N} d\Omega$$

$$\mathbf{K}_{4-4} = \int_\Omega \mathbf{N}^T \frac{\partial d_5^r}{\partial S_n} \dot{p}_w^r \mathbf{N} d\Omega + \int_\Omega \mathbf{N}^T \frac{\partial d_6^r}{\partial S_n} \dot{S}_n^r \mathbf{N} d\Omega + \int_\Omega \mathbf{N}^T \frac{\partial d_7^r}{\partial S_n} \dot{T}^r \mathbf{N} d\Omega$$
$$+ \int_\Omega \mathbf{N}^T \frac{\partial d_8^r}{\partial S_n} \mathbf{m}^T \mathbf{L} \dot{\mathbf{u}}^r \mathbf{N} d\Omega + \int_\Omega \nabla \mathbf{N}^T \cdot \frac{\partial \mathbf{c}_2^r}{\partial S_n} \nabla p_w^r \mathbf{N} d\Omega + \int_\Omega \nabla \mathbf{N}^T \cdot \mathbf{c}_3^r \nabla \mathbf{N} d\Omega$$
$$+ \int_\Omega \nabla \mathbf{N}^T \cdot \frac{\partial \mathbf{c}_3^r}{\partial S_n} \nabla S_n^r \mathbf{N} d\Omega - \int_\Omega \nabla \mathbf{N}^T \cdot \frac{\partial \mathbf{G}_2^r}{\partial S_n} \mathbf{N} d\Omega$$

$$\mathbf{K}_{4-5} = \int_\Omega \mathbf{N}^T \frac{\partial d_5^r}{\partial S_n} \dot{p}_w^r \mathbf{N}_d^* d\Omega + \int_\Omega \mathbf{N}^T \frac{\partial d_6^r}{\partial S_n} \dot{S}_n^r \mathbf{N}_d^* d\Omega + \int_\Omega \mathbf{N}^T \frac{\partial d_7^r}{\partial S_n} \dot{T}^r \mathbf{N}_d^* d\Omega$$
$$+ \int_\Omega \mathbf{N}^T \frac{\partial d_8^r}{\partial S_n} \mathbf{m}^T \mathbf{L} \dot{\mathbf{u}}^r \mathbf{N}_d^* d\Omega + \int_\Omega \nabla \mathbf{N}^T \cdot \frac{\partial \mathbf{c}_2^r}{\partial S_n} \nabla p_w^r \mathbf{N}_d^* d\Omega + \int_\Omega \nabla \mathbf{N}^T \cdot \mathbf{c}_3^r \nabla \mathbf{N}_d^* d\Omega$$
$$+ \int_\Omega \nabla \mathbf{N}^T \cdot \frac{\partial \mathbf{c}_3^r}{\partial S_n} \nabla S_n^r \mathbf{N}_d^* d\Omega - \int_\Omega \nabla \mathbf{N}^T \cdot \frac{\partial \mathbf{G}_2^r}{\partial S_n} \mathbf{N}_d^* d\Omega$$

$$\mathbf{K}_{4-6} = \int_\Omega \mathbf{N}^T \frac{\partial d_5^r}{\partial T} \dot{p}_w^r \mathbf{N} d\Omega + \int_\Omega \mathbf{N}^T \frac{\partial d_6^r}{\partial T} \dot{S}_n^r \mathbf{N} d\Omega + \int_\Omega \mathbf{N}^T \frac{\partial d_7^r}{\partial T} \dot{T}^r \mathbf{N} d\Omega$$
$$+ \int_\Omega \mathbf{N}^T \frac{\partial d_8^r}{\partial T} \mathbf{m}^T \mathbf{L} \dot{\mathbf{u}}^r \mathbf{N} d\Omega + \int_\Omega \nabla \mathbf{N}^T \cdot \frac{\partial \mathbf{c}_2^r}{\partial T} \nabla p_w^r \mathbf{N} d\Omega + \int_\Omega \nabla \mathbf{N}^T \cdot \frac{\partial \mathbf{c}_3^r}{\partial T} \nabla S_n^r \mathbf{N} d\Omega$$
$$- \int_\Omega \nabla \mathbf{N}^T \cdot \frac{\partial \mathbf{G}_2^r}{\partial T} \mathbf{N} d\Omega$$

$$\mathbf{K}_{4-10} = -\int_{\Gamma_c} \mathbf{N}^T \mathbf{N}' d\Gamma; \quad \mathbf{K}_{4-11} = \mathbf{N}^T \Big|_{\mathbf{x}_{\text{ap}}}$$

$$\mathbf{K}_{5-3} = \int_\Omega \mathbf{N}_d^{*T} \frac{\partial d_5^r}{\partial p_w} \dot{p}_w^r \mathbf{N} d\Omega + \int_\Omega \mathbf{N}_d^{*T} \frac{\partial d_6^r}{\partial p_w} \dot{S}_n^r \mathbf{N} d\Omega + \int_\Omega \mathbf{N}_d^{*T} \frac{\partial d_7^r}{\partial p_w} \dot{T}^r \mathbf{N} d\Omega$$
$$+ \int_\Omega \mathbf{N}_d^{*T} \frac{\partial d_8^r}{\partial p_w} \mathbf{m}^T \mathbf{L} \dot{\mathbf{u}}^r \mathbf{N} d\Omega + \int_\Omega \nabla \mathbf{N}_d^{*T} \cdot \mathbf{c}_2^r \nabla \mathbf{N} d\Omega + \int_\Omega \nabla \mathbf{N}_d^{*T} \cdot \frac{\partial \mathbf{c}_2^r}{\partial p_w} \nabla p_w^r \mathbf{N} d\Omega$$
$$+ \int_\Omega \nabla \mathbf{N}_d^{*T} \cdot \frac{\partial \mathbf{c}_3^r}{\partial p_w} \nabla S_n^r \mathbf{N} d\Omega - \int_\Omega \nabla \mathbf{N}_d^{*T} \cdot \frac{\partial \mathbf{G}_2^r}{\partial p_w} \mathbf{N} d\Omega$$

$$\mathbf{K}_{5-4} = \int_\Omega \mathbf{N}_d^{*T} \frac{\partial d_5^r}{\partial S_n} \dot{p}_w^r \mathbf{N} d\Omega + \int_\Omega \mathbf{N}_d^{*T} \frac{\partial d_6^r}{\partial S_n} \dot{S}_n^r \mathbf{N} d\Omega + \int_\Omega \mathbf{N}_d^{*T} \frac{\partial d_7^r}{\partial S_n} \dot{T}^r \mathbf{N} d\Omega$$
$$+ \int_\Omega \mathbf{N}_d^{*T} \frac{\partial d_8^r}{\partial S_n} \mathbf{m}^T \mathbf{L} \dot{\mathbf{u}}^r \mathbf{N} d\Omega + \int_\Omega \nabla \mathbf{N}_d^{*T} \cdot \frac{\partial \mathbf{c}_2^r}{\partial S_n} \nabla p_w^r \mathbf{N} d\Omega + \int_\Omega \nabla \mathbf{N}_d^{*T} \cdot \mathbf{c}_3^r \nabla \mathbf{N} d\Omega$$
$$+ \int_\Omega \nabla \mathbf{N}_d^{*T} \cdot \frac{\partial \mathbf{c}_3^r}{\partial S_n} \nabla S_n^r \mathbf{N} d\Omega - \int_\Omega \nabla \mathbf{N}_d^{*T} \cdot \frac{\partial \mathbf{G}_2^r}{\partial S_n} \mathbf{N} d\Omega$$

$$\mathbf{K}_{5-5} = \int_\Omega \mathbf{N}_d^{*T} \frac{\partial d_5^r}{\partial S_n} \dot{p}_w^r \mathbf{N}_d^* d\Omega + \int_\Omega \mathbf{N}_d^{*T} \frac{\partial d_6^r}{\partial S_n} \dot{S}_n^r \mathbf{N}_d^* d\Omega + \int_\Omega \mathbf{N}_d^{*T} \frac{\partial d_7^r}{\partial S_n} \dot{T}^r \mathbf{N}_d^* d\Omega$$
$$+ \int_\Omega \mathbf{N}_d^{*T} \frac{\partial d_8^r}{\partial S_n} \mathbf{m}^T \mathbf{L} \dot{\mathbf{u}}^r \mathbf{N}_d^* d\Omega + \int_\Omega \nabla \mathbf{N}_d^{*T} \cdot \frac{\partial \mathbf{c}_2^r}{\partial S_n} \nabla p_w^r \mathbf{N}_d^* d\Omega$$
$$+ \int_\Omega \nabla \mathbf{N}_d^{*T} \cdot \mathbf{c}_3^r \nabla \mathbf{N}_d^* d\Omega + \int_\Omega \nabla \mathbf{N}_d^{*T} \cdot \frac{\partial \mathbf{c}_3^r}{\partial S_n} \nabla S_n^r \mathbf{N}_d^* d\Omega - \int_\Omega \nabla \mathbf{N}_d^{*T} \cdot \frac{\partial \mathbf{G}_2^r}{\partial S_n} \mathbf{N}_d^* d\Omega$$

$$\mathbf{K}_{5-6} = \int_\Omega \mathbf{N}_d^{*T} \frac{\partial d_5^r}{\partial T} \dot{p}_w^r \mathbf{N} d\Omega + \int_\Omega \mathbf{N}_d^{*T} \frac{\partial d_6^r}{\partial T} \dot{S}_n^r \mathbf{N} d\Omega + \int_\Omega \mathbf{N}_d^{*T} \frac{\partial d_7^r}{\partial T} \dot{T}^r \mathbf{N} d\Omega$$
$$+ \int_\Omega \mathbf{N}_d^{*T} \frac{\partial d_8^r}{\partial T} \mathbf{m}^T \mathbf{L} \dot{\mathbf{u}}^r \mathbf{N} d\Omega + \int_\Omega \nabla \mathbf{N}_d^{*T} \cdot \frac{\partial \mathbf{c}_2^r}{\partial T} \nabla p_w^r \mathbf{N} d\Omega$$
$$+ \int_\Omega \nabla \mathbf{N}_d^{*T} \cdot \frac{\partial \mathbf{c}_3^r}{\partial T} \nabla S_n^r \mathbf{N} d\Omega - \int_\Omega \nabla \mathbf{N}_d^{*T} \cdot \frac{\partial \mathbf{G}_2^r}{\partial T} \mathbf{N} d\Omega$$

$$\mathbf{K}_{5-10} = -\int_{\Gamma_c} \mathbf{N}_d^{*T} \mathbf{N}' d\Gamma; \quad \mathbf{K}_{5-11} = \mathbf{N}_d^{*T} \Big|_{\mathbf{x}_{\text{ap}}}$$

$$\mathbf{K}_{6-3} = \int_\Omega \mathbf{N}^T \frac{\partial d_9^r}{\partial p_w} \dot{T}^r \mathbf{N} d\Omega + \int_\Omega \mathbf{N}^T \frac{\partial d_{10}^r}{\partial p_w} \dot{p}_w^r \mathbf{N} d\Omega + \int_\Omega \mathbf{N}^T \frac{\partial d_{11}^r}{\partial p_w} \dot{S}_n^r \mathbf{N} d\Omega$$
$$- \int_\Omega \nabla \mathbf{N}^T \frac{\partial \boldsymbol{\beta}_1^r}{\partial p_w} T^r \mathbf{N} d\Omega + \int_\Omega \nabla \mathbf{N}^T \frac{\partial \boldsymbol{\beta}_2^r}{\partial p_w} \nabla p_w^r T^r \mathbf{N} d\Omega + \int_\Omega \nabla \mathbf{N}^T \boldsymbol{\beta}_2^r T^r \nabla \mathbf{N} d\Omega$$
$$+ \int_\Omega \nabla \mathbf{N}^T \frac{\partial \boldsymbol{\beta}_3^r}{\partial p_w} \nabla S_n^r T^r \mathbf{N} d\Omega$$

$$\mathbf{K}_{6-4} = \int_\Omega \mathbf{N}^T \frac{\partial d_9^r}{\partial S_n} \dot{T}^r \mathbf{N} d\Omega + \int_\Omega \mathbf{N}^T \frac{\partial d_{10}^r}{\partial S_n} \dot{p}_w^r \mathbf{N} d\Omega + \int_\Omega \mathbf{N}^T \frac{\partial d_{11}^r}{\partial S_n} \dot{S}_n^r \mathbf{N} d\Omega$$
$$- \int_\Omega \nabla \mathbf{N}^T \frac{\partial \boldsymbol{\beta}_1^r}{\partial S_n} T^r \mathbf{N} d\Omega + \int_\Omega \nabla \mathbf{N}^T \cdot \frac{\partial \mathbf{c}_4^r}{\partial S_n} \nabla T^r \mathbf{N} d\Omega + \int_\Omega \nabla \mathbf{N}^T \frac{\partial \boldsymbol{\beta}_2^r}{\partial S_n} \nabla p_w^r T^r \mathbf{N} d\Omega$$
$$+ \int_\Omega \nabla \mathbf{N}^T \frac{\partial \boldsymbol{\beta}_3^r}{\partial S_n} \nabla S_n^r T^r \mathbf{N} d\Omega + \int_\Omega \nabla \mathbf{N}^T \boldsymbol{\beta}_3^r T^r \nabla \mathbf{N} d\Omega$$

$$\mathbf{K}_{6-5} = \int_\Omega \mathbf{N}^T \frac{\partial d_9^r}{\partial S_n} \dot{T}^r \mathbf{N}_d^* d\Omega + \int_\Omega \mathbf{N}^T \frac{\partial d_{10}^r}{\partial S_n} \dot{p}_w^r \mathbf{N}_d^* d\Omega + \int_\Omega \mathbf{N}^T \frac{\partial d_{11}^r}{\partial S_n} \dot{S}_n^r \mathbf{N}_d^* d\Omega$$
$$- \int_\Omega \nabla \mathbf{N}^T \frac{\partial \boldsymbol{\beta}_1^r}{\partial S_n} T^r \mathbf{N}_d^* d\Omega + \int_\Omega \nabla \mathbf{N}^T \frac{\partial \mathbf{c}_4^r}{\partial S_n} \nabla T^r \mathbf{N}_d^* d\Omega + \int_\Omega \nabla \mathbf{N}^T \frac{\partial \boldsymbol{\beta}_2^r}{\partial S_n} \nabla p_w^r T^r \mathbf{N}_d^* d\Omega$$
$$+ \int_\Omega \nabla \mathbf{N}^T \frac{\partial \boldsymbol{\beta}_3^r}{\partial S_n} \nabla S_n^r T^r \mathbf{N}_d^* d\Omega + \int_\Omega \nabla \mathbf{N}^T \boldsymbol{\beta}_3^r T^r \nabla \mathbf{N}_d^* d\Omega$$

$$\mathbf{K}_{6-6} = \int_\Omega \mathbf{N}^T \frac{\partial d_9^r}{\partial T} \dot{T}^r \mathbf{N} d\Omega + \int_\Omega \mathbf{N}^T \frac{\partial d_{10}^r}{\partial T} \dot{p}_w^r \mathbf{N} d\Omega + \int_\Omega \mathbf{N}^T \frac{\partial d_{11}^r}{\partial T} \dot{S}_n^r \mathbf{N} d\Omega$$
$$- \int_\Omega \nabla \mathbf{N}^T \boldsymbol{\beta}_1^r \mathbf{N} d\Omega - \int_\Omega \nabla \mathbf{N}^T \frac{\partial \boldsymbol{\beta}_1^r}{\partial T} T^r \mathbf{N} d\Omega + \int_\Omega \nabla \mathbf{N}^T \boldsymbol{\beta}_2^r \nabla p_w^r \mathbf{N} d\Omega$$
$$+ \int_\Omega \nabla \mathbf{N}^T \frac{\partial \boldsymbol{\beta}_2^r}{\partial T} \nabla p_w^r T^r \mathbf{N} d\Omega + \int_\Omega \nabla \mathbf{N}^T \boldsymbol{\beta}_3^r \nabla S_n^r \mathbf{N} d\Omega + \int_\Omega \nabla \mathbf{N}^T \frac{\partial \boldsymbol{\beta}_3^r}{\partial T} \nabla S_n^r T^r \mathbf{N} d\Omega$$
$$+ \int_\Omega \nabla \mathbf{N}^T \cdot \mathbf{c}_4^r \nabla \mathbf{N} d\Omega - \int_{\Gamma_c} \mathbf{N}^T \frac{\partial \left(Q_{\text{adv}}^{\Gamma_c} \right)^r}{\partial T} \mathbf{N} d\Gamma - \int_{\Gamma_c} \mathbf{N}^T \frac{\partial \left(Q_{\text{conv}}^{\Gamma_c} \right)^r}{\partial T} \mathbf{N} d\Gamma$$
$$+ \mathbf{N}\big|_{\mathbf{x}_{\text{ap}}}^T \frac{\partial \left(Q_{\text{adv}}^{\text{ap}} \right)^r}{\partial T} \mathbf{N}\big|_{\mathbf{x}_{\text{ap}}}$$

$$\mathbf{K}_{6-7} = -\int_{\Gamma_c} \mathbf{N}^T \frac{\partial\left(Q_{\text{adv}}^{\Gamma_c}\right)^r}{\partial v_m'} \mathbf{N}' d\Gamma + \mathbf{N}\big|_{\mathbf{x}_{\text{ap}}}^T \frac{\partial\left(Q_{\text{adv}}^{\text{ap}}\right)^r}{\partial v_m'} \mathbf{N}'\big|_{x_{\text{ap}}'}$$

$$\mathbf{K}_{6-8} = -\int_{\Gamma_c} \mathbf{N}^T \frac{\partial\left(Q_{\text{adv}}^{\Gamma_c}\right)^r}{\partial p'} \mathbf{N}' d\Gamma - \int_{\Gamma_c} \mathbf{N}^T \frac{\partial\left(Q_{\text{adv}}^{\Gamma_c}\right)^r}{\partial T'} \frac{\partial T'}{\partial p'} \mathbf{N}' d\Gamma$$
$$+ \mathbf{N}\big|_{\mathbf{x}_{\text{ap}}}^T \frac{\partial\left(Q_{\text{adv}}^{\text{ap}}\right)^r}{\partial p'} \mathbf{N}'\big|_{x_{\text{ap}}'}$$

$$\mathbf{K}_{6-9} = -\int_{\Gamma_c} \mathbf{N}^T \frac{\partial\left(Q_{\text{conv}}^{\Gamma_c}\right)^r}{\partial T'} \frac{\partial T'^r}{\partial \rho_m'} \mathbf{N}' d\Gamma - \int_{\Gamma_c} \mathbf{N}^T \frac{\partial\left(Q_{\text{adv}}^{\Gamma_c}\right)^r}{\partial \rho_m'} \mathbf{N}' d\Gamma$$
$$+ \mathbf{N}\big|_{\mathbf{x}_{\text{ap}}}^T \frac{\partial\left(Q_{\text{adv}}^{\text{ap}}\right)^r}{\partial \rho_m'} \mathbf{N}'\big|_{x_{\text{ap}}'}$$

$$\mathbf{K}_{6-10} = -\int_{\Gamma_c} \mathbf{N}^T \frac{\partial\left(Q_{\text{adv}}^{\Gamma_c}\right)^r}{\partial q_n^{\Gamma_c}} \mathbf{N}' d\Gamma; \quad \mathbf{K}_{6-11} = \mathbf{N}\big|_{\mathbf{x}_{\text{ap}}}^T \frac{\partial\left(Q_{\text{adv}}^{\text{ap}}\right)^r}{\partial q_n^{\text{ap}}}$$

$$\mathbf{K}_{7-2} = \int_{\Gamma_c} \mathbf{N}'^T \dot{\rho}_m'^r \mathbf{n}_{\Gamma_c} \cdot \left[\!\left[\mathbf{N}_u^*\right]\!\right] d\Gamma - \int_{\Gamma_c} \mathbf{A}'^T \rho_m'^r v_m'^r \mathbf{n}_{\Gamma_c} \cdot \left[\!\left[\mathbf{N}_u^*\right]\!\right] d\Gamma n$$

$$\mathbf{K}_{7-7} = -\int_{\Gamma_c} \mathbf{A}'^T \rho_m'^r \left[\!\left[u_{y'}\right]\!\right]^r \mathbf{N}' d\Gamma$$

$$\mathbf{K}_{7-9} = \int_{\Gamma_c} \mathbf{N}'^T \left[\!\left[\dot{u}_{y'}\right]\!\right]^r \mathbf{N}' d\Gamma - \int_{\Gamma_c} \mathbf{A}'^T v_m'^r \left[\!\left[u_{y'}\right]\!\right]^r \mathbf{N}' d\Gamma$$

$$\mathbf{K}_{7-10} = \int_{\Gamma_c} \mathbf{N}'^T \mathbf{N}' d\Gamma; \quad \mathbf{K}_{7-11} = -\mathbf{N}'\big|_{x_{\text{ap}}'}^T$$

$$\mathbf{K}_{8-2} = \int_{\Gamma_c} \mathbf{N}'^T \dot{\rho}_m'^r v_m'^r \mathbf{n}_{\Gamma_c} \cdot \left[\!\left[\mathbf{N}_u^*\right]\!\right] d\Gamma + \int_{\Gamma_c} \mathbf{N}'^T \rho_m'^r \dot{v}_m'^r \mathbf{n}_{\Gamma_c} \cdot \left[\!\left[\mathbf{N}_u^*\right]\!\right] d\Gamma$$
$$- \int_{\Gamma_c} \mathbf{A}'^T \left(\rho_m'^r v_m'^{r2} + \gamma'^r\right) \mathbf{n}_{\Gamma_c} \cdot \left[\!\left[\mathbf{N}_u^*\right]\!\right] d\Gamma + \int_{\Gamma_c} \mathbf{N}'^T \frac{\partial p'^r}{\partial x'} \mathbf{n}_{\Gamma_c} \cdot \left[\!\left[\mathbf{N}_u^*\right]\!\right] d\Gamma$$
$$+ \int_{\Gamma_c} \mathbf{N}'^T p'^r \mathbf{n}_{\Gamma_c} \cdot \left[\!\left[\nabla \mathbf{N}_u^* \cdot \mathbf{t}_{\Gamma_c}\right]\!\right] d\Gamma - \int_{\Gamma_c} \mathbf{N}'^T \rho_m'^r \mathbf{g} \cdot \mathbf{t}_{\Gamma_c} \left(\mathbf{n}_{\Gamma_c} \cdot \left[\!\left[\mathbf{N}_u^*\right]\!\right]\right) d\Gamma$$

$$\mathbf{K}_{8-7} = \int_{\Gamma_c} \mathbf{N}'^T \dot{\rho}_m'^r \left[\!\left[u_{y'}\right]\!\right]^r \mathbf{N}' d\Gamma + \int_{\Gamma_c} \mathbf{N}'^T \rho_m'^r \left[\!\left[\dot{u}_{y'}\right]\!\right]^r \mathbf{N}' d\Gamma$$
$$- \int_{\Gamma_c} \mathbf{A}'^T \left(2\rho_m'^r v_m' + \frac{\partial \gamma'^r}{\partial v_m'}\right) \left[\!\left[u_{y'}\right]\!\right]^r \mathbf{N}' d\Gamma$$
$$+ \int_{\Gamma_c} \mathbf{N}'^T \frac{1}{4} \mathrm{sign}\left(v_m'^r\right) \frac{\partial f'^r}{\partial \mathrm{Re}'} \frac{\partial \mathrm{Re}'^r}{\partial v_m'} \rho_m'^r v_m'^{r2} \mathbf{N}' d\Gamma$$
$$+ \int_{\Gamma_c} \mathbf{N}'^T \frac{1}{2} \mathrm{sign}\left(v_m'^r\right) f'^r \rho_m'^r v_m'^r \mathbf{N}' d\Gamma + \int_{\Gamma_c} \mathbf{N}'^T \frac{\partial \left(Q_{\mathrm{mo}}^{\Gamma_c}\right)^r}{\partial v_m'} \mathbf{N}' d\Gamma$$
$$- \mathbf{N}'\big|_{x'_{\mathrm{ap}}}^T \frac{\partial \left(Q_{\mathrm{mo}}^{\mathrm{ap}}\right)^r}{\partial v_m'} \mathbf{N}'\big|_{x'_{\mathrm{ap}}}$$

$$\mathbf{K}_{8-8} = \int_{\Gamma_c} \mathbf{N}'^T \left[\!\left[u_{y'}\right]\!\right]^r \mathbf{A}' d\Gamma + \int_{\Gamma_c} \mathbf{N}'^T \frac{\partial \left[\!\left[u_{y'}\right]\!\right]^r}{\partial x'} \mathbf{N}' d\Gamma - \int_{\Gamma_c} \mathbf{A}'^T \frac{\partial \gamma'^r}{\partial p'} \left[\!\left[u_{y'}\right]\!\right]^r \mathbf{N}' d\Gamma$$
$$+ \int_{\Gamma_c} \mathbf{N}'^T \frac{1}{4} \mathrm{sign}\left(v_m'^r\right) \frac{\partial f'^r}{\partial \mathrm{Re}'} \frac{\partial \mathrm{Re}'^r}{\partial \mu_m'} \frac{\partial \mu_m'^r}{\partial p'} \rho_m'^r v_m'^{r2} \mathbf{N}' d\Gamma$$

$$\mathbf{K}_{8-9} = \int_{\Gamma_c} \mathbf{N}'^T \dot{v}_m'^r \left[\!\left[u_{y'}\right]\!\right]^r \mathbf{N}' d\Gamma + \int_{\Gamma_c} \mathbf{N}'^T v_m'^r \left[\!\left[\dot{u}_{y'}\right]\!\right]^r \mathbf{N}' d\Gamma$$
$$- \int_{\Gamma_c} \mathbf{A}'^T \left(v_m'^{r2} + \frac{\partial \gamma'^r}{\partial \rho_m'}\right) \left[\!\left[u_{y'}\right]\!\right]^r \mathbf{N}' d\Gamma - \int_{\Gamma_c} \mathbf{N}'^T \left[\!\left[u_{y'}\right]\!\right]^r \mathbf{g} \cdot \mathbf{t}_{\Gamma_c} \mathbf{N}' d\Gamma$$
$$+ \int_{\Gamma_c} \mathbf{N}'^T \frac{1}{4} \mathrm{sign}\left(v_m'^r\right) \frac{\partial f'^r}{\partial \mathrm{Re}'} \left(\frac{\partial \mathrm{Re}'^r}{\partial \rho_m'} - \frac{\partial \mathrm{Re}'^r}{\partial \mu_m'} \frac{\partial \mu_m'^r}{\partial \rho_m'}\right) \rho_m'^r v_m'^{r2} \mathbf{N}' d\Gamma$$
$$+ \int_{\Gamma_c} \mathbf{N}'^T \frac{1}{4} \mathrm{sign}\left(v_m'^r\right) f'^r v_m'^{r2} \mathbf{N}' d\Gamma$$

$$\mathbf{K}_{8\text{–}10} = \int_{\Gamma_c} \mathbf{N}'^T \frac{\partial\left(Q_{\text{mo}}^{\Gamma_c}\right)^r}{\partial q_n^{\Gamma_c}} \mathbf{N}' d\Gamma; \quad \mathbf{K}_{8\text{–}11} = -\mathbf{N}'\big|_{x'_{\text{ap}}}^T \frac{\partial\left(Q_{\text{mo}}^{\text{ap}}\right)^r}{\partial q_n^{\text{ap}}} \mathbf{N}'\big|_{x'_{\text{ap}}}$$

$$\begin{aligned}
\mathbf{K}_{9\text{–}2} = & \int_{\Gamma_c} \mathbf{N}'^T \dot{\rho}_m'^r \left(h_m'^r + \frac{1}{2} v_m'^{r2}\right) \mathbf{n}_{\Gamma_c} \cdot \left[\!\left[\mathbf{N}_u^*\right]\!\right] d\Gamma + \int_{\Gamma_c} \mathbf{N}'^T \rho_m'^r \frac{\partial h_m'^r}{\partial \rho_m'} \dot{\rho}_m'^r \mathbf{n}_{\Gamma_c} \cdot \left[\!\left[\mathbf{N}_u^*\right]\!\right] d\Gamma \\
& + \int_{\Gamma_c} \mathbf{N}'^T \rho_m'^r v_m'^r \dot{v}_m'^r \mathbf{n}_{\Gamma_c} \cdot \left[\!\left[\mathbf{N}_u^*\right]\!\right] d\Gamma - \int_{\Gamma_c} \mathbf{A}'^T \rho_m'^r v_m'^r \left(h_m'^r + \frac{1}{2} v_m'^{r2}\right) \mathbf{n}_{\Gamma_c} \cdot \left[\!\left[\mathbf{N}_u^*\right]\!\right] d\Gamma \\
& - \int_{\Gamma_c} \mathbf{N}'^T \rho_m'^r v_m'^r \left(\mathbf{g} \cdot \mathbf{t}_{\Gamma_c}\right) \mathbf{n}_{\Gamma_c} \cdot \left[\!\left[\mathbf{N}_u^*\right]\!\right] d\Gamma + \int_{\Gamma_c} \mathbf{N}'^T \rho_m'^r \frac{\partial h_m'^r}{\partial p'} \dot{p}'^r \mathbf{n}_{\Gamma_c} \cdot \left[\!\left[\mathbf{N}_u^*\right]\!\right] d\Gamma \\
& - \int_{\Gamma_c} \mathbf{N}'^T \dot{p}'^r \mathbf{n}_{\Gamma_c} \cdot \left[\!\left[\mathbf{N}_u^*\right]\!\right] d\Gamma
\end{aligned}$$

$$\mathbf{K}_{9\text{–}6} = \int_{\Gamma_c} \mathbf{N}'^T \frac{\partial\left(Q_{\text{conv}}^{\Gamma_c}\right)^r}{\partial T} \mathbf{N} d\Gamma + \int_{\Gamma_c} \mathbf{N}'^T \frac{\partial\left(Q_{\text{adv}}^{\Gamma_c}\right)^r}{\partial T} \mathbf{N} d\Gamma - \mathbf{N}'\big|_{x'_{\text{ap}}}^T \frac{\partial\left(Q_{\text{adv}}^{\text{ap}}\right)^r}{\partial T} \mathbf{N}\big|_{\mathbf{x}_{\text{ap}}}$$

$$\begin{aligned}
\mathbf{K}_{9\text{–}7} = & \int_{\Gamma_c} \mathbf{N}'^T \dot{\rho}_m'^r v_m'^r \left[\!\left[u_{y'}\right]\!\right]^r \mathbf{N}' d\Gamma + \int_{\Gamma_c} \mathbf{N}'^T \rho_m'^r \dot{v}_m'^r \left[\!\left[u_{y'}\right]\!\right]^r \mathbf{N}' d\Gamma \\
& + \int_{\Gamma_c} \mathbf{N}'^T \rho_m'^r v_m'^r \left[\!\left[\dot{u}_{y'}\right]\!\right]^r \mathbf{N}' d\Gamma - \int_{\Gamma_c} \mathbf{A}'^T \rho_m'^r \left(h_m'^r + \frac{1}{2} v_m'^{r2}\right) \left[\!\left[u_{y'}\right]\!\right]^r \mathbf{N}' d\Gamma \\
& - \int_{\Gamma_c} \mathbf{A}'^T \rho_m'^r v_m'^{r2} \left[\!\left[u_{y'}\right]\!\right]^r \mathbf{N}' d\Gamma - \int_{\Gamma_c} \mathbf{N}'^T \rho_m'^r \left[\!\left[u_{y'}\right]\!\right]^r \mathbf{g} \cdot \mathbf{t}_{\Gamma_c} \mathbf{N}' d\Gamma \\
& + \int_{\Gamma_c} \mathbf{N}'^T \frac{\partial\left(Q_{\text{adv}}^{\Gamma_c}\right)^r}{\partial v_m'} \mathbf{N}' d\Gamma - \mathbf{N}'\big|_{x'_{\text{ap}}}^T \frac{\partial\left(Q_{\text{adv}}^{\text{ap}}\right)^r}{\partial v_m'} \mathbf{N}'\big|_{x'_{\text{ap}}}
\end{aligned}$$

$$\mathbf{K}_{9\text{–}8} = \int_{\Gamma_c} \mathbf{N}'^T \dot{\rho}_m'^r \frac{\partial h_m'^r}{\partial p'} \left[\!\left[u_{y'} \right]\!\right]^r \mathbf{N}' d\Gamma + \int_{\Gamma_c} \mathbf{N}'^T \rho_m'^r \frac{\partial^2 h_m'^r}{\partial p'^2} \dot{p}'^r \left[\!\left[u_{y'} \right]\!\right]^r \mathbf{N}' d\Gamma$$
$$+ \int_{\Gamma_c} \mathbf{N}'^T \rho_m'^r \frac{\partial h_m'^r}{\partial p'} \left[\!\left[\dot{u}_{y'} \right]\!\right]^r \mathbf{N}' d\Gamma - \int_{\Gamma_c} \mathbf{A}'^T \rho_m'^r v_m'^r \frac{\partial h_m'^r}{\partial p'} \left[\!\left[u_{y'} \right]\!\right]^r \mathbf{N}' d\Gamma$$
$$+ \int_{\Gamma_c} \mathbf{N}'^T \rho_m'^r \frac{\partial^2 h_m'^r}{\partial \rho_m' \partial p'} \dot{\rho}_m'^r \left[\!\left[u_{y'} \right]\!\right]^r \mathbf{N}' d\Gamma - \int_{\Gamma_c} \mathbf{N}'^T \left[\!\left[\dot{u}_{y'} \right]\!\right]^r \mathbf{N}' d\Gamma$$
$$+ \int_{\Gamma_c} \mathbf{N}'^T \frac{\partial \left(Q_{\text{conv}}^{\Gamma_c} \right)^r}{\partial T'} \frac{\partial T'^r}{\partial p'} \mathbf{N}' d\Gamma + \int_{\Gamma_c} \mathbf{N}'^T \frac{\partial \left(Q_{\text{adv}}^{\Gamma_c} \right)^r}{\partial p'} \mathbf{N}' d\Gamma$$
$$- \mathbf{N}'\big|_{x'_{\text{ap}}}^T \frac{\partial \left(Q_{\text{adv}}^{\text{ap}} \right)^r}{\partial p'} \mathbf{N}'\big|_{x'_{\text{ap}}}$$

$$\mathbf{K}_{9\text{–}9} = \int_{\Gamma_c} \mathbf{N}'^T \dot{\rho}_m'^r \frac{\partial h_m'^r}{\partial \rho_m'} \left[\!\left[u_{y'} \right]\!\right]^r \mathbf{N}' d\Gamma + \int_{\Gamma_c} \mathbf{N}'^T \frac{\partial h_m'^r}{\partial \rho_m'} \dot{\rho}_m'^r \left[\!\left[u_{y'} \right]\!\right]^r \mathbf{N}' d\Gamma$$
$$+ \int_{\Gamma_c} \mathbf{N}'^T \rho_m'^r \frac{\partial^2 h_m'^r}{\partial \rho_m'^2} \dot{\rho}_m'^r \left[\!\left[u_{y'} \right]\!\right]^r \mathbf{N}' d\Gamma + \int_{\Gamma_c} \mathbf{N}'^T v_m'^r \dot{v}_m'^r \left[\!\left[u_{y'} \right]\!\right]^r \mathbf{N}' d\Gamma$$
$$+ \int_{\Gamma_c} \mathbf{N}'^T \left(h_m'^r + \frac{1}{2} v_m'^{r2} \right) \left[\!\left[\dot{u}_{y'} \right]\!\right]^r \mathbf{N}' d\Gamma + \int_{\Gamma_c} \mathbf{N}'^T \rho_m'^r \frac{\partial h_m'^r}{\partial \rho_m'} \left[\!\left[\dot{u}_{y'} \right]\!\right]^r \mathbf{N}' d\Gamma$$
$$- \int_{\Gamma_c} \mathbf{A}'^T v_m'^r \left(h_m'^r + \frac{1}{2} v_m'^{r2} \right) \left[\!\left[u_{y'} \right]\!\right]^r \mathbf{N}' d\Gamma - \int_{\Gamma_c} \mathbf{A}'^T \rho_m'^r v_m'^r \frac{\partial h_m'^r}{\partial \rho_m'} \left[\!\left[u_{y'} \right]\!\right]^r \mathbf{N}' d\Gamma$$
$$+ \int_{\Gamma_c} \mathbf{N}'^T \frac{\partial h_m'^r}{\partial p'} \dot{p}'^r \left[\!\left[u_{y'} \right]\!\right]^r \mathbf{N}' d\Gamma + \int_{\Gamma_c} \mathbf{N}'^T \rho_m'^r \frac{\partial^2 h_m'^r}{\partial \rho_m' \partial p'} \dot{p}'^r \left[\!\left[u_{y'} \right]\!\right]^r \mathbf{N}' d\Gamma$$
$$+ \int_{\Gamma_c} \mathbf{N}'^T \frac{\partial \left(Q_{\text{adv}}^{\Gamma_c} \right)^r}{\partial \rho_m'} \mathbf{N}' d\Gamma - \mathbf{N}'\big|_{x'_{\text{ap}}}^T \frac{\partial \left(Q_{\text{adv}}^{\text{ap}} \right)^r}{\partial \rho_m'} \mathbf{N}'\big|_{x'_{\text{ap}}}$$
$$- \int_{\Gamma_c} \mathbf{N}'^T v_m'^r \left[\!\left[u_{y'} \right]\!\right]^r \mathbf{g} \cdot \mathbf{t}_{\Gamma_c} \mathbf{N}' d\Gamma + \int_{\Gamma_c} \mathbf{N}'^T \frac{\partial \left(Q_{\text{conv}}^{\Gamma_c} \right)^r}{\partial T'} \frac{\partial T'^r}{\partial \rho_m'} \mathbf{N}' d\Gamma$$

$$\mathbf{K}_{9\text{–}10} = \int_{\Gamma_c} \mathbf{N}'^T \frac{\partial \left(Q_{\text{adv}}^{\Gamma_c} \right)^r}{\partial q_n^{\Gamma_c}} \mathbf{N}' d\Gamma; \quad \mathbf{K}_{9\text{–}11} = -\mathbf{N}'\big|_{x'_{\text{ap}}}^T \frac{\partial \left(Q_{\text{adv}}^{\text{ap}} \right)^r}{\partial q_n^{\text{ap}}}$$

$$\mathbf{K}_{10-3} = \int_{\Gamma_c} \mathbf{N}'^T \frac{\partial \eta_n^r}{\partial p_w}\left(p_w^r + p_c^r - p'^r\right)\mathbf{N}d\Gamma + \int_{\Gamma_c} \mathbf{N}'^T \eta_n^r \mathbf{N}d\Gamma$$

$$\mathbf{K}_{10-4} = \int_{\Gamma_c} \mathbf{N}'^T \frac{\partial \eta_n^r}{\partial S_n}\left(p_w^r + p_c^r - p'^r\right)\mathbf{N}d\Gamma + \int_{\Gamma_c} \mathbf{N}'^T \eta_n^r \frac{\partial p_c^r}{\partial S_n}\mathbf{N}d\Gamma$$

$$\mathbf{K}_{10-5} = \int_{\Gamma_c} \mathbf{N}'^T \frac{\partial \eta_n^r}{\partial S_n}\left(p_w^r + p_c^r - p'^r\right)\mathbf{N}_d^* d\Gamma + \int_{\Gamma_c} \mathbf{N}'^T \eta_n^r \frac{\partial p_c^r}{\partial S_n}\mathbf{N}_d^* d\Gamma$$

$$\mathbf{K}_{10-6} = \int_{\Gamma_c} \mathbf{N}'^T \frac{\partial \eta_n^r}{\partial T}\left(p_w^r + p_c^r - p'^r\right)\mathbf{N}d\Gamma; \quad \mathbf{K}_{10-8} = -\int_{\Gamma_c} \mathbf{N}'^T \eta_n^r \mathbf{N}'d\Gamma$$

$$\mathbf{K}_{10-10} = \int_{\Gamma_c} \mathbf{N}'^T \mathbf{N}'\, d\Gamma$$

$$\mathbf{K}_{11-3} = -k^{\mathrm{ap}} \frac{\partial\left(\eta_n^{\mathrm{ap}}\right)^r}{\partial p_w}\left(p_w\big|_{\mathbf{x}_{\mathrm{ap}}}^r + p_c\big|_{\mathbf{x}_{\mathrm{ap}}}^r - p'\big|_{x'_{\mathrm{ap}}}^r\right)\mathbf{N}\big|_{\mathbf{x}_{\mathrm{ap}}} - k^{\mathrm{ap}}\left(\eta_n^{\mathrm{ap}}\right)^r \mathbf{N}\big|_{\mathbf{x}_{\mathrm{ap}}}$$

$$\mathbf{K}_{11-4} = -k^{\mathrm{ap}} \frac{\partial\left(\eta_n^{\mathrm{ap}}\right)^r}{\partial S_n}\left(p_w\big|_{\mathbf{x}_{\mathrm{ap}}}^r + p_c\big|_{\mathbf{x}_{\mathrm{ap}}}^r - p'\big|_{x'_{\mathrm{ap}}}^r\right)\mathbf{N}\big|_{\mathbf{x}_{\mathrm{ap}}} - k^{\mathrm{ap}}\eta_n^{\mathrm{ap}r} \frac{\partial\, p_c\big|_{\mathbf{x}_{\mathrm{ap}}}^r}{\partial S_n}\mathbf{N}\big|_{\mathbf{x}_{\mathrm{ap}}}$$

$$\mathbf{K}_{11-5} = -k^{\mathrm{ap}} \frac{\partial\left(\eta_n^{\mathrm{ap}}\right)^r}{\partial S_n}\left(p_w\big|_{\mathbf{x}_{\mathrm{ap}}}^r + p_c\big|_{\mathbf{x}_{\mathrm{ap}}}^r - p'\big|_{x'_{\mathrm{ap}}}^r\right)\mathbf{N}_d^*\Big|_{\mathbf{x}_{\mathrm{ap}}} - k^{\mathrm{ap}}\eta_n^{\mathrm{ap}r} \frac{\partial\, p_c\big|_{\mathbf{x}_{\mathrm{ap}}}^r}{\partial S_n}\mathbf{N}_d^*\Big|_{\mathbf{x}_{\mathrm{ap}}}$$

$$\mathbf{K}_{11-6} = -k^{\mathrm{ap}} \frac{\partial\left(\eta_n^{\mathrm{ap}}\right)^r}{\partial T}\left(p_w\big|_{\mathbf{x}_{\mathrm{ap}}}^r + p_c\big|_{\mathbf{x}_{\mathrm{ap}}}^r - p'\big|_{x'_{\mathrm{ap}}}^r\right)\mathbf{N}\big|_{\mathbf{x}_{\mathrm{ap}}}$$

$$\mathbf{K}_{11-8} = k^{\mathrm{ap}}\left(\eta_n^{\mathrm{ap}}\right)^r \mathbf{N}'\big|_{x'_{\mathrm{ap}}}; \quad \mathbf{K}_{11-11} = 1$$

C matrix terms

$$\mathbf{C}_{3-1} = \int_{\Omega} \mathbf{N}^T d_4^r \mathbf{m}^T \mathbf{B} d\Omega; \quad \mathbf{C}_{3-2} = \int_{\Omega} \mathbf{N}^T d_4^r \mathbf{m}^T \mathbf{B}^* d\Omega; \quad \mathbf{C}_{3-3} = \int_{\Omega} \mathbf{N}^T d_1^r \mathbf{N} d\Omega$$

$$\mathbf{C}_{3-4} = \int_{\Omega} \mathbf{N}^T d_2^r \mathbf{N} d\Omega; \quad \mathbf{C}_{3-5} = \int_{\Omega} \mathbf{N}^T d_2^r \mathbf{N}_d^* d\Omega; \quad \mathbf{C}_{3-6} = \int_{\Omega} \mathbf{N}^T d_3^r \mathbf{N} d\Omega$$

$$\mathbf{C}_{4-1} = \int_{\Omega} \mathbf{N}^T d_8^r \mathbf{m}^T \mathbf{B} d\Omega; \quad \mathbf{C}_{4-2} = \int_{\Omega} \mathbf{N}^T d_8^r \mathbf{m}^T \mathbf{B}^* d\Omega; \quad \mathbf{C}_{4-3} = \int_{\Omega} \mathbf{N}^T d_5^r \mathbf{N} d\Omega$$

$$\mathbf{C}_{4-4} = \int_{\Omega} \mathbf{N}^T d_6^r \mathbf{N} d\Omega; \quad \mathbf{C}_{4-5} = \int_{\Omega} \mathbf{N}^T d_6^r \mathbf{N}_d^* d\Omega; \quad \mathbf{C}_{4-6} = \int_{\Omega} \mathbf{N}^T d_7^r \mathbf{N} d\Omega$$

$$\mathbf{C}_{5-1}=\int_{\Omega}\mathbf{N}_d^{*T}d_8^r\mathbf{m}^T\mathbf{B}d\Omega;\quad \mathbf{C}_{5-2}=\int_{\Omega}\mathbf{N}_d^{*T}d_8^r\mathbf{m}^T\mathbf{B}^*d\Omega;\quad \mathbf{C}_{5-3}=\int_{\Omega}\mathbf{N}_d^{*T}d_5^r\mathbf{N}d\Omega$$

$$\mathbf{C}_{5-4}=\int_{\Omega}\mathbf{N}_d^{*T}d_6^r\mathbf{N}d\Omega;\quad \mathbf{C}_{5-5}=\int_{\Omega}\mathbf{N}_d^{*T}d_6^r\mathbf{N}_d^*d\Omega;\quad \mathbf{C}_{5-6}=\int_{\Omega}\mathbf{N}_d^{*T}d_7^r\mathbf{N}\delta d\Omega$$

$$\mathbf{C}_{6-3}=\int_{\Omega}\mathbf{N}^Td_{10}^r\mathbf{N}d\Omega;\quad \mathbf{C}_{6-4}=\int_{\Omega}\mathbf{N}^Td_{11}^r\mathbf{N}d\Omega;\quad \mathbf{C}_{6-5}=\int_{\Omega}\mathbf{N}^Td_{11}^r\mathbf{N}_d^*d\Omega$$

$$\mathbf{C}_{6-6}=\int_{\Omega}\mathbf{N}^Td_9^r\mathbf{N}d\Omega$$

$$\mathbf{C}_{7-2}=\int_{\Gamma_c}\mathbf{N}'^T\rho_m'^r\mathbf{n}_{\Gamma_c}\cdot\left[\!\left[\mathbf{N}_u^*\right]\!\right]d\Gamma;\quad \mathbf{C}_{7-9}=\int_{\Gamma_c}\mathbf{N}'^T\left[\!\left[u_{y'}\right]\!\right]^r\mathbf{N}'d\Gamma$$

$$\mathbf{C}_{8-2}=\int_{\Gamma_c}\mathbf{N}'^T\rho_m'^rv_m'^r\mathbf{n}_{\Gamma_c}\cdot\left[\!\left[\mathbf{N}_u^*\right]\!\right]d\Gamma;\quad \mathbf{C}_{8-7}=\int_{\Gamma_c}\mathbf{N}'^T\rho_m'^r\left[\!\left[u_{y'}\right]\!\right]^r\mathbf{N}'d\Gamma$$

$$\mathbf{C}_{8-9}=\int_{\Gamma_c}\mathbf{N}'^Tv_m'^r\left[\!\left[u_{y'}\right]\!\right]^r\mathbf{N}'d\Gamma$$

$$\mathbf{C}_{9-2}=\int_{\Gamma_c}\mathbf{N}'^T\rho_m'^r\left(h_m'^r+\frac{1}{2}v_m'^r2\right)\mathbf{n}_{\Gamma_c}\cdot\left[\!\left[\mathbf{N}_u^*\right]\!\right]d\Gamma-\int_{\Gamma_c}\mathbf{N}'^Tp'\mathbf{n}_{\Gamma_c}\cdot\left[\!\left[\mathbf{N}_u^*\right]\!\right]d\Gamma$$

$$\mathbf{C}_{9-7}=\int_{\Gamma_c}\mathbf{N}'^T\rho_m'^rv_m'^r\left[\!\left[u_{y'}\right]\!\right]^r\mathbf{N}'d\Gamma$$

$$\mathbf{C}_{9-8}=-\int_{\Gamma_c}\mathbf{N}'^T\left[\!\left[u_{y'}\right]\!\right]\mathbf{N}'d\Omega+\int_{\Gamma_c}\mathbf{N}'^T\rho_m'^r\frac{\partial h_m'^r}{\partial p'}\left[\!\left[u_{y'}\right]\!\right]^r\mathbf{N}'d\Gamma$$

$$\mathbf{C}_{9-9}=\int_{\Gamma_c}\mathbf{N}'^T\left(h_m'^r+\frac{1}{2}v_m'^r2\right)\left[\!\left[u_{y'}\right]\!\right]^r\mathbf{N}'d\Gamma+\int_{\Gamma_c}\mathbf{N}'^T\rho_m'^r\frac{\partial h_m'^r}{\partial\rho_m'}\left[\!\left[u_{y'}\right]\!\right]^r\mathbf{N}'d\Gamma$$

K_0 matrix terms

$$\mathbf{K}_{1-1}^0=-\int_{\Omega}\mathbf{B}^T\mathbf{D}\mathbf{B}d\Omega;\quad \mathbf{K}_{1-2}^0=-\int_{\Omega}\mathbf{B}^T\mathbf{D}\mathbf{B}^*d\Omega;\quad \mathbf{K}_{1-3}^0=\int_{\Omega}\mathbf{B}^T\mathbf{m}\alpha\mathbf{N}d\Omega;$$

$$\mathbf{K}_{1-4}^0=\int_{\Omega}\mathbf{B}^T\mathbf{m}\alpha p_c^r\mathbf{N}d\Omega;\quad \mathbf{K}_{1-5}^0=\int_{\Omega}\mathbf{B}^T\mathbf{m}\alpha p_c^r\mathbf{N}_d^*d\Omega;$$

$$\mathbf{K}_{1-6}^0=\int_{\Omega}\mathbf{B}^T\mathbf{D}\frac{1}{3}\mathbf{m}\beta_s\mathbf{N}d\Omega;$$

$$\mathbf{K}_{2-1}^{0}=-\int_{\Omega}\mathbf{B}^{*T}\mathbf{D}\mathbf{B}d\Omega;\quad \mathbf{K}_{2-2}^{0}=-\int_{\Omega}\mathbf{B}^{*T}\mathbf{D}\mathbf{B}^{*}d\Omega;\quad \mathbf{K}_{2-3}^{0}=\int_{\Omega}\mathbf{B}^{*T}\mathbf{m}\alpha\mathbf{N}d\Omega$$

$$\mathbf{K}_{2-4}^{0}=\int_{\Omega}\mathbf{B}^{*T}\mathbf{m}\alpha p_c^{r}\mathbf{N}d\Omega;\quad \mathbf{K}_{2-5}^{0}=\int_{\Omega}\mathbf{B}^{*T}\mathbf{m}\alpha p_c^{r}\mathbf{N}_d^{*}d\Omega;$$

$$\mathbf{K}_{2-6}^{0}=\int_{\Omega}\mathbf{B}^{*T}\mathbf{D}\frac{1}{3}\mathbf{m}\beta_s\mathbf{N}d\Omega;\quad \mathbf{K}_{2-8}^{0}=\int_{\Gamma_c}\left[\!\left[\mathbf{N}_u^{*T}\right]\!\right]\alpha\mathbf{n}_{\Gamma_c}\mathbf{N}'d\Gamma$$

$$\mathbf{K}_{3-3}^{0}=\int_{\Omega}\nabla\mathbf{N}^{T}\cdot\mathbf{c}_1^{r}\nabla\mathbf{N}d\Omega;$$

$$\mathbf{K}_{4-3}^{0}=\int_{\Omega}\nabla\mathbf{N}^{T}\cdot\mathbf{c}_2^{r}\nabla\mathbf{N}d\Omega;\quad \mathbf{K}_{4-4}^{0}=\int_{\Omega}\nabla\mathbf{N}^{T}\cdot\mathbf{c}_3^{r}\nabla\mathbf{N}d\Omega$$

$$\mathbf{K}_{4-5}^{0}=\int_{\Omega}\nabla\mathbf{N}^{T}\cdot\mathbf{c}_3^{r}\nabla\mathbf{N}_d^{*}d\Omega$$

$$\mathbf{K}_{5-3}^{0}=\int_{\Omega}\nabla\mathbf{N}_d^{*T}\cdot\mathbf{c}_2^{r}\nabla\mathbf{N}d\Omega;\quad \mathbf{K}_{5-4}^{0}=\int_{\Omega}\nabla\mathbf{N}_d^{*T}\cdot\mathbf{c}_3^{r}\nabla\mathbf{N}d\Omega;$$

$$\mathbf{K}_{5-5}^{0}=\int_{\Omega}\nabla\mathbf{N}_d^{*T}\cdot\mathbf{c}_3^{r}\nabla\mathbf{N}_d^{*}d\Omega$$

$$\mathbf{K}_{6-6}^{0}=-\int_{\Omega}\nabla\mathbf{N}^{T}\boldsymbol{\beta}_1^{r}\mathbf{N}d\Omega+\int_{\Omega}\nabla\mathbf{N}^{T}\boldsymbol{\beta}_2^{r}\nabla p_w^{r}\mathbf{N}d\Omega+\int_{\Omega}\nabla\mathbf{N}^{T}\boldsymbol{\beta}_3^{r}\nabla S_n^{r}\mathbf{N}d\Omega$$
$$+\int_{\Omega}\nabla\mathbf{N}^{T}\cdot\mathbf{c}_4^{r}\nabla\mathbf{N}d\Omega$$

$$\mathbf{K}_{7-7}^{0}=-\int_{\Gamma_c}\mathbf{A}'^{T}\rho_m'^{r}\left[\!\left[u_{y'}\right]\!\right]^{r}\mathbf{N}'d\Gamma$$

$$\mathbf{K}_{8-7}^{0}=-\int_{\Gamma_c}\mathbf{A}'^{T}\rho_m'^{r}v_m'^{r}\left[\!\left[u_{y'}\right]\!\right]^{r}\mathbf{N}'d\Gamma+\int_{\Gamma_c}\mathbf{N}'^{T}\frac{1}{4}\mathrm{sign}\left(v_m'^{r}\right)f'^{r}\rho_m'^{r}v_m'^{r}\mathbf{N}'d\Gamma$$

$$\mathbf{K}_{8-8}^{0}=\int_{\Gamma_c}\mathbf{N}'^{T}\left[\!\left[u_{y'}\right]\!\right]^{r}\mathbf{A}'d\Gamma+\int_{\Gamma_c}\mathbf{N}'^{T}\frac{\partial\left[\!\left[u_{y'}\right]\!\right]^{r}}{\partial x'}\mathbf{N}'d\Gamma$$

$$\mathbf{K}_{9-7}^{0}=-\int_{\Gamma_c}\mathbf{A}'^{T}\rho_m'^{r}\left(h_m'^{r}+\frac{1}{2}v_m'^{r2}\right)\left[\!\left[u_{y'}\right]\!\right]^{r}\mathbf{N}'d\Gamma$$

$$\mathbf{K}_{10-3}^{0}=\int_{\Gamma_c}\mathbf{N}'^{T}k\eta_n^{r}\mathbf{N}d\Gamma;\quad \mathbf{K}_{10-8}^{0}=-\int_{\Gamma_c}\mathbf{N}'^{T}k\eta_n^{r}\mathbf{N}'d\Gamma$$

$$\mathbf{K}_{10-10}^{0}=\int_{\Gamma_c}\mathbf{N}'^{T}\mathbf{N}'d\Gamma;$$

$$\mathbf{K}_{11-3}^{0}=-k^{\mathrm{ap}}\left(\eta_n^{\mathrm{ap}}\right)^{r}\mathbf{N}\big|_{\mathbf{x}_{\mathrm{ap}}};\quad \mathbf{K}_{11-8}^{0}=k^{\mathrm{ap}}\left(\eta_n^{\mathrm{ap}}\right)^{r}\mathbf{N}'\big|_{x'_{\mathrm{ap}}};\quad \mathbf{K}_{11-11}^{0}=1$$

C_0 matrix terms

$$\mathbf{C}^0_{3-1}=\int_\Omega \mathbf{N}^T d_4^r \mathbf{m}^T \mathbf{B} d\Omega;\quad \mathbf{C}^0_{3-2}=\int_\Omega \mathbf{N}^T d_4^r \mathbf{m}^T \mathbf{B}^* d\Omega \quad \mathbf{C}^0_{3-3}=\int_\Omega \mathbf{N}^T d_1^r \mathbf{N} d\Omega$$

$$\mathbf{C}^0_{3-4}=\int_\Omega \mathbf{N}^T d_2^r \mathbf{N} d\Omega;\quad \mathbf{C}^0_{3-5}=\int_\Omega \mathbf{N}^T d_2^r \mathbf{N}_d^* d\Omega;\quad \mathbf{C}^0_{3-6}=\int_\Omega \mathbf{N}^T d_3^r \mathbf{N} d\Omega$$

$$\mathbf{C}^0_{4-1}=\int_\Omega \mathbf{N}^T d_8^r \mathbf{m}^T \mathbf{B} d\Omega;\quad \mathbf{C}^0_{4-2}=\int_\Omega \mathbf{N}^T d_8^r \mathbf{m}^T \mathbf{B}^* d\Omega;\quad \mathbf{C}^0_{4-3}=\int_\Omega \mathbf{N}^T d_5^r \mathbf{N} d\Omega$$

$$\mathbf{C}^0_{4-4}=\int_\Omega \mathbf{N}^T d_6^r \mathbf{N} d\Omega;\quad \mathbf{C}^0_{4-5}=\int_\Omega \mathbf{N}^T d_6^r \mathbf{N}_d^* d\Omega;\quad \mathbf{C}^0_{4-6}=\int_\Omega \mathbf{N}^T d_7^r \mathbf{N} d\Omega$$

$$\mathbf{C}^0_{5-1}=\int_\Omega \mathbf{N}_d^{*T} d_8^r \mathbf{m}^T \mathbf{B} d\Omega;\quad \mathbf{C}^0_{5-2}=\int_\Omega \mathbf{N}_d^{*T} d_8^r \mathbf{m}^T \mathbf{B}^* d\Omega;\quad \mathbf{C}^0_{5-3}=\int_\Omega \mathbf{N}_d^{*T} d_5^r \mathbf{N} d\Omega$$

$$\mathbf{C}^0_{5-4}=\int_\Omega \mathbf{N}_d^{*T} d_6^r \mathbf{N} d\Omega;\quad \mathbf{C}^0_{5-5}=\int_\Omega \mathbf{N}_d^{*T} d_6^r \mathbf{N}_d^* d\Omega;\quad \mathbf{C}^0_{5-6}=\int_\Omega \mathbf{N}_d^{*T} d_7^r \mathbf{N} d\Omega$$

$$\mathbf{C}^0_{6-3}=\int_\Omega \mathbf{N}^T d_{10}^r \mathbf{N} d\Omega;\quad \mathbf{C}^0_{6-4}=\int_\Omega \mathbf{N}^T d_{11}^r \mathbf{N} d\Omega;\quad \mathbf{C}^0_{6-5}=\int_\Omega \mathbf{N}^T d_{11}^r \mathbf{N}_d^* d\Omega$$

$$\mathbf{C}^0_{6-6}=\int_\Omega \mathbf{N}^T d_9^r \mathbf{N} d\Omega$$

$$\mathbf{C}^0_{7-2}=\int_{\Gamma_c} \mathbf{N}'^T \rho_m'^r \mathbf{n}_{\Gamma_c} \cdot \left[\!\left[\mathbf{N}_u^*\right]\!\right] d\Gamma;\quad \mathbf{C}^0_{7-9}=\int_{\Gamma_c} \mathbf{N}'^T \left[\!\left[u_{y'}\right]\!\right]^r \mathbf{N}' d\Gamma$$

$$\mathbf{C}^0_{8-2}=\int_{\Gamma_c} \mathbf{N}'^T \rho_m'^r v_m'^r \mathbf{n}_{\Gamma_c} \cdot \left[\!\left[\mathbf{N}_u^*\right]\!\right] d\Gamma;\quad \mathbf{C}^0_{8-7}=\int_{\Gamma_c} \mathbf{N}'^T \rho_m'^r \left[\!\left[u_{y'}\right]\!\right]^r \mathbf{N}' d\Gamma$$

$$\mathbf{C}^0_{8-9}=\int_{\Gamma_c} \mathbf{N}'^T v_m'^r \left[\!\left[u_{y'}\right]\!\right]^r \mathbf{N}' d\Gamma$$

$$\mathbf{C}^0_{9-2}=\int_{\Gamma_c} \mathbf{N}'^T \rho_m'^r \left(h_m'^r+\frac{1}{2}v_m'^{r2}\right)\mathbf{n}_{\Gamma_c} \cdot \left[\!\left[\mathbf{N}_u^*\right]\!\right] d\Gamma-\int_{\Gamma_c} \mathbf{N}'^T p' \mathbf{n}_{\Gamma_c} \cdot \left[\!\left[\mathbf{N}_u^*\right]\!\right] d\Gamma$$

$$\mathbf{C}^0_{9-7}=\int_{\Gamma_c} \mathbf{N}'^T \rho_m'^r v_m'^r \left[\!\left[u_{y'}\right]\!\right]^r \mathbf{N}' d\Gamma$$

$$\mathbf{C}^0_{9-8}=-\int_{\Gamma_c} \mathbf{N}'^T \left[\!\left[u_{y'}\right]\!\right] \mathbf{N}' d\Omega+\int_{\Gamma_c} \mathbf{N}'^T \rho_m'^r \frac{\partial h_m'^r}{\partial p'} \left[\!\left[u_{y'}\right]\!\right]^r \mathbf{N}' d\Gamma$$

$$\mathbf{C}^0_{9-9}=\int_{\Gamma_c} \mathbf{N}'^T \left(h_m'^r+\frac{1}{2}v_m'^{r2}\right)\left[\!\left[u_{y'}\right]\!\right]^r \mathbf{N}' d\Gamma+\int_{\Gamma_c} \mathbf{N}'^T \rho_m'^r \frac{\partial h_m'^r}{\partial \rho_m'} \left[\!\left[u_{y'}\right]\!\right]^r \mathbf{N}' d\Gamma$$

f vector terms

$$\mathbf{f}_1 = -\int_\Omega \mathbf{N}_u^T \rho_{eff}^r \mathbf{g} d\Omega - \int_{\Gamma_q} \mathbf{N}_u^T \hat{\mathbf{t}} d\Gamma \quad ;$$

$$\mathbf{f}_2 = -\int_\Omega \mathbf{N}_u^{*T} \rho_{eff}^r \mathbf{g} d\Omega - \int_{\Gamma_q} \mathbf{N}_u^{*T} \hat{\mathbf{t}} d\Gamma + \int_{\Gamma_c} \mathbf{N}_u^{*T} \mathbf{t}_c^r d\Gamma$$

$$\mathbf{f}_3 = \int_\Omega \nabla \mathbf{N}^T \cdot \mathbf{G}_1^r d\Omega - \int_{\Gamma_q} \mathbf{N}^T \hat{q}_w d\Gamma$$

$$\mathbf{f}_4 = \int_\Omega \nabla \mathbf{N}^T \cdot \mathbf{G}_2^r d\Omega - \int_{\Gamma_q} \mathbf{N}^T \hat{q}_n d\Gamma + \int_{\Gamma_c} \mathbf{N}^T q_n^{\Gamma_c} d\Gamma - \mathbf{N}\big|_{\mathbf{x}_{\text{ap}}}^T \left(q_n^{\text{ap}}\right)^r$$

$$\mathbf{f}_5 = \int_\Omega \nabla \mathbf{N}_d^{*T} \cdot \mathbf{G}_2^r d\Omega - \int_{\Gamma_q} \mathbf{N}_d^{*T} \hat{q}_n d\Gamma + \int_{\Gamma_d} \mathbf{N}_d^{*T} q_n^{\Gamma_d} d\Gamma$$
$$+ \int_{\Gamma_c} \mathbf{N}_d^{*T} q_n^{\Gamma_c} d\Gamma - \mathbf{N}_d^*\big|_{\mathbf{x}_{\text{ap}}}^T \left(q_n^{\text{ap}}\right)^r$$

$$\mathbf{f}_6 = -\int_{\Gamma_q} \mathbf{N}^T \hat{Q}_{\text{conv}} d\Gamma - \int_{\Gamma_q} \mathbf{N}^T \hat{Q}_{\text{cond}} d\Gamma + \int_{\Gamma_c} \mathbf{N}^T \left(Q_{\text{conv}}^{\Gamma_c}\right)^r d\Gamma$$
$$+ \int_{\Gamma_c} \mathbf{N}^T \left(Q_{\text{cond}}^{\Gamma_c}\right)^r d\Gamma - \mathbf{N}\big|_{\mathbf{x}_{\text{ap}}}^T \left(Q_{\text{conv}}^{\text{ap}}\right)^r$$

$$\mathbf{f}_7 = -\int_{\Gamma_c} \mathbf{N}'^T q_n^{\Gamma_c} d\Gamma + \mathbf{N}'\big|_{x'_{\text{ap}}}^T \left(q_n^{\text{ap}}\right)^r$$

$$\mathbf{f}_8 = \int_{\Gamma_c} \mathbf{A}'^T \gamma'^r \left[\!\left[u_{y'}\right]\!\right]^r d\Gamma + \int_{\Gamma_c} \mathbf{N}'^T \rho_m'^r \left[\!\left[u_{y'}\right]\!\right]^r \mathbf{g} \cdot \mathbf{t}_{\Gamma_c} d\Gamma$$
$$- \int_{\Gamma_c} \mathbf{N}'^T \left(Q_{\text{mo}}^{\Gamma_c}\right)^r d\Gamma + \mathbf{N}'\big|_{x'_{\text{ap}}}^T \left(Q_{\text{mo}}^{\text{ap}}\right)^r$$

$$\mathbf{f}_9 = \int_{\Gamma_c} \mathbf{N}'^T \rho_m'^r v_m'^r \left[\!\left[u_{y'}\right]\!\right]^r \mathbf{g} \cdot \mathbf{t}_{\Gamma_c} d\Gamma - \int_{\Gamma_c} \mathbf{N}'^T \left(Q_{\text{cond}}^{\Gamma_c}\right)^r d\Gamma$$
$$- \int_{\Gamma_c} \mathbf{N}'^T \left(Q_{\text{conv}}^{\Gamma_c}\right)^r d\Gamma + \mathbf{N}'\big|_{x'_{\text{ap}}}^T \left(Q_{\text{conv}}^{\text{ap}}\right)^r$$

$$\mathbf{f}_{10} = -\int_{\Gamma_c} \mathbf{N}'^T k \eta_n^r p_c^r d\Gamma \quad ; \quad \mathbf{f}_{11} = k^{\text{ap}} \left(\eta_n^{\text{ap}}\right)^r p_c\big|_{\mathbf{x}_{\text{ap}}}^r$$

6

Conclusions and Recommendations

6.1 Conclusion

Effective appraisal between an immediate demand to build CCS projects and their economic and environmental risks necessitates the development of computational tools capable of accurately modeling the geoenvironmental impact of CO_2 sequestration on short and long terms. They assist engineers and authorities to make effective feasibility studies for such projects. However, developing proper computational tools for such a system is complex and typically involves numerous theoretical and numerical challenges. It involves strong coupling between physical phenomena and hydro-mechanical processes occurring in complicated geometries, ranging from micro-scale to mega-scale (regional level), and containing solid deformation, heat transfer, fluid flow and phase change. Forces and flow events in a region of several square kilometers are relevant to forces and flow events occurring on a scale of a few meters. The formation of CO_2 plume with a distinguished front traveling under a combination of diffusive, advective, viscous, mechanical and gravitational forces constitutes another challenge. Furthermore, the modeling involves different domains including porous media, hollow wellbores, and fracture cavities which entails different physics, and hence, different governing equations. As a result, a proper coupling techniques between these domains is essential.

All these would make a typical computational tool not only complicated but rather expensive. Currently, modelers spend significant time and efforts to conduct detailed analyses for designing and analyzing CO_2 geosequestration sites. A great deal is spent on generating the numerical grids or meshes, and on inputting the material and geometrical parameters, and the initial and boundary conditions. To avoid these, engineers, in many cases ignore the detailed geometrical features of the geological formations, or overlook some aspects of the involved physical processes, in favor of

saving pre-processing or running time of the simulations. This kind of practice, though in many cases successful, can have significant consequences in the near and long term futures. The simulation might be inaccurate that might lead to excessive leakage of CO_2 or solid deformation. The situation worsens especially if the domain is intersected by abandoned wellbores, or the reservoir exhibits fracturing. The later necessitates incorporation of adaptive and extra fine meshes, which is an additional burden for the engineers.

One of the main objectives of this work is to overcome the above shortcomings, via introducing an accurate, geometry- and mesh-independent, and computationally efficient numerical model. Deriving such a model, requires a well-designed conceptual model, a descriptive mathematical formulation and an innovative numerical method. To achieve this, a mixed discretization scheme, together with a multidomain coupling technique, are employed. In the mixed discretization scheme, state variables exhibiting different physical nature are treated using different numerical discretization techniques. The standard Galerkin (SG) method is utilized to model continuous and diffusive fields, and the PUM, within the framework of the extended finite element method (XFEM), is utilized to discretize the stationary or moving discontinuous fields. The discontinuities include fluid saturation discontinuities at the boundary between layers, which is fixed; discontinuities at the front between the CO_2 and the air in the wellbore, which is moving; and solid displacement discontinuities due to crack propagation, which is propagating through the domain. The multidomain coupling techniques comprise a staggered-multiple time-stepping technique for the reservoir-wellbore coupling, and a fully coupled technique for the matrix-fracture interaction.

Four computational models have been developed in this thesis. These models cover leakage via formation layers, abandoned wellbores and fractures, together with solid deformation and crack propagation. Following the extensive numerical examples, it is found that, for the normal initial and boundary conditions encountered in CO_2 geo-sequestration, leakage via abandoned wellbores and leakage via formation layers can be equally important. They both constitute the main concern in CO_2 geosequestration technology. Deformation and fracturing, together with leakage via the fractures seem, following the studied cases, a secondary concern. Although the leakage via abandoned wellbores and the leakage via formation layers appear to be equally important in terms of the quantity of leaked CO_2, the leakage through the wellbore comes with a greater risk because it can rapidly reach the ground surface. The numerical examples show that, upon the arrival of the CO_2 plume to a leaky wellbore plug, it takes around one hour for the CO_2 to reach the ground surface, and this occurs with an average velocity of approximately 0.3 m/s. The leakage velocity in the wellbore is directly related to the effective permeability of the defective plug. A several orders of magnitude increase in the effective permeability of the faulty plug, which is very likely to occur due to aging and chemical reaction between the CO_2 and the plug material, can lead to a remarkably high velocity of CO_2 in the wellbore. The temperature drop at the wellbore bottom hole, which is a result of the Joule–Thomson effect, is another concern. This gives rise to the

formation of ice (though not modelled in this thesis), which can lead to concrete shrinkage that would eventually increase the permeability of the plug. To reduce such an effect, it is suggested to examine, and improve the plugging of any abandoned wellbore within the possible reach of a CO_2 plume. The improvements can include:

- Increasing the thickness of the bottom hole plug, . This will retard the deterioration of the plug, and directly reduces the effective permeability increment rate of the plug,
- Plugging the abandoned wellbore in multiple locations, such that, in case of defect of the first plug, there is still a redundant barrier against leakage,
- Using proper capping materials.

The results of leakage via the fractures show that, in case of having a relatively less permeable cap-rock, the risk of leakage via the fractures increases. This occurs due to the capillary pressure built up beneath the impermeable layer, which in turn, increases the crack fluid pressure. This gives rise to, not only leakage via the crack, but also crack propagation itself. Hence, in case of having an impermeable cap-rock, the risk of fracturing increases as compared to the case of a relatively permeable cap layer. This sounds in contradiction to common practice, which recommends storing the CO_2 in reservoirs covered by totally impermeable cap rocks. This study clearly indicates that a totally impermeable cap rock is not necessarily the optimal solution to CO_2 geosequestration.

6.2 Recommendations for future work

The set of models presented in this work can be utilized as a framework for the development of efficient and comprehensive computational software, in such a way that engineers can carry out realistic simulations on relatively limited hardware resources and CPU time. This is possible thanks to the computational efficiency of the models, which are introduced in this thesis.

Further extensions of this work include: tailoring to other applications, improvement of the constitutive model of the solid phase, adding crack initiation and velocity, and adding dynamic forces effects to the solid medium in order to account for seismic simulations. These items are subsequently treated in the following.

Other applications

This work can be utilized as a framework for the development of computational software that can be utilized, not only for CO_2 sequestration simulations, but also for applications, which involve multiphase flow in fracturing/layered porous media, including, but not limited to,

- Hydraulic fracturing
- High enthalpy geothermal systems
- Compressed air, or other gases, energy storages

- Fluid infiltration
- Enhanced oil recovery

Constitutive models of solids

The focus in this work is placed on the fluid flow, with less emphasis on the constitutive behavior of the solid phase. The solid phase is assumed linear elastic. Adding a more complex constitutive model for the solid phase is recommended as a follow-up step.

Partially cracked elements and crack propagation velocity

In this work, the crack propagation is modeled by assuming that the crack crosses a whole element per increment. In principle, the crack might stop anywhere inside the element and can exhibit a propagation velocity. Thus, it is recommended to implement a partially cracked element (Asferg et al. 2007; Belytschko and Black 1999), together with crack propagation velocity (Schrefler et al. 2006) such that a crack can stop anywhere in the element or cross more than one element. This will improve the mesh-independency feature of the model, such that a coarse mesh allows for relatively fine crack increment sizes.

Dynamic forces effects

Dynamic forces effects (inertia terms) in the porous matrix are not considered in this work. It is recommended to include solid dynamic effects in order to simulate seismic wave generation and propagation, which extends the applicability of the models to earthquake risk assessment.

References

Adams, J.J., Bachu, S.: Equations of state for basin geofluids: algorithm review and intercomparison for brines. Geofluids 2(4), 257-271 (2002).

Al-Khoury, R., Kölbel, T., Schramedei, R.: Efficient numerical modeling of borehole heat exchangers. Computers & Geosciences 36(10), 1301-1315 (2010).

Al-Khoury, R., Sluys, L.J.: A computational model for fracturing porous media. Int. J. Numer. Methods Eng. 70(4), 423-444 (2007).

Al-Yaarubi, A.H., Pain, C.C., Grattoni, C.A., Zimmerman, R.W.: Navier-Stokes Simulations of Fluid Flow Through a Rock Fracture. Paper presented at the Second International Symposium on Dynamics of fluids and transport in fractured rock,

Arbogast, T., Wheeler, M.F.: A characteristics-mixed finite element method for advection-dominated transport problems. SIAM Journal on Numerical analysis 32(2), 404-424 (1995).

Arzanfudi, M.M., Al-Khoury, R.: On the theory of CO2 geo-sequestration. In: Al-Khoury, R., Bundschuh, J. (eds.) Computational Models for CO2 Geo-sequestration & Compressed Air Energy Storage. Sustainable Energy Developments, pp. 11-77. CRC Press, (2014)

Arzanfudi, M.M., Al-Khoury, R.: A compressible two-fluid multiphase model for CO2 leakage through a wellbore. International Journal for Numerical Methods in Fluids 77(8), 477-507 (2015).

Arzanfudi, M.M., Al-Khoury, R.: Thermo-hydrodynamic-mechanical multiphase flow model for crack propagation in deformable porous media. International Journal for Numerical Methods in Fluids, Under Review (2016).

Arzanfudi, M.M., Al-Khoury, R., Sluys, L.J.: A computational model for fluid leakage in heterogeneous layered porous media. Advances in Water Resources 73, 214-226 (2014).

Arzanfudi, M.M., Saeid, S., Al-Khoury, R., Sluys, L.J.: Multidomain-staggered coupling technique for Darcy-Navier Stokes multiphase flow: An application to CO2 Geosequestration. Finite Elements in Analysis and Design 121, 52-63 (2016).

Asferg, J.L., Poulsen, P.N., Nielsen, L.O.: A consistent partly cracked XFEM element for cohesive crack growth. International Journal for Numerical Methods in Engineering 72(4), 464-485 (2007).

Babuška, I., Melenk, J.M.: The Partition of Unity Method. Int. J. Numer. Methods Eng. 40(4), 727-758 (1997).

Barenblatt, G.I., Zheltov, I.P., Kochina, I.N.: Basic concepts in the theory of seepage of homogeneous liquids in fissured rocks [strata]. Journal of Applied Mathematics and Mechanics 24(5), 1286-1303 (1960).

Barrett, J., Knabner, P.: Finite Element Approximation of the Transport of Reactive Solutes in Porous Media. Part 1: Error Estimates for Nonequilibrium Adsorption Processes. SIAM J Numer Anal 34(1), 201-227 (1997).

Belytschko, T., Black, T.: Elastic crack growth in finite elements with minimal remeshing. International journal for numerical methods in engineering 45(5), 601-620 (1999).

Brenner, K., Cancès, C., Hilhorst, D.: Finite volume approximation for an immiscible two-phase flow in porous media with discontinuous capillary pressure. Comput Geosci 17(3), 573-597 (2013).

Brill, J.P., Mukherjee, H.: Multiphase flow in wells. Richardson, Tex.: Henry L. Doherty Memorial Fund of AIME, Society of Petroleum Engineers, (1999)

Brooks, R.H., Corey, A.T.: Hydraulic properties of porous media. Hydrology Paper No. 3, Colorado State Univ., Fort Collins, Colorado (1964).

Brown, S.R., Stockman, H.W., Reeves, S.J.: Applicability of the Reynolds equation for modeling fluid flow between rough surfaces. Geophysical Research Letters 22(18), 2537-2540 (1995).

Cances, C.: Finite volume scheme for two-phase flows in heterogeneous porous media involving capillary pressure discontinuities. ESAIM: Math Model Numer Anal 43(05), 973-1001 (2009).

Chen, Z.-X.: Transient flow of slightly compressible fluids through double-porosity, double-permeability systems—a state-of-the-art review. Transport in Porous Media 4(2), 147-184 (1989).

Cho, M.H., Choi, H.G., Yoo, J.Y.: A direct reinitialization approach of level-set/splitting finite element method for simulating incompressible two-phase flows. International Journal for Numerical Methods in Fluids, n/a-n/a (2010).

Class, H., Ebigbo, A., Helmig, R., Dahle, H., Nordbotten, J., Celia, M., Audigane, P., Darcis, M., Ennis-King, J., Fan, Y., Flemisch, B., Gasda, S., Jin, M., Krug, S., Labregere, D., Naderi Beni, A., Pawar, R., Sbai, A., Thomas, S., Trenty, L., Wei, L.: A benchmark study on problems related to CO2 storage in geologic formations. Comput. Geosci. 13(4), 409-434 (2009).

Cronshaw, M., Bolling, J.: A numerical model of the non-isothermal flow of carbon dioxide in wellbores. In: SPE California Regional Meeting 1982

Daubert, T.E., Danner, R.P.: Physical and thermodynamic properties of pure chemicals: data compilation. Design Institute for Physical Property Data, (1989)

De Borst, R., Réthoré, J., Abellan, M.-A.: Two-scale approaches for fracture in fluid-saturated porous media. Interaction and Multiscale Mechanics: an International Journal 1, 83-101 (2007).

Ebigbo, A., Class, H., Helmig, R.: CO2 leakage through an abandoned well: problem-oriented benchmarks. Computational Geosciences 11(2), 103-115 (2007).

Faghri, A., Zhang, Y.: Transport phenomena in multiphase systems. Academic Press, (2006)

Farhat, C., Park, K.C., Dubois-Pelerin, Y.: An unconditionally stable staggered algorithm for transient finite element analysis of coupled thermoelastic problems. Computer Methods in Applied Mechanics and Engineering 85(3), 349-365 (1991).

Fenghour, A., Wakeham, W.A., Vesovic, V.: The viscosity of carbon dioxide. J. Phys. Chem. Ref. Data 27(1), 31-44 (1998).

Freeston, D., Hadgu, T.: Comparison of results from some wellbore simulators using a data bank. In: Proceedings of the 10th Geothermal Workshop, New Zealand 1988, pp. 299-305

Fries, T.-P., Belytschko, T.: The extended/generalized finite element method: An overview of the method and its applications. International Journal for Numerical Methods in Engineering 84(3), 253-304 (2010).

Friis, H.A., Evje, S.: Numerical treatment of two-phase flow in capillary heterogeneous porous media by finite-volume approximations. Int. J. Numer. Anal. Model. 9(3), 505-528 (2011).

Fučík, R., Mikyška, J.: Mixed-hybrid finite element method for modelling two-phase flow in porous media. J Math Ind. 3(2), 9-19 (2011).

Ghafouri, H.R., Lewis, R.W.: A finite element double porosity model for heterogeneous deformable porous media. International Journal for Numerical and Analytical Methods in Geomechanics 20(11), 831-844 (1996).

Green, D.W.: Perry's chemical engineers' handbook, 8 ed. McGraw-hill, New York (2008)

Hadgu, T., Zimmerman, R.W., Bodvarsson, G.S.: Coupled reservoir-wellbore simulation of geothermal reservoir behavior. Geothermics 24(2), 145-166 (1995).

Hasan, A.R., Kabir, C.S.: Modeling two-phase fluid and heat flows in geothermal wells. Journal of Petroleum Science and Engineering 71(1–2), 77-86 (2010).

Hasan, A.R., Kabir, C.S., Sarica, C.: Fluid flow and heat transfer in wellbores. Society of Petroleum Engineers Richardson, TX, (2002)

Hassanizadeh, M., Gray, W.G.: Mechanics and thermodynamics of multiphase flow in porous media including interphase boundaries. Adv. Water Resour. 13(4), 169-186 (1990).

Helmig, R., Huber, R.: Comparison of Galerkin-type discretization techniques for two-phase flow in heterogeneous porous media. Adv. Water Resour. 21(8), 697-711 (1998).

IAPWS: Revised release on the IAPWS industrial formulation 1997 for the thermodynamic properties of water and steam. In. The International Association for the Properties of Water and Steam, (2007)

Ishii, M., Hibiki, T.: Thermo-fluid dynamics of two-phase flow. 2006: Springer Science. Springer, IN, USA (2006)

Kraaijeveld, F., Huyghe, J., Remmers, J., De Borst, R.: Two-dimensional mode I crack propagation in saturated ionized porous media using partition of unity finite elements. Journal of Applied Mechanics 80(2), 020907 (2013).

Kumagai, A., Yokoyama, C.: Viscosities of aqueous NaCl solutions containing CO_2 at high pressures. J. Chem. Eng. Data 44(2), 227-229 (1999).

Lewis, R., Pao, W.: Numerical Simulation of Three-Phase Flow in Deforming Fractured Reservoirs. Oil & Gas Science and Technology - Rev. IFP 57(5), 499-514 (2002).

Lewis, R.W., Ghafouri, H.R.: A novel finite element double porosity model for multiphase flow through deformable fractured porous media. International Journal for Numerical and Analytical Methods in Geomechanics 21(11), 789-816 (1997).

Lewis, R.W., Nithiarasu, P., Seetharamu, K.: Fundamentals of the finite element method for heat and fluid flow. In. John Wiley & Sons Ltd, Southern Gate, Chichester, West Sussex PO19, England, (2004)

Lewis, R.W., Schrefler, B.A.: The finite element method in the static and dynamic deformation and consolidation of porous media. Wiley, Chichester [u.a.] (1998)

Lindeberg, E.: Modelling pressure and temperature profile in a CO2 injection well. Energy Procedia 4(0), 3935-3941 (2011).

Livescu, S., Durlofsky, L.J., Aziz, K., Ginestra, J.C.: A fully-coupled thermal multiphase wellbore flow model for use in reservoir simulation. Journal of Petroleum Science and Engineering 71(3–4), 138-146 (2010).

Lu, M., Connell, L.D.: Non-isothermal flow of carbon dioxide in injection wells during geological storage. International Journal of Greenhouse Gas Control 2(2), 248-258 (2008).

Masud, A., Hughes, T.J.: A stabilized mixed finite element method for Darcy flow. Computer Methods in Applied Mechanics and Engineering 191(39), 4341-4370 (2002).

Michaelides, E.E.: Thermodynamic properties of geothermal fluids. Trans.-Geotherm. Resour. Counc. 5, 361-364 (1981).

Mohammadnejad, T., Khoei, A.R.: Hydro-mechanical modeling of cohesive crack propagation in multiphase porous media using the extended finite element method. International Journal for Numerical and Analytical Methods in Geomechanics 37(10), 1247-1279 (2013).

Mourzenko, V., Thovert, J.-F., Adler, P.: Permeability of a single fracture; validity of the Reynolds equation. Journal de Physique II 5(3), 465-482 (1995).

Nicholl, M., Rajaram, H., Glass, R., Detwiler, R.: Saturated flow in a single fracture: Evaluation of the Reynolds equation in measured aperture fields. Water Resources Research 35(11), 3361-3373 (1999).

Nordbotten, J.M., Celia, M.A., Bachu, S., Dahle, H.K.: Semianalytical Solution for CO2 Leakage through an Abandoned Well. Environmental Science & Technology 39(2), 602-611 (2004).

OPM (Open Porous Media) initiative, DuMux documentation. http://www.dumux.org/doxygen-trunk/html/class_dumux_1_1_regularized_brooks_corey.php. Accessed June 16, 2014

Pan, L., Oldenburg, C.M.: Rigorous process simulation of compressed air energy storage (CAES) in porous media systems. In: Al-Khoury, R., Bundschuh, J. (eds.) Computational Models for CO2 Geo-sequestration & Compressed Air Energy Storage. Sustainable Energy Developments, vol. 10, p. 574. CRC Press, (2014)

Pan, L., Oldenburg, C.M., Pruess, K., Wu, Y.-S.: Transient CO2 leakage and injection in wellbore-reservoir systems for geologic carbon sequestration. Greenhouse Gases: Science and Technology 1(4), 335-350 (2011a).

Pan, L., Oldenburg, C.M., Wu, Y.-S., Pruess, K.: Wellbore flow model for carbon dioxide and brine. Energy Procedia 1(1), 71-78 (2009).

Pan, L., Webb, S.W., Oldenburg, C.M.: Analytical solution for two-phase flow in a wellbore using the drift-flux model. Advances in Water Resources 34(12), 1656-1665 (2011b).

Paolucci, S.: On the Filtering of Sound from the Navier–Stokes Equations. In. Albuquerque, NM, (1982)

Park, K., Felippa, C., DeRuntz, J.: Stabilization of staggered solution procedures for fluid-structure interaction analysis. Computational methods for fluid-structure interaction problems, 95-124 (1977).

Park, K.C.: Partitioned Transient Analysis Procedures for Coupled-Field Problems: Stability Analysis. Journal of Applied Mechanics 47(2), 370-376 (1980).

Paterson, L., Lu, M., Connell, L., Ennis-King, J.: Numerical modeling of pressure and temperature profiles including phase transitions in carbon dioxide wells. In: SPE Annual Technical Conference and Exhibition 2008

Pawar, R.J., Watson, T.L., Gable, C.W.: Numerical Simulation of CO2 Leakage through Abandoned Wells: Model for an Abandoned Site with Observed Gas Migration in Alberta, Canada. Energy Procedia 1(1), 3625-3632 (2009).

Pop, I.S., Radu, F., Knabner, P.: Mixed finite elements for the Richards' equation: linearization procedure. J Comput Appl Math 168(1–2), 365-373 (2004).

Principe, J., Codina, R.: Mathematical models for thermally coupled low speed flows. Advances in Theoretical and Applied Mechanics 2, 93-112 (2009).

Probst, A., Gunn, C., Andersen, G.: A preliminary comparison of pressure drop models used in simulating geothermal production wells. In: 14th New Zealand Geothermal Workshop, Auckland University 1992, pp. 139-144

Pruess, K.: Thermal Effects During CO2 Leakage from a Geologic Storage Reservoir. In. Lawrence Berkeley National Laboratory, (2004)

Qin, L., Peszynska, M., Wheeler, M.F.: A parallel multiblock black-oil model in multimodel implementation. SPE J 7(03), 278-287 (2002).

Rathakrishnan, E.: Fluid Mechanics : An Introduction, Third ed. PHI, New Delhi (2012)

Reddy, J.N., Gartling, D.K.: The finite element method in heat transfer and fluid dynamics, Third ed. CRC press, Boca Raton, FL (2010)

Rehm, R.G., Baum, H.R.: The Equations of Motion for Thermally Driven, Buoyant Flows. J. Res. Bur. Stand. 83(3), 297-308 (1978).

Remoroza, A.I., Moghtaderi, B., Doroodchi, E.: Coupled wellbore and 3d reservoir simulation of a co2 egs. In: Proceedings, SGP-TR-191, 36th Workshop on Geothermal Reservoir Engineering, Stanford University, Stanford, California 2011

Réveillère, A., Rohmer, J.: Managing the risk of CO2 leakage from deep saline aquifer reservoirs through the creation of a hydraulic barrier. Energy Procedia 4, 3187-3194 (2011).

Salimzadeh, S., Khalili, N.: A three-phase XFEM model for hydraulic fracturing with cohesive crack propagation. Computers and Geotechnics 69, 82-92 (2015).

Schlumberger: ECLIPSE Simulators. http://www.software.slb.com/products/foundation/Pages/eclipse-black-oil.aspx (2015). Accessed 11 June 2015

Schrefler, B.A., Secchi, S., Simoni, L.: On adaptive refinement techniques in multi-field problems including cohesive fracture. Computer Methods in Applied Mechanics and Engineering 195(4–6), 444-461 (2006).

Sengers, J.V., Watson, J.T.R.: Improved international formulations for the viscosity and thermal conductivity of water substance. J. Phys. Chem. Ref. Data 15(4), 1291-1314 (1986).

Shi, H., Holmes, J., Durlofsky, L., Aziz, K., Diaz, L., Alkaya, B., Oddie, G.: Drift-flux modeling of two-phase flow in wellbores. Spe Journal 10(1), 24-33 (2005).

Span, R., Wagner, W.: A new equation of state for carbon dioxide covering the fluid region from the triple-point temperature to 1100 K at pressures up to 800 MPa. J. Phys. Chem. Ref. Data 25(6), 1509-1596 (1996).

Spycher, N., Pruess, K., Ennis-King, J.: CO_2-H_2O mixtures in the geological sequestration of CO_2. I. Assessment and calculation of mutual solubilities from 12 to 100°C and up to 600 bar. Geochim. Cosmochim. Acta 67(16), 3015-3031 (2003).

Stone, T., Edmunds, N., Kristoff, B.: A comprehensive wellbore/reservoir simulator. In: SPE Symposium on Reservoir Simulation 1989

Szymkiewicz, A., Helmig, R., Kuhnke, H.: Two-phase flow in heterogeneous porous media with non-wetting phase trapping. Transp Porous Media 86(1), 27-47 (2011).

Talebian, M., Al-Khoury, R., Sluys, L.J.: A computational model for coupled multiphysics processes of CO2 sequestration in fractured porous media. Adv Water Resour 59(0), 238-255 (2013a).

Talebian, M., Al-Khoury, R., Sluys, L.J.: Coupled electrokinetic–hydromechanic model for CO2 sequestration in porous media. Transp. Porous Media 98, 287–321 (2013b).

Turns, S.: Thermal-fluid sciences: an integrated approach, 1 ed. Cambridge University Press, NY, USA (2006)

van den Bosch, M.J., Schreurs, P.J.G., Geers, M.G.D.: An improved description of the exponential Xu and Needleman cohesive zone law for mixed-mode decohesion. Engineering Fracture Mechanics 73(9), 1220-1234 (2006).

Van Duijn, C., Mikelic, A., Pop, I.S.: Effective equations for two-phase flow with trapping on the micro scale. SIAM J Appl Math 62(5), 1531-1568 (2002).

Van Duijn, C., Molenaar, J., De Neef, M.: The effect of capillary forces on immiscible two-phase flow in heterogeneous porous media. Transp Porous Media 21(1), 71-93 (1995).

Van Duijn, C.J., De Neef, M.J.: Similarity solution for capillary redistribution of two phases in a porous medium with a single discontinuity. Adv. Water Resour. 21(6), 451-461 (1998).

van Genuchten, M.T.: A closed-form equation for predicting the hydraulic conductivity of unsaturated soils. Soil Sci. Soc. Am. J. 44(5), 892-898 (1980).

Vogel, T., Gerke, H., Zhang, R., Van Genuchten, M.T.: Modeling flow and transport in a two-dimensional dual-permeability system with spatially variable hydraulic properties. Journal of Hydrology 238(1), 78-89 (2000).

Wallis, G.B.: One-dimensional two-phase flow, vol. 1. McGraw-Hill New York, (1969)

Wells, G., Sluys, L.: A new method for modelling cohesive cracks using finite elements. International Journal for Numerical Methods in Engineering 50(12), 2667-2682 (2001).

Yeo, I.W., Ge, S.: Applicable range of the Reynolds equation for fluid flow in a rock fracture. Geosciences Journal 9(4), 347-352 (2005).

Zeng, F., Zhao, G., Zhu, L.: Detecting CO2 leakage in vertical wellbore through temperature logging. Fuel (2011).

Zi, G., Belytschko, T.: New crack-tip elements for XFEM and applications to cohesive cracks. Int. J. Numer. Meth. Engng 57, 2221-2240 (2003).

Zienkiewicz, O., Taylor, R., Zhu, J.: The finite element method: its basis and fundamentals. In. Elsevier Butterworth-Heinemann, (2005)

Zienkiewicz, O.C., Paul, D.K., Chan, A.H.C.: Unconditionally stable staggered solution procedure for soil-pore fluid interaction problems. International Journal for Numerical Methods in Engineering 26(5), 1039-1055 (1988).

Zimmerman, R.W., Chen, G., Hadgu, T., Bodvarsson, G.S.: A numerical dual-porosity model with semianalytical treatment of fracture/matrix flow. Water resources research 29(7), 2127-2137 (1993).

Zuber, N., Findlay, J.: Average volumetric concentration in two-phase flow systems. Journal of Heat Transfer 87(4), 453-468 (1965).

Propositions

Accompanying the dissertation

Computational Modeling of
Multiphysics Multidomain Multiphase Flow in Fracturing Porous Media

Leakage Hazards in CO_2 Geosequestration

by

Mehdi MUSIVAND ARZANFUDI

1. None of the CO_2 emission mitigation technologies, including CO_2 geo-sequestration, can solely solve the greenhouse effect problem. After all, we have to deploy a combination of several of them.
2. CO_2 geo-sequestration, if well designed and properly implemented, does not necessarily change the balance in the subsurface.
3. Full-scale experimental investigation of CO_2 geo-sequestration risks is essential, but obviously, this will be a treatment after death. That's why simulation tools are indispensable requirements for CO_2 geo-sequestration projects.
4. Deriving an accurate, geometry- and mesh-independent, and computationally efficient transient model for thermo-hydrodynamic-mechanical behavior of a multiphase domain, exhibiting deformation and crack propagation requires a well-designed conceptual model, a descriptive mathematical formulation and an innovative numerical method.
5. In order for a computational model to be a representative of reality, the physics has to be described and formulated properly.
6. Computational efficiency cannot be achieved by merely optimizing the codes, algorithms and solvers, and keep on using the standard discretization procedures. The mixed discretization scheme is a powerful remedy.
7. No matter how powerful and accessible the high performance computing (HPC) facilities become, the need for more computational efficiency always remains, as far as geoenvironmental simulations are concerned.
8. Development of non-standard computational tools might be more complex than development of standard tools; however, they can be much easier and efficient in operation.
9. Yesterday, I was clever, so I wanted to change the world. Today, I am wise, so I am changing myself. Rumi, 13th-century Persian poet

These propositions are regarded as opposable and defendable, and have been approved as such by the supervisors, dr. ir. R. Al-Khoury and prof. dr. ir. L.J. Sluys.

Stellingen
behorende bij het proefschrift

Numerieke Modellering van
Multifysische Multidomein Multifase Stroom in Scheurende Poreuze Media
Gevaren van Lekkage bij CO_2-Geosequestratie

door
Mehdi MUSIVAND ARZANFUDI

1. Geen van de CO_2-uitstoot beperkende technologieën, waaronder CO_2 geo-sequestratie, kan het broeikaseffect probleem alleen oplossen. We moeten een combinatie van verschillende oplossingstechnieken inzetten.
2. CO_2 geo-sequestratie, mits goed ontworpen en correct uitgevoerd, hoeft niet persé het evenwicht in de ondergrond te veranderen.
3. Experimenteel onderzoek op volledige schaalgrootte van de CO_2 geo-sequestratie risico's is van essentieel belang, maar uiteraard is dit een behandeling na de dood. Daarom zijn simulatie-gereedschappen onmisbaar voor CO_2 geo-sequestratie projecten.
4. Het afleiden van een nauwkeurig, geometrie- en mesh-onafhankelijk tijdsafhankelijk model voor thermo-hydrodynamisch-mechanisch gedrag van een multifase domein, dat vervorming en scheurgroei toelaat, vereist een goed ontworpen conceptueel model, een beschrijvende wiskundige formulering en een innovatief numerieke methode.
5. Om een numeriek model de werkelijkheid te laten vertegenwoordigen, moet de fysica goed beschreven en goed uitgewerkt worden.
6. Numerieke efficiëntie kan door slechts het optimaliseren van de codes, algoritmen en solvers niet worden bereikt, als vastgehouden wordt aan de standaard discretisatie. De gemengde discretisatie is een krachtige oplossing.
7. Het maakt niet uit hoe krachtig en toegankelijk de high performance computing (HPC) voorzieningen worden, er blijft altijd de behoefte aan meer numerieke efficiëntie voor zover het milieu-technische simulaties betreft.
8. De ontwikkeling van niet-standaard numerieke gereedschappen is wellicht complexer dan de ontwikkeling van standaard gereedschappen; zij kunnen echter veel gemakkelijker en efficiënte zijn in het gebruik.
9. Gisteren was ik slim, dus wilde ik de wereld veranderen. Vandaag ben ik verstandig, dus verander ik mezelf. *Rumi, 13de-eeuwse Perzische dichter*

Deze stellingen worden opponeerbaar en verdedigbaar geacht, en zijn als zodanig goedgekeurd door de copromotor, dr. ir. R. Al-Khoury, en promotor prof. dr. ir. L. J. Sluys.

Acknowledgements

Starting to write the acknowledgements for a PhD thesis, conveys several meanings. First, it is a good sign that a several years effort has come to a satisfactory conclusion. But besides that, it shows that there have been valuable support and collaborations that need to be appreciated. I personally believe that without these support and collaborations, I would not have been able to accomplish my PhD, at least with the same quality as it is. When I think about the achievements of my PhD, I realize that getting to know all these supportive people is as important as my PhD itself.

Firstly, I gratefully acknowledge the financial support for my project by Agentschap NL (Dutch Ministry of Economic Affairs), and in particular, my sincere appreciation goes to the project leader, ir. Jos Reijnders, for his support, comments and encouragement.

Then and foremost, I would like to express my genuine gratitude to my supervisor Dr. Rafid Al-Khoury for advising me on my PhD study, and for his encouragement, patience, dedication, motivation, and immense knowledge. He has been a tremendous mentor as well as a supportive and reliable friend.

I would like to express my special appreciation and thanks to my promotor Prof. Bert Sluys, for giving me the opportunity to join his group, and for the continuous support of my PhD study. His insightful advices on my research have been precious to me.

Besides my advisors, I would like to thank the rest of my thesis committee: Prof. Robert W. Zimmerman, Prof. Bernhard A. Schrefler, Prof. Cristina Jommi, Prof. Rainer Helmig, and Prof. Michael A. Celia, for their careful reading of my thesis and their comments and encouragement. Thanks also to Erik Jan Lingen from Dynaflow Research Group, for the support on Jem/Jive C++ library. I also express my gratefulness to Sanaz Saeid for her collaboration.

I am utterly grateful to Erik Simons and Nynke Verhulst who helped me translating my thesis summary and propositions into Dutch. My sincere thanks go to Mojtaba Talebian who has always been a genuine friend, supportive colleague and awesome officemate. Then I would like to express my words of gratitude to Salar Mostofizadeh who has been a terrific friend and motivating colleague and officemate. My special appreciation goes to Amin Karamnejad, who is a reliable and fantastic friend as well as a supportive colleague. I am extremely thankful to Luis Magalhaes Pereira and Noori Bni Lam, for being such wonderful friends and colleagues. I was also fortunate to share office with Marcello Malagù, a nice colleague and a good friend.

I thank the rest of the Computational Mechanics (CM) group, those who have left the group, and those who are still there, for all the collaborations, stimulating discussions, as well as all the friendship and fun we have had during the last several years: Adriaan Sillem, Ali Paknahad, Angelo Simone, Behrouz Arash, Benoit Mercatoris, Davide Grazioli, Fariborz Ghavamian, Franciscus Everdij, Frans van der Meer, Jaap Weerheijm, Jafar Amani Dashlejeh, Jitang Fan, Kai Li, Lars Voormeeren, Liting Qiu, Mingzhao Zhuo, Mohammad Latifi, Mohsen Goudarzi, Nghi Le, Oriol Lloberas Valls, Osvalds Verners, Prashanth Srinivasan, Prithvi Mandapalli, Tiziano li Piani, Wouter Steenstra, Yangyueye Cao, Yaolu Liu, Awais Ahmed, Jafar Amani Dashlejeh, and Somaieh Akbar. My special thanks go to our supportive and kind secretary Anneke Meijer.

I would also like to thank all other colleagues and friends who have directly or indirectly contributed to my PhD work, and those who have helped to turn my working environment into a likable and pleasant atmosphere.

Last, but not least, I thank my family for their precious spiritual support. Words cannot express how grateful I am to my mother, for her unconditional support and love.

About the Author

Mehdi M. Arzanfudi received his BSc, MSc and PhD degrees in Aerospace Engineering from Amirkabir University of Technology, Tehran (PhD in 2007). During his PhD in Amirkabir University of Technology, he developed computational methods for meshfree (a.k.a. meshless) simulation of structures. He also worked, till 2012, in Automotive Industries mostly as CAE (Computer Aided Engineering) Engineer, where he utilized simulations, mostly using commercial packages, in support of product design and development process. He started a PhD in Civil Engineering and Geoscience Faculty of Delft University of Technology in 2012. During his PhD in TU Delft, he has developed finite element computational models for simulation of multiphysics multidomain multiphase flow in fracturing porous media, with applications in geo-environment, and in particular, leakage hazards in CO2 sequestration.

Modeling CO_2 leakage in a deformable and fracturing porous medium constitutes the focal point of this thesis.

To this aim, a computationally efficient multiphysics multidomain multiphase numerical modeling framework has been developed which accounts for all important physical processes, interacting domains, and material phases.